

Imperial College of Science, Technology and Medicine  
University of London

# **Simulation of Unsteady Turbomachinery Flows for Forced Response Predictions**

by  
Luca Sbardella

A thesis submitted to the University of London  
for the degree of Doctor of Philosophy

Centre of Vibration Engineering  
Department of Mechanical Engineering  
Imperial College of Science, Technology and Medicine  
Exhibition Road, London SW7 2BX  
United Kingdom

June 2000

*Dedicated to  
Franca, Osvaldo ed Elena*

# Acknowledgments

This thesis represents the conclusion of a twenty two year episode in my life dedicated almost entirely to formal education. In such moment I feel very fortunate to have shared important experiences with so many friends and teachers.

During my permanence at Imperial college I had the pleasure to have worked with Dr. Mehmet Imregun who has been a constant source of good ideas and guidance as well as letting me the freedom of research and travel. I would also like to thanks Dr. Mehdi Vahdati, Dr. Naser Sayma and Dr. Cirille Bréard for their support and useful discussions throughout the duration of the research project.

# Preface

The flow through the various stages of turbomachines is inherently unsteady, primarily due to the relative motion between adjacent stator and rotor blade rows, though other factors such as aerodynamic mistuning, temperature distortions due to blocked burners may also become significant. The unsteadiness can persist through several stages and may excite either a structural or an acoustic mode and such resonances can cause severe vibration problems. The overall picture is further complicated because of other events such as surge, stall and rotating stall. In any case, such unstable phenomena are increasingly becoming limiting factors in developing improved-efficiency designs, especially when flexible, slender and unshrouded blades are used. From an industrial prospective, it is clear that there is a pressing need for formulating validated predictive models to reduce the design cycle and, consequently, cost.

Such is the aim of the present work and two different methods of simulating 3D viscous unsteady turbomachinery flows were developed: non-linear time marching and frequency linearised method. The contributions to CFD modelling include an efficient discretisation of the viscous terms, the linearisation of the turbulence model and the development of a multigrid methodology for viscous unsteady flows. Although both the non-linear and linearised methods can use general unstructured meshes, a novel semi-structured mesh generator was developed for computational efficiency. Over standard structured meshes, such a route provides a significant improvement both in the smoothness of the grid-spacing and in resolving particular aspects of the blade passage geometry. Leading- and trailing-edge regions are discretised without generating superfluous points, while wakes and shocks can be captured using local refinement techniques. A particular feature of the methodology is the use of mixed element grids, consisting of triangles and quadrilaterals in 2D, and of tetrahedra, pyramids, triangular prisms and hexahedra in 3D.

The final part of the thesis presents a detailed unsteady flow analysis for forced

response prediction of a 3D transonic turbine stage. The main aim is to compare the performance of the non-linear time-marching and linearised flow simulation methods when predicting the unsteadiness due to stator-rotor interactions. The results obtained with the two method were found to be quantitatively similar although non-linearities are evident in the leading-edge region where the potential flow interaction is dominant.

Finally, an analysis of the different unsteady effects caused by potential flow and wake-blade interactions was also made.

# Contents

<b>Acknowledgments</b>	i
<b>Preface</b>	ii
<b>Contents</b>	iv
<b>Nomenclature</b>	viii
<b>List of Figures</b>	xii
<b>1 Introduction</b>	1
1.1 Unsteady Turbomachinery Flows . . . . .	1
1.1.1 Forced response . . . . .	2
1.1.2 Flutter . . . . .	5
1.1.3 Inherent unsteadiness . . . . .	7
1.1.4 Further aspects of unsteady flows in turbomachines . . . . .	8
1.2 Computational Prediction Methods . . . . .	9
1.2.1 Methods for linearised unsteady aerodynamics . . . . .	10
1.2.2 Non-linear time-marching methods . . . . .	11
1.3 CFD Methods for Compressible Flows . . . . .	13
1.3.1 A brief review of flux discretisation methods . . . . .	14
1.3.2 Structured versus unstructured grid debate . . . . .	15
1.3.3 Time integration using multigrid methods . . . . .	17
1.3.4 Non-reflecting boundary conditions . . . . .	20
1.4 Objectives . . . . .	22
1.5 Contributions of the Thesis . . . . .	23
1.5.1 CFD methods . . . . .	23
1.5.2 Understanding of unsteady flows . . . . .	25

<b>2 Semi-structured Mesh Generator for Turbomachinery Blades</b>	<b>30</b>
2.1 Introduction . . . . .	30
2.2 Generation of Prismatic Grid . . . . .	33
2.2.1 Geometry modelling . . . . .	34
2.2.2 Unstructured mesh generation . . . . .	36
2.2.3 Quasi-conformal mapping . . . . .	37
2.3 The Program LEVMAP . . . . .	39
2.4 Concluding Remarks . . . . .	40
<b>3 Hybrid Grid Solver for Turbulent Viscous Flow</b>	<b>45</b>
3.1 Introduction . . . . .	46
3.2 Favre Averaged Navier-Stokes Equations . . . . .	48
3.2.1 Mean flow equations . . . . .	48
3.2.2 Boundary conditions . . . . .	51
3.3 Spatial Discretisation . . . . .	53
3.3.1 Inviscid discretisation . . . . .	54
3.3.2 Viscous discretisation . . . . .	58
3.4 Time Integration . . . . .	60
3.4.1 Steady state algorithm . . . . .	60
3.4.2 Unsteady time-marching algorithm . . . . .	61
3.5 Test Cases . . . . .	63
3.5.1 Steady flow over a turbine rotor blade . . . . .	63
3.5.2 Impulsively accelerated flat plate . . . . .	67
3.5.3 Vortex shedding past a cylinder . . . . .	70
3.5.4 Transonic buffeting over a bicircular airfoil . . . . .	73
3.6 Concluding Remarks . . . . .	75
<b>4 Linearised Unsteady Navier-Stokes Solver</b>	<b>80</b>
4.1 Towards Viscous linearised representations . . . . .	80
4.2 Time-linearised Navier-Stokes Equations . . . . .	82
4.2.1 Linearisation . . . . .	82
4.2.2 Boundary conditions . . . . .	84
4.3 Numerical Implementation . . . . .	88
4.3.1 Inviscid fluxes . . . . .	88
4.3.2 Viscous terms . . . . .	89

4.3.3	Time integration . . . . .	90
4.4	Test Cases . . . . .	91
4.4.1	Linear flat-plate cascade . . . . .	91
4.4.2	Unsteady laminar boundary layer on a flat plate . . . . .	96
4.4.3	Turbine cascade . . . . .	97
4.5	Concluding Remarks . . . . .	103
<b>5</b>	<b>Stator-Rotor Interaction in a Transonic Turbine Stage</b>	<b>112</b>
5.1	Introduction . . . . .	112
5.1.1	Description of the problem . . . . .	113
5.1.2	Experimental details . . . . .	115
5.2	Steady State Flow Analysis . . . . .	116
5.2.1	Computational mesh . . . . .	117
5.2.2	Boundary conditions and computational details . . . . .	120
5.2.3	Results of steady-state flow calculation . . . . .	120
5.2.4	Secondary and tip-clearance flow . . . . .	121
5.3	Rotor Unsteady Flow Analysis . . . . .	124
5.3.1	Sources of unsteadiness . . . . .	124
5.3.2	Comparison with measured data . . . . .	125
5.3.3	Vortical-flow interaction effects . . . . .	126
5.3.4	Potential-flow interaction effects . . . . .	128
5.3.5	Summary of the main findings . . . . .	130
5.4	Linear versus Non-linear Analysis . . . . .	131
5.4.1	Analysis at mid-height section . . . . .	131
5.4.2	Reconstructed wave-forms . . . . .	132
5.5	Concluding Remarks . . . . .	133
<b>6</b>	<b>Conclusions and Racomendations for Further Work</b>	<b>160</b>
	<b>Bibliography</b>	<b>165</b>
<b>A</b>	<b>Non-Dimensional Variables</b>	<b>182</b>
<b>B</b>	<b>Spalart Allmaras Turbulence Model</b>	<b>184</b>
B.1	One Equation Spalart-Allmaras Model . . . . .	184
B.2	Linearised Turbulence Model . . . . .	185

<b>C Aerodynamic Forcing Functions</b>	<b>187</b>
C.1 Spatial Non-uniformities . . . . .	187
C.2 Vortical, Potential and Entropy Splitting . . . . .	189
C.3 Matching Linear Theory and Available Data . . . . .	192
C.4 Example . . . . .	193
<b>D Preconditioned Agglomeration Multigrid for Hybrid Grids</b>	<b>195</b>
D.1 Introduction . . . . .	195
D.2 Algorithm Description . . . . .	197
D.2.1 FAS scheme . . . . .	199
D.2.2 Transfer Operators . . . . .	200
D.3 Smoother . . . . .	201
D.3.1 Time-stepping . . . . .	202
D.3.2 Preconditioners . . . . .	203
D.4 Example . . . . .	206
D.5 Concluding Remarks . . . . .	206

# Nomenclature

## Latin

$c$	Dimensionless speed of sound and airfoil chord
$\mathcal{D}$	Artificial dissipation column vector
$E$	Dimensionless total energy per unit mass
$f$	Dimensional frequency [Hz]
$\vec{\mathbf{F}}$	Inviscid fluxes vector with Cartesian column vector components ( $\mathbf{F}_1, \mathbf{F}_2, \mathbf{F}_3$ )
$\mathcal{F}$	Numerical inviscid flux function
$\vec{\mathbf{G}}$	Viscous fluxes vector with Cartesian column vector components ( $\mathbf{G}_1, \mathbf{G}_2, \mathbf{G}_3$ )
$\mathcal{G}$	Numerical viscous flux function
$H$	Dimensionless total enthalpy per unit mass
$i$	$\sqrt{-1}$
$[\mathbf{I}]$	Identity matrix
$I$	Mesh point
$\text{Im}$	Imaginary part of complex number
$J_s$	Mesh point connected to $I$ by an edge
$L_\tau$	Pseudo time-stepping operator
$\mathcal{L}$	Pseudo-Laplacian operator for 4th order artificial dissipation
$m$	Fourier mode number
$M$	Mach number
$N$	Test function of Finite Element method
$\vec{n}$	Unit normal vector
$p$	Dimensionless static pressure
$[\mathbf{P}]$	Preconditioner matrix

$Pr$	Prandtl number
$r$	radial coordinate (cylindrical coordinate system $x, r, \theta$ )
$\mathbf{R}$	Right hand side, residual vector
$Re$	Reference Reynolds number
$\text{Re}$	Real part of complex number
$\mathcal{S}$	Boundary of control volume $\mathcal{V}$
$\mathbf{S}$	Column vector of source terms
$St$	Strouhal number
$t$	Physical time
$T$	Dimensionless static temperature
$\vec{u}$	Dimensionless fluid velocity vector in the relative frame of reference
$u_1, u_2, u_3$	Components of $\vec{u}$ in Cartesian coordinate system
$u_x, u_r, u_\theta$	Components of $\vec{u}$ in cylindrical coordinate system
$\mathbf{U}$	Column vector of dimensionless conservative variables
$\vec{v}$	Dimensionless fluid velocity vector in the absolute frame of reference
$v_1, v_2, v_3$	Components of $\vec{v}$ in Cartesian coordinate system
$v_x, v_r, v_\theta$	Components of $\vec{v}$ in cylindrical coordinate system
$\mathcal{V}$	Control volume
$\vec{x}$	Cartesian coordinate vector
$x, y, z$	Cartesian coordinate components

## Greek

$\gamma$	Specific heat ratio
$\delta_{ij}$	Kroneker delta function
$\Delta\theta$	Blade pitch (rad)
$\Delta t$	Physical time step
$\Delta\tau$	Pseudo time step
$\vec{\eta}_{IJs}$	Metric vector associated with edge $IJs$
$\theta$	Tangential coordinate (cylindrical coordinate system $x, r, \theta$ )
$\mu$	Dimensionless dynamic viscosity
$\nu$	Dimensionless kinematic viscosity
$\rho$	Dimensionless static density

$\sigma$	Courant Friedrichs Lewy (CFL) number
$\tau_{IJ_s}$	Laplacian weight associated with edge $IJ_s$
$\phi$	Interblade phase angle
$\psi$	Limiting function for inviscid fluxes
$\omega$	Reduced frequency (equation A.8)
$\Omega$	Dimensionless angular velocity

## Subscript

$\infty$	Far field
$imp$	Implicit time marching algorithm
$is$	Isentropic
$l$	Laminar or Laplacian
$m$	Fourier mode number or mixed derivative
$q$	Runge-Kutta stage level
$ref$	Reference value of physical quantity
$t$	Turbulent
$0$	Stagnation value of thermodynamic quantity

## Superscript

$l$	Pseudo time level
$n$	Physical time level
$T$	Transpose

## Standard abbreviations

ALE	Arbitrary Lagrangian-Eulerian
ALiNNS	Hybrid grid flow solver
CFL	Courant Friedrichs Lewy number
CPU	Central processing unit (time)
EO	Engine order
FV	Finite volume
GFE	Galerkin finite element

LEO	Low engine order
LEVMAP	Semi-structured mesh generator
LP	Low pressure (turbine)
HP	High pressure (turbine)
ODE	Ordinary differential equation
NGV	Nozzle guide vane
TVD	Total variation diminishing
VKI	Von Karman Institute
1D	one dimensional
2D	two dimensional
3D	three dimensional

# List of Figures

1.1	Campbell diagram for a rotor blade (from Sisto 1987). x non-synchronous excitation (flutter), o forced response resonance. . . . .	26
1.2	Blade flutter boundaries on compressor map (from Sisto 1987) . . . . .	27
1.3	Turbine stage with different number of blades in each row . . . . .	28
1.4	Three blade rows computational mesh for a 11 struts, 33 VIGVs and 36 rotor blades (from Sayma et al. 1999) . . . . .	29
2.1	Typical structured H-mesh for a fan blade geometry . . . . .	31
2.2	Fully unstructured mesh on suction surface . . . . .	32
2.3	Geometry definition of an NGV blade at different radial levels . . . . .	35
2.4	Parametric 2D planes for four different radial levels . . . . .	36
2.5	Meshes in the master plane . . . . .	38
2.6	Mapping procedure . . . . .	41
2.7	Structured meshes for mapping and corresponding mapped unstructured meshes at three radial levels . . . . .	42
2.8	Semi-structured mesh for a radial-flow turbomachine . . . . .	43
2.9	Semi-structured mesh for a snubbed fan assembly . . . . .	44
3.1	Direction of blade rotation . . . . .	49
3.2	Control volume for node $I$ and metric vector $\vec{\eta}_{IJ_s}$ for edge $IJ_s$ . . . . .	54
3.3	Stencils for a quadrilateral mesh . . . . .	56
3.4	Contribution of diagonal links to Laplacian weight for a quadrilateral mesh . . . . .	60
3.5	VKI LS59 rotor blade. Computational mesh with zoom views at leading- and trailing-edges . . . . .	64
3.6	VKI LS59 rotor blade. Agglomerated grids . . . . .	65
3.7	VKI LS59 rotor blade. $M_{is2} = 1$ , $Re_2 = 7.6 \cdot 10^5$ . Isentropic Mach number distribution . . . . .	66

3.8	VKI LS59 rotor blade. $M_{is2} = 1$ , $Re_2 = 7.6 \cdot 10^5$ . Computed solution	67
3.9	VKI LS59 rotor blade. Computed solutions . . . . .	68
3.10	VKI LS59 rotor blade. Residual history . . . . .	69
3.11	Impulsively started flat plate. $M_\infty = 0.2$ , $Re_\infty = 40,000$ . Velocity profiles and residual history . . . . .	71
3.12	Circular cylinder. Computational mesh . . . . .	72
3.13	Circular cylinder. Agglomerated grids . . . . .	73
3.14	Circular cylinder. Computed Strouhal number and $c_p$ evolution . .	74
3.15	Circular cylinder. Instantaneous particle traces . . . . .	77
3.16	Bicircular airfoil. $M_\infty = 0.775$ , $Re_\infty = 7 \cdot 10^6$ . Instantaneous Mach number contours . . . . .	78
3.17	Bicircular airfoil. Computed pressure coefficient . . . . .	79
4.1	Flat plate cascade. Geometry and computational domain . . . . .	92
4.2	LINSUB test case. Pressure jump on flat plate due to wake/rotor interaction ( $\omega = \pi$ , $\phi = -90^\circ$ ) . . . . .	93
4.3	LINSUB test case. Pressure jump on flat plate due to upstream acoustic wave ( $\omega = 2$ , $\phi = 0^\circ$ ) . . . . .	94
4.4	LINSUB test case. Pressure jump on flat plate due to bending oscillation ( $\omega = 2$ , $\phi = 90^\circ$ ) . . . . .	95
4.5	Computational domain for laminar flow over a flat plate cascade . .	96
4.6	Steady laminar flow over a cascade of flat plates . . . . .	98
4.7	Unsteady wall shear stresses for an oscillating laminar boundary layer	99
4.8	$11^{th}$ Standard configuration. Viscous mesh . . . . .	100
4.9	$11^{th}$ Standard configuration - subsonic case. Steady-state Mach contours . . . . .	101
4.10	$11^{th}$ Standard configuration - subsonic case. Isentropic Mach number distribution on the blade . . . . .	105
4.11	$11^{th}$ Standard configuration - transonic case. Steady-state Mach contours . . . . .	106
4.12	$11^{th}$ Standard configuration - transonic case. Isentropic Mach number distribution on the blade . . . . .	107
4.13	$11^{th}$ Standard configuration - subsonic case. Amplitude of $\tilde{c}_p$ ( $\omega = 0.21$ , $\phi = 180^\circ$ ) . . . . .	108

4.14	$11^{th}$ Standard configuration - subsonic case. Phase of of $\tilde{c}_p$ ( $\omega = 0.21$ , $\phi = 180^\circ$ ) . . . . .	109
4.15	$11^{th}$ Standard configuration - transonic case. Amplitude of $\tilde{c}_p$ ( $\omega = 0.15$ , $\phi = 180^\circ$ ) . . . . .	110
4.16	$11^{th}$ Standard configuration - transonic case. Phase of of $\tilde{c}_p$ ( $\omega = 0.15$ , $\phi = 180^\circ$ ) . . . . .	111
5.1	Meridional view of the RT27a turbine stage . . . . .	115
5.2	Computational mesh of RT27a turbine stage (564,660 points) . . . . .	118
5.3	Computational mesh at tip end wall of RT27a rotor blade . . . . .	119
5.4	Computational mesh at mid-height section of RT27a turbine stage .	134
5.5	Boundary conditions of RT27a turbine stage . . . . .	135
5.6	Steady state pressure contours $\frac{p}{p_{01}}$ and particle traces on the RT27a rotor surface . . . . .	135
5.7	Isentropic steady-state Mach number distribution at mid-height section of RT27a rotor blade . . . . .	136
5.8	RT27a rotor leading-edge pressure levels. (*) Leading-edge kulite measured data, (-) computed . . . . .	137
5.9	RT27a rotor blade: isentropic steady-state Mach number distribution at different span-wise positions . . . . .	138
5.10	Steady state pressure contours $\frac{p}{p_{01}}$ and particle traces at 1% span of RT27a rotor blade . . . . .	139
5.11	Pressure contours $\frac{p}{p_{01}}$ and particle traces at different $r\theta - r$ planes in the RT27a rotor passage . . . . .	140
5.12	Steady state pressure contours $\frac{p}{p_{01}}$ and particle traces inside the RT27a rotor tip-gap region . . . . .	141
5.13	Steady state solution at the RT27a NGV outlet boundary (2 passages)	142
5.14	First (left) and second (right) Fourier components of spatial non-uniformities of RT27a NGV outlet solution (1 passage) . . . . .	143
5.15	Vortical and potential components of dimensionless absolute velocity variation at RT27a NGV outlet (reconstructed using first twenty harmonics) . . . . .	144
5.16	Amplitude (left) and Phase (right) of first Fourier component of unsteady pressure $p/p_0$ in the RT27a rotor blade. Potential mode (blue), vortical mode (red), superposed (black) and measured (*). .	145

5.17 Amplitude (left) and Phase (right) of second Fourier component of unsteady pressure $p/p_0$ in the RT27a rotor blade. Potential mode (blue), vortical mode (red) and superposed (black), measured (stars).	146
5.18 Vortical-flow interaction in the RT27a rotor passage at mid-height section (first Fourier component). Unsteady dimensionless absolute velocity fluctuations (left) and unsteady particle traces superimposed on dimensionless unsteady pressure fluctuations (right) . . . . .	147
5.19 Vortical-flow interaction in the RT27a rotor passage at mid-height section (first Fourier component) continued. Unsteady dimensionless absolute velocity fluctuations (left) and unsteady particle traces superimposed on dimensionless unsteady pressure fluctuations (right)	148
5.20 Unsteady pressure on RT27a rotor blade due to Wake-rotor interaction (first Fourier component) . . . . .	149
5.21 Unsteady pressure on RT27a rotor blade due to Wake-rotor interaction (second Fourier component) . . . . .	150
5.22 Unsteady pressure on RT27a rotor blade due to potential flow interaction (first Fourier component) . . . . .	151
5.23 Unsteady pressure on RT27a rotor blade due to potential flow interaction (second Fourier component) . . . . .	152
5.24 Steady-state Mach number contours on RT27a rotor mid-section and Kulite sensor position . . . . .	153
5.25 RT27a rotor blade mid-section. First Fourier component of dimensionless unsteady pressure. Linear method (blue), non-linear method (red) and measured data (stars). . . . .	154
5.26 RT27a rotor blade mid-section. Second Fourier component of dimensionless unsteady pressure. Linear method (blue), non-linear method (red) and measured data (stars). . . . .	155
5.27 RT27a rotor blade mid-section. Third Fourier component of dimensionless unsteady pressure. Linear method (blue), non-linear method (red) and measured data (stars). . . . .	156
5.28 RT27A rotor blade mid-section. Comparison of unsteady pressure between linear results (blue), nonlinear results (red) and measured data (black) . . . . .	157

5.29 RT27A rotor blade mid-section (continued 1). Comparison of unsteady pressure between linear results (blue), nonlinear results (red) and measured data (black) . . . . .	158
5.30 RT27A rotor blade mid-section (continued 2). Comparison of unsteady pressure between linear results (blue), nonlinear results (red) and measured data (black) . . . . .	159
C.1 Comparison between the computed steady data and the reconstructed vortical, potential and entropy components using first 10 harmonics.	194
D.1 Example of two agglomerated coarse grid volumes . . . . .	198
D.2 Stability region and contours defined by $ \psi(Z)  = 0.2, 0.4, \dots, 1$ for a 5-stage Runge-Kutta time stepping scheme. . . . .	204
D.3 11 <sup>th</sup> Standard Configuration. Directional lines . . . . .	207
D.4 11 <sup>th</sup> Standard Configuration (turbulent flow calculation up to the wall). Agglomerated control volumes . . . . .	208
D.5 11 <sup>th</sup> Standard Configuration (turbulent flow calculation up to the wall): convergence histories . . . . .	209

# Chapter 1

## Introduction

This Chapter introduces unsteady turbomachinery flows and the computational fluid dynamics (CFD) methods that are currently used for simulating such phenomena. A comprehensive description of the different unsteady flow phenomena is first given. The causes of such phenomena and their effects on turbomachinery performance are discussed in some detail. The second part the Chapter is focused on the application of CFD methodos to simulate unsteady turbomachinery flows for forced response prediction. Different numerical techniques are described together with their assumptions and limitations. The last part of the Chapter outlines the objectives of the thesis, the approach that will be followed throughout the research project and its expected contribution to the field.

### 1.1 Unsteady Turbomachinery Flows

Turbomachinery stages are designed to produce work on the fluid flow which passes through them. This is true for both turbine rotor blades, where the air flow decreases its total enthalpy in order to allow the blade rotation; and for compressor rotor blades, where the fluid receives energy from the rotation of the blade, thus increasing its total enthalpy. For a flow with negligible body forces, the first low of thermodynamics can be written as

$$\frac{DH}{Dt} = \frac{1}{\rho} \frac{\partial p}{\partial t} \quad (1.1)$$

where  $H$  is the total enthalpy,  $p$  the pressure and  $\rho$  the density of the fluid with  $\frac{D}{Dt}$  indicating the convective (or total) derivative. Equation (1.1) shows that, in

order to produce work, i.e. changing the total enthalpy of the fluid, the fluid flow within turbomachinery blade rows must be unsteady. This is consistent with the fact that, in the case of a turbine rotor blade, where the total enthalpy decreases, a stationary observer would see, at a fixed viewpoint, a decreasing pressure with time ( $\frac{\partial p}{\partial t} < 0$ ) since first the pressure and then the suction side of the passage will go past the observer's point of view. This relative blade row motion is essential for turbomachines to produce work.

On the other hand, the relative motion causes complicated unsteady interactions between adjacent blade rows which can persist through several stages and can cause severe vibration problems. The wake shed by the downstream blade is unsteady for the upstream one; the potential field associated with blade lifts also causes unsteadiness for adjacent blade rows. Other factors, such as aerodynamic mistuning, i.e. stator throat width variations due to assembly tolerances, temperature distortions, due to blocked burners, may also become significant in causing unsteady excitation forces with low-order harmonics, the so-called low engine order excitation (LEO). Blade vibration is another source of unsteadiness and the overall picture is further complicated because of other inherently unsteady phenomena such as vortex shedding, surge, stall and rotating stall, though some are associated with part-speed only.

Such unsteady phenomena play a crucial role in the aeroelastic and aeroacoustic behaviour of the blades and they are increasingly becoming limiting factors in the developing improved-efficiency designs, especially when flexible, slender and unshrouded blades are used. From an industrial prospective, it is clear that there is a pressing need for formulating validated predictive models to reduce the design cycle and, consequently, cost.

This thesis will address such a problem and focus on the numerical simulation of unsteady turbomachinery flows for forced response predictions.

### **1.1.1 Forced response**

When the rotating blades pass through flow defects created by the upstream and downstream blade rows, the ensuing large unsteady aerodynamic forces can cause excessive vibration levels, hence the term forced response. One of the first design steps, for minimizing the response levels, is the Campbell diagram of Fig. 1.1 which indicates the possibility of an assembly mode being excited at a particular

rotational speed or its multiples, the so-called engine order (EO) excitation. The Campbell diagram is a plot of the bladed disc mode family frequency against rotor speed, onto which the engine order lines are superimposed. Forced response occurs when a particular engine order and the assembly frequency lines cross, as indicated by circles in Fig. 1.1. For this reason, forced response is also called synchronous vibration as it occurs when two frequencies match.

Forced response problems may be alleviated by reducing the aerodynamic forcing, or by controlling the resulting vibration<sup>1</sup>. It may be removed entirely by moving coincident frequencies out of the running range. Unfortunately, it is not usually possible to move all resonances out of the running range because aeroengines operate over a wide range of speeds and aerodynamic conditions. So, it is of paramount importance to be able to evaluate the unsteady aerodynamic loads in order to calculate the magnitude of aerodynamic responses for fatigue life predictions. This problem is usually more severe in HP turbines, where the blades are already under large thermal and centrifugal loading. Jay & Fleeter (1987) give an overview of the various aspects of forced response investigation. An assessment of unsteady flows in turbines caused by the relative blade motion is given by Sharma et al. (1992). In aerospace engineering, it is common practice to display engine test results in the form of a modified Campbell diagram from which both flutter and forced response behaviour can be seen. In such cases, the out-of-plane axis represents the vibration amplitude and flutter is observed at nearly constant frequency, usually across several engine-order lines (Fig. 1.1).

The main sources of unsteadiness, which can cause forced blade vibrations, can be due to the wake passing from upstream blade rows (wake-blade interaction) and the potential field of up/downstream blade rows.

**Wake-rotor interaction.** The stator wakes, which can be assumed to be approximatively steady in the stator frame of reference, are unsteady in the rotor frame of reference since the rotor is moving through the wakes and, consequently, unsteady pressure waves are created. Although the generation of stator wakes is viscous phenomenon, the subsequent interaction with the rotor blade is primarily an inviscid process and hence can be modelled, as a first approximation, by the Euler equations. This allows two different approaches in numerical modeling. The first is to perform a full Navier-Stokes calculation for both the stator and ro-

---

<sup>1</sup>A way of achieving this is the use of under platform dampers

tor blades (Rai 1987, 1990, Arnone 1995. The second is to perform an unsteady inviscid calculation for just the rotor blade row, with the wakes being somehow specified as unsteady inflow boundary conditions (Hodson 1985, Giles 1987, Korakianitis 1992a, 1992b, 1993). This latter approach is computationally much more efficient, but assumes that one is not concerned about the unsteady heat transfer and other viscous effects on the rotor blades and that the wake is steady in the stator frame of reference.

**Potential interaction.** Such interaction cause unsteadiness due to the fact that the pressure in the region between the stator and rotor blade rows can be decomposed approximately into a part which is steady and uniform, a part that is non-uniform but steady in the rotor frame and a part that is non-uniform but steady in the stator frame. Therefore, as the rotor blades move, the stator trailing edges experience an unsteady pressure due to the non-uniform part that is locked to the rotors, and the rotor leading edges experience an unsteady pressure due to the non-uniform part that is locked to the stator. This is a purely inviscid interaction , hence the term potential interaction. There are again two modelling approaches: the first is an unsteady inviscid calculation of the stator and rotor blade rows (Giles 1990b, Suddhoo et al. 1997, Rai 1987, 1990, Sbardella & Peiró 1997). The second is an unsteady inviscid calculation for just one of the blade rows, either the stator or the rotor, with the unsteady pressure being specified as boundary condition (Korakianitis 1992a, 1992b, 1993, Manwaring & Wisler 1993). The latter approach is more efficient but, unfortunately, the potential stator/rotor interaction becomes important when the spacing between the stator and the rotor is extremely small, and/or there are shock waves moving in the region between them. Consequently, one does not usually know what to specify as unsteady boundary conditions.

**Low engine order (LEO) excitation.** Both wake-rotor and potential-flow interaction can be regarded as classical forced response problems related to blade passing frequency. For such forced response problems, the frequency of the excitation forces is a known function of the number of the up/downstream blades and the rotational speed. The second type of forced response is much more difficult to deal with as the controlling parameters and the exact excitation mechanisms are poorly understood. However, the unsteady aerodynamic forcing function is known to be made of low-order harmonics as it is responsible for exciting low-order nodal

diameter assembly modes, hence the term LEO forced response. From an industrial perspective, the LEO forced response may be more important than the classical forced response as there are no established design procedures for its avoidance. Many factors, such as flow angle, rotor-stator axial gap, combustion effects, effects of up-downstream stages, are thought to influence the LEO excitation mechanism but no symmetric trends can be observed. Sayma (1998) gives an overview of different factors which may effect the LEO forced response. Manwaring & Kirkeng (1997) present an investigation for forced response on a low pressure (LP) turbine blade row, due to low-engine order temperature distortions caused by the upstream combustor. Sayma et al. (2000) predicted the LEO excitation arising from a stator blade throat width variations.

### 1.1.2 Flutter

Flutter is defined as an unstable and self-excited vibration of a body in an air-stream and it results from a continuous interaction between the fluid and the structure, either or both of which may be non-linear in nature. Flutter is an aeroelastic phenomenon. Collar (1946) define aeroelasticity as the study of the mutual interaction that takes place within the triangle of inertial, elastic and aerodynamic forces on structural members exposed to an airstream.

In turbomachinery blade rows, the structure to fluid mass ratio tends to be high while the same parameter is much lower for wings. Thus, whereas the wing flutter usually occurs as a result of coupling between the (bending and torsional) modes, turbomachinery blade flutter tends to be a single mode phenomenon as the aerodynamic forces, which remain much smaller than the inertial and stiffness ones, cannot usually cause modal coupling. In the former case, the aeroelastic mode can be significantly different from the structural one, in both frequency and mode shape, while this is usually not the situation in the latter case. However, there may still be discrepancies between the aeroelastic mode and the corresponding structural mode. Coupled mode turbomachinery flutter cannot be ruled out, and may occur in modern designs where blading tends to become thinner and more highly loaded to improve the aerodynamic efficiency. In any case, flutter is a particularly difficult problem in turbomachinery cases since there are many additional features with not fully-understood consequences: flow distortions due to up and downstream blade rows, intake effects, coupling of assembly modes, loss of spatial periodicity of

vibration due to aerodynamic effects and blade-to-blade manufacturing differences, a feature which is known as mistuning (Ewins 1974).

Reviews of advances in the field of aeroelasticity in turbomachine applications have been published by Sisto (1953), Fleeter (1979), Platzer (1982), Sisto (1987b), Dowell et al. (1989), Bendiksen (1991), Gerolymos (1992), Marshall & Imregun (1996).

A typical compressor map which indicates the different flutter regions is shown in Fig. 1.2. This map shows the various possible flutter regimes: stall flutter, choke flutter and various type of supersonic flutter. Sisto (1987a) gives an overview of the different types of flutter in modern compressor and fan. In this review paper particular attention has been devoted to the illustration of classical and modern prediction models.

**Stall flutter.** As shown in Fig. 1.2, the aerodynamic conditions, at which stall flutter tends to occur, are at part-speed with high back pressure. In such conditions, the incidence onto the blades is high and the blade boundary layer becomes thicker. At transonic flow conditions, which are typical of front stage fans, a shock wave stands outside the blade passage, i.e. misses the leading-edge of the next blade. This leads to strong shock/boundary-layer interaction, which may be an important part of the stall flutter mechanism. Stall flutter differs considerably from classical flutter, i.e. with attached flow (Sisto 1987b). The mechanism for net energy transfer from the airstream to an oscillating blade need not to rely on elastic or aerodynamic coupling between two modes, nor upon a phase lag between a displacement and its aerodynamic reaction. The essential feature of stall flutter is the non-linear aerodynamic reaction to the motion of the blades. Dowel et al. (1989) describe a models for bending and torsional stall flutter including the basic instability mechanism and its principal features. Adamczyk et al. (1982) present an analysis of supersonic stall flutter of modern fan assemblies.

**Choke flutter.** Compared to stall flutter, choke flutter usually occurs at the opposite end of the compressor map. Here the incidence onto the blades decreases and becomes negative. At subsonic flow conditions, this may lead to the separation of the boundary layer from the pressure surface, and the flutter mechanism is similar to that of stall flutter. At transonic conditions, choke will normally occur before stall and large unsteady pressures from oscillatory shocks may cause flutter. Choke

flutter is described qualitatively by Dowel et al. (1989).

Although low-pressure turbine stages are also known to be prone to flutter (Sayma et al. 1997), fan flutter stability is usually considered to be more critical as this component can be exposed to effects such as inlet distortion due to gusts, cross-winds and foreign object damage. Therefore, a higher flutter margin needs to be incorporated into its design.

### 1.1.3 Inherent unsteadiness

Several unsteady phenomena may result from aerodynamic instabilities of the fluid. Such instabilities are primarily due to the viscosity of the fluid and apply to both turbine and compressor blades. Two main aerodynamic instabilities are of concern in turbomachinery flows: vortex shedding and rotating stall.

**Vortex Shedding.** Trailing edge vortex shedding is a major source of unsteadiness in turbomachinery when viscous flow exits via a blunt blade trailing-edge. This unsteadiness is particularly pronounced in turbines where very thick trailing-edges are needed to accommodate blade cooling passages. Some experimental works suggested that the wake loss in a turbine is largely due to the formation of a vortex shed. Unfortunately, the detailed mechanism of vortex shedding loss production is still not quite clear. One observation is that, when vortex shedding occurs, the total pressure just downstream of the trailing edge (base region) is significantly lower than that of the free-stream, producing a base pressure loss (Wilson 1989). Predicting the base pressure is an important part of predicting the loss produced by the vortex shedding. Because vortex shedding in turbomachines has a small length scale and high frequency, the experimental and numerical investigations are difficult and expensive. However, understanding and predicting trailing-edge vortex shedding is important to reduce the total losses further in turbine designs and is receiving more and more attention. Cicarelli & Sieverding (1996) present a numerical simulation in order to assess the effects of vortex shedding on the unsteady pressure distribution around the trailing-edge of a turbine cascade. Magagnato (1999) uses different forms of two equation turbulence models in order to predict the experimentally observed vortex shedding from a turbine trailing edge. The results indicates a strong dependency on the particular turbulence model used.

Denton (1993) discusses turbine vortex shedding in term of losses due to entropy generation.

**Rotating stall.** Stall may occur when a compressor blade runs off design, and the incidence on the blade increases (above the working line in Fig. 1.2). As a consequence, at least three different instabilities may occur: the first is stall flutter, described above; the second is *surge*, where the higher pressure downstream of the stalling stage causes the whole flow to reverse. This serious system instability can cause structural damage very suddenly. The third instability, rotating stall, occurs when, due to differences in the flow around the annulus (inlet distortion or upstream obstruction) only some of the blades stall. The stalled cell then causes a higher incidence onto the blades nearest in the opposite direction to the rotation (causing those to stall), and a lower incidence onto the blades nearest in the rotating direction (causing those to recover). Thus the stalled cell rotates around the annulus in the opposite direction to the rotor rotation. This phenomenon obviously causes large unsteady forces on the blades, so at least some forced vibration would be expected to accompany rotating stall. The propagative behaviour of rotating stall was initially described by Emmons et al. (1955). Advances in the area of rotating stall has been reported by Greitzer (1976a, 1976b), Cumpsty (1989).

#### 1.1.4 Further aspects of unsteady flows in turbomachines

There are two main parameters which are of paramount importance in turbomachinery unsteady flows and these are the *interblade phase angle* and the *reduced frequency*. The interblade phase angle can be associated with both flutter and forced response problems (stator/rotor interaction). This quantity, firstly introduced by Lane (1956) for flutter problems, indicate the phase difference between vibrating neighboring blades. The possible values of the interblade phase angle in a flutter analysis are defined by

$$\phi = \frac{2\pi n}{N_b} \quad (1.2)$$

where  $N_b$  represents the number of blade in the annulus and  $n$  represents the wave number ( $n = 0, 1, \dots, N_b$ ).

For stator/rotor interaction an equivalent definition can be formulated. This time, the interblade phase angle is decided by the pitch ratio of neighboring blade rows.

For example, for a single turbine stage shown in Fig. 1.3, the stator blade row has a blade pitch given  $P_s = \frac{2\pi}{N_s}$  and the rotor blade a pitch given by  $P_r = \frac{2\pi}{N_r}$ , where  $N_s$  and  $N_r$  are the blade numbers. Assuming  $N_s \leq N_r$ , the interblade phase angle between the upper and periodic boundaries is:

$$\phi = 2\pi \left(1 - \frac{N_s}{N_r}\right) \quad (1.3)$$

The interblade phase angle determinates the number of blade passages that must be included in the calculations unless some other assumption are introduced to limit the computational domain to a single passage (Erdos et al. 1977, Giles 1987, Verdon 1993).

The reduced frequency is defined in (A.8). For stator/rotor interaction the reduced frequency is related to the interblade phase angle and the relative rotation speed of the two rows as indicated in (C.7). The reduced frequency can be interpreted as the ratio of the time taken for a fluid particle to go past the blade chord (or pitch) to the period of the flow unsteadiness. For small values of the reduced frequency, the flow is quasi-steady, while unsteady effects dominate for large values.

## 1.2 Computational Prediction Methods

The development of numerical methods for the prediction of unsteady flows in turbomachinery applications has been motivated primarily by the need to predict, within a prescribed level of accuracy, the aeroelastic and aeroacoustic behaviour of the blading. For the numerical prediction of the flutter margins and the actual level of blade vibration, an unsteady aerodynamic analysis is only one component of an overall design prediction system. However, because of the complexity of the unsteady fluid dynamic environment, this component has generally been regarded as the one requiring the most research attention.

The unsteady aerodynamic analysis which have been used in aeroelastic and aeroacoustic design applications was based on classical 2D subsonic and supersonic analysis, supplemented by a good deal of empiricism. This classical 2D methods are based on linearised flow theories which can essentially applied to lightly loaded thin airfoil cascades. Whitehead (1987) gives a review of these methods. Classical methods provide very efficient unsteady aerodynamic response predictions that are useful near design operating conditions, but they are not appropriate off design,

where blade loading effects are important, or for transonic flows with embedded shock discontinuities.

To overcome the limitations of the classical methods, the unsteady flow representation needed to be improved taking into account effects due to the blade loading and the steady state mean flow which is highly non linear. During the last past decade, significant advances in unsteady aerodynamic prediction based on CFD (Computational Fluid Dynamics) methodologies have been achieved. At the present time there are two main approaches which deal with the prediction of unsteady flows in turbomachines: i) the time linearised methods and ii) the fully non-linear time marching methods.

### **1.2.1 Methods for linearised unsteady aerodynamics**

These methods are based upon the assumption that the unsteadiness is a small perturbation about a non-linear, steady-state flow field. Although solutions based on these methods require significantly more computer time than classical solutions, the improvement in the physical modelling, coupled with advances in CFD solution procedures, are making them an increasingly attractive for aeroelastic and aeroacoustic design applications. In fact, the linearisation of the unsteadiness allows the calculations to be performed using a single passage for any interblade phase angle. On the other hand, because these methods are all in the frequency domain, a new calculation is needed for each frequency considered. The development history of such methods is given by Verdon (1987, 1993).

An improvement over classical linearised inviscid flow methods was provided by linearised potential methods, in which the steady flow is taken to be a solution of the non-linear 2D full potential equation. Verdon & Caspar (1984) developed a numerical method for solving the linear equations that result from assuming that the unsteadiness is sinusoidal in time. This class of methods takes into account the blade geometry and loading, and remains valid at high vibration frequencies. Such potential methods are all for 2D flows, with the addition of stream-tube thickness and radius change to introduce some 3D effects. The complexities of extending the potential analysis to 3D flows, the computational cost of the standard matrix solution methods and the need to capture the flow details more accurately led to the development of linearised Euler methods.

Hall & Crawley (1989) developed a finite element method for solving the linear Eu-

ler equations in 2D, following the preliminary research by Ni & Sisto (1975). Hall & Crawley (1989) predicted subsonic unsteady cascade flows, and used a shock-fitting technique to calculate unsteady shock displacements in a 2D duct. However, they were not able to extend the shock-fitting ideas to cascade geometries because shock structures in real turbomachines can be complex and shocks can appear in unexpected locations, requiring much more “intelligence” of a shock fitting algorithm than is possible at present. The present area of research is therefore focused on the implementation of linearised 2d and 3D Euler method which use shock capturing techniques as those used for non-linear aerodynamics. Lindquist & Giles (1991) have proven that, if correctly formulated and implemented, shock capturing can produce the same results as shock fitting. Further work with shock capturing techniques have been reported by Hall & Clark (1993), Hall & Lorence (1993), Hall et al. (1994), Montgomery & Verdon (1997a, 1997b).

An active area of current research is to develop linearised Navier-Stokes methods, including the linearisation of the turbulent eddy viscosity (Cizmas & Hall 1995 and by Holmes et al. 1997). An original formulation will also be reported in this thesis.

### **1.2.2 Non-linear time-marching methods**

Although linearised analyses meet the needs of turbomachinery designers for efficient predictions, they cannot model important unsteady flow phenomena associated with finite amplitude unsteadiness (large shock excursion, shock-boundary layer interaction, unsteady separation etc.). Over the last twenty years, there has been a great deal of work on methods for calculating non-linear unsteady flows by time-marching methods. Such methods provide a very useful research tool to increase the understanding of unsteady flows in turbomachinery. However, axial gas turbine engines are multi-stage and, in a whole engine context, non-linear time-marching methods are prohibitively expensive for the foreseeable future. The main complicating factor, which leads to extraordinarily large computing times, is the problem of the periodic boundary conditions. While linearised methods allow calculations on a single blade passage for any interblade phase angle, non-linear methods needs to include in the calculations a number of blade passages which depends upon the interblade phase angle (1.2,1.3) unless some additional assumption are made.

The pioneering of work was by Erdos et al. (1977) presented a 2D, unsteady,

inviscid flow calculation of a fan stage with unequal pitches using a *phase-shifted* periodicity condition. For the upper periodic boundary of each blade, this condition can be expressed as:

$$U(x, y, t) = U(x, y - P, t - \Delta t) \quad (1.4)$$

where the *time lag*  $\Delta t$  is equal to the difference in pitches divided by the rotor wheel speed (Fig. 1.3).

$$\Delta t = \frac{P_s - P_r}{V} \quad (1.5)$$

The values on the lower periodic line are obtained by assuming that the flow is periodic in time, with a period equal to the blade passing period  $T = \frac{P}{V}$ . This allows the solution domain to be restricted to a single blade passage region, but a large amount of computer memory is still needed to store the unsteady flow variables at the two periodic boundaries over an entire period. However, the major drawback of this method is the assumption of temporal periodicity. Hodson (1985) modified Denton (1983) program and used Erdos' technique to calculate wake-rotor interactions in a low speed turbine. The incoming wake was specified as a boundary condition, allowing the calculation to be performed with only the rotor blade. The results showed that many phenomena associated with rotor-stator interactions are dominated by inviscid rather than viscous effects. Rai (1987) published a paper showing that stator/rotor interaction can be calculated using the thin-layer Navier-Stokes equations. This paper generated considerable interest and sparked a lot of research activity. However, in order to be able to perform the unsteady calculations with few blade passages, without using the Erdos' technique, Rai considered some simple stator/rotor pitch ratios such as 1:1, 2:3 or 3:4 (Rai 1990). Further work is reported by Jorgenson & Chima (1989), Giles (1990b), He (1990), He & Denton (1991a, 1991b), Arnone (1995), Vahdati & Imregun (1995), Saxer & Felici (1996), Sbardella & Peiró (1997), Sayma et al. (2000).

Giles (1987, 1990b), introduced the concept of *time tilting* in order to solve wake-rotor and stator-rotor interactions with different blade pitches without assuming that the flow is temporally periodic. In this approach, the governing equations are rewritten in time inclined computational coordinates. This method eliminates the temporal periodicity and the storage requirements of the phase-shifted periodicity

approach by Erdos but introduces additional complexities into the solution procedure. Giles (1991) presented the numerical implementation of his time tilting method into the 2D program UNSFLO.

However if one is interested in multistage calculations, then both Erdos' and Giles' simplified methods become impractical. As soon as there is more than one stage, there is an unavoidable problem. If one considers a  $1\frac{1}{2}$  stage calculation in which the first and second stator rows have different numbers of blades with no common factor, then each of the second stator row blades will experience a different unsteady force depending in its circumferential position relative to the blades in the first stator row. There is no mathematically correct way around this problem (Giles 1992). The only correct treatment is to analyse all three blade rows. This approach is too expensive although some early attempts have been made by Sayma et al. (1999) who presented the forced response analysis of a fan using the non-linear time marching technique of Sayma at al. (2000). The computation is performed on three whole blade rows, consisting of 11 struts, 33 variable inlet guide vanes (VIGVs) and 26 rotor blades. A view of the computational mesh, which contains about 4.2 million grid points, is shown in Fig. 1.4.

### 1.3 CFD Methods for Compressible Flows

Both linear and non-linear unsteady flow CFD methods are primarily based on the solution of compressible inviscid or turbulent viscous flow equations. CFD techniques have evolved rapidly as a discipline and are increasingly being used to complement wind tunnels, both for preliminary and advanced design. Based on the mathematical foundations laid by Godunov (1959) and Lax (1973) among others, the field has come into its own in the last twenty years. Very significant advances have been made in the areas of spatial discretisation, grid generation and solution strategies. Tremendous advances in computer architecture and parallel processing have also contributed to the very rapid advances seen over the last ten years.

When dealing with the numerical discretisation of the Navier-Stokes equations, several distinct issues need to be addressed.

- i) Spatial discretisation of the inviscid fluxes. The system of Euler equations mathematically belongs to a class called *hyperbolic systems of conservation laws* which have, as their main feature, the possibility to develop discontinuities even when the initial data are smooth. This means that a numerical algorithm needs to be

designed to be able to deal with such possibilities.

- ii) The discretisation of the computational domain with structured, block-structured, unstructured or mixed-element grids.
- iii) Explicit or implicit time integration. This represents a very broad distinction since several other techniques, such as preconditioning and multigrid, can be employed in order to accelerate convergence.
- iv) Boundary conditions. The stability and accuracy of the numerical scheme may hinge on how the boundary are treated.

### 1.3.1 A brief review of flux discretisation methods

The accurate and efficient discretisation of the hyperbolic conservation laws of fluid dynamics has been studied by several authors. Roe (1981) developed an approximate version of the Riemann solver used by Godunov (1959) in his pioneering work, and this approach is still one of the best numerical schemes for the discretisation of the Euler equations. The Roe scheme belongs to the class of methods called *Flux Difference Splitting* (FDS) where the numerical flux function is obtained through a flow decomposition into acoustic, entropy and vorticity waves. Each wave is then discretised according to its propagation speed in an upwind way. Other FDS methods have been developed by Osher (1984), Pandolfi (1984), Harten (1983b), Leveque (1985) and Einfeldt (1988, 1991).

In parallel with the FDS methods, a different class of schemes has been developed where the spatial discretisation is obtained using central differencing stabilized by an artificial dissipation term. Such methods, developed Beam & Warming (1976) and by Jameson et al. (1981), are computationally more efficient than the FDS ones but their stability relies on the explicit addition of artificial viscosity. This requires the empirical determination of the so-called “free parameters”. On the other hand, the upwind FDS method are considered to be parameter free. A third class of methods, first developed by Stager & Warming (1981) and by van Leer (1982), is known as *Flux Vector Splitting* (FVS). These methods introduce, in the numerical discretisation, the signs of the wave propagation speeds (eigenvalues of the flux Jacobian) but they do not attempt to solve an approximate Riemann problem. Different types of FVS have been developed over the last decade with the goal of devising an accurate numerical scheme for capturing shock and contact discontinuity with minimal numerical dissipation and oscillation. Among other

FVS methods, it is worth mentioning the AUSM (Advection Upstream Splitting Method) scheme of Liou & Steffen (1993, 1996), the CUSP (Convective Upwind Split Pressure) scheme by Jameson (1993, 1995) and the gas kinetic analogy of Prendergast & Xu (1994).

Several authors extended the schemes above to second order accuracy (labelled high resolution schemes by Harten), using different mathematical formulations. Harten (1983a) introduced the important concept of TVD (Total Variational Diminishing) to extend Roe's first order flux-difference scheme to second order. Van Leer (1974, 1977a, 1977b, 1979) tackled the problem in a geometric sense introducing the MUSCL schemes (Monotone Upstream-centered Schemes for Conservation Laws). Osher (1984), Osher & Chakravarthy (1984) contributed to the mathematical foundation of these concepts and providing the CFD community with solid basis to simulate high-speed flows with shock waves and other type of discontinuity.

One of the most spectacular outcomes of the analysis and development of TVD schemes is the realization that a bridge can be established between the upwind FDS, FVS and central discretisation schemes. This allows central schemes to be formulated with adapted dissipation satisfying TVD requirements. Key papers which show the relationship between central difference and upwind schemes are given by Swanson & Turkel (1992) and Jorgenson & Turkel (1993). Comparisons of different numerical schemes are given by Woodward & Colella (1984) and Swanson et al. (1997).

### **1.3.2 Structured versus unstructured grid debate**

The mathematical formulation of the above schemes is developed in 1D because the TVD analysis is not possible for multidimensional problem. On structured body-fitted grids, these 1D models were extended to 2D and 3D in a natural by using the so-called generalized coordinates. However, the task of generating efficient structured grids for complex configurations remains a serious challenge. The desire of computing flows over complex configurations spawned a surge of activity in the area of unstructured grids<sup>2</sup>. The development of both structured and unstructured grid solvers will now be examined in some detail.

In recent years, the rapid development of numerical methods for the solution of the

---

<sup>2</sup>The term unstructured refers to grids where the number of cells surrounding a typical node does not necessarily remain constant.

flow equations and the availability of powerful computers led to the emergence of various systems for the prediction of complex turbomachinery flows. Most prediction methods for turbomachinery flows use structured grids (Denton 1983, 1990, Rai 1987, 1990, Dawes 1988, Arnone & Swanson 1993, Arnone 1995, Saxon & Feli 1996) On the other hand, unstructured grids received a great deal of research and development for external compressible flows. Barth & Jespersen (1989), Barth (1990, 1991, 1993), Peraire et al. (1992), Frink (1992, 1996), Mavriplis (1995a), and Venkatakrishnan (1995a) give overviews of the status of compressible Euler and Navier-Stokes solvers on unstructured grids. Different spatial and temporal discretisation options for steady and unsteady flows are discussed.

It is only in recent years that unstructured tetrahedral grids found their way into 3D turbomachinery applications (Dawes 1992, 1993, Vahdati & Imregun 1995, Sayma et al. 2000). While unstructured grid methods provide flexibility for discretising complex geometries, they have the drawback of requiring larger computer storage and more CPU effort than their structured counterparts. Due to the relatively simple shape of turbomachinery blades, structured grids are considered to be as the most suitable route by many researchers for their discretisation. Design considerations increasingly require the inclusion of complex features such as over tip gap leakage, cooling holes in turbine blades, snubbed fan blades, fan assemblies with intake ducts, struts and various other structural elements. Due to the complexity of such geometries, the natural way forward is to use unstructured grids. Although tetrahedral grids, the choice of which appears obvious, are relatively easy to generate for inviscid flow calculations and away from the walls for viscous flow calculations, the situation becomes more complicated in boundary layers, where large aspect ratio cells are required for computational efficiency. In large parts of the solution domain, the gradients normal to the walls are several orders of magnitude larger than those along the walls, thus more grid points are required in the former direction than in the latter. Tetrahedral grids are not ideal for use in boundary layers where very small angles degrade the accuracy of the solution (Aftosmis et al. 1994).

Such considerations led to the development of hybrid grid models where hexahedral or prismatic cells can be used in the boundary layers and tetrahedral and prismatic cells can be used to fill the domain away from the walls. The idea of using mixed elements in an unstructured mesh technique is by no means novel, and has been previously advocated by several authors (Barth 1990, Parthasarathy et al. 1995).

In fact, many have recognized the benefits of mixed elements, but have nevertheless advocated the use of standard tetrahedral grids, due to the homogeneity in the data structures and relative discretisation simplicity. Mavriplis & Venkatakrishnan (1995a), Moinier et al. (1999) presented unified solution techniques which can handle mixed-elements grids.

For turbomachinery blades, Sbardella et al. (1997, 2000) presented a method to generate hybrid semi-structured grids where the boundary layers are filled with hexahedral cells and the rest of the domain is filled with triangular prisms. Such a route not only provides a very efficient spatial discretisation over standard unstructured grids but it also provides a much better grid quality over its fully structured counterparts. When dealing with 3D blades, the present work will use semi-structured grids for their computational efficiency, although the solver is written for general hybrid unstructured grids. This is achieved by using an edge-data structure to construct the discretisation over all element types. In this approach, the grid is presented to the solver as a set of node pairs connected by edges. The edge weights representing the inter-cell boundaries are computed in a separate preprocessor stage. Consequently, the solver has a unified data structure where the nature of the hybrid mesh is concealed from the main calculations loops.

### 1.3.3 Time integration using multigrid methods

Traditionally, time integration techniques may be classified into five groups: explicit, implicit direct method, iterative implicit method, preconditioning techniques and multigrid methods. However, some techniques can be shown to be equivalent to others and state-of-the-art time-stepping algorithms combine techniques from several areas. Venkatakrishnan (1995b) gives an overview of the different time marching techniques for solving both steady and unsteady flows. Unstructured grid methods are compared to those used for structured, body-fitted grids. The convergence characteristics of various implicit methods are compared for a number of test cases.

Explicit methods represent a straightforward way of integrating the system of ordinary differential equations (ODEs) which arises from the spatial discretisation, since they do not require any matrix inversion. Multistage Runge-Kutta explicit methods have been widely used in the CFD community (Jameson et al. 1981, Jorgenson & Chima 1989). The coefficients for these Runge-Kutta schemes techniques

are optimised in order to yield a large CFL number and good damping properties (Jameson 1985, Van Leer 1989). Local time stepping (Jameson et al. 1981, Denton 1983) and residual smoothing (Jameson et al. 1981, Arnone 1995) are employed to accelerate convergence. Even with this methodology, the convergence to steady state is usually unacceptably slow. For unsteady flow, multistage Runge-Kutta algorithms are ideal for high-frequency unsteadiness<sup>3</sup> where the choice of the time-step is not restricted by stability considerations. However, the may result inefficient for low-frequency unsteady flow and for viscous turbulent flow simulations.

Implicit direct methods, in where the Jacobian matrix is directly inverted, are non-competitive for large problems since the matrix inversion procedure scales with  $n^3$ , where  $n$  is the number of unknowns (Venkatakrishnan & Barth 1989). Moreover the governing equations are non-linear, thus a direct method cannot produce an answer in a single iteration and must therefore be used iteratively.

Rather than inverting the Jacobian matrix directly at each time-step, a linearised system of equations may be solved at each time-step using an iterative method. This can substantially reduce the overall computational requirements since the approximate linear system need not be solved to a high degree of accuracy. Also, iterative methods generally exhibit lower computational complexity than direct inversion methods. In deriving the implicit system, a common practice is the use of a *defect correction procedure* which leads to a discretised Jacobian matrix which is a order less accurate than the right-hand side (Tidriri 1995, Mavriplis 1998c). This is not only due to storage considerations and computational complexity, but also to the fact that the resulting lower-order matrix is better conditioned. However, the mismatch between the discretisation and the Jacobian operators implies that the resulting system is only moderately implicit. For unstructured meshes, the formulation of an efficient iterative technique can be quite complicated. For this reason, point-Jacobi iterative procedures have been widely used (Brenneis & Eberle 1990, Anderson and Bonhaus 1994, Sayma et al. 2000). Slack et al. (1994) compare the point-Jacobi, Gauss-Seidel and LU decomposition time integration techniques for inviscid flows on unstructured meshes.

Krylov methods<sup>4</sup> represent an alternative to iterative methods. The general idea is to obtain improved updates to the solution by using information generated at previous updates. There are a number of different Krylov methods which have

---

<sup>3</sup>This is the case of computational aeroacoustics.

<sup>4</sup>A review of Krylov methods is given by Venkatakrishnan (1995).

been developed, but for CFD problems the most prevalent Krylov method is the GMRES method (Saad & Schultz 1986).

These classical implicit methods work relatively well for inviscid-flow calculation but they may prove inadequate for high Reynolds number viscous flows because of two reasons: (i) the need to use high aspect ratio cells to represent the steep gradients in the boundary layer regions, and (ii) the overall increase in the number of mesh points for practical 3D aerodynamic configurations. A suitable algorithm should be devised in order to take into account the interaction between the discretised method, the computational mesh and the physics of the viscous flow. Moreover, the right balance between the operation count, storage requirements and parallel scalability is also very important. A general solution strategy, which is suitable for devising efficient solution algorithms, is the multigrid approach (Wesseling 1992). The basic idea of a multigrid strategy is to accelerate the rate solution convergence on a fine grid by using a series of coarser grids.

Explicit multigrid smoothers have been widely used in the CFD community for solving both steady and unsteady flows. A popular explicit multigrid method is the semi-discrete scheme of Jameson et al. (1981) which uses multi-stage Runge-Kutta time stepping to integrate the system of ODEs resulting from the spatial discretisation. Local time-stepping was also used in order to accelerate convergence. Several researchers used the technique proposed by Jameson et al. (1981) to obtain efficient solution procedures: Jameson (1985, 1993), Denton (1983), Mulder (1989, 1992) Peraire et al. (1992), Mavriplis & Martinelli (1994), Mavriplis & Venkatakrishnan (1995b), Mavriplis (1995a), Melson et al. (1993), Parthasarathy et al. (1995) and Arnone (1995).

However, despite considerable success for Euler computations, the multigrid approach have shortcomings for Navier-Stokes computations, especially high aspect ratio cells are used inside the boundary layer region. One way of decreasing the discrete stiffness caused by highly stretched cells is to use of a matrix time step or preconditioner. Recently, considerable amount of research has been devoted to the formulation of preconditioner multigrid algorithms for computing high Reynolds number viscous flows. Point-Jacobi preconditioners (Pierce & Giles 1997, Pierce et al. 1997) and line-Jacobi preconditioners (Mavriplis 1998b, 1998a) have been reported in the literature. While point-Jacobi and line-Jacobi preconditioners are used to decrease the stiffness arising from the grid anisotropy in boundary layer regions, another class of preconditioners is also available for reducing the stiffness

associated with low-speed compressible flows: Turkel (1987, 1993), Turkel et al. (1996), Van Leer et al. (1991), Choi & Merkle (1993). An overview of modern acceleration techniques, such as preconditioned multigrid, is given by Mavriplis (1998c).

Appendix D presents a detailed literature review of the current state-of-the-art multigrid techniques and develops a hybrid-grids Jacobi-preconditioned multigrid method for turbomachinery steady and unsteady flow computations.

### 1.3.4 Non-reflecting boundary conditions

For convection dominated phenomena, such as those described by the compressible Navier-Stokes equations, the formulation of correct boundary conditions is extremely important and its impact on the numerical scheme is often dominating. The reason for this strong influence can be traced back to the physical nature of the convection propagation phenomena (Hirsh 1990). When obtaining a numerical solution for the Euler or Navier-Stokes equations, one has no choice but to truncate the computational domain. This is particularly true for internal flow simulations where the inlet/outlet boundaries are placed typically less than one chord away from the blade. For such configurations, the far-field flow contains a significant component of several different wave numbers, especially for flows which are supersonic in the flow direction but subsonic in the axial direction. In this case shocks propagate indefinitely and can be reflected by improper boundary conditions.

The term non-reflecting boundary condition (or absorbing boundary conditions) indicates a far-field boundary treatment which should prevent any non-physical reflection of waves which are leaving the computational domain. Specialized treatments exist for steady-state flows, unsteady frequency-domain flows and unsteady time-domain flows. The milestone paper by Engquist & Majda (1977) reported a hierarchy of approximate non-reflecting boundary conditions for multidimensional problems. The authors constructed a non-local perfectly absorbing boundary condition for the scalar wave equation and derived highly absorbing local approximations by mean of Taylor series around the incidence angle of the outgoing waves. The first-order approximation represents the so-called *1D approximation*, or *method of characteristics*, where only the waves which travel in the direction normal to the far-field boundary are perfectly absorbed. This approach is the most commonly used one for time-domain unsteady flow computations (Thompson 1987, 1990).

An overview of different types of non-reflecting boundary conditions is given by Givoli (1991) for a large number of problems.

Unfortunately, the paper by Engquist & Majda (1977) was written for mathematicians, specialized in the analysis of partial differential equations and hence its acceptance and implementation by the CFD community has been slow. Hedstrom (1979) applied the 1D boundary conditions of Engquist & Majda to the unsteady 1D Euler equations. Higdon (1986b) discussed the initial-boundary value problem theory for linear hyperbolic systems and gave a physical interpretation in terms of wave propagation. Furthermore, Higdon (1986a, 1987) formulated a discrete numerical version of the analytical absorbing boundary condition of Engquist & Majda (1977).

During the late 1980s, a considerable amount of manpower was devoted towards the formulation and implementation of accurate boundary conditions for the multidimensional Euler equations. Engquist & Gustafsson (1987) investigated steady-state non-reflecting boundary conditions and their impact on the rate of convergence in practical steady-state flow calculations. Gustafsson (1988) applied Engquist & Majda (1977) theory to the 2D time-dependent Euler equations. For such a problem, the perfectly absorbing boundary condition requires first a Laplace-transform at the boundary, and then a Fourier-transform along in the boundary. Such exact non-local boundary conditions are, in a mathematical sense, the best possible solution of the problem. However, they are computationally cumbersome and they are only available for simple problems with constant properties.

Giles (1988, 1990a) reported a unified theory for the construction of steady-state and unsteady non-reflecting boundary conditions for the Euler equations. The analysis was carried out using a decomposition of the linearised Euler equations into Fourier modes. The single-frequency boundary conditions were used for constructing both the steady-state version (no time variation at steady-state, thus frequency equal to zero) and the unsteady frequency-domain version (single known frequency assumed for the unsteadiness). For non-linear unsteady aerodynamics, Giles constructed approximate versions based on Taylor expansions, similar to the formulation by Engquist & Majda (1977). Giles (1990a) applied the steady-state version of these boundary conditions to 2D turbomachinery flows, showing their effectiveness in avoiding numerical reflections from the computational inflow/outflow boundaries. An extension to 3D is reported by Saxer & Giles (1993). Ferm (1995) presented accurate steady-state boundary-conditions for channel-flow configura-

tions. He also studied the importance of a correct implementation in order to enhance convergence.

Although accurate boundary condition formulations are now available to the CFD community, their application has been mainly restricted to steady-state flows or linearised frequency-domain unsteady flows. The implementation of accurate non-reflecting boundary conditions for time-domain unsteady flows has been reported in computational aeroacoustics (Tam & Webb 1993). For these applications, the boundary conditions are constructed from an asymptotic solution of the governing equations for large distances, the so-called *radiation boundary conditions*. A comparison between 1D characteristic (Thompson 1987, 1990), Fourier decomposition (Giles 1988, 1990a) and radiation boundary conditions (Tam & Webb 1993), is given by Hixon et al. (1995), in the framework of computational aeroacoustics. It is shown that, for unsteady time-domain method, the only acceptable outflow boundary treatment is that by Tam & Webb (1993). Other schemes become acceptable only in special cases when the flow is nearly perpendicular to the boundary. However, the radiation boundary conditions by Tam & Webb (1993) were developed for the case of a uniform mean flow only.

An interesting way forward could involve the use of the absorbing boundary conditions for linearised Euler equations via a perfectly matched layer (PML). This method, developed by Hu (1996), uses additional computational regions adjacent to the far-field boundaries of the computational domain. In these regions the governing equations are modified so that outgoing waves are either damped, accelerated to supersonic conditions, decelerated or attenuated by combinations thereof. Analysis and applications of such sophisticated boundary conditions can be found in Tam et al. (1993), Hesthaven (1998) and Abarbanel et al. (1999).

## 1.4 Objectives

This thesis deals with the development and application of a numerical tool for the simulation of unsteady turbomachinery flows for forced response predictions. The main goal is not only to produce a method suitable for industrial design but also to explore its bounds of applicability to practical cases. Both linear and non-linear time-marching unsteady flow models have been implemented using an advanced finite volume algorithm on unstructured meshes. The research code, called ALiNNS (Advanced Linear-Nonlinear Navier-Stokes code), uses state-of-the-art CFD tech-

niques for both spatial discretisation and temporal integration of the governing flow equations. The main features of the methodology are the use of mixed-element grids (also called hybrid grids) and a preconditioned agglomeration multigrid. Moreover a semi-unstructured mesh generator, LEVMAP (LEVel MAPping), was developed in order to exploit the optimum discretisation features of such an approach on 3D turbomachinery passages. LEVMAP and ALiNNS were used to predict the unsteady pressure fluctuations, due to relative blade rotation, on a typical HP turbine stage. The analysis was carried out using both linearised and non-linear aerodynamics. Comparisons with experimental data were made in order to assess the validity and the range of applicability of the linear method.

The main objectives of the research project can be summarised as follow:

- The development of a semi-structured mesh generator for an efficient representation of 3D turbomachinery blades.
- The development of an efficient viscous flux discretisation algorithm for mixed element grids and of a preconditioned agglomeration multigrid for efficient time integration.
- The development of a 3D linearised viscous unsteady flow model.
- The application of the developed non-linear and linearised flow models to a representative case in order to asses the applicability bounds of the linearised methodology.

## 1.5 Contributions of the Thesis

### 1.5.1 CFD methods

The main contributions are summarised below.

**Semi-structured meshes.** The discretisation methodology uses a combination of structured and unstructured meshes, the former in the radial direction and the latter in the axial and tangential directions in order to exploit the fact that blade-like structures are not strongly 3D since the radial variation is usually small. Such a formulation was found to have a number of advantages over its structured

counterparts. There is a significant improvement in the smoothness of the grid-spacing and in capturing particular aspects of the blade passage geometry. It was also found that the leading- and trailing-edge regions could be discretised without generating superfluous points in the far field and that further refinements of the mesh to capture wake and shock effects were relatively easy to implement. The methodology is reported by Sbardella et al. (1997, 2000) and Sbardella (1998). A detailed description is given in Chapter 2.

**Hybrid-grid flow-solver.** Compared with their structured counterparts, standard unstructured grid solvers have lower computational efficiency in terms of speed and storage. Unstructured grids often use tetrahedral elements only, an approach which often leads to numerical problems when the region to be discretised has a preferred direction such as the boundary layer for a high-Reynolds number flow. However, there are no fundamental difficulties in extending tetrahedral meshes to include further element types such as triangular prisms, pentahedra and hexahedra. Although both the discretisation of the computational domain and the flow solver will become more complex, such a mixed-element approach will offer a better, more efficient approximation than using tetrahedral elements only. For instance, hexahedral elements will handle boundary layer flows much better than tetrahedral elements because they can be made very slender without creating excessively small or large internal angles. In order to handle mixed-element meshes, the spatial discretisation of the governing equations needs to be formulated in such a way that the numerical algorithms can be applied in a uniform way to all element types. Chapter 3 describes the development and application of a finite volume scheme for the solution of the Favre-averaged Navier-Stokes equations on mixed-element grids, consisting of triangles and quadrilaterals in 2D, and of tetrahedra, pyramids, triangular prisms and hexahedra in 3D. Some of the findings have already been reported in Sayma et al. (2000).

**Edge-data Laplacian weight.** A novel feature of the spatial discretisation employed in the ALiNNS flow solver is the use of a edge-data based Laplacian weight. This Laplacian weight is used to compute the Laplacian terms of the viscous fluxes and it results in a nearest neighbour stencils. Chapter 3 describes how to evaluate the Laplacian weight for mixed-element meshes using an approximation of the Galerkin finite volume *node-pair* formula. The findings are also reported in

Sbardella & Imregun (1999, 2000).

**Preconditioned Multigrid.** A preconditioned directional-implicit agglomeration multigrid method has been developed for the solution of the linear and non-linear Navier-Stokes equations on highly anisotropic 2D and 3D unstructured hybrid grids. The coarse grid levels are constructed automatically from the fine grid by agglomerating fine grid control volumes together. Since the coarse grid control volumes may have arbitrary polygonal shapes, the type of elements constituting the fine grid is irrelevant. The discrete equations on coarse grid levels are assembled automatically without the explicit creation of a coarse grid. The multigrid smoother consists of a preconditioned point- or line-Jacobi Runge-Kutta relaxation algorithm, which guarantees efficient damping of high-frequency error modes on highly stretched grids. Appendix D gives a literature review of preconditioned multigrid methods and describes the actual multigrid algorithm that is implemented in ALiNNS.

### 1.5.2 Understanding of unsteady flows

Chapter 5 presents a detailed numerical analysis of a stator-rotor interaction in the case of typical HP turbine stage using both linear and non linear unsteady flow representations. The main contributions are summarised below.

- Detailed analysis of the rotor steady-state flow with discussion of secondary and tip leakage flow.
- Calculation of the aerodynamic forcing functions from the stator outlet steady-state solution. These forcing functions are obtained splitting the non-linear steady-state flow into potential and vortical components using the theory reported in Appendix C.
- Analysis of the distinct influence of potential and vortical forcing functions on the rotor unsteady aerodynamics using a time-linearised approach.
- Assessment of the predicted results by comparing them with experimental data and predicted non-linear results.

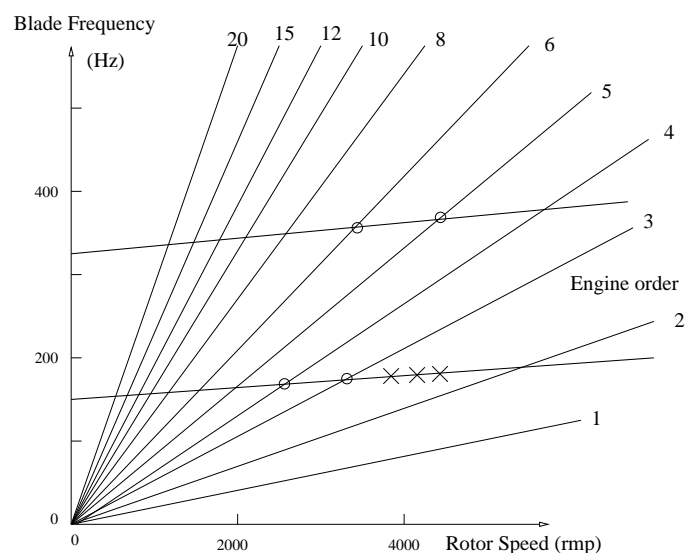


Figure 1.1: Campbell diagram for a rotor blade (from Sisto 1987). x non-synchronous excitation (flutter), o forced response resonance.

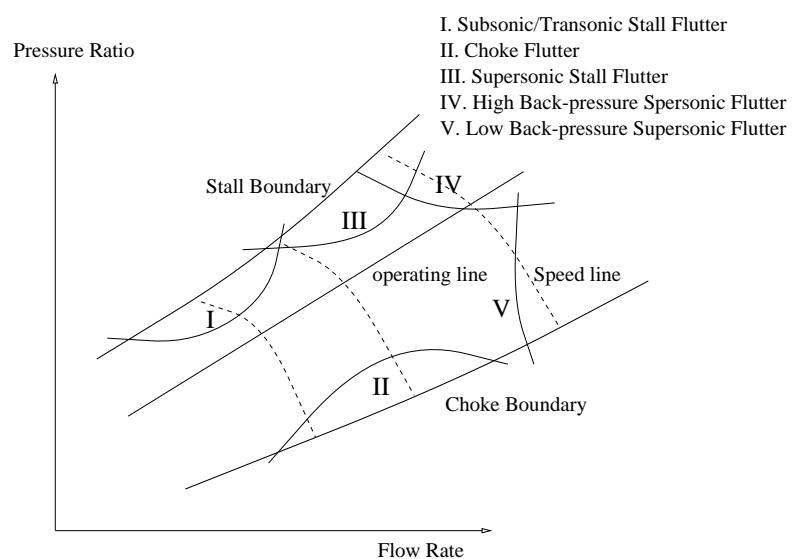


Figure 1.2: Blade flutter boundaries on compressor map (from Sisto 1987)

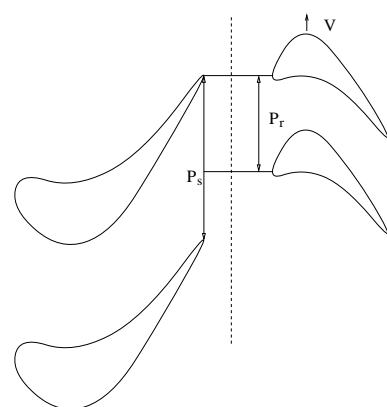


Figure 1.3: Turbine stage with different number of blades in each row

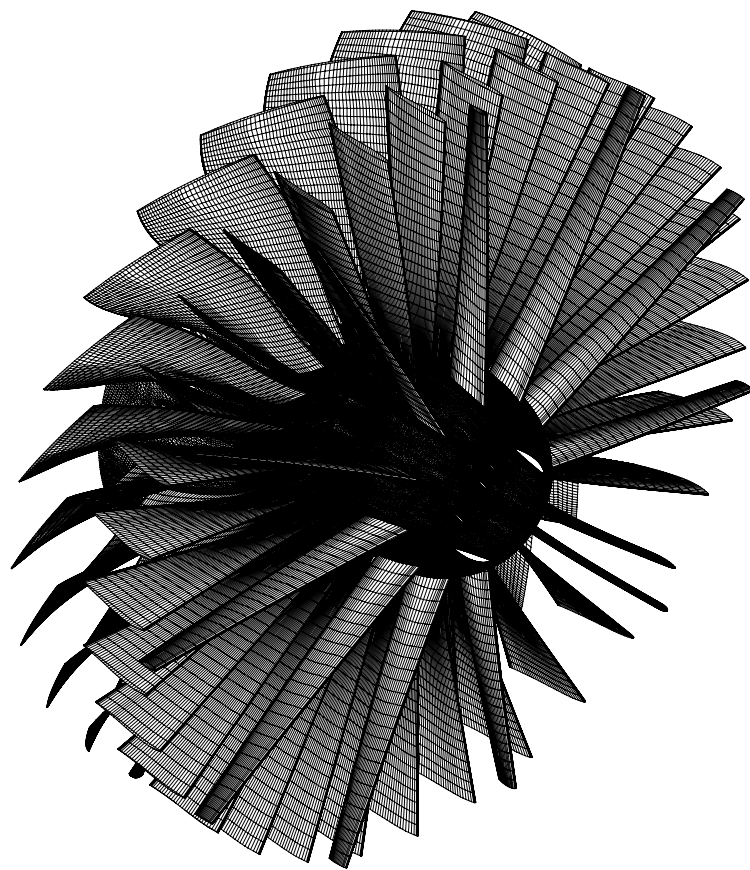


Figure 1.4: Three blade rows computational mesh for a 11 struts, 33 VIGVs and 36 rotor blades (from Sayma et al. 1999)

# Chapter 2

## Semi-structured Mesh Generator for Turbomachinery Blades

This chapter describes the development of a novel mesh generator for the flow analysis of turbomachinery blades. The proposed method uses a combination of structured and unstructured meshes, the former in the radial direction and the latter in the axial and tangential directions in order to exploit the fact that blade-like structures are not strongly 3D since the radial variation is usually small. The proposed semi-structured mesh formulation was found to have a number of advantages over its structured counterparts. There is a significant improvement in the smoothness of the grid-spacing and in capturing particular aspects of the blade passage geometry. It was also found that the leading- and trailing-edge regions could be discretised without generating superfluous points in the far field and that further refinements of the mesh to capture wake and shock effects were relatively easy to implement.

### 2.1 Introduction

It is well known that the grid structure must be selected carefully in order to achieve an accurate resolution of complex flow fields typical of axial-flow turbomachines. The minimization of skewness and the optimization of smoothness generally result in a faster convergence as well as less solution dependence on the grid density, therefore reducing computational cost both in terms of memory and CPU time. As a consequence, the grid generation procedure should be considered an integral

part of the numerical method.

When performing a numerical simulation of turbulent-viscous flow in turbomachinery passage, the following aspects are of importance: i) accurate leading- and trailing-edge flow descriptions, ii) wake resolution, iii) proper gridding in the throat area where most of the shock is expected to occur, and iv) imposition of periodicity. Historically, mesh generation techniques for turbomachinery blades use structured hexahedral representations, the most commonly used ones being H-type, C-type, and O-type. These meshes are obtained either by using an algebraic approach (Kallinderis & Ward 1992) or by solving a system of elliptic partial differential equations (Thompson et al. 1974, Steger & Sorenson 1979, Brackbill & Saltzman 1982) or by solving hyperbolic partial differential equations (Steger & Chaussee 1980). H-type meshes have been by far the most common choice in turbomachinery applications as they are very easy to generate, the imposition of periodicity is straightforward and the mesh density before, inside, and after the blade passage can be easily controlled. However, the leading- and trailing-edge descriptions are poor and a large amount of superfluous points is generated in the region between the inflow and the leading-edge. A classical H-mesh for a transonic blade is shown in Fig. 2.1. O-type grids are not very effective in capturing the wake and their

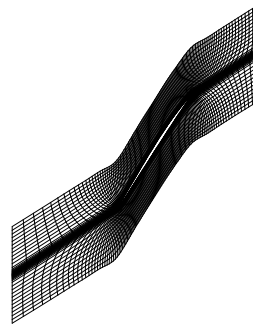


Figure 2.1: Typical structured H-mesh for a fan blade geometry

quality outside the passage is very poor. This can smear the bow shock away from the leading edge of a transonic compressor or the outgoing shock of a transonic turbine blade. On the other hand, C-type meshes can capture the wake structure

if they are carefully generated but their quality in the region between the inflow and the leading-edge is not suitable to resolve bow shock accurately.

A different approach is to use unstructured triangular meshes for 2D turbomachinery calculations. Fully unstructured grids offer good flexibility and most of the flow features can be captured with good accuracy via mesh refinement. 3D unstructured meshes are widely used in external aerodynamics but they have rarely been applied to turbomachinery cases. The main difficulty associated with such meshes is their isotropic nature. The very fact that tetrahedral unstructured meshes do not exhibit any preferred direction is what makes them ideal for discretising arbitrarily complex configurations. In fact most of the unstructured mesh generation techniques rely on this property. However, when a configuration with a preferred direction, such as a turbomachinery blade, is to be discretised, and different resolutions are desired in the various directions, unstructured mesh generation techniques are known to experience great difficulties in meeting such requirements. Turbomachine blades require high resolution near their leading and trailing edges and radial spacing can be relatively coarse. When using an isotropic unstructured mesh, the high leading and trailing edge resolution requirements also result in a high radial resolution in these areas, a feature greatly increases the number of grid points. Such a degree of radial resolution is superfluous, since the radial gradients are known to be relatively small for turbomachinery blade flows. Similar difficulties occur in the boundary layer regions near a wall for high Reynolds number viscous flows, where the normal gradients are several orders of magnitude greater than the stream-wise gradients. To illustrate the unsuitability of unstructured meshes for such applications, a fully unstructured mesh was created for fan blade geometry using an advancing front technique (Morgan et al. 1992), the suction side being shown in Fig. 2.2. It is

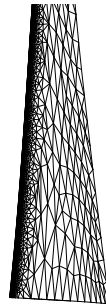


Figure 2.2: Fully unstructured mesh on suction surface

clearly seen that a large number of points are needed in the leading edge area in order to satisfy the resolution requirements, a feature which creates an unacceptably high overhead in the total number of points. It should also be noted that, for this particular geometry, the generation of an efficient viscous mesh will be very difficult using a totally unstructured grid because of the boundary layer considerations. The considerations above lead to the use of semi-structured meshes for turbomachinery blades. The aim of this chapter is to present a novel approach for discretising turbomachinery blades by using a combination of structured and unstructured meshes, the former in the radial direction and the latter in the axial and tangential directions. The basic idea relies on the fact that blade-like structures are not strongly 3D since the radial variation is usually small. It is therefore possible to start with a structured and body-fitted 2D O-grid around a given aerofoil section to resolve the boundary layer. This core mesh is then extended in an unstructured fashion up to the far-field boundaries, the triangulation being performed using an advancing front technique (Morgan et al. 1992, Mavriplis 1995b). Once this 2D grid is generated, it is projected to the remaining radial sections via quasi-conformal mapping techniques. When all such radial sections are formed, a 3D prismatic grid is obtained by simply connecting the corresponding points of different layers. In this way, hexahedral elements are generated in the viscous region and triangular prisms in the rest of the solution domain. Again, such an approach presents a distinct advantage over totally unstructured grids which are usually confined to tetrahedral elements only, though this limitation is usually a consequence of the unavailability of general viscous mesh generators.

## 2.2 Generation of Prismatic Grid

The Section is focused on the proposed semi-unstructured mesh generator which has six main stages:

- Projection of all radial levels, which define the blade geometry, into 2D parametric planes, using local coordinates.
- Generation of a 2D unstructured hybrid-mesh for a given projected radial level, the so-called master plane.
- Generation of a coarse body-fitted structured mesh for all projected radial

levels, including the master plane.

- Inverse mapping of the unstructured hybrid-mesh into the structured one in the master plane.
- Direct mapping to obtain the final unstructured mesh at all radial levels.
- Inverse projection of all unstructured meshes into the original 3D radial levels.
- Generation of 3D prismatic grid by connecting the corresponding points at consecutive radial levels.

### 2.2.1 Geometry modelling

. Turbomachinery blade geometry is usually defined at a number of radial levels. In the general case, these radial levels will lie on 3D surfaces  $\sigma_i(x, r, \theta)$ , where  $i$  indicates the section index, and  $r, \theta$  are the polar coordinates. Using parametric coordinates  $u$  and  $v$ , a typical surface can be defined as:

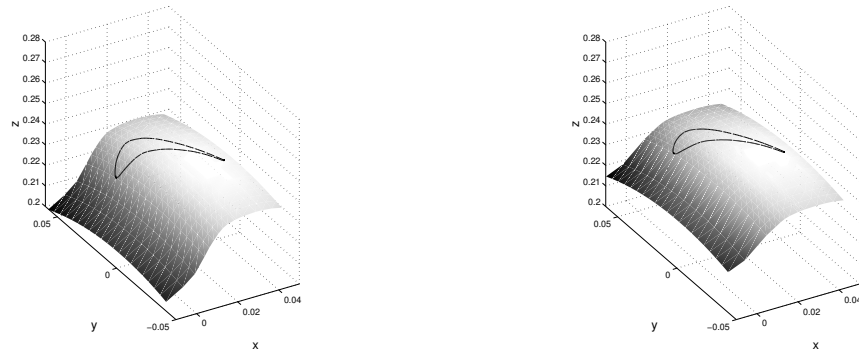
$$\sigma_i(x, r, \theta) = \begin{cases} x_\sigma &= x(u, v) \\ r_\sigma &= r(u, v) \\ \theta_\sigma &= \theta(u, v) \end{cases} \quad (2.1)$$

The starting point of the present method is the projection of the radial sections into parametric 2D planes, using the local coordinate system  $u$  and  $v$ . In this way, the mesh-generation procedure will deal with plane sections only, thus the geometric dimension is reduced from three to two. Fig. 2.3 shows four different radial levels for a typical nozzle guide vane from a well-known aeroengine manufacturer. In this example  $\sigma_i(x, r, \theta)$  is a surface of revolution around the  $x$ -axis, i.e.  $r_\sigma = r(x)$ . The parametric coordinates  $u$  and  $v$  are defined as:

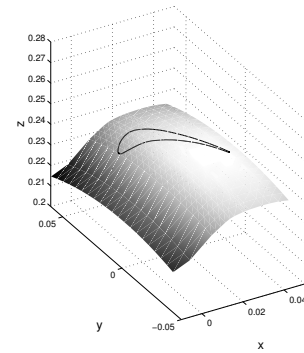
$$u = \int_{x_0}^x r(s) ds \quad (2.2)$$

$$v = r(x) \theta \quad (2.3)$$

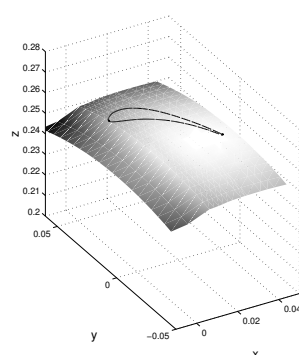
Fig. 2.4 shows the projection of the four radial levels shown in Fig. 2.3.



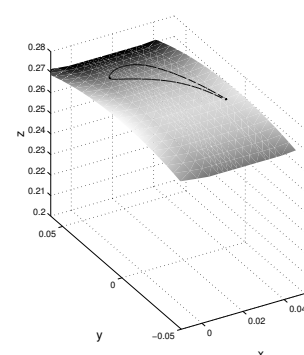
(a) Hub section



(b) Hub-middle section (25% span)



(c) Tip-middle section (75% span)



(d) Tip section

Figure 2.3: Geometry definition of an NGV blade at different radial levels

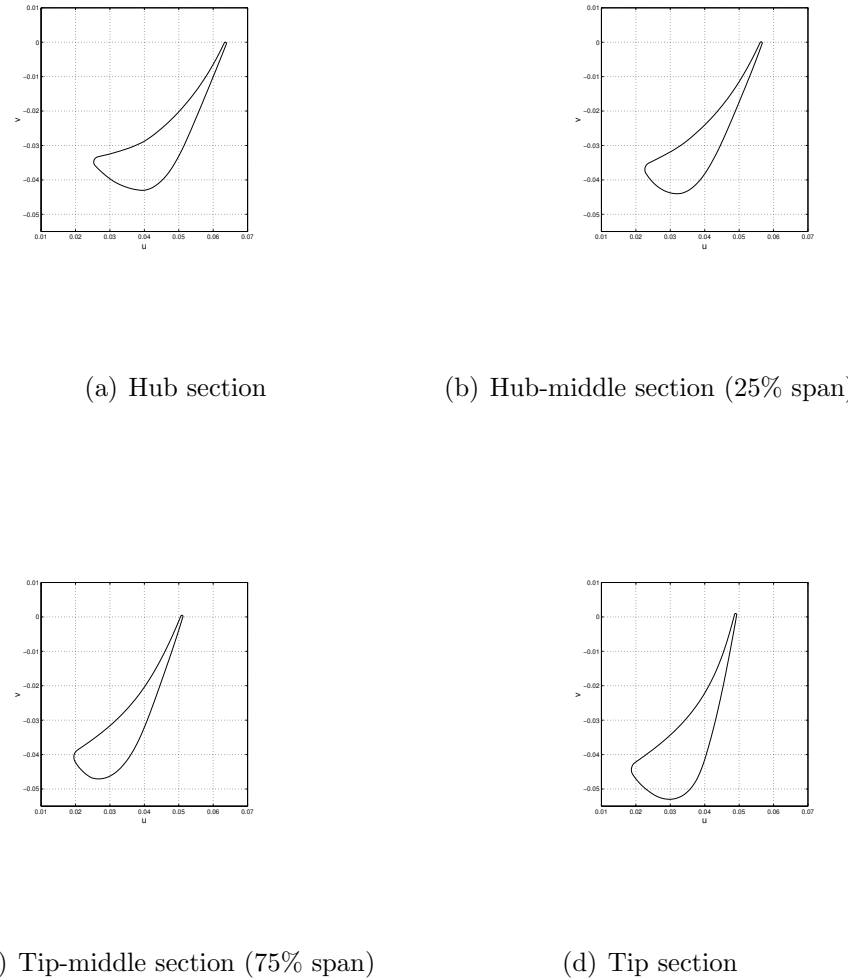


Figure 2.4: Parametric 2D planes for four different radial levels

## 2.2.2 Unstructured mesh generation

Once all radial sections are projected into 2D planes, a hybrid quadrilateral-triangular mesh is generated in the 2D master plane which corresponds to a certain radial level (usually the middle one). The quadrilateral part of the mesh takes the form of a body-fitted O-grid which is generated using an advancing normal method. The orthogonality of this structured mesh is very important for an accurate resolution of the turbulent-boundary layer which originates from high Reynolds number flows. This point will be stressed further in the next chapter where a novel finite-volume discretisation of the Navier-Stokes equations on hybrid grids will be

explored. The remaining part of the domain is discretised using an unstructured mesh generator which uses an advancing front algorithm (Morgan et al. 1992, Mavriplis 1995b). A distinctive feature of this method is that both triangles and points are generated simultaneously. Such an approach enables the generation of elements with variable sizes and stretching, and hence it differs from Delaunay-type mesh generators (Baker 1990, Mavriplis 1995b).

Fig. 2.5b shows the final unstructured hybrid-grid of the NGV in Fig. 2.3 in the 2D master plane which, in this case, corresponds to the projected middle section of the 3D blade.

### 2.2.3 Quasi-conformal mapping

An important part of the mesh-generation strategy is the mapping procedure to project the 2D unstructured mesh of the master plane back to all radial blade-definition levels. A necessary condition for a mapping function is that it must associate a given point of the master plane with one, and only one, point of the target plane. Moreover a mapping function should also guarantee that a given angle in the master plane is mapped into a similar-valued angle in the target plane (quasi-conformal mapping). This last property is essential in order to minimize the skewness of the mesh, especially for highly-twisted blades.

The starting point for the quasi-conformal mapping is the generation of coarse structured quadrilateral grids for all projected radial levels, including the master plane. Following the approach of Steger & Sorenson (1979), these meshes are obtained by solving a system of elliptic partial-differential equations. An essential requirement for such structured meshes is that they must be generated in exactly the same manner, i.e. with the same number of points and quadrilaterals for all radial levels. Fig. 2.5 shows the structured quadrilateral grid and the unstructured hybrid-grid in the master plane, which correspond to the middle radial section. The mapping procedure is divided into three different steps.

**Geometry searching in the master plane.** Each point  $J$  of the unstructured 2D mesh in Fig 2.5b must be located on quadrilateral  $E$  of the structured mesh in Fig 2.5a.

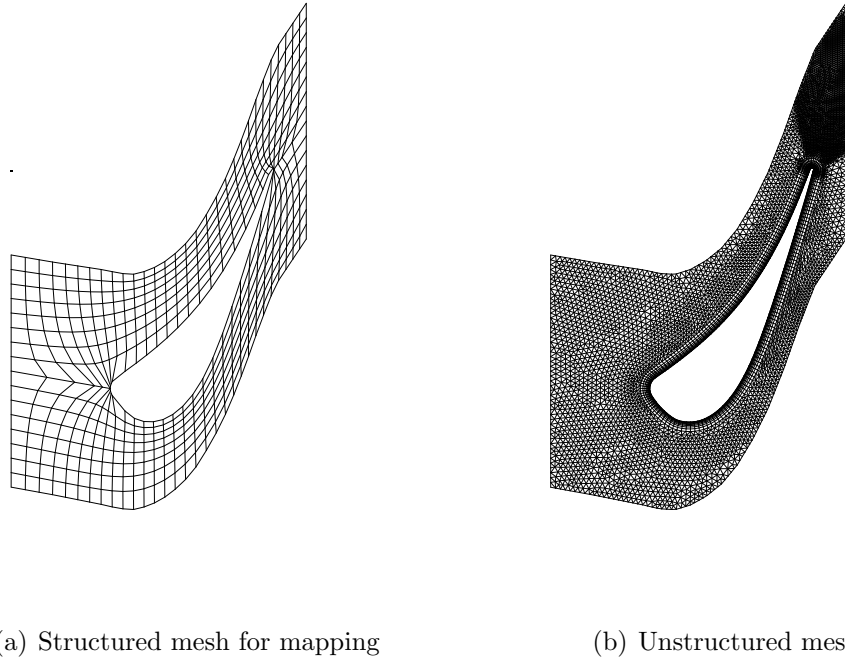


Figure 2.5: Meshes in the master plane

**Inverse mapping in the master plane.** The Cartesian coordinates  $\vec{x}_J = (x_J, y_J)$  of point  $J$ , associated with the quadrilateral  $E$  are given by

$$\vec{x}_J = \sum_{I=1}^4 \vec{x}_I N_I (\xi_J, \eta_J) \quad (2.4)$$

where  $(\xi_J, \eta_J)$  represent the local-coordinates,  $\vec{x}_I$  represents the Cartesian coordinates of nodes  $I = 1, \dots, 4$  of the quadrilateral  $E$  and  $N_I$  is the standard finite-element bilinear shape-function which takes the form (Zienkiewicz & Morgan 1983):

$$N_I = \frac{1}{4} \begin{cases} (1 - \xi)(1 - \eta) \\ (1 + \xi)(1 - \eta) \\ (1 + \xi)(1 + \eta) \\ (1 - \xi)(1 + \eta) \end{cases} \quad (2.5)$$

A Newton-Raphson method is used in order to obtain the values of  $\xi_J$  and  $\eta_J$ .

**Direct mapping.** Once all points  $J$  of the unstructured mesh in the master plane are associated with quadrilateral  $E$  and local-coordinates  $(\xi_J, \eta_J)$  are determined,

coordinates  $\vec{x}_j$  of points on the remaining projected radial sections are obtained directly using equation (2.4).

The above-described steps are shown in Fig. 2.6. The mapping method becomes fully conformal if (i) a given element of the 2D hybrid mesh lies within a single quadrilateral of the structured grid. (ii) In addition, the angles of this quadrilateral must remain the same for all radial sections. If the above two conditions are not satisfied, the conformal property is not guaranteed and, for this reason, the procedure has been labelled quasi-conformal here. Finally, it is worth noting that the algorithm is not CPU-intensive, since the geometry searching and the inverse-mapping are performed once only.

Fig. 2.7 shows the structured meshes used for mapping and the corresponding mapped unstructured hybrid-grids at three radial levels. Once the unstructured mesh has been mapped to all radial blade surfaces, a prismatic mesh is obtained by simply connecting the corresponding points at consecutive levels. Moreover, in order to enhance the quality of the 3D mesh, a smoothing procedure is performed. This operation alters the positions of the interior nodes without changing the topology of the mesh. The element sides are considered as springs of stiffness proportional to the length of the side. The nodes are moved until the spring system is in equilibrium, the position of which is found by Jacobi iterations.

## 2.3 The Program LEVMAP

The semi-structured mesh generation technique proposed in this Chapter has been implemented in the program LEVMAP (LEVel MAPping) written in Fortran 90. The LEVMAP program became a standard facility not only at the Vibration Centre but also at major aeroengine manufacturer. It is now used by many researchers and engineers for aerelasticity calculations on turbomachinery blades. A user's guide is available for the second release of the program (Sbardella 1998). Grosclaude et al. (1999) extended LEVMAP to radial-flow turbomachine blades by modifying the 3D to 2D projection of Section 2.2.1. An example of a semi-structured mesh for a radial turbomachinery assembly is shown in Fig. 2.8. Further improvements of LEVMAP include automatic meshing of fan assembly + intake-duct, non-axisymmetric hub and tip, hub gap and snubber blades. Fig. 2.9 shows an exemple of semi-unstructured mesh for a snubbed fan blade assembly.

## 2.4 Concluding Remarks

A method to generate semi-structured prismatic meshes for turbomachinery blades has been presented. The unstructured mesh in the axial and tangential directions offers more flexibility than standard structured H-type, O-type and C-type meshes, both in terms of skewness minimization and smoothness optimization. The use of fully unstructured viscous meshes for blade like geometries is likely to require a much larger number of grid points and hence there are distinct advantages in using semi-structured meshes. Such was the success of the method that it was adopted by a major aeroengine manufacturer within one year of it being available.

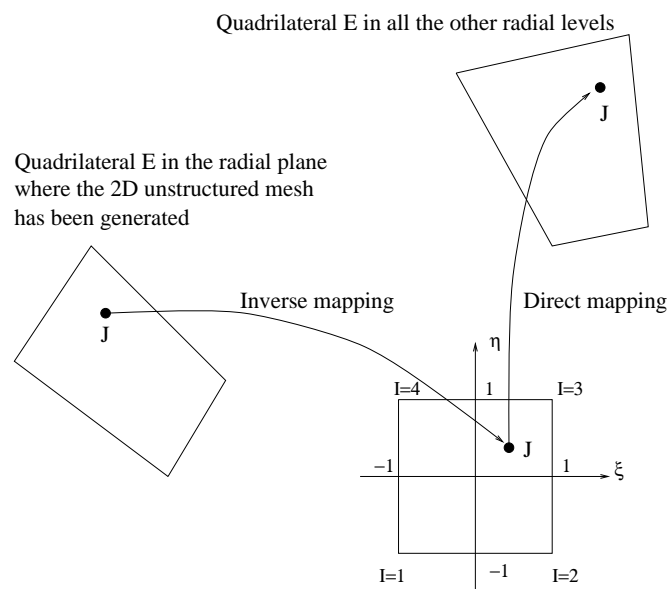
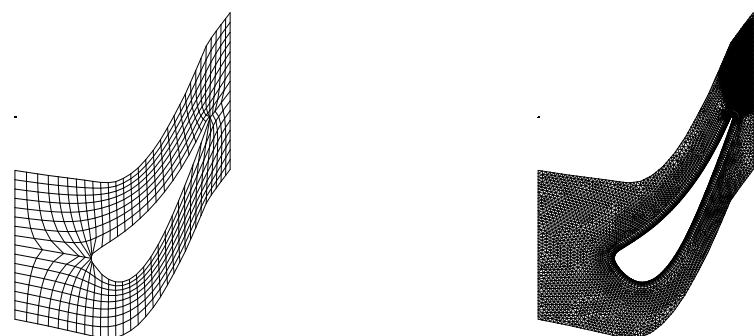


Figure 2.6: Mapping procedure



(a) Hub section



(b) Middle section



(c) Tip section

Figure 2.7: Structured meshes for mapping and corresponding mapped unstructured meshes at three radial levels

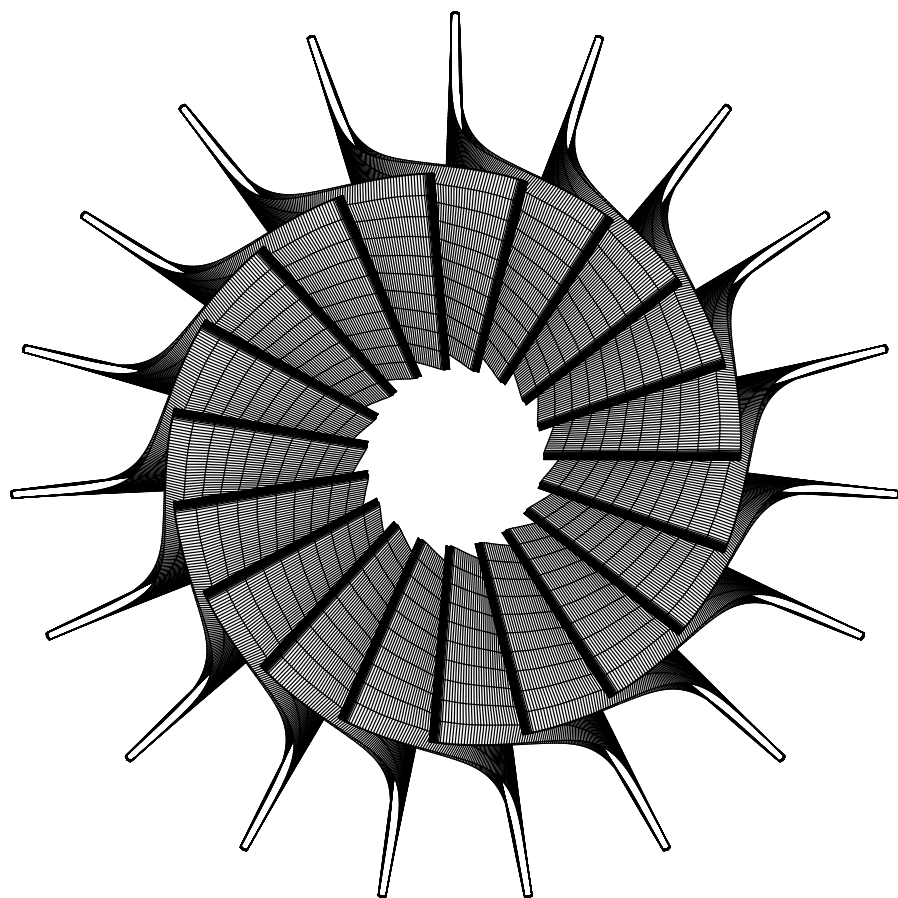


Figure 2.8: Semi-structured mesh for a radial-flow turbomachine

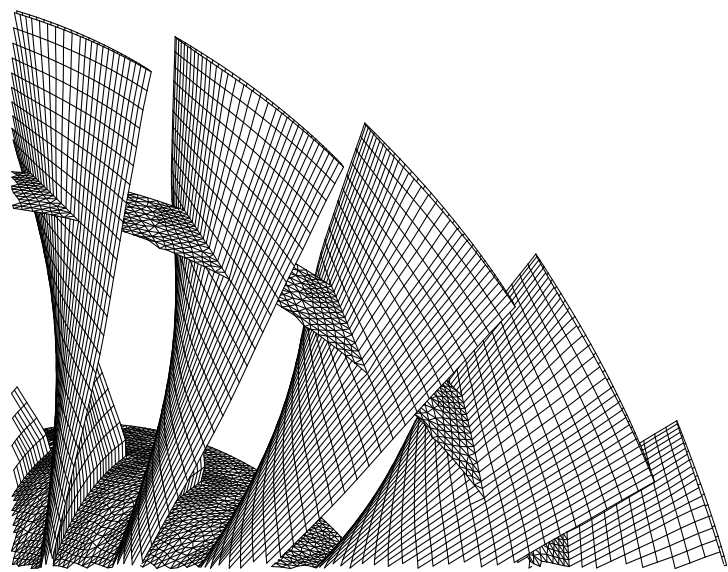


Figure 2.9: Semi-structured mesh for a snubbed fan assembly

# Chapter 3

## Hybrid Grid Solver for Turbulent Viscous Flow

This chapter presents a method for solving steady and unsteady, compressible, turbulent viscous flows for 2D and 3D turbomachinery blades. The flow model is based on the Favre-averaged Navier-Stokes equations, together with a one equation turbulence model. The space discretisation uses a node-centered finite volume scheme on unstructured mixed element grids, consisting of triangles and quadrilaterals in 2D, and of tetrahedra, pyramids, triangular prisms and hexahedra in 3D. The important features of the present approach are the discretisation of the domain via a single, unified *edge-data structure* for mixed-element meshes and the use of a Laplacian weight which results in nearest neighbour stencils. The Laplacian weight is evaluated using an approximation of the Galerkin finite element method. In order to allow a straightforward implementation of fluid-structure coupling, the numerical solution is based on the Arbitrary Lagrangian-Eulerian method in which the grid points may be moved in an arbitrary but specified way. The pseudo time integration for steady-state problems is obtained using a preconditioned agglomeration multigrid method designed for highly anisotropic unstructured hybrid grids. In order to use the same preconditioned multigrid algorithm employed in the steady-state cases, a dual time-stepping technique is used for unsteady computations.

### 3.1 Introduction

Over the last decade, significant advances have been made in the area of turbulent-viscous simulations using unstructured grids. However, compared with their structured counterparts, standard unstructured grid solvers have lower computational efficiency in terms of speed and storage. Unstructured grids often use tetrahedral elements only, an approach which often leads to numerical problems when the region to be discretised has a preferred direction such as the boundary layer for a high-Reynolds number flow. However, there are no fundamental difficulties in extending tetrahedral meshes to include further element types such as triangular prisms, pentahedra and hexahedra. Although both the discretisation of the computational domain and the flow solver will become more complex, such a mixed-element approach will offer a better, more efficient approximation than using tetrahedral elements only. For instance, hexahedral elements will handle boundary layer flows much better than tetrahedral elements because they can be made very slender without creating excessively small internal angles. In order to handle mixed-element meshes, the spatial discretisation of the governing equations needs to be formulated in such a way that the numerical algorithms can be applied in a uniform way to all element types. A relatively simple way of achieving such consistent numerical treatment is to employ an edge-based data structure, which can be obtained from either a finite volume (FV) or a finite element (FE) formulation if the mesh consists of tetrahedral elements only. In this particular case, all nodes are connected directly without any internal diagonals. However, quadrilaterals in 2D and hexahedrals in 3D have not only edges but also diagonal links. Therefore, to create an edge-based data structure from mixed meshes, one cannot use a FE technique because of the non-zero shape function contributions from the diagonally-opposed nodes for which there are no direct edges. Consequently, we will use a FV technique to obtain an edge-based data structure from mixed element meshes but, as reported by Barth (1990), Parthasarathy et al. (1995), Mavriplis & Venkatakrishnan (1995a) for unstructured meshes of tetrahedra, the discretisation of the viscous terms, remains a major problem. The FV edge-based data structure is usually obtained by discretising the viscous terms in two sequential loops, the so-called two-loop approach. The first loop is used to construct the gradients at all points, and the second one forms the second derivatives from the computed gradient information. Using such a technique, the viscous fluxes are treated in an analogous

manner to the inviscid ones and no extra storage is required. However, this strategy, used by several authors (see Peraire et al. 1992, Vahdati & Imregun 1995) has at least three serious drawbacks. First, the *odd-even decoupling* can destabilize the numerical scheme in regions where the viscous effects are important, e.g. the boundary layer. Second, for a 1D mesh of spacing  $h$ , the scheme will reduce to a second difference on a stencil of  $2h$ , a feature which will lower numerical accuracy. Since packing enough points into the viscous layer is one of the main difficulties associated with viscous flow computations, a scheme that operates on every other point is highly undesirable. The third problem is the difficulty of implementing a viscous Jacobian which becomes important if an implicit time integration scheme is employed.

An alternative approach, based on Galerkin finite element (GFE) approximation where velocity and temperature are made dependent variables, is the derivation of the six node-pair coefficients for the Hessian matrix (Mavriplis 1995a, Selmin & Formaggia 1996). Each coefficient is associated with two nodes only, hence the term "node-pair GFE". As mentioned earlier, such a formulation is not edge-based for non-tetrahedral meshes because of the possible diagonal links between the nodes of a hexahedral element. On the other hand, the final discrete viscous terms of such a GFE formulation form a nearest neighbour stencil. Therefore, using the Hessian node-pair coefficients, six second derivatives can be calculated for each node. Since the viscous terms can be expressed as a summation of the product of the node-pair coefficients and the unknowns, the construction of a viscous Jacobian becomes straightforward by explicit differentiation. Furthermore, the odd-even decoupling is avoided and the accuracy is improved. Unfortunately, this approach needs additional storage for the six node-pair coefficients and its applicability is restricted to triangular/tetrahedral elements if an edge-based data structure needs be employed.

In summary, when dealing with mixed-element meshes, FV formulations can yield edge-based data structures but viscous flux discretisation remains problematic. On the other hand, GFE formulations are more efficient but the edge-based data structure cannot be preserved for non tetrahedral elements. Therefore, the discretisation of the viscous fluxes can be improved by combining the storage efficiency of the two-loop FV approach with the numerical efficiency of the node-pair GFE method in an edge-based FV framework.

## 3.2 Favre Averaged Navier-Stokes Equations

The system of Navier-Stokes equations constitute the most complete description of viscous, heat-conducting flows and represents the highest level of approximation for continuous fluids. However, from the point of view of computational fluid dynamics, the vast majority of flow situations occurring in engineering applications enter into a particular form of instability, called *turbulence*. This occurs in most flow situations when the inertial forces exceed the viscous forces by more than four orders of magnitude (the ratio of these two forces is called *Reynolds number*). This form of instability can be represented by statistical fluctuations of the flow quantities around mean or averaged values. Moreover, the space scale of these fluctuations is so small that their direct calculation is beyond the reach of computational capabilities for engineering applications.

Therefore, time-averaged Navier-Stokes equations need to be considered in most situations. In the case of compressible flow equations, this averaging is called Favre averaging (Wilcox 1993). Because of the non-linearity of the Navier-Stokes equations, this procedure generates additional unknowns which will be solved using a suitable turbulence model. In this work, the Spalart Allmaras (1992) one equation turbulence model has been used (Appendix B).

### 3.2.1 Mean flow equations

The unsteady, compressible, Favre-averaged Navier-Stokes equations for a blade row in 3D can be cast in terms of absolute velocity  $\vec{v}$  but solved in a relative non-Newtonian reference frame rotating along with the blade about the  $x$  axis with angular velocity  $\boldsymbol{\Omega}$  as shown in Fig. 3.1. This system of equations, written in a dimensionless, Arbitrary Lagrangian-Eulerian (ALE), integral conservative form (Donea et al. 1982) for a control volume  $\mathcal{V}(t)$  with boundary  $\mathcal{S}(t)$  in Cartesian coordinates  $\vec{x} = (x, y, z)$ , takes the form

$$\frac{\partial}{\partial t} \int_{\mathcal{V}(t)} \mathbf{U} d\mathcal{V} + \oint_{\mathcal{S}(t)} \left[ \vec{\mathbf{F}}(\mathbf{U}, \vec{u}) - \frac{1}{Re} \vec{\mathbf{G}}(\mathbf{U}, \nabla \mathbf{U}) \right] \cdot \vec{n} d\mathcal{S} = \int_{\mathcal{V}(t)} \mathbf{S} d\mathcal{V} \quad (3.1)$$

The viscous term  $\vec{\mathbf{G}}$  on the left-hand side of (3.1) is scaled by the reference Reynolds number so that flow variables are non-dimensionalised consistently. The dimensionless quantities are evaluated from their dimensional counterparts using the dimensional reference values reported in Appendix A.  $\vec{n}$  represents the outward unit

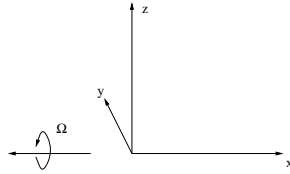


Figure 3.1: Direction of blade rotation

vector of the control volume boundary  $\mathcal{S}(t)$ . The vector  $\vec{u}$ , which represents the velocity in the relative frame of reference minus the velocity  $\frac{d\vec{x}}{dt}$  of the boundary  $\mathcal{S}(t)$ , can be written as:

$$\vec{u} = \vec{v} - \vec{\Omega} \times \vec{x} - \frac{d\vec{x}}{dt} \quad (3.2)$$

where  $\vec{\Omega} = (-\Omega, 0, 0)$ . The sign of the angular velocity vector is determined by the assumption that the positive rotational speed is the one indicated in Fig. 3.1. The solution vector of conservative variables  $\mathbf{U}$  is given by:

$$\mathbf{U} = \begin{bmatrix} \rho & \rho v_1 & \rho v_2 & \rho v_3 & \rho E \end{bmatrix}^T \quad (3.3)$$

The inviscid flux vector  $\vec{\mathbf{F}}(\mathbf{U}, \vec{u})$  has the following components<sup>1</sup>:

$$\mathbf{F}_j = \mathbf{U} u_j + \mathbf{F}_{p_j} \quad (3.4)$$

$$\mathbf{F}_{p_j} = \begin{bmatrix} 0 & p\delta_{1j} & p\delta_{2j} & p\delta_{3j} & v_j p \end{bmatrix}^T \quad (3.5)$$

where  $\delta_{ij}$  represents the Kronecker delta function. The static pressure  $p$  and the total energy  $E$  are related, in a non-dimensional fashion, to the density  $\rho$ , absolute

---

<sup>1</sup> $\mathbf{U} u_j$  represents the  $j$  component of the convective flux, while  $\mathbf{F}_{p_j}$  represents the  $j$  component of the pressure flux.

velocity  $\vec{v}$  and total enthalpy  $H$  by the following two equations which assume perfect gas with a constant ratio  $\gamma$  of specific heat.

$$p = (\gamma - 1) \rho \left[ E - \frac{|\vec{v}|^2}{2} \right], \quad H = E + \frac{p}{\rho} \quad (3.6)$$

Following the approach of Sbardella & Imregun (1999, 2000), the viscous part of the governing equations is split into two distinct components, namely:

$$\vec{\mathbf{G}} = \vec{\mathbf{G}}_l + \vec{\mathbf{G}}_m \quad (3.7)$$

where

$$\vec{\mathbf{G}}_l = \begin{bmatrix} 0 \\ \mu \vec{\nabla} v_1 \\ \mu \vec{\nabla} v_2 \\ \mu \vec{\nabla} v_3 \\ \mu \sum_{j=1}^3 v_j \vec{\nabla} v_j + \frac{\gamma}{\gamma-1} \left( \frac{\mu_l}{Pr_l} + \frac{\mu_t}{Pr_t} \right) \vec{\nabla} T \end{bmatrix} \quad (3.8)$$

$T = p/\rho$  is the non-dimensional static temperature of the fluid. The  $j$ -component of the second term on the left-hand side of (3.7) is:

$$\mathbf{G}_{m_j} = \begin{bmatrix} 0 \\ \mu \frac{\partial v_j}{\partial x_1} + \left( \lambda \vec{\nabla} \cdot \vec{v} \right) \delta_{1j} \\ \mu \frac{\partial v_j}{\partial x_2} + \left( \lambda \vec{\nabla} \cdot \vec{v} \right) \delta_{2j} \\ \mu \frac{\partial v_j}{\partial x_3} + \left( \lambda \vec{\nabla} \cdot \vec{v} \right) \delta_{3j} \\ \mu \left( \vec{v} \cdot \vec{\nabla} v_j \right) + \lambda v_j \left( \vec{\nabla} \cdot \vec{v} \right) \end{bmatrix} \quad (3.9)$$

In (3.8) and (3.9),  $\mu$  represents the total dynamic viscosity of the fluid and is given by the summation of the laminar (physical) dynamic viscosity  $\mu_l$  and the turbulent dynamic viscosity  $\mu_t$ . The value of  $\lambda$  is given by the Stokes relation  $\lambda = -\frac{2}{3}\mu$  which is valid for the majority of the flow situations with the exception of very high temperature or pressure ranges. It is easily seen that the component  $\vec{\mathbf{G}}_l$  in (3.8) includes the Laplacian operators of the three velocity components and temperature only. The second component,  $\vec{\mathbf{G}}_m$ , contains the mixed derivative terms, while the

vector of source terms  $\mathbf{S}$  on the right-hand side of (3.1) takes into accounts for the blade rotation

$$\mathbf{S} = \begin{bmatrix} 0 & 0 & \rho\Omega v_3 & -\rho\Omega v_2 & 0 \end{bmatrix}^T \quad (3.10)$$

The derivation of the constitutive relations of viscous flows is discussed in detail by Schlichting (1979) and White (1991).

### 3.2.2 Boundary conditions

For convection dominated phenomena, such as those described by the compressible Navier-Stokes equations, the formulation of correct boundary conditions is extremely important and its impact on the numerical scheme is often dominating. The reason for this strong influence can be traced back to the physical nature of the convection propagation phenomena (Hirsh 1990). If all the variables were known at a boundary from the knowledge of the physical input, there would be no difficulty; however this is generally not the case with hyperbolic systems of partial differential equations. The number of physical variables that can be freely imposed at a boundary is dependent on the propagation properties of the system and, in particular, on the information propagated from the boundary towards the inside of the flow region. These are known as *physical boundary conditions*. The remaining variables will depend on the details of the flow and are, therefore, part of the solution. However from a numerical point of view, information about all variables is required at the boundary. This additional information gives rise to *numerical boundary conditions* (Hirsch 1990).

The presence of viscosity and heat conduction transforms the conservation laws of momentum and energy into second-order partial differential equations. The system of Navier Stokes equations is therefore an hybrid system consisting of parabolic momentum and energy equations and of a hyperbolic continuity equation. A direct consequence is the need for a greater number of physical boundary conditions when dealing with viscous flows instead of inviscid flows.

**Flow-tangency.** Also known as the inviscid wall condition, this boundary condition at the solid walls is expressed by the requirement that there is no flow through the surface of the moving wall. Only one physical boundary condition can

be imposed at this boundary because only the forward travelling acoustic wave is entering the domain. Mathematically, this condition is expressed by the vanishing of the velocity normal to the wall.

$$\vec{u} \cdot \vec{n} = 0 \quad (3.11)$$

Expressed in a *weak sense*, i.e. through the fluxes, (3.11) becomes:

$$\oint_{wall} \vec{\mathbf{F}} d\mathcal{S} = \oint_{wall} \vec{\mathbf{F}}_p d\mathcal{S} = \begin{bmatrix} 0 \\ p n_1 d\mathcal{S} \\ p n_2 d\mathcal{S} \\ p n_3 d\mathcal{S} \\ p \left( \vec{\Omega} \times \vec{x} + \frac{d\vec{x}}{dt} \right) \cdot \vec{n} d\mathcal{S} \end{bmatrix} \quad (3.12)$$

**No-slip condition.** The no-slip condition at the solid walls is expressed by the requirement that the fluid velocity relative to the moving wall must be zero. Mathematically this can be expressed as:

$$\vec{u} = \vec{v} - \vec{\Omega} \times \vec{x} - \frac{d\vec{x}}{dt} = 0 \quad (3.13)$$

In addition to (3.13), an additional information is required due to the presence of the second derivative terms in the Navier-Stokes equations<sup>2</sup>. Here this additional information is for an adiabatic wall

$$\vec{n} \cdot \vec{\nabla} T = 0 \quad (3.14)$$

**Inflow and outflow boundaries.** The quasi-3D non-reflecting boundary conditions developed by Saxer & Giles (1993) are used for steady-state computations. These boundary conditions are obtained from a Fourier mode analysis of the linearised Euler equations at the far-field boundaries. Implemented in a turbomachinery environment, the approach assumes that the solution at the boundary is circumferentially decomposed into Fourier modes, the 0<sup>th</sup> mode corresponding to the averaged solution. The 0<sup>th</sup> mode is treated according to the standard 1D boundary

---

<sup>2</sup>The no-slip condition is valid for viscous flow only.

condition (Thompson 1987, 1990) which allows the user to specify certain physical quantities at the boundaries. Such averaged quantities are:

- **Inflow:** stagnation temperature, stagnation pressure and flow angles.
- **Outflow:** static pressure.

The remaining part of the solution, represented by the sum of the harmonics, is treated according to the exact<sup>3</sup> 2D theory of Giles (1988, 1990a). Since this method considers radial flow variations in the 0<sup>th</sup> mode only, it is called quasi-3D non-reflecting boundary conditions. In the absence of any radial variations, the boundary conditions are exact within the 2D linear theory.

The standard 1D characteristic boundary conditions of Thompson (1987, 1990) are used for unsteady time-marching aerodynamics.

**Periodic boundaries.** Taking advantage of the edge-based data structure, the periodicity is handled in a straightforward way as long as the points in the two periodic boundaries are located at same axial and radial coordinates.

$$\mathbf{U}_{\theta_0 + \Delta\theta} = \mathbf{U}_{\theta_0} \quad (3.15)$$

### 3.3 Spatial Discretisation

The development of a FV edge-based data structure for unstructured mixed-element meshes will now be described in detail.

As shown for the 2D mesh of Fig. 3.2, using a node-centered approach and choosing the median dual mesh as control volume<sup>4</sup>, a FV discretisation of (3.1), written in a semi-discrete form, is given by:

$$\frac{\partial (\mathcal{V}_I \mathbf{U}_I)}{\partial t} = - \sum_{s=1}^{m_I} [|\vec{\eta}_{IJ_s}| (\mathcal{F}_{IJ_s} - \mathcal{G}_{m_{IJ_s}}) - \tau_{IJ_s} \mathcal{G}_{l_{IJ_s}}] + \mathcal{V}_I \mathbf{S}_I \quad (3.16)$$

As shown in Fig. 3.2, node  $I$  is connected by edges to  $m_I$  ( $m_I = 6$  in Fig. 3.2) nodes  $J_s$ ,  $\mathcal{V}_I$  representing the control volume associated with it.  $\mathcal{F}$ ,  $\mathcal{G}_m$  and  $\mathcal{G}_l$  correspond to the inviscid and viscous vectors  $\tilde{\mathbf{F}}$ ,  $\tilde{\mathbf{G}}_m$  and  $\tilde{\mathbf{G}}_l$ .  $\vec{\eta}_{IJ_s}$  is the metric vector

---

<sup>3</sup>The term exact refers to the solution of the linear problem. Since the linear problem is itself an approximation to the nonlinear one, there will be errors which are proportional to the square of the amplitude of the non-uniformities at the far-field boundaries.

<sup>4</sup>A discussion of different control volume definitions is given by Barth & Jespersen 1989.

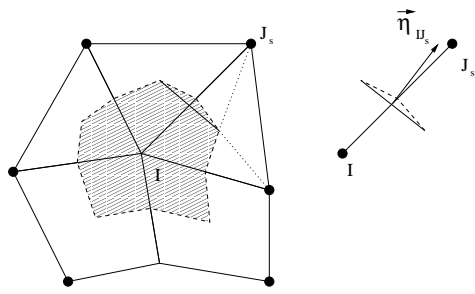


Figure 3.2: Control volume for node  $I$  and metric vector  $\vec{\eta}_{IJ_s}$  for edge  $IJ_s$

associated with the surface area of edge  $IJ_s$  while  $\tau_{IJ_s}$  represents the Laplacian weight associated with the same edge. The summation in (3.16) has been obtained applying the Green's formula to the surface integral of (3.1) and choosing as path the median dual mesh (Barth & Jespersen 1989, Barth 1991). Of particular interest here is the use of the GFE node-pair formula for the Laplacian operator  $\tau_{IJ_s}$  in order to construct an approximate version for the FV edge-data scheme (Sbardella & Imregun 1999, 2000).

### 3.3.1 Inviscid discretisation

The discretisation of the inviscid flow terms in (3.16) is given by:

$$\sum_{s=1}^{m_I} |\vec{\eta}_{IJ_s}| \mathcal{F}_{IJ_s} \quad (3.17)$$

where  $\mathcal{F}_{IJ_s}$  represents the inviscid flux function along edge  $IJ_s$  which is obtained using a central difference scheme with added matrix artificial dissipation. This

artificial dissipation is a blend of second and fourth order differences. The fourth order terms ensure the stability of the scheme in smooth regions of the flow, while the second order terms are required to damp numerical oscillations in the vicinity of discontinuities. The inviscid flux function is expressed as:

$$\mathcal{F}_{IJs} = \frac{\vec{\mathbf{F}}_I + \vec{\mathbf{F}}_{Js}}{2} \cdot \frac{\vec{\eta}_{IJs}}{|\vec{\eta}_{IJs}|} - \mathcal{D}_{IJs} \quad (3.18)$$

where the artificial dissipation  $\mathcal{D}_{IJs}$  along the edge is given by:

$$\mathcal{D}_{IJs} = \frac{1}{2} |\mathbf{A}_{IJs}| [\psi \Delta \mathbf{U} - \epsilon_4 (1 - \psi) \Delta \mathcal{L}(\mathbf{U})] \quad (3.19)$$

Here  $\Delta$  represents the difference operator along edge  $IJs$

$$\Delta(\cdot) = (\cdot)_{Js} - (\cdot)_I \quad (3.20)$$

$|\mathbf{A}_{IJs}|$  is the standard Roe matrix (Roe 1981) between the two stages  $\mathbf{U}_I$  and  $\mathbf{U}_{Js}$ ,  $\epsilon_4 \approx 1/16$  is the fourth order artificial dissipation coefficient.  $\mathcal{L}_I(\mathbf{U})$  is a pseudo-Laplacian operator, at node  $I$ , given by:

$$\mathcal{L}_I(\mathbf{U}) = \left( \sum_{s=1}^{m_I} \frac{\mathbf{U}_{Js} - \mathbf{U}_I}{s_{IJs}} \right) \left( \sum_{s=1}^{m_I} \frac{1}{s_{IJs}} \right)^{-1} \quad (3.21)$$

where

$$s_{IJs} = |\vec{x}_{Js} - \vec{x}_I| \quad (3.22)$$

$\psi$  represents the limiter function which varies between 0 and 1 and it is required in order to switch the scheme to first order ( $\psi = 1$ ) in the vicinity of discontinuities (Jorgenson & Turkel 1993).

### Evaluation of metric vector

The metric vector  $\vec{\eta}_{IJs}$  is obtained via a summation of the two dual median lengths around the edges, multiplied by their normals. For example the metric vector of the edge connecting nodes  $I$  and  $Js$  is shown in Fig. 3.2 for a 2D mesh. Another

way of calculating  $\vec{\eta}_{IJs}$  is the use of the GFE scheme in a node-pair formulation (Selmin & Formaggia 1996):

$$\vec{\eta}_{IJs} = \sum_{e \in IJ_s} \int_{\mathcal{V}_e} \left( N_I \vec{\nabla} N_{Js} - N_{Js} \vec{\nabla} N_I \right) d\mathcal{V} \quad (3.23)$$

where  $e \in IJs$  indicates the set of elements which share nodes  $I$  and  $J_s$ , and  $N_i$  is the test function of the GFE method. In the derivation of (3.23), no a-priori assumptions were made regarding element types or the space dimensionality of the flow. If the FE test function  $N$  is linear, both FV and GFE schemes will result in the same neighbouring stencil on triangular and tetrahedral meshes. Since all nearest neighbours are joined to the vertex under consideration by an edge, the node-pair formulation of (3.23) is equivalent to an edge-based data structure (Bath & Jespersen 1989, Selmin & Formaggia 1996). However, for quadrilaterals in 2D,



(a) Galerkin finite element (GFE) (b) Finite volume (FV)

Figure 3.3: Stencils for a quadrilateral mesh

and pyramids, wedges and hexahedra in 3D, the edge-data structure of a standard FV discretisation is no longer equivalent to the node-pair formulation of the GFE method. For example, in the case of a quadrilateral element, the GFE formulation takes into account the diagonal links. This approach results in a 9-point stencil, involving all corner points of the 4 quadrilaterals which share the vertex under

consideration. On the other hand, the classical FV formulation considers the edge-based links only, resulting in a 5-point stencil (Fig. 3.3). Similarly, for a hexahedral element, the GFE method results in a 27-point stencil whereas the FV results in a 9-point stencil. Consequently, the GFE method is more expensive than the standard FV method but it has less dependence on mesh quality. For instance, when a mesh of quadrilateral or hexahedral elements is not orthogonal, the FV scheme still retains its conservation properties but its accuracy degenerates from second to first order (Essers et al. 1995). For distorted meshes, the FV scheme is unable to recover the correct gradient values for a linear field on such elements. However, in the present formulation, the gradient information is used only for the evaluation of the limiter  $\psi$  in (3.19). By adopting a suitable limiter function, as that developed by Jorgenson & Turkel (1993), the FV scheme should retain its overall second order accuracy.

### **Artificial dissipation and limiter function**

Central-difference type schemes, such that in (3.18), are commonly used for the solution of the Euler and Navier-Stokes equations. The artificial dissipation  $\mathcal{D}_{IJs}$  in (3.19) plays a crucial role in the determination of the quality of the numerical method. One of the first central-difference schemes used the scalar artificial dissipation model developed by Jameson et al. (1981). During the 1980s, a considerable amount of research effort has been devoted towards the construction of more sophisticated schemes by minimising the added artificial dissipation. The paper by Swanson & Turkel (1992) summarises such effort and shows how central difference schemes with matrix artificial dissipation, as that in (3.19), are related to upwind schemes which utilize concepts from the characteristic theory in order to determine the direction of spatial differencing (Roe 1981, Harten 1983b, Osher 1984, Pandolfi 1984, Roe 1986). In fact, scheme (3.18) with  $\psi = 1$  is equivalent to the first-order upwind scheme of Roe (1981). Also, upwind schemes can be designed to have the TVD property in the case of scalar conservation laws (Harten 1983a, Osher 1984). The TVD property is very useful in constructing limiter functions for second-order numerical schemes (Sweby 1984). Swanson & Turkel (1992) introduced flux limiter functions that are consistent with the central-difference dissipation models using the TVD property.

The limiter function used here is a multidimensional extension of the modified,

van Leer central difference limiter, proposed by Swanson & Turkel (1992). For an equispaced 1D mesh, the limiter function at point  $I$  is defined as:

$$\psi_I = \frac{|p_{I+1} - 2p_I + p_{I-1}|}{(1-\chi)(|p_{I+1} - p_I| + |p_I - p_{I-1}|) + \chi(p_{I+1} + 2p_I + p_{I-1})} \quad (3.24)$$

where  $0 \leq \chi \leq 1$ . If  $\chi = 0$ ,  $\psi_I$  becomes the van Leer central difference TVD limiter. If  $\chi = 1$ ,  $\psi_I$  is equivalent to that used by Jameson et al. (1981). For a 3D mesh the limiter function associated with node  $I$  and side  $IJs$  becomes:

$$\psi_I|_{IJs} = 2 \frac{|p_{Js} - p_I - \vec{\nabla}p_{Js} \cdot \vec{s}_{IJs}|}{(1-\chi)(|p_{Js} - p_I| + |p_I - p_{Js} + \vec{\nabla}p_{Js} \cdot \vec{s}_{IJs}|) + 2\chi(p_{Js} + p_I)} \quad (3.25)$$

where  $\vec{s}_{IJs}$  is given in (3.22). The final value of  $\psi_I$  is than given by the maximum value of (3.25) of all sides  $IJs$  associated with node  $I$ :

$$\psi_I = \max(\psi_I|_{IJs}) \quad (3.26)$$

The central-difference scheme in (3.18) is slightly more dissipative than a second-order upwind scheme and this is for two reasons. First  $\psi_I = \max(\psi_I|_{IJs})$ , is multidirectional, while  $\psi_I$  is usually chosen along a particular direction in upwind schemes. Second, upwind limiters allow to have negative viscosity but still retaining the TVD property while central-difference scheme cannot have negative artificial dissipation. In any case, to compensate for this slight increase in dissipation, central-difference schemes are simpler to program and require less computer time per time step, especially if used in conjunction with multistage time stepping techniques where the artificial dissipation is evaluated at alternate stages (Appendix D).

### 3.3.2 Viscous discretisation

The viscous fluxes associated with the mixed derivatives in  $\vec{\mathbf{G}}_m$  of (3.9) are treated in the same way as their inviscid counterparts and their contribution to (3.16) is given by:

$$\mathcal{G}_{mIJs} = \frac{1}{Re} (\vec{\mathbf{G}}_{mI} + \vec{\mathbf{G}}_{mJs}) \cdot \frac{\vec{\eta}_{IJs}}{|\eta_{IJs}|} \quad (3.27)$$

Here, the Laplacian terms will be treated in a novel way in order to improve both the accuracy and the robustness of the numerical scheme (Sbardella & Imregun 2000). In (3.16), these terms take the form:

$$\mathcal{G}_{l_{IJs}=\frac{1}{Re}} \begin{bmatrix} 0 \\ \mu_{IJs} \Delta v_1 \\ \mu_{IJs} \Delta v_2 \\ \mu_{IJs} \Delta v_3 \\ (\mu \vec{v})_{IJs} \cdot \Delta \vec{v} + \frac{\gamma}{\gamma-1} \left( \frac{\mu_l}{Pr_l} + \frac{\mu_t}{Pr_t} \right)_{IJs} \Delta T \end{bmatrix} \quad (3.28)$$

The subscript  $IJs$  indicates an arithmetic mean over nodes  $I$  and  $Js$ :

$$(\cdot)_{IJs} = \frac{(\cdot)_{Js} + (\cdot)_I}{2} \quad (3.29)$$

The difference operator  $\Delta$  in (3.28) is given in (3.20). In the present formulation, that deals with mixed-element meshes, the Laplacian weight  $\tau_{IJs}$  in (3.16) is evaluated using an approximation of the GFE node-pair relation. For a generic 2D or 3D element, the GFE Laplacian weight can be written as (Selmin & Formaggia 1996):

$$\tau_{IJs} = - \sum_{e \in IJs} \int_{\mathcal{V}_e} \vec{\nabla} N_I \cdot \vec{\nabla} N_{Js} d\mathcal{V} \quad (3.30)$$

As for (3.23), the Laplacian node-pair coefficient can be used for triangle/tetrahedral elements only if the data structure is edge based. Equation (3.30) will now be extended to other types of elements so that an approximate Laplacian weight, that is suitable for an edge-data FV implementation, can be evaluated. Let us consider the quadrilateral element of Fig. 3.4 to illustrate such an approach. In (3.30), the two integrals involving the diagonal links between nodes  $(I_1 - I_3)$  and  $(I_2 - I_4)$  are not zero. Since the diagonal links are not present in the FV formulation, in the present method their contribution is added to the edge links  $(I_1 - I_2)$ ,  $(I_2 - I_3)$ ,  $(I_3 - I_4)$  and  $(I_1 - I_4)$ . As sketched in Fig. 3.4, each diagonal link contributes by a factor of 1/2 to the Laplacian operator of any of the four edges of the quadrilateral element. An equivalent treatment is adopted for pyramids, wedges and hexahedra. The integration of (3.30) is obtained using a one point Gauss quadrature for all type of elements. If the mesh is orthogonal, this approach will recover the second-order Laplacian weight of the GFE method.

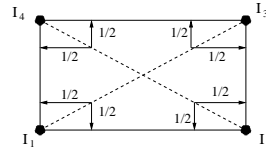


Figure 3.4: Contribution of diagonal links to Laplacian weight for a quadrilateral mesh

## 3.4 Time Integration

After discretising the governing equations in space, the semi-discrete system of coupled ordinary differential equations (ODE) in (3.16) is obtained. Such system of coupled ODEs can be expressed in a compact form as:

$$\frac{d(\mathcal{V}_I \mathbf{U}_I)}{dt} = \mathbf{R}_I (\mathbf{U}) \quad (3.31)$$

where  $\mathbf{R}_I$  represents the discretised form of the inviscid fluxes, viscous fluxes and source terms at node  $I$ .

A preconditioned multigrid algorithm has been used as an iterative method for calculating both steady-state solutions and unsteady time-marching solutions via a fully implicit scheme.

### 3.4.1 Steady state algorithm

If a steady state solution is sought, time accuracy is not an issue and the time integration can be seen as relaxation method towards steady-state. Equation (3.31) is then written in the following form:

$$[\mathbf{P}]^{-1} L_\tau \delta \mathbf{U}_I = \mathbf{R}_I(\mathbf{U}) \quad (3.32)$$

As discussed in Appendix D,  $L_\tau$  represents a multistage Runge-Kutta operator while  $[\mathbf{P}]^{-1}$  represents a preconditioner developed for accelerating steady-state calculations.  $\delta$  indicate the change over a pseudo time step. Such a preconditioned Runge-Kutta relaxation algorithm is used as a smoother in an agglomeration multigrid algorithm. The principle behind this algorithm is that errors associated with high frequencies are damped by the smoother while the errors associated with the low frequencies are damped on the coarser grids where these frequencies manifest themselves as high frequencies.

A complete description of the algorithm is given in Appendix D.

### 3.4.2 Unsteady time-marching algorithm

A numerical scheme to solve time-marching unsteady aerodynamics is described. The scheme is fully implicit and uses the same preconditioned multigrid algorithm developed for steady-state predictions, in order to iteratively invert the equations at each physical time step. The design objective of the method is unconditional stability. This means that the choice of the time-step is based on the physical to be resolved, rather than limited by numerical stability, which is particularly important for meshes with large variations in size.

It has been demonstrated that A-stable schemes<sup>5</sup> cannot have an order of accuracy higher than two (Jameson 1991). The trapezoidal scheme has the smallest truncation error of all second order A-stable methods but it becomes undamped for large time steps<sup>6</sup>. Consequently a second order implicit backward difference scheme, which is A-stable and damped for  $\Delta t \rightarrow \infty$ , has been preferred for this work.

A second order implicit backward time integration of (3.31) can be expressed as:

$$\frac{3(\mathcal{V}_I \mathbf{U}_I)^{n+1} - 4(\mathcal{V}_I \mathbf{U}_I)^n + (\mathcal{V}_I \mathbf{U}_I)^{n-1}}{2\Delta t} = \mathbf{R}_I(\mathbf{U}^{n+1}) \quad (3.33)$$

where  $n$  denotes the physical time level. The implicit non-linear system of equations given by (3.33) needs to be solved every time-step. Indicating with  $\mathbf{U}^l$  the  $l^{th}$

---

<sup>5</sup>An A-stable scheme is stable for all values of the time step of  $\Delta t$

<sup>6</sup>This can be demonstrated by performing a stability analysis of the 1D convection equation.

approximation to  $\mathbf{U}^{n+1}$  and with  $\delta\mathbf{U}_I = \mathbf{U}^{l+1} - \mathbf{U}^l$ , an iterative equation is constructed, from (3.33), by simply adding a pseudo-time derivative term  $[\mathbf{P}]^{-1} L_\tau \delta\mathbf{U}_I$  to the left-hand side.

$$[\mathbf{P}]^{-1} L_\tau \delta\mathbf{U}_I + \frac{3\mathcal{V}_I \delta\mathbf{U}_I + 3(\mathcal{V}\mathbf{U})_I^l - 4(\mathcal{V}\mathbf{U})_I^n + (\mathcal{V}\mathbf{U})_I^{n-1}}{2\Delta t} = \mathbf{R}_I(\mathbf{U}^l) \quad (3.34)$$

This expression can be written in a compact form, similar to (3.32), as:

$$[\mathbf{P}]_{imp}^{-1} L_\tau \delta\mathbf{U}_I = \mathbf{R}_{I_{imp}}(\mathbf{U}^l) \quad (3.35)$$

where  $[\mathbf{P}]_{imp}^{-1}$  and  $\mathbf{R}_{I_{imp}}$  are given by

$$[\mathbf{P}]_{imp}^{-1} = [\mathbf{P}]^{-1} + 3\frac{\mathcal{V}_I}{2\Delta t} [\mathbf{I}] \quad (3.36)$$

$$\mathbf{R}_{I_{imp}}(\mathbf{U}^l) = \mathbf{R}_I(\mathbf{U}^l) - 3\frac{\mathcal{V}_I}{2\Delta t} \mathbf{U}_I^l + \mathbf{E}_I^n \quad (3.37)$$

$\mathbf{E}_I^n$  involves the portion of the physical time derivative at previous time steps and is invariant during the iteration process.

$$\mathbf{E}_I^n = \frac{4(\mathcal{V}\mathbf{U})_I^n - (\mathcal{V}\mathbf{U})_I^{n-1}}{2\Delta t} \quad (3.38)$$

The preconditioner  $[\mathbf{P}]_{imp}^{-1}$  on the left-hand side of (3.35) contains a portion of the physical-time derivative as suggested by Melson et al. (1993) in order to produce a stable numerical scheme for any choice of the physical time step  $\Delta t$ .

In order to clarify this point, let us consider, for a moment, a scalar preconditioner, also called local time step:

$$[\mathbf{P}]^{-1} = \frac{\mathcal{V}_I}{\sigma \Delta \tau} [\mathbf{I}] \quad (3.39)$$

where  $\Delta \tau$  is the local time step at node  $I$ , and  $\sigma$  represents the CFL number. Substituting (3.39) into (3.36), one can obtain

$$[\mathbf{P}]_{imp}^{-1} = \frac{\mathcal{V}_I}{\sigma \Delta \tau_{imp}} [\mathbf{I}] \quad (3.40)$$

$$\Delta \tau_{imp} = \frac{\Delta \tau}{1 + \frac{3}{2} \frac{\Delta \tau}{\Delta t} \sigma} \quad (3.41)$$

From (3.41), it is apparent that the effect of the implicit treatment is to reduce the time step in regions of the flow where the ratio of pseudo/physical time steps,  $\frac{\Delta\tau}{\Delta t}$  becomes large. For low-frequency unsteady problems, accuracy constraints permit a large physical time step  $\Delta t$ , so that the time step ratio  $\frac{\Delta\tau}{\Delta t}$ , is generally very small throughout most of the computational domain, and the implicit treatment plays a minimal role. However, near the far-field, large mesh cell will produce correspondingly large pseudo-time stability limits,  $\Delta\tau$ , and the implicit treatment becomes a useful mechanism to ensure stability.

## 3.5 Test Cases

The numerical procedure described up to now can be utilized to analyse steady and unsteady flow at various levels of approximation. Obviously, the computational cost in terms of CPU time and memory increases with the complexity of the modelling from simple 2D steady flows to 3D unsteady multi-passage analyses. Four examples of the code application to turbomachinery and external flow field prediction will be presented in this Section along with discussion in order to show the capabilities and limits of the procedure. The first example deals with the steady-state flow prediction of turbomachinery flow for a 2D geometry. The remaining three test cases illustrate the use of the dual-time-stepping code for predicting unsteady flows for which analytical or experimental data is available in the literature.

For these computation the preconditioned agglomeration multigrid described in Appendix D has been used. In the boundary layer, agglomerated grids are obtained by coarsening in the normal direction with a fine-to-coarse cell ratio of 4:1. A line-implicit Jacobi preconditioner has been used for all four test cases presented.

### 3.5.1 Steady flow over a turbine rotor blade

The calculations presented in this Section are for the 2D Von Karman Institute gas turbine rotor blade (VKI LS59). This blade represents a challenging test for a transonic flow solver and it has been used by several researchers for code validation (Arnone and Swanson 1993). The flow is turned about 96° by the blade, with an exit Mach number which varies from 0.81 up to 1.20. The blade passage is convergent and originally designed to work up to sonic conditions. In fact, the suction side is curved even after the throat region, which produces a strong trailing

edge shock in transonic regimes. Klock et al. (1986) provide the geometry and detailed experimental data for this rotor blade.

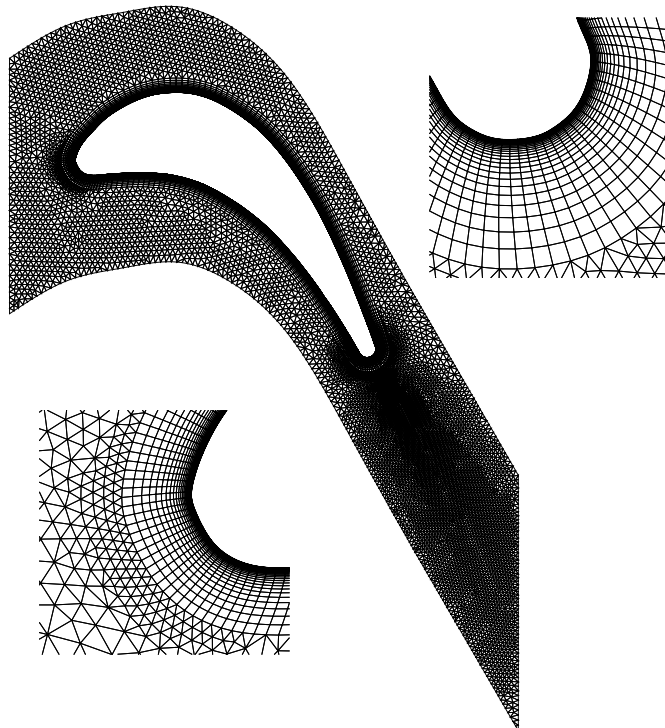


Figure 3.5: VKI LS59 rotor blade. Computational mesh with zoom views at leading- and trailing-edges

The inlet flow angle is  $30^\circ$  while the Reynolds number based on the blade chord and outlet conditions is in the range from  $6.2 \cdot 10^5$  up to  $8.3 \cdot 10^5$ . A view of the computational mesh is shown in Fig. 3.5. This mesh contains 7,440 quadrilaterals in the boundary layer region and 12,842 triangles in the rest of the domain which yields a total of 14,203 points. Three successively agglomerated meshes were used

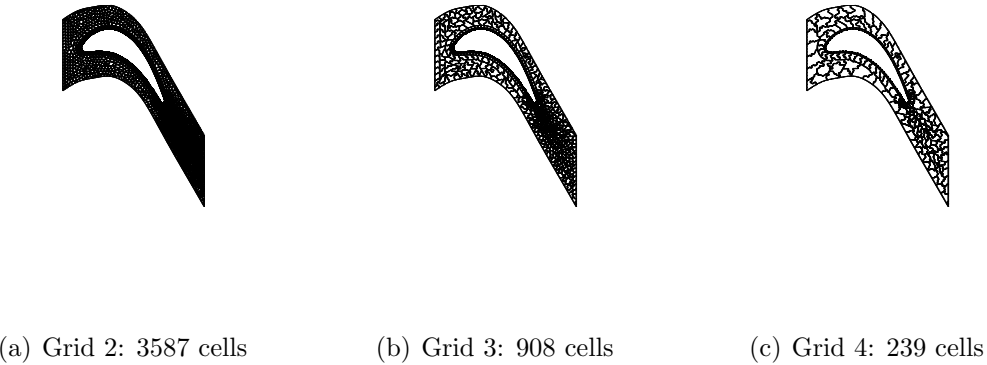


Figure 3.6: VKI LS59 rotor blade. Agglomerated grids

in a four grid W-type cycle in conjunction with the line-implicit preconditioner described in Appendix D. Fig. 3.6 shows the control volumes associated with these agglomerated grids.

The isentropic Mach number distribution on the blade surface is given in Fig. 3.7 for the case with an isentropic outlet Mach of unity. The sonic conditions are obtained at  $x/c \approx 0.47$  on the suction side and at the trailing edge in the pressure side resulting in fairly straight sonic line across the blade passage as shown in the Mach number contours of Fig. 3.8a. The flow is accelerated along the suction side up to  $x/c = 0.6$  followed by a moderate deceleration downstream. For this blade, the experimental data of Kiocok et al. (1986) include exit flow angles, inlet Mach number and loss coefficient defined as  $\xi = 1 - \frac{|v_2|}{|v_{is2}|}$ , where  $v_{is2}$  represents the isentropic outlet velocity. The comparison between the experimental and the computed values of such quantities as a function of the outlet Mach number is reported in Fig. 3.9.

Fig. 3.10 compares the convergence history obtained using the line-implicit solver of Appendix D, on a single grid and on four grid W-type cycle. The convergence history of a single grid, point-Jacobi, iterative implicit scheme as the one used by Sayma et al. (2000), is also plotted. It is evident that the single grid solution is not converged and the reason of this could be blamed to the grid anisotropy as well as to the blunt trailing edge of the blade which causes a recirculation bubble which could be inherently unsteady (Fig. 3.8b). The single grid implicit scheme of Sayma et al. (1997) converges very slowly because not designed to be effective in

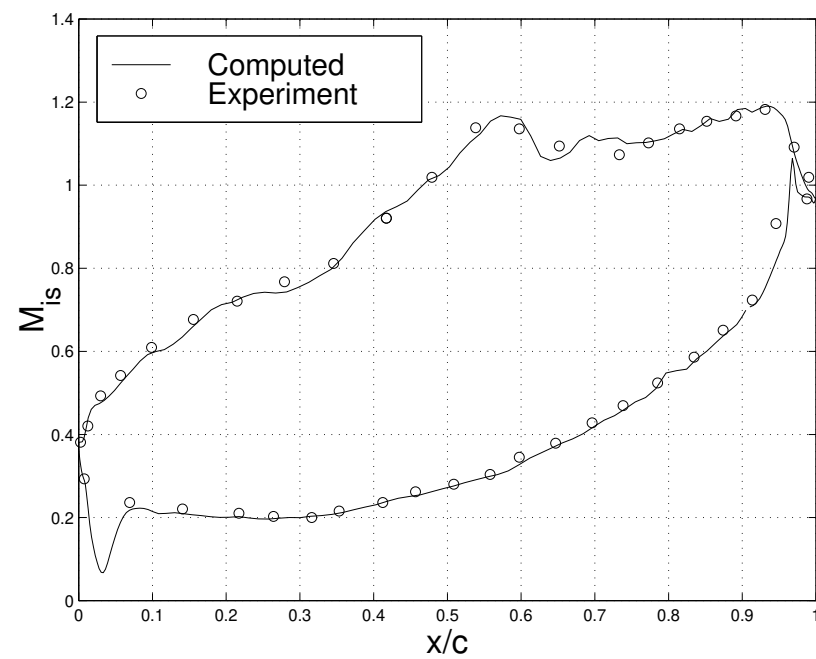


Figure 3.7: VKI LS59 rotor blade.  $M_{is2} = 1$ ,  $Re_2 = 7.6 \cdot 10^5$ . Isentropic Mach number distribution

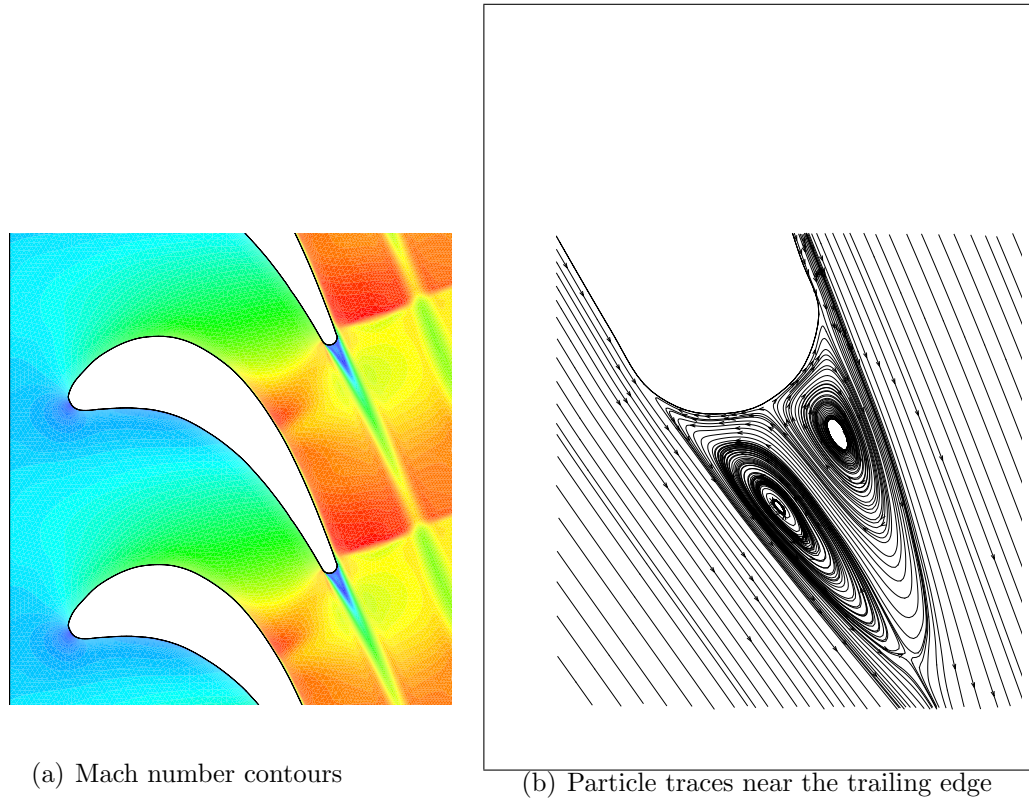


Figure 3.8: VKI LS59 rotor blade.  $M_{is2} = 1$ ,  $Re_2 = 7.6 \cdot 10^5$ . Computed solution

damping error arising from highly stretched meshes.

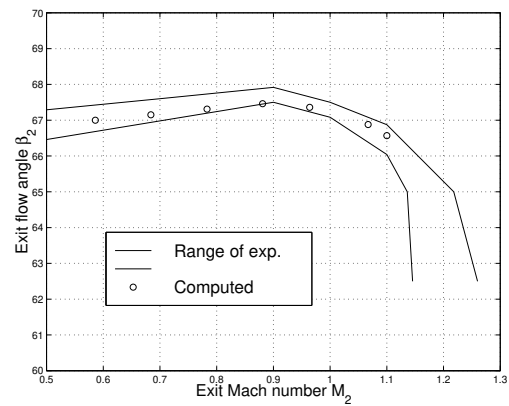
### 3.5.2 Impulsively accelerated flat plate

To demonstrate the capability of the present method for unsteady flow, the solution of an impulsively accelerated flat plate in the laminar regime is presented. This example is also known as Stokes first problem and an analytical solution for incompressible flow is available (Schlichting 1979, Mattioli 1989). This analytical solution shows that the time dependent solution collapses to a single solution of nondimensional velocity versus the similarity parameter  $\eta$  defined as

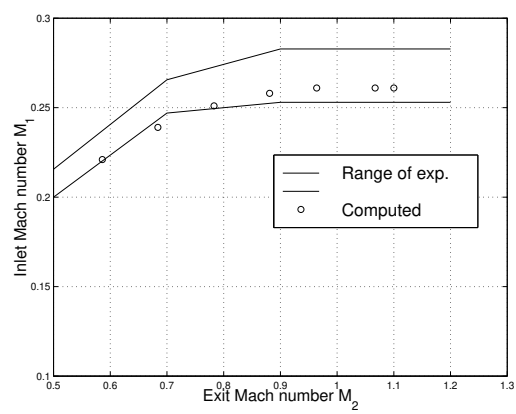
$$\eta = \frac{y}{2\sqrt{\nu t}} \quad (3.42)$$

where  $y$  is the normal distance from the flat plate,  $\nu$  is the kinematic viscosity and  $t$  is the physical time. The analytical solution take the simple form

$$\frac{u}{u_\infty} = \operatorname{erf}(\eta) \quad (3.43)$$



(a) Exit flow angle



(b) Inlet Mach number

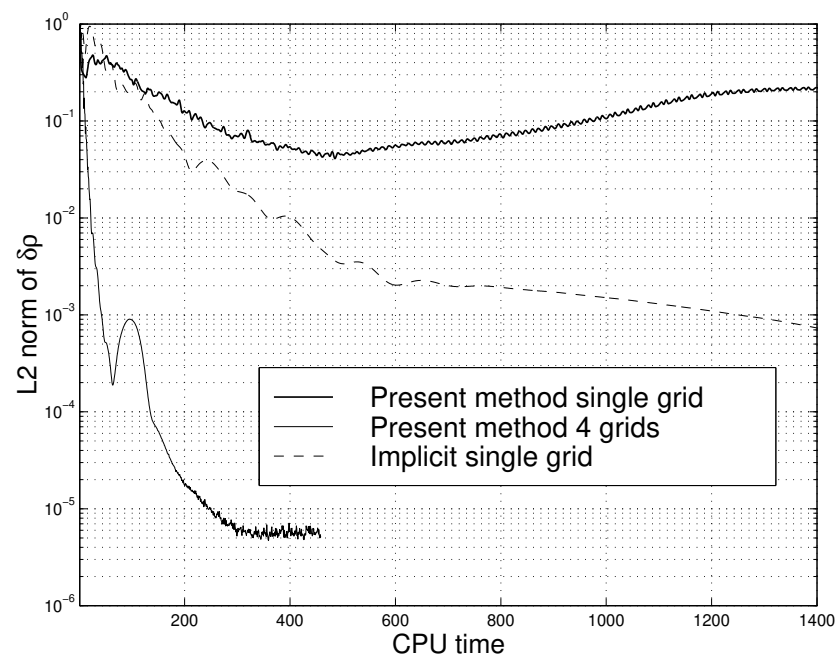


Figure 3.10: VKI LS59 rotor blade. Residual history

where  $\text{erf}$  represents the error function (Schlichting 1979).

Three calculations were performed with the present method with 1, 5 and 10 physical time steps to reach the same physical time  $t = 0.001 \text{ sec}$ . The maximum ratio between the physical and pseudo time step,  $\Delta t / \Delta \tau$ , was of around 17,000 for the case where a single time step was used to reached  $t = 0.001 \text{ sec}$ . Fig. 3.11a shows the comparison between the numerical and analytical solutions. As expected, the smaller the physical time step, the better the agreement. If one used an explicit method to calculate the unsteady flow at the same physical time level, than it should have performed around 15,000 time steps using a CFL number of 1.5. For the case of 5 time step the convergence of (3.35) for a given time level was obtained with  $\approx 15$  W multigrid cycles using four grids. In terms of CPU time this means that with 5 time steps the present method was  $\approx 120$  times faster than an explicit Runge-Kutta integration method.

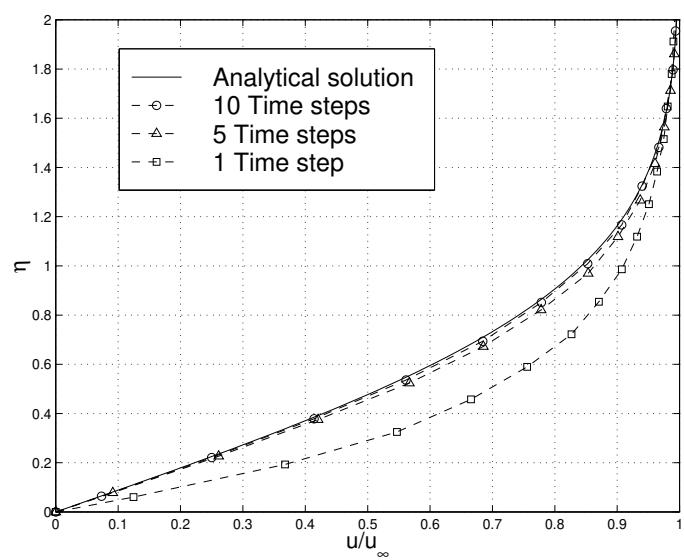
Fig. 3.11b shows the comparison of the residual within a given physical time step, using a single grid and a four grids W-type cycle. As one would expected, the convergece to a new physical time level improves if more the one grid are used. However such improvement does not compare with the one obtained for steady-state computations. Convergence histories similar to the one shown in Fig. 3.11b represents the best result obtained for unsteady flows.

### 3.5.3 Vortex shedding past a cylinder

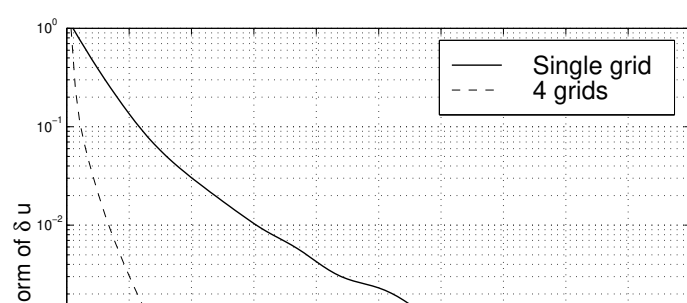
This test case is intended to predict the natural vortex shedding past a cylinder in a laminar incompressible flow regime. Vortex shedding is one of many viscous flows which, though posed with fixed and steady boundary conditions, evolve into unsteady motions because of flow instability. If one consider a circular cylinder with diameter  $d$ , then the incompressible flow field generated by a uniform velocity at infinity  $u_\infty$  is dependent solely upon the Reynolds number  $Re_d$

$$Re_d = \frac{\rho_\infty u_\infty d}{\mu_\infty} \quad (3.44)$$

If  $Re_d < 40$  the flow is steady. If  $Re_d > 40$  the flow becomes unstable and consequently unsteady when  $Re_d > 50$ . The flow field is caracterised by a unsteady wake which consists of pairs of vortices shed alternately from the upper and lower part of the cylinder surface. If  $50 < Re_d < 150$  such a wake structure is well organised



(a) Velocity profiles



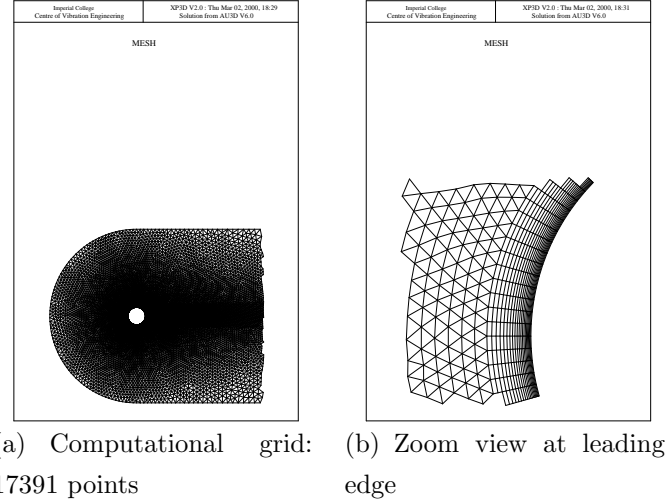


Figure 3.12: Circular cylinder. Computational mesh

and is called Karman vortex sheet after a paper by Karman (1911) explaining this alternation to be a stable configuration for vortex pairs (Schlichting 1979). An important feature of this flow is that the dimensionless cylinder frequency or Strouhal number

$$St = \frac{fd}{u_\infty} \quad (3.45)$$

remains constant  $\approx 0.21$  for  $100 < Re_d < 10,000$ . Thus, in this Reynolds number range, the shedding cycle takes place during the time that the free-stream moves approximately five cylinder diameters.

Fig. 3.12 shows the computational mesh used for this test case, it contains 2280 quadrilaterals in the boundary layer and 29863 triangles in the rest of the domain for a total number of point of 17391. Fig. 3.13 shows the three agglomerated grids used in the time accurate multigrid algorithm. Four different calculations were performed for various Reynolds numbers with an inlet Mach number of 0.2 and the computed Strouhal number is reported in Fig. 3.14a together with the experimental value of 0.21. The comparison is satisfactory for all four test cases. Fig. 3.14b reports the evolution in time of the pressure coefficient at a point in the wake close to the cylinder. The time history refers to three cycles of oscillations after a periodic flow conditions is reached. The very periodic behaviour of the flow is evident and proves the robustness and accuracy of the scheme.

The time step for those calculations was set to have 50 divisions over a cycle. This

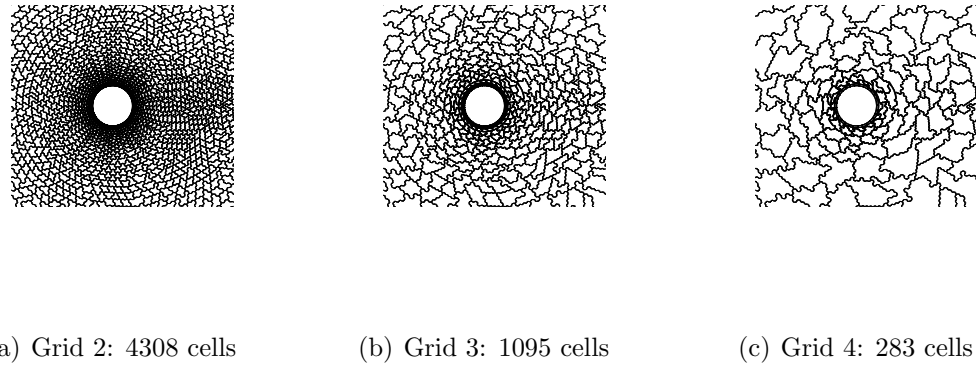


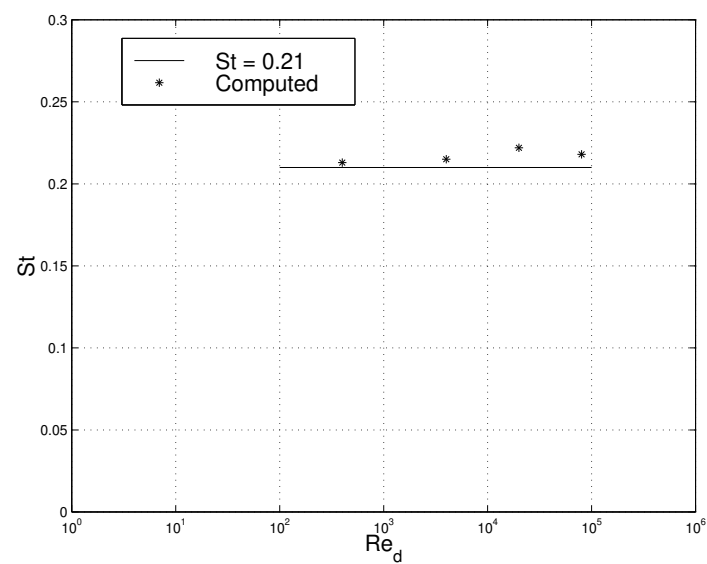
Figure 3.13: Circular cylinder. Agglomerated grids

correspond to a local CFL number between two in the far field and three thousand in the boundary layer region.

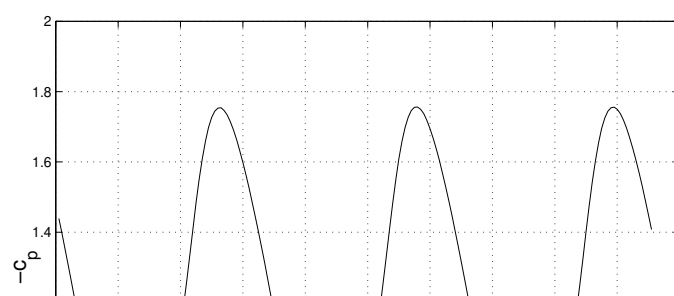
Figs. 3.15 reports the instantaneous particle traces in six instants over a cycle (the seventh position would be equivalent to the first) for two different  $Re_d$ . The shedding of the vortex is evident as well as the mechanism of their formation with a vortex merging. This is evident in Fig. 3.15a between instants 3 and 4, and 6 and 1. It is worth to note the different pattern followed by the vortices for the two Reynolds number under consideration. For  $Re_d = 400$  the shedding structure is well organised while for  $Re_d = 4,000$  the inertial forces play a more important role in the wake flow with formations of large recirculation bubbles which are propagated with small dissipation.

### 3.5.4 Transonic buffeting over a bicircular airfoil

Starting for about 1976, several experiments were carried out on transonic buffeting over bicircular-arc airfoils at NASA Ames research center with the intent to provide basic data to guide further development of computer codes (McDevitt et al. 1976). The wind tunnel used for those experiments was designed for this purpose in order to minimize upper and lower wall interference effects. The tests were conducted at free-stream Reynolds numbers, based on airfoil chord length, ranging from 1 to 17 million. The test Mach number was varied from near the critical value of 0.71 to the highest possible without the airfoil chocking the channel. McDevitt et al. (1976) presented unsteady results for a biconvex circular-arc airfoil with thickness-



(a) Computed Strouhal number



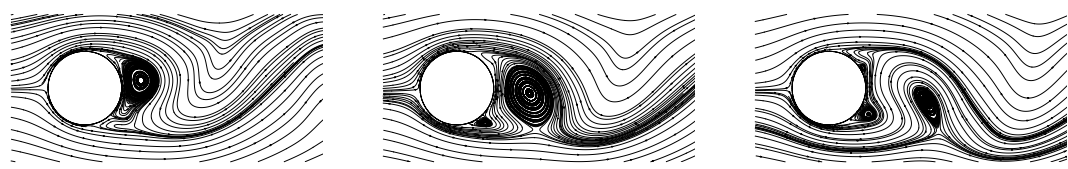
chord ratio of 0.18. The nominal test Mach for this airfoil is 0.775 and the wind tunnel end walls were designed to minimize wall effects for this flow condition. At a free-stream Reynolds number of 7 million, experiments suggest transonic buffeting at a free stream Mach number in the range from 0.76 to 0.78. On the contrary, the calculations show unsteadiness in the Mach number range from 0.765 up to 0.83. The computed buffeting reduced frequency  $\pi f c / u_\infty$  matches the experimental one of  $\approx 0.5$ .

Fig. 3.16 reports instantaneous Mach number contours in eleven instants over a cycle while Fig. 3.17a shows the average and range of pressure coefficient distribution in the airfoil surface. Fig. 3.17b reports the evolution in time of the pressure coefficient at a point in the airfoil corresponding to  $x/c = 0.7$ . The time history refers to three cycles of oscillation after a periodic flow condition is reached. The calculations were performed using roughly 45 divisions over a cycle (as indicated in Fig. 3.17b). This correspond to a local CFL number between 0.1 in the far-field and 10,000 in the boundary layer.

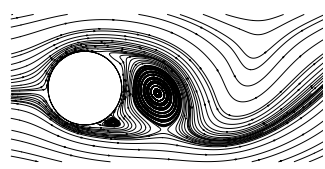
## 3.6 Concluding Remarks

- A FV scheme for the solution of the Favre averaged Navier-Stokes equations has been presented. The method employs an edge-based data structure as well as a nearest-neighbour stencil for the discretisation of the Laplacian operator. The method enables the use of 2D and 3D unstructured, structured or block structured mixed-element grids without any modifications to the numerical scheme.
- A drawback of this approach is the need to evaluate the mixed derivative terms of the viscous fluxes by using a standard FV method which does not yield a nearest neighbour stencil. However, in cases where the viscous effects are in the boundary layer only, such terms are very small and hence the method is expected to be well suited to engineering applications.
- The same time relaxation multigrid algorithm has been applied to both steady and unsteady time-marching aerodynamics. The benefit of unconditional stability has been demonstrated by computing unsteady viscous flow with time-steps corresponding to CFL numbers on the range 1000 - 10,000.

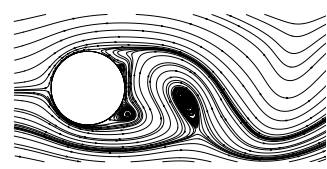
- The multigrid technique efficiently performs for steady-state flow computations even though its robustness needs to be improved for 3D turbulent flow simulations. For time-marching unsteady flows, the multigrid technique does not perform as well. Convergence histories similar to the one shown in Fig. 3.11b represents the best result obtained. The reason for such a break down is not clear. However the stability restriction in (3.41) could play an important part near the far-field boundaries.
- For unsteady computations, an attractive way forward could be the implementation of an adaptive scheme which selects different time-marching techniques in different zones depending on the local situation.
- The scheme produces good and stable results for highly distorted meshes as demonstrated by Sbardella & Imregun (2000).



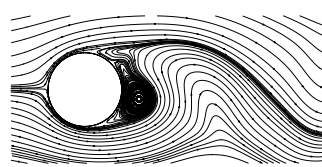
Time 1



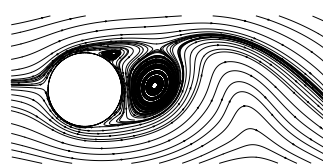
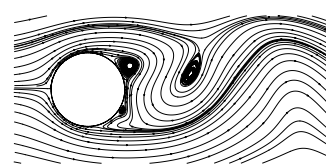
Time 2



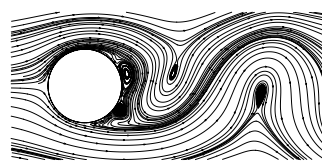
Time 3



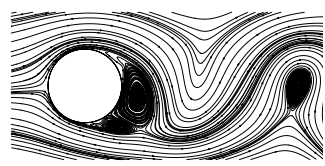
Time 4

Time 5  
(a)  $Re_d = 400$ 

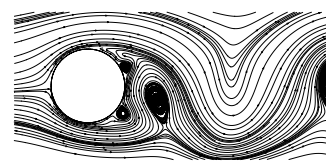
Time 6



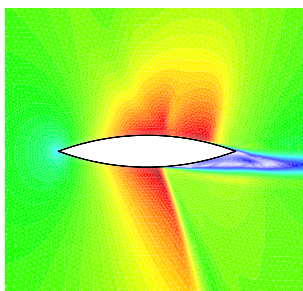
Time 1



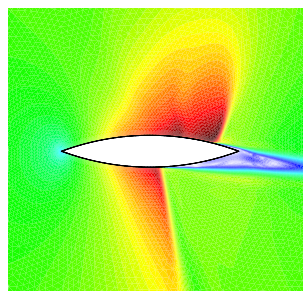
Time 2



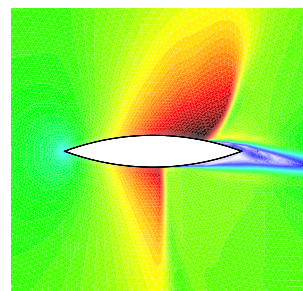
Time 3



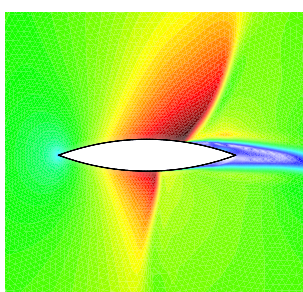
(a) Time 1



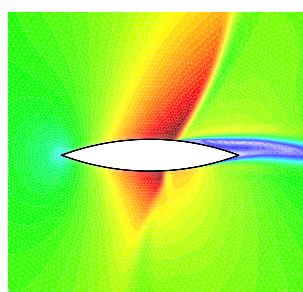
(b) Time 2



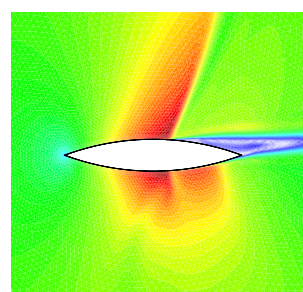
(c) Time 3



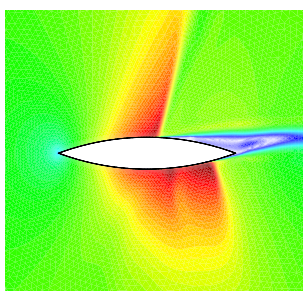
(d) Time 4



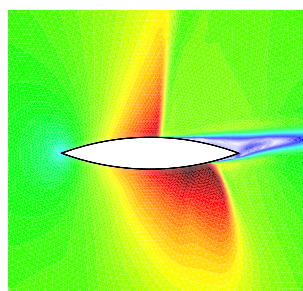
(e) Time 5



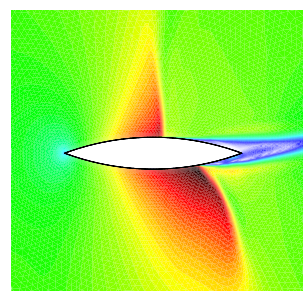
(f) Time 6



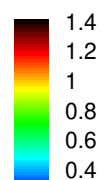
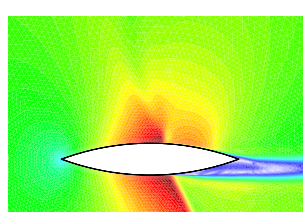
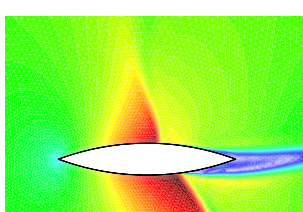
(g) Time 7

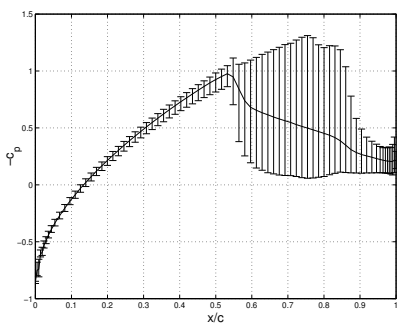


(h) Time 8

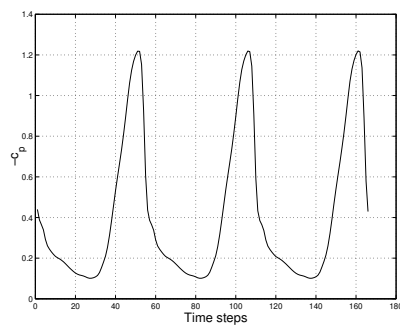


(i) Time 9





(a) pressure coefficient distribution



(b) pressure coefficient evolution

Figure 3.17: Bicircular airfoil. Computed pressure coefficient

# Chapter 4

## Linearised Unsteady Navier-Stokes Solver

This Chapter extends the hybrid grid flow solver of in the previous Chapter, to a time-linearised version of the unsteady Favre-averaged Navier-Stokes equations. The linearised unsteady viscous flow equations are derived by assuming small harmonic perturbations from a steady-state flow and the resulting equations are solved using a pseudo-time marching technique. Such an approach enables the same numerical algorithm to be used for both the non-linear steady and the linearised unsteady flow computations. An important feature of the work is the full linearisation of the Spalart-Allmaras turbulence model. The methodology was validated for a number of 2D test cases such as linear flat-plate cascades and flat plates with laminar boundary layers. A more advanced study is given for two different flow regimes past a turbine cascade, the so-called 11th International Standard Configuration, for which there are both steady and unsteady flow measurements. Linearised unsteady flow predictions were discussed for several modelling levels: inviscid, viscous with frozen turbulence and fully turbulent viscous. The findings highlighted the need for a full linearisation in cases where the steady-state flow exhibits significant viscous effects such as separation and recirculation.

### 4.1 Towards Viscous linearised representations

In Section 1.2.1 a literary survey on linearised method is given. The methods presented were based on an inviscid flow representation and thus they cannot deal

with cases where viscous effects are important: shock-boundary layer interaction, flow separation and recirculation. It should be noted that such features are particularly important for turbomachinery unsteady flows because most investigations are conducted at off-design conditions. For instance, generally speaking, fan blades do not encounter flutter problems at the design speed but part-speeds may cause some concern. The flow behaviour at these lower speeds is dominated by viscous effects and hence the linearised analysis tools must somewhat include the necessary features.

One of the first time-linearised Navier-Stokes analyses of a cascade unsteady flow was reported by Cizmas & Hall (1995). The computational domain was divided into two parts: a viscous flow near the airfoil and in the wake region, and an inviscid flow in the rest of the domain. The viscous flow was modelled using a finite difference discretisation of the boundary layer equations while the inviscid flow was modelled using a finite element discretisation of the full potential equation. However the analysis was limited to incompressible flows and to prescribed boundary layer assumption. Ning & He (1991b) presented a novel quasi 3D non-linear harmonic Euler/Navier-Stokes method which combines the computational efficiency of linearised techniques and some of the accuracy of non-linear formulations. Holmes et al. (1997) are amongst the first researchers to present a 3D time-linearised Navier-Stokes analysis with a  $k - \omega$  turbulence model. Their results were limited to flows with a thin attached boundary layer and whether or not the turbulence model itself needed to be linearised was discussed in detail. Although this issue will be dealt with later in this Chapter, an overview will be given here. Avoiding the linearisation of the turbulence model and using the mean-flow values for the eddy viscosity, the so-called frozen turbulence model, is relatively straightforward. On the other hand, the linearisation of the turbulence model may require significant algebra and coding effort. The mathematical formulation of a specific turbulence model and its mesh density requirement near the blade surface are further important considerations. For instance, a very fine mesh requirement may well negate some of the computational advantages. In any case, an important contribution is made by Clark & Hall (1999) who reported a 2D linearised Navier-Stokes analysis using the one-equation Spalart-Allmaras (1992) turbulence model. They predicted the aeroelasticity behaviour of a fan blade at some off-design condition which involved high incidence and flow separation over much of the suction surface. Their results showed good overall agreement with the available experimental data.

The present Chapter describes a 2D/3D finite-volume (FV) scheme for a full discretisation of the time-linearised Navier-Stokes equations. The important features of the present work are the discretisation of the domain via a single, unified edge-data structure for mixed-element meshes and the use of a Laplacian weight which results in nearest neighbour stencils. Furthermore, the one-equation turbulence model of Spalart-Allmaras (1992), which has the form of a sixth conservation equation, was linearised for a consistent formulation. Such a unified approach allows the use of 2D and 3D structured, unstructured or block-structured grids with mixed elements under the same numerical scheme. The results were validated against available analytical and experimental data. The differences between linearising inviscid, frozen turbulence and fully-turbulence models are discussed in some detail for the case of the 11<sup>th</sup> International Standard Configuration.

## 4.2 Time-linearised Navier-Stokes Equations

This Section deals with the linearisation of the 3D unsteady, compressible, Favre-averaged Navier-Stokes equations (3.1) and the correspondent boundary conditions. Since (3.1) as been written in a ALE formulation, the inclusion of linearised blade oscillation becomes straightforward by simply linearising the mesh motion as well as the flow equations.

### 4.2.1 Linearisation

The linearisation of the governing equations around a steady-state solution starts by expressing the conservation variables and the coordinates as a sum of a mean steady-state value and a small perturbation:

$$\vec{x}(\vec{x}, t) = \bar{x} + \tilde{x}(\vec{x}, t) \quad (4.1)$$

$$\mathbf{U}(\vec{x}, t) = \bar{\mathbf{U}}(\vec{x}) + \widetilde{\mathbf{U}}(\vec{x}, t) \quad (4.2)$$

It is then possible to express the unsteady flux vector  $\vec{\mathbf{F}}$  in (3.4) as a summation of three different terms:

$$\vec{\mathbf{F}} = \bar{\vec{\mathbf{F}}} + \tilde{\vec{\mathbf{F}}} - \widetilde{\vec{\mathbf{F}}}_g \quad (4.3)$$

where  $\bar{\vec{F}}$  represents the mean steady value of the inviscid fluxes,  $\tilde{\vec{F}}$  is the unsteady part of the inviscid fluxes which does not include the grid motion while  $\tilde{\vec{F}}_g$  includes the unsteady terms due to the grid motion only. To first order, using (3.2) and (3.4) the terms above can be expressed as:

$$\bar{\vec{F}} = \bar{\mathbf{U}} (\bar{v} - \vec{\Omega} \times \bar{\vec{x}}) + \bar{\vec{F}}_p \quad (4.4)$$

$$\tilde{\vec{F}} = \tilde{\mathbf{U}} (\bar{v} - \vec{\Omega} \times \bar{\vec{x}}) + \bar{\mathbf{U}} \tilde{v} + \tilde{\vec{F}}_p \quad (4.5)$$

$$\tilde{\vec{F}}_g = \bar{\mathbf{U}} \left( \vec{\Omega} \times \tilde{\vec{x}} + \frac{d\tilde{\vec{x}}}{dt} \right) \quad (4.6)$$

Substituting in (3.1), one obtains:

$$\begin{aligned} \frac{\partial}{\partial t} \int_{\mathcal{V}} (\bar{\mathbf{U}} + \tilde{\mathbf{U}}) (d\bar{\mathcal{V}} + d\tilde{\mathcal{V}}) + \oint_{\mathcal{S}} (\bar{\vec{F}} + \tilde{\vec{F}} - \tilde{\vec{F}}_g) \cdot (\bar{n}d\bar{\mathcal{S}} + \tilde{n}d\tilde{\mathcal{S}}) - \\ \frac{1}{Re} \oint_{\mathcal{S}} (\bar{\mathbf{G}} + \tilde{\mathbf{G}}) \cdot (\bar{n}d\bar{\mathcal{S}} + \tilde{n}d\tilde{\mathcal{S}}) - \int_{\mathcal{V}} (\bar{\mathbf{S}} + \tilde{\mathbf{S}}) (d\bar{\mathcal{V}} + d\tilde{\mathcal{V}}) &= 0 \end{aligned} \quad (4.7)$$

By dropping the steady-state terms which must always satisfy (3.1) and by neglecting second-order terms like  $\tilde{\mathbf{U}}d\tilde{\mathcal{V}}$ , (4.7) becomes:

$$\begin{aligned} \frac{\partial}{\partial t} \int_{\mathcal{V}} \tilde{\mathbf{U}} d\bar{\mathcal{V}} + \oint_{\mathcal{S}} \left( \tilde{\vec{F}} - \frac{1}{Re} \tilde{\mathbf{G}} \right) \cdot \bar{n}d\bar{\mathcal{S}} - \int_{\mathcal{V}} \tilde{\mathbf{S}} d\bar{\mathcal{V}} = \int_{\mathcal{V}} \bar{\mathbf{S}} d\tilde{\mathcal{V}} - \frac{\partial}{\partial t} \int_{\mathcal{V}} \bar{\mathbf{U}} d\tilde{\mathcal{V}} \\ - \oint_{\mathcal{S}} \left( \bar{\vec{F}} - \frac{1}{Re} \bar{\mathbf{G}} \right) \cdot \tilde{n}d\tilde{\mathcal{S}} + \oint_{\mathcal{S}} \tilde{\vec{F}}_g \cdot \bar{n}d\bar{\mathcal{S}} \end{aligned} \quad (4.8)$$

The system of equations in (4.8) is linear in the sense that all the coefficients multiplying the unsteady flow term  $\tilde{\mathbf{U}}$  depend upon the steady-state flow term  $\bar{\mathbf{U}}$  and geometric properties but not on time. In other words, a general solution of (4.8) can be represented via the following summations:

$$\tilde{\vec{x}}(\bar{\vec{x}}, t) = \text{Re} \sum_{\omega} \hat{\vec{x}}(\bar{\vec{x}}, \omega) e^{-i\omega t} \quad (4.9)$$

$$\tilde{\mathbf{U}}(\bar{\vec{x}}, t) = \text{Re} \sum_{\omega} \hat{\mathbf{U}}(\bar{\vec{x}}, \omega) e^{-i\omega t} \quad (4.10)$$

where  $\hat{\vec{x}}$  represents the first-order complex amplitude of grid motion about the mean position  $\bar{\vec{x}}$ , and  $\hat{\mathbf{U}}$  represent the complex amplitude of the small unsteady perturbation of the conservation variables. By substituting the assumed solutions

(4.9) and (4.10) for a single reduced frequency  $\omega$  into the linearised system of equations (4.8), one obtains:

$$\begin{aligned} \oint_{\bar{\mathcal{S}}} \left( \hat{\vec{\mathbf{F}}} - \frac{1}{Re} \hat{\vec{\mathbf{G}}} \right) \cdot \vec{n} d\bar{\mathcal{S}} - \int_{\bar{\mathcal{V}}} (i\omega \hat{\vec{\mathbf{U}}} + \hat{\vec{\mathbf{S}}}) d\bar{\mathcal{V}} &= \int_{\bar{\mathcal{V}}} (i\omega \bar{\vec{\mathbf{U}}} + \bar{\vec{\mathbf{S}}}) d\hat{\mathcal{V}} - \\ \oint_{\bar{\mathcal{S}}} \left( \bar{\vec{\mathbf{F}}} - \frac{1}{Re} \bar{\vec{\mathbf{G}}} \right) \cdot \vec{n} d\bar{\mathcal{S}} + \oint_{\bar{\mathcal{S}}} \bar{\vec{\mathbf{U}}} (\vec{\Omega} \times \hat{\vec{x}} - i\omega \hat{\vec{x}}) \cdot \vec{n} d\bar{\mathcal{S}} \end{aligned} \quad (4.11)$$

In equation (4.11) the left-hand side contains homogeneous terms only, while the right-hand side contains non-homogeneous terms which depend on the (known) steady-state flow and the prescribed grid motion. The non-homogeneous terms are identically zero if there is no grid motion ( $\hat{\vec{x}} = 0$ ), as is the case for forced response problems.

Since the Jacobian with respect to the steady-state flow variables are real quantities, the homogeneous terms of the form  $i\omega \int_{\bar{\mathcal{V}}} \hat{\vec{\mathbf{U}}} d\bar{\mathcal{V}}$ , which represent the time rate of change of the perturbed conservation variables, couple the real and imaginary parts of the perturbed flow equations.

Indicating with  $\hat{\mathbf{H}}(\bar{\vec{\mathbf{U}}}, \hat{\vec{x}})$  the summation of the non-homogeneous terms on the right-hand side of (4.11) and introducing a pseudo-time derivative so that standard time-marching algorithms can be used, (4.11) becomes:

$$\frac{\partial}{\partial \tau} \int_{\bar{\mathcal{V}}} \hat{\vec{\mathbf{U}}} d\bar{\mathcal{V}} + \oint_{\bar{\mathcal{S}}} \left( \hat{\vec{\mathbf{F}}} - \frac{1}{Re} \hat{\vec{\mathbf{G}}} \right) \cdot \vec{n} d\bar{\mathcal{S}} - \int_{\bar{\mathcal{V}}} (i\omega \hat{\vec{\mathbf{U}}} + \hat{\vec{\mathbf{S}}}) d\bar{\mathcal{V}} = \hat{\mathbf{H}}(\bar{\vec{\mathbf{U}}}, \hat{\vec{x}}) \quad (4.12)$$

## 4.2.2 Boundary conditions

There are five different sets of boundary conditions: flow tangency for inviscid flow calculations, no-slip condition for viscous flow calculations, periodic boundaries, inflow and outflow.

### Flow tangency

The flow tangency condition at the solid walls is expressed by the requirement that there is no flow through the surface of the moving wall. Therefore, the local fluid velocity relative to the moving wall has no component normal to the wall. Mathematically this can be expressed as:

$$\vec{u} \cdot \vec{n} = \left( \vec{v} - \vec{\Omega} \times \vec{x} - \frac{d\vec{x}}{dt} \right) \cdot \vec{n} = 0 \quad (4.13)$$

Linearising and keeping zeroth- and first-order terms gives the mean flow and the linearised tangency conditions respectively:

$$(\bar{\vec{v}} - \vec{\Omega} \times \bar{\vec{x}}) \cdot \bar{\vec{n}} = 0 \quad (4.14)$$

$$(\hat{\vec{v}} - \vec{\Omega} \times \hat{\vec{x}} + i\omega \hat{\vec{x}}) \cdot \bar{\vec{n}} + (\bar{\vec{v}} - \vec{\Omega} \times \bar{\vec{x}}) \cdot \hat{\vec{n}} = 0 \quad (4.15)$$

Applying condition (4.15) to the evaluation of the flux term for a solid wall surface yields:

$$\oint_{wall} \left[ \hat{\vec{F}} - \bar{\vec{U}} (\vec{\Omega} \times \hat{\vec{x}} - i\omega \hat{\vec{x}}) \right] \cdot \bar{n} d\bar{S} + \oint_{wall} \bar{\vec{F}} \cdot \hat{\vec{n}} d\hat{S} \\ = \begin{bmatrix} 0 \\ \hat{p} \bar{n}_x d\bar{S} + \bar{p} \hat{n}_x d\hat{S} \\ \hat{p} \bar{n}_y d\bar{S} + \bar{p} \hat{n}_y d\hat{S} \\ \hat{p} \bar{n}_z d\bar{S} + \bar{p} \hat{n}_z d\hat{S} \\ \hat{p} (\vec{\Omega} \times \bar{\vec{x}}) \cdot \bar{n} d\bar{S} + \bar{p} [(\vec{\Omega} \times \bar{\vec{x}}) \cdot \hat{n} d\hat{S} + (\vec{\Omega} \times \hat{\vec{x}} - i\omega \hat{\vec{x}}) \cdot \bar{n} d\bar{S}] \end{bmatrix} \quad (4.16)$$

### No-slip condition

The no-slip condition at the solid walls is expressed by the requirement that the local fluid velocity relative to the moving wall must be zero. Mathematically this can be expressed as:

$$\vec{u} = \vec{v} - \vec{\Omega} \times \vec{x} - \frac{d\vec{x}}{dt} = 0 \quad (4.17)$$

As before, linearising and keeping zeroth- and first-order terms gives the mean flow and the linearised no-slip conditions respectively:

$$\bar{\vec{v}} - \vec{\Omega} \times \bar{\vec{x}} = 0 \quad (4.18)$$

$$\hat{\vec{v}} - \vec{\Omega} \times \hat{\vec{x}} + i\omega \hat{\vec{x}} = 0 \quad (4.19)$$

### Periodic boundaries

The periodic boundary conditions are somewhat more complicated than those for the steady-state flow equations. In a flutter application, the blade may oscillate with a non-zero phase shift with respect to its neighbours. Similarly, in a

wake/rotor interaction, there will be a phase difference in the unsteady pressure distributions experienced by neighbouring rotor blades if there is no one-to-one correspondence between the wakes and the rotor blades. Such phase differences are represented by the interblade phase angle  $\phi$ . Using an axisymmetric coordinate system, the periodic boundary condition can be written as:

$$\widehat{\mathbf{U}}_{\theta_0 + \Delta\theta} = \exp(-i\phi) \widehat{\mathbf{U}}_{\theta_0} \quad (4.20)$$

where  $\widehat{\mathbf{U}}$  is the state variable at position  $\theta_0$ ,  $\Delta\theta$  representing the angular pitch of the blade-to-blade passage. The same equation can be used for a 2D cascade, by replacing  $\theta_0$  and  $\Delta\theta$  by  $y_0$  and  $P$  in a Cartesian coordinate system.

### Inflow and outflow boundaries

Unsteady flow computations require non-reflecting boundary conditions at the far-field boundaries to prevent spurious inwards reflections of outgoing waves. The single-frequency non-reflecting boundary conditions of Giles (1990a) will be used here. These boundary conditions are constructed with the aid of the 1D characteristic variables. The equations relating the harmonic primitive variables and the harmonic characteristic variables can be written as:

$$\begin{bmatrix} \widehat{w}_1 \\ \widehat{w}_2 \\ \widehat{w}_3 \\ \widehat{w}_4 \\ \widehat{w}_5 \end{bmatrix} = \begin{bmatrix} -\bar{c}^2 & 0 & 0 & 0 & 1 \\ 0 & 0 & \bar{\rho}\bar{c} & 0 & 0 \\ 0 & 0 & 0 & \bar{\rho}\bar{c} & 0 \\ 0 & \bar{\rho}\bar{c} & 0 & 0 & 1 \\ 0 & -\bar{\rho}\bar{c} & 0 & 0 & 1 \end{bmatrix} \begin{bmatrix} \widehat{\rho} \\ \widehat{v}_x \\ \widehat{v}_\theta \\ \widehat{v}_r \\ \widehat{p} \end{bmatrix} \quad (4.21)$$

The first characteristic variable represents the 1D entropy wave, the second and third represent the two 1D vorticity waves while the fourth and the fifth characteristic variables represent the forward and backward 1D pressure waves. These 1D characteristic variables can be expressed as a sum of spatial harmonics satisfying the periodicity condition with the correct interblade phase angle.

$$\widehat{w}_n = \sum_m \widehat{w}_n^m \exp \left[ i\theta \frac{2\pi m - \phi}{\Delta\theta} \right] \quad (4.22)$$

Following the work of Giles (1990a), it is possible to express the  $m$ -th harmonic of the incoming 1D characteristic variables as a function of the  $m$ -th harmonic of the outgoing ones. At the inflow, the boundary condition is:

$$\begin{bmatrix} \hat{w}_1^m \\ \hat{w}_2^m \\ \hat{w}_3^m \\ \hat{w}_4^m \end{bmatrix} = \begin{bmatrix} 0 \\ \frac{(1-M_x)\beta_m}{1-M_\theta\beta_m+T_m} \\ 0 \\ \frac{(1-M_x)^2\beta_m^2}{(1-M_\theta\beta_m+T_m)^2} \end{bmatrix} \hat{w}_5^m \quad (4.23)$$

while at the outflow it becomes:

$$\hat{w}_5^m = \frac{2 - M_x\beta_m}{1 - M_\theta\beta_m + T_m} \hat{w}_2^m + \frac{1 - M_\theta\beta_m - T_m}{1 - M_\theta\beta_m + T_m} \hat{w}_4^m \quad (4.24)$$

In both cases  $\beta_m$  is an inverse reduced frequency defined by:

$$\beta_m = \frac{2\pi m - \phi}{r\Delta\theta\omega} \bar{c} \quad (4.25)$$

where  $\bar{c}$  is the average speed of sound and  $r\Delta\theta$  is the product of radius and angular pitch.  $T_m$  in (4.24) is defined by:

$$T_m^2 = (1 - M_\theta\beta_m)^2 - (1 - M_x^2)\beta_m^2 \quad (4.26)$$

$$T_m = \begin{cases} \text{sign}(1 - M_\theta\beta_m) \sqrt{T_m^2} & T_m^2 > 0 \\ \text{sign}(\omega) i \sqrt{-T_m^2} & T_m^2 < 0 \end{cases} \quad (4.27)$$

Giles (1990a) suggested that the periodic boundary conditions should be lagged when using pseudo-time marching, though this was not found necessary with the particular solver used here. Equations (4.23) & (4.24) are the exact 2D analytical boundary conditions. These can be extended to 3D problems by imposing them in a strip-theory fashion at each spanwise radial station at the domain boundary, the so-called quasi-3D non-reflecting boundary conditions (Saxer & Giles 1993). One limitation of such an approach is the inherent assumption that the radial variation in the mean and unsteady flow fields is considerably smaller than that in the tangential direction. This is not necessarily the case in aeroacoustic applications. A more general 3D approach, developed by Hall et al. (1993), is a mixed analytical/numerical boundary condition treatment. The assumption is that the

mean flow field is axisymmetric and uniform in the axial direction, but may have significant radial variation. The unsteady flow-field is decomposed into Fourier modes in the circumferential direction, and a radial eigenvalue problem is solved to determine the wave numbers and the radial mode shapes of the unsteady flow modes. The modal information is then used to construct highly non-reflective boundary conditions. However, in some special cases, the identification of the incoming and outgoing modes may be difficult and truncation errors may affect the scheme adversely. Nevertheless, the approach is probably the most general boundary condition treatment that is currently available.

## 4.3 Numerical Implementation

The extension of the finite volume FV edge-based scheme, described in Chapter 3, to the linearised equations will be described in this Section. Similar to (3.16), the semi-discrete form of (4.12) takes the form:

$$\frac{\partial (\mathcal{V}_I \widehat{\mathbf{U}}_I)}{\partial \tau} + \sum_{s=1}^{m_I} [|\vec{\eta}_{IJ_s}| (\widehat{\mathcal{F}}_{IJ_s} - \widehat{\mathcal{G}}_{m_{IJ_s}}) - \tau_{IJ_s} \widehat{\mathcal{G}}_{l_{IJ_s}}] = \mathcal{V}_I (i\omega \widehat{\mathbf{U}}_I + \widehat{\mathbf{S}}_I + \widehat{\mathbf{H}}_I) \quad (4.28)$$

### 4.3.1 Inviscid fluxes

The discretisation of the inviscid flow terms in (4.28) is given by:

$$\sum_{s=1}^{m_I} |\vec{\eta}_{IJ_s}| \widehat{\mathcal{F}}_{IJ_s} \quad (4.29)$$

where  $\widehat{\mathcal{F}}_{IJ_s}$  represents the inviscid flux function along edge  $IJ_s$  which is obtained using a central difference scheme with added matrix artificial dissipation. This artificial dissipation is a blend of second and fourth order differences. The fourth order terms ensure the stability of the scheme in smooth regions of the flow, while the second order terms are required to damp numerical oscillations in the vicinity of discontinuities. The inviscid flux function is expressed as:

$$\widehat{\mathcal{F}}_{IJ_s} = \frac{\widehat{\mathbf{F}}_I + \widehat{\mathbf{F}}_{J_s}}{2} \cdot \frac{\vec{\eta}_{IJ_s}}{|\vec{\eta}_{IJ_s}|} - \widehat{\mathcal{D}}_{IJ_s} \quad (4.30)$$

where the linearised artificial dissipation  $\widehat{\mathcal{D}}_{IJ_s}$  along the edge  $IJ_s$  is given by:

$$\widehat{\mathcal{D}}_{IJ_s} = \frac{1}{2} \left| \overline{\mathbf{A}}_{IJ_s} \right| \left[ \overline{\psi} \Delta \widehat{\mathbf{U}} - \epsilon_4 (1 - \overline{\psi}) \Delta \mathcal{L} (\widehat{\mathbf{U}}) \right] \quad (4.31)$$

The difference operator  $\Delta$  is given in (3.20).  $\left| \overline{\mathbf{A}}_{IJ_s} \right|$  is the standard Roe matrix (Roe 1981) between the two steady-state stages  $\overline{\mathbf{U}}_I$  and  $\overline{\mathbf{U}}_{J_s}$ ;  $\epsilon_4 \approx 1/16$  is the fourth order artificial dissipation coefficient.  $\mathcal{L}$  is the pseudo-Laplacian operator reported in (3.21) while  $\overline{\psi}$  represents the limiting function which varies between 0 and 1 and it is required in order to switch the scheme to first order ( $\overline{\psi} = 1$ ) in the vicinity of discontinuities. This limiter is computed for the steady-state flow only and its expression is given by (3.25) and (3.26).

### 4.3.2 Viscous terms

The viscous fluxes associated with the mixed derivatives  $\mathcal{G}_m$  in (4.28) are treated in the same way as their inviscid counterparts and their contribution to (4.28) is given by:

$$\widehat{\mathcal{G}}_{m_{IJ_s}} = \frac{1}{Re} \left( \widehat{\mathbf{G}}_{m_I} + \widehat{\mathbf{G}}_{m_{J_s}} \right) \cdot \frac{\vec{\eta}_{IJ_s}}{|\vec{\eta}_{IJ_s}|} \quad (4.32)$$

where

$$\widehat{\mathbf{G}}_m = \widehat{\mathbf{G}}_m \Big|_{\overline{\mu}} + \widehat{\mathbf{G}}_m \Big|_{\Delta \overline{\mathbf{U}}} \quad (4.33)$$

The first term on the left-hand side of (4.33) contains the contribution due to the gradients of the unsteady flow velocity and temperature at constant viscosity  $\mu$ . The second term takes into account the variation of the unsteady viscosity only. The Laplacian terms are treated in a different way in order to improve both the accuracy and the robustness of the numerical scheme. In (4.28), these terms take the form:

$$\widehat{\mathcal{G}}_{l_{IJ_s}} = \widehat{\mathcal{G}}_{l_{IJ_s}} \Big|_{\overline{\mu}} + \widehat{\mathcal{G}}_{l_{IJ_s}} \Big|_{\Delta \overline{\mathbf{U}}} \quad (4.34)$$

where

$$\hat{\mathcal{G}}_{l_{IJ_s}} \Big|_{\bar{\mu}} = \frac{1}{Re} \begin{bmatrix} 0 \\ \bar{\mu}_{IJ_s} \Delta \hat{v}_1 \\ \bar{\mu}_{IJ_s} \Delta \hat{v}_2 \\ \bar{\mu}_{IJ_s} \Delta \hat{v}_3 \\ (\bar{\mu} \bar{v})_{IJ_s} \cdot \Delta \hat{v} + \frac{\gamma}{\gamma-1} \left( \frac{\bar{\mu}_l}{Pr_l} + \frac{\bar{\mu}_t}{Pr_t} \right)_{IJ_s} \Delta \hat{T} \end{bmatrix} \quad (4.35)$$

$$\hat{\mathcal{G}}_{l_{IJ_s}} \Big|_{\Delta \bar{U}} = \frac{1}{Re} \begin{bmatrix} 0 \\ \hat{\mu}_{IJ_s} \Delta \bar{v}_1 \\ \hat{\mu}_{IJ_s} \Delta \bar{v}_2 \\ \hat{\mu}_{IJ_s} \Delta \bar{v}_3 \\ (\bar{\mu} \hat{v} + \hat{\mu} \bar{v})_{IJ_s} \cdot \Delta \bar{v} + \frac{\gamma}{\gamma-1} \left( \frac{\hat{\mu}_l}{Pr_l} + \frac{\hat{\mu}_t}{Pr_t} \right)_{IJ_s} \Delta \bar{T} \end{bmatrix} \quad (4.36)$$

The subscript  $IJ_s$  indicates an arithmetic mean over nodes  $I$  and  $J_s$  as indicated in (3.29) and  $\Delta$  is given in (3.20).

The evaluation of terms  $\hat{\mathbf{G}}_m \Big|_{\Delta \bar{U}}$  and  $\hat{\mathcal{G}}_{l_{IJ_s}} \Big|_{\Delta \bar{U}}$  requires the linearisation of the turbulence model used in the steady flow solver. If these terms are neglected, the linearised viscous terms can still be represented by simply using the mean-flow values for the eddy viscosity, the so-called frozen turbulence approach. Such a scheme is relatively simple to implement for any turbulence model, while a full linearisation will depend on the particular type of the turbulence model used. A linearised version of the Spalart-Allmaras (1992) turbulence model is given in the Appendix B.

### 4.3.3 Time integration

The pseudo-time derivative introduced in (4.12) allows the use of standard time-marching algorithms when solving the linearised equations. A compact form of (4.28) can be written as

$$\frac{\partial (\mathcal{V}_I \hat{\mathbf{U}}_I)}{\partial \tau} = \mathbf{R}_I (\hat{\mathbf{U}}) \quad (4.37)$$

Many different approaches are possible. For instance, Hall & Clark (1991) use an explicit Lax-Wendroff technique together with local time-stepping and multigrid in order to accelerate convergence to a steady-state. Marshall & Giles (1997) use an explicit multistage Runge-Kutta technique with local-time stepping. Montgomery

& Verdon (1997a) proposed a two-point backward implicit difference and the expansion of the residual about the  $n$ th time level.

Here, the same preconditioned multigrid algorithm developed for steady-state and non-linear unsteady time-marching aerodynamics is used. In a compact form the algorithm is written as

$$[\bar{\mathbf{P}}]^{-1} L_\tau \delta \widehat{\mathbf{U}}_I = \mathbf{R}_I(\widehat{\mathbf{U}}) \quad (4.38)$$

$L_\tau$  represents a multistage Runge-Kutta operator while  $[\bar{\mathbf{P}}]^{-1}$  represents a preconditioner developed for accelerating steady-state calculations, evaluated using the steady-state unknowns.

Such a preconditioned Runge-Kutta relaxation algorithm is used as a smoother in an agglomeration multigrid algorithm described in Appendix D.

## 4.4 Test Cases

This Section presents three different test cases for the validation of the present method. The first test case is a comparison against the classical subsonic flat plate cascade theory of Smith (1972), the so-called LINSUB benchmark code (Whitehead 1987). The second test case checks the computational results against the asymptotic analytical solution derived by Lighthill (1954) for an unsteady laminar flow. The third test case examines the implications of using inviscid, frozen-turbulence and fully-turbulent models when linearising the unsteady flow over a transonic turbine blade, the so-called 11th International Standard Configuration (Fransson et al. 1998).

### 4.4.1 Linear flat-plate cascade

Small-amplitude perturbations of a uniform, inviscid steady-state flow past an unloaded flat-plate cascade are studied first. Such cascades can be used for a variety of applications: wake/blade interaction, potential/blade interaction, aeroelasticity studies by including the blade's bending and torsional motion. The main aerodynamic parameters are the Mach number, reduced frequency, pitch-to-chord ratio, stagger angle and the interblade phase angle.

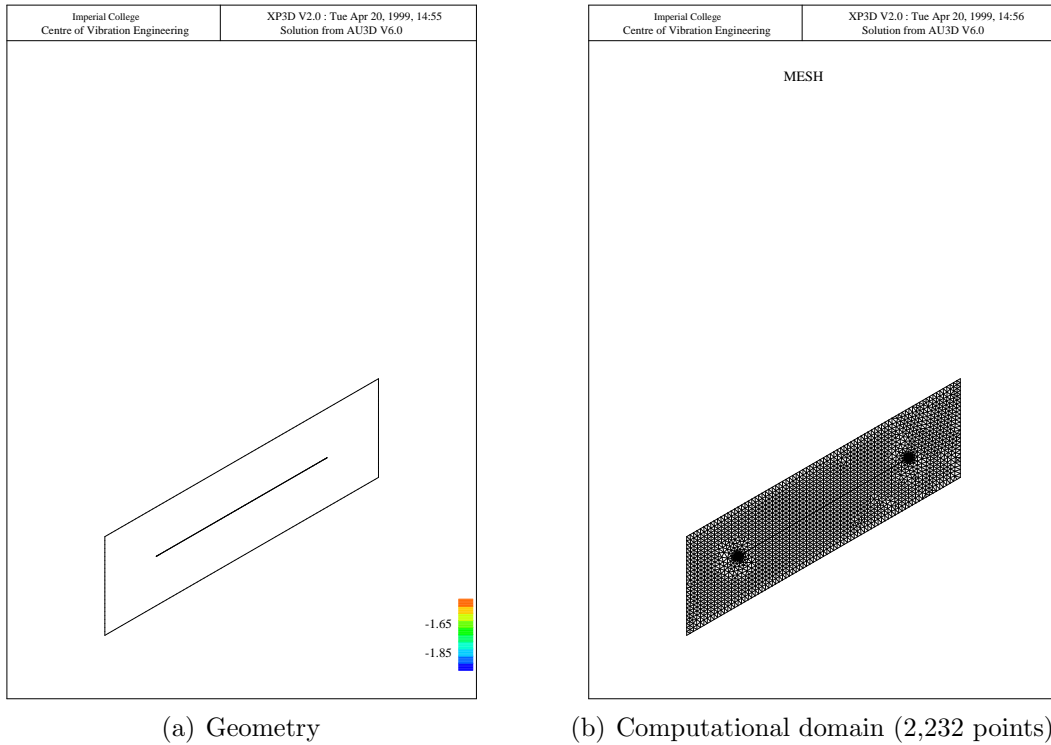
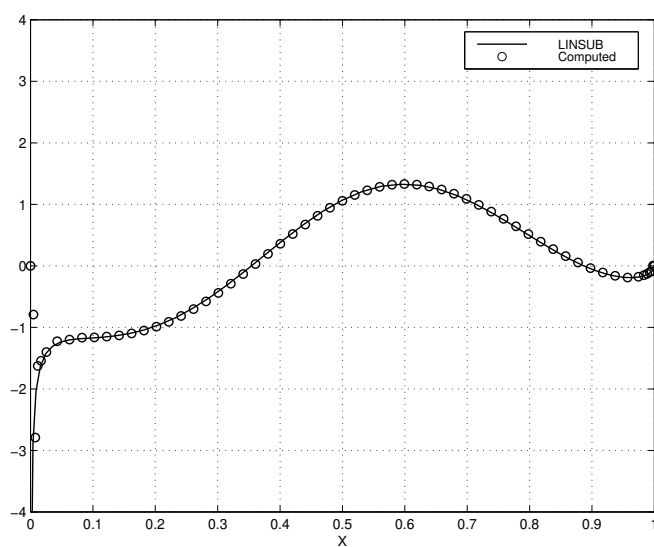


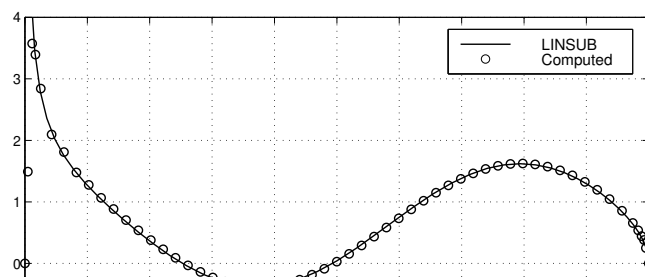
Figure 4.1: Flat plate cascade. Geometry and computational domain

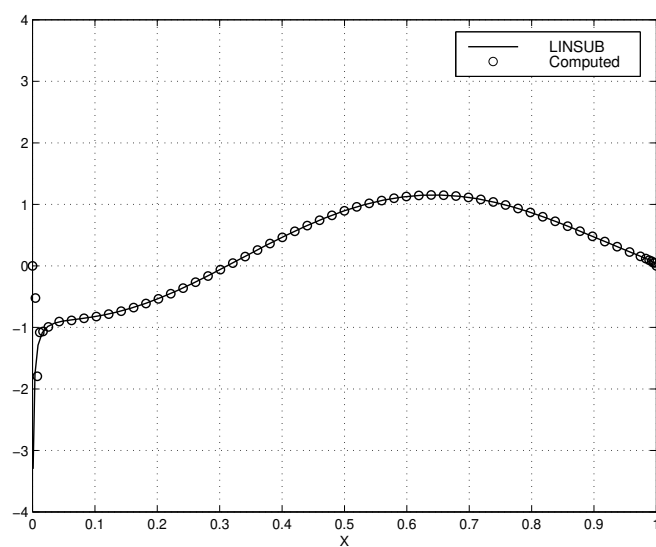
Three different disturbances were studied for a pitch-to-chord ratio of 0.5, a stagger angle of  $30^\circ$  and a mean-flow Mach number of 0.7. For all three cases, the results were checked against the benchmark LINSUB code by plotting the real and imaginary parts of the (complex) unsteady pressure difference across the plate. The geometry and the computational domain are shown in Fig. 4.1. The mesh has high resolution around the trailing and leading edges in order to handle the singularities which occur in these regions.

The first disturbance simulates a wake/blade interaction, an incoming sinusoidal wake with a reduced frequency of  $\pi$  being specified at the inflow boundary. The interblade phase angle is  $-90^\circ$ . Fig. 4.2 shows excellent agreement between the present method and the benchmark program LINSUB. The second disturbance simulates potential/blade interaction, an incoming pressure wave with a reduced frequency of 2.0 being specified at the outflow boundary. The interblade phase angle is  $0^\circ$ . Fig. 4.3 shows excellent agreement between the present method and the benchmark program LINSUB. The last disturbance studied is for a bending motion with a reduced frequency of 2.0 and an interblade phase angle of  $90^\circ$ . Once again, excellent agreement is observed from Fig. 4.4.

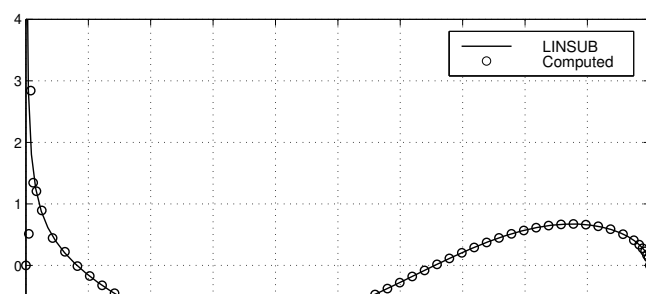


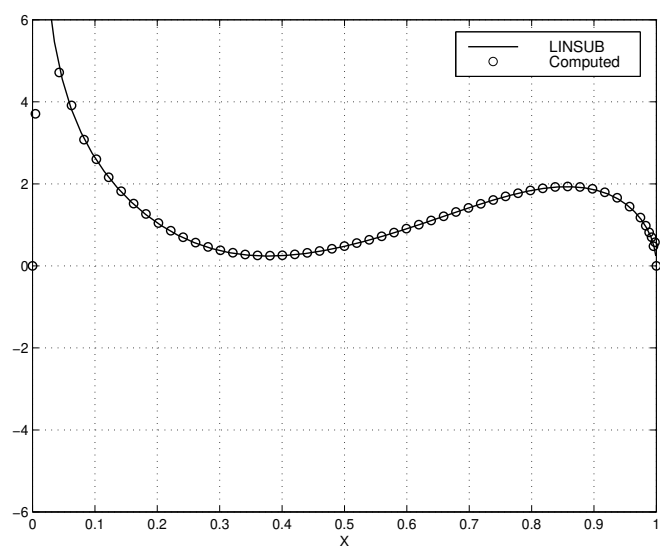
(a) Real part



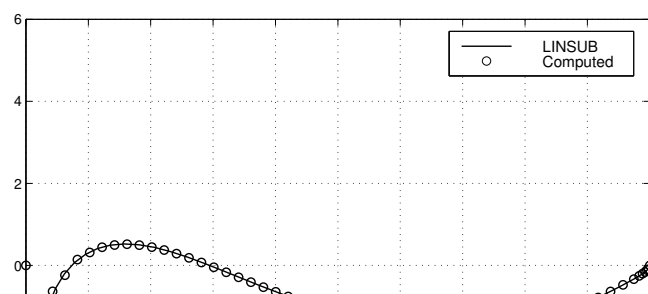


(a) Real part





(a) Real part



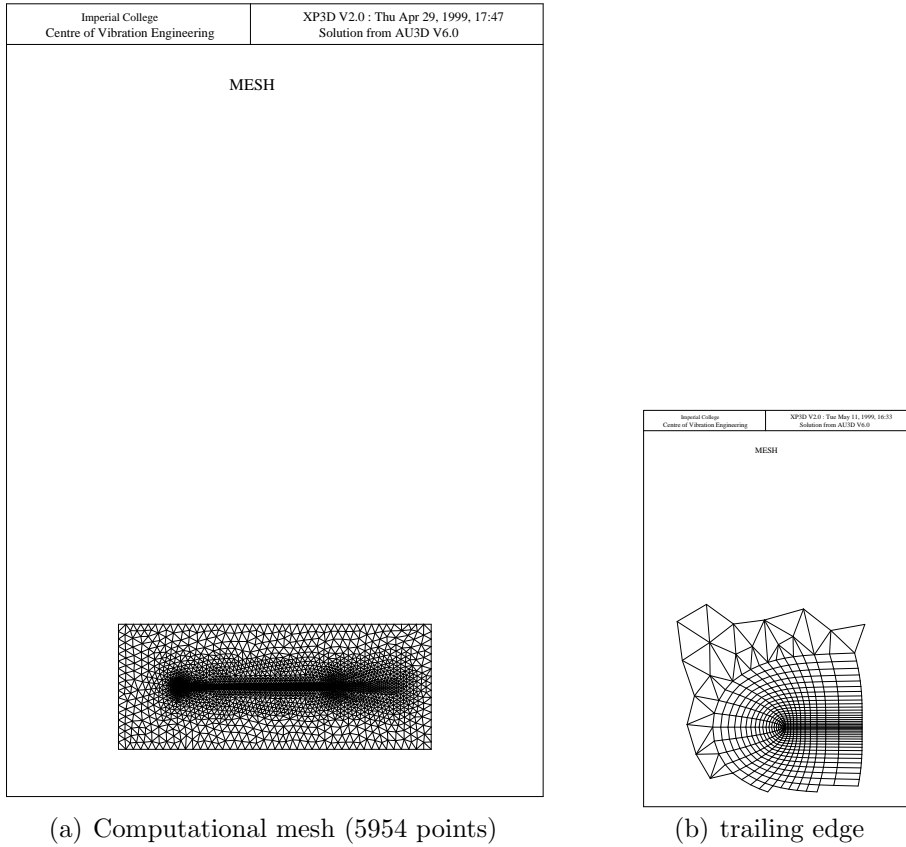


Figure 4.5: Computational domain for laminar flow over a flat plate cascade

#### 4.4.2 Unsteady laminar boundary layer on a flat plate

This test case studies an unsteady laminar boundary layer with fluctuations in external velocity. The computational mesh is shown in Fig. 4.5. The boundary layer region is discretised using 15 layers of quadrilateral elements, while the rest of the domain consists of triangles. The pitch to chord ratio of this cascade is unity so that the flow is as close as possible to that over an isolated flat plate. The steady-state flow over an unstaggered flat plate cascade was obtained for a Mach number of 0.2. The freestream Reynolds number is 60,000. Such a case is well within the incompressible flow regime, thus enabling a meaningful comparison with the Blasius solution. Indeed, the computed steady-state velocity profile and the skin friction coefficient are found to be in very good agreement with the incompressible laminar boundary layer theory of Blasius (Fig. 4.6). Once the steady-state flow has been validated, the next stage is to study a velocity perturbation of the form:

$$u = \varepsilon u_\infty e^{-i\omega t} \quad (4.39)$$

where  $u_\infty$  is the freestream velocity and  $\varepsilon$  a small value ( $\ll 1$ ). The disturbance is along the plate, in the freestream direction, denoted by co-ordinate  $x$ . Lighthill's (1954) theory provides two asymptotic values for the unsteady skin friction coefficient, one for very small and the other for very large reduced frequency values. Fig. 4.7a shows the wall shear stress amplitude variation with reduced frequency  $\omega x/u_\infty$  while Fig. 4.7b shows the computed phase angle between shear stress and external velocity. As expected, the computed results become asymptotic for the limiting cases of very small and very large reduced frequency. Similar comparisons between numerical results and Lighthill's theory are also reported by Cebeci (1977).

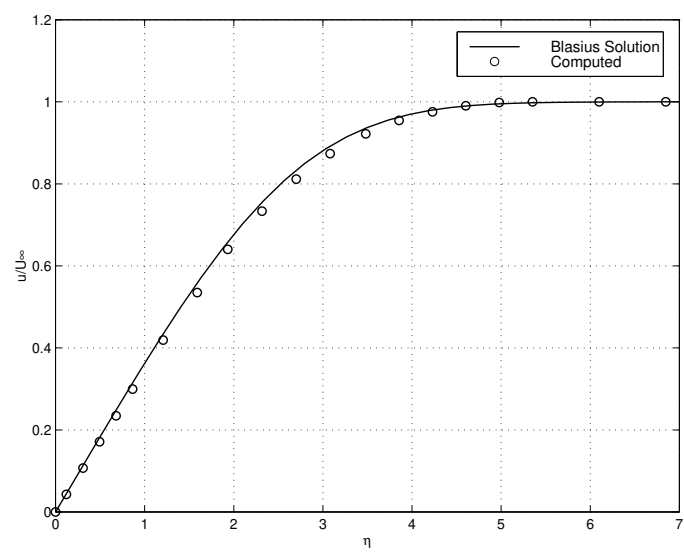
#### 4.4.3 Turbine cascade

In this Section the steady and unsteady flow due to bending motion of a turbine blade in the direction normal to its chord is analysed. The turbine blade geometry under consideration represents the 11<sup>th</sup> International Standard Configuration which have been studied for several flow regimes by Fransson et al. (1998)<sup>1</sup>. Two particular flows will be considered here: a subsonic attached flow and a transonic flow showing a separation bubble on the suction surface. Fig. 4.8 shows the computational mesh used for all viscous calculations. There are 9,312 quadrilaterals in the boundary layer region and 7,751 triangles in the rest of the domain, the total number of points being 13,481. A second mesh, used for the inviscid calculations, has been obtained from the viscous mesh of Fig. 4.8 by simply removing the quadrilateral elements in the boundary layer.

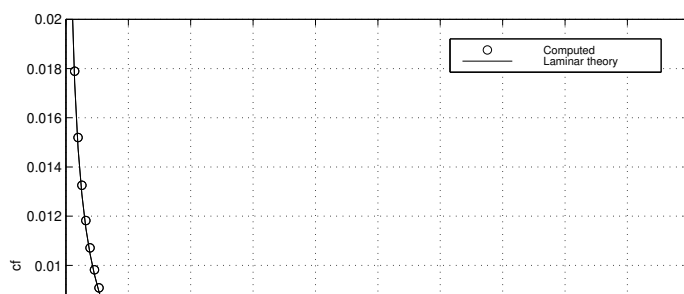
**Steady-state flow results.** For the subsonic flow case the inlet flow angle is  $-15.2^\circ$ , the outlet isentropic Mach number is 0.69 and the inlet Reynolds number, based on the blade's chord, is 650,000. The maximum value of  $y+$  is of around 4 which guarantees a good resolution of the viscous sublayer using the Spalart-Allmaras turbulence model. The predicted Mach number contours are shown in Fig. 4.9 while a comparison of the inviscid and viscous analyses with measured

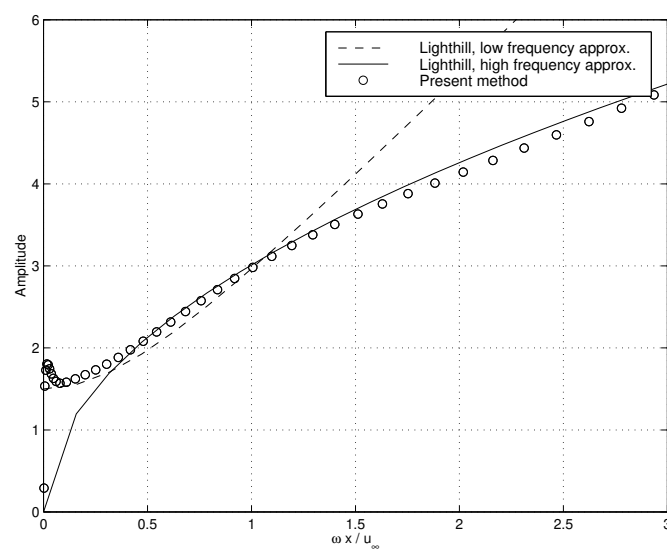
---

<sup>1</sup>The data for the International Standard Configurations can be found at <http://www.egi.kth.se/ekv/stcf/>

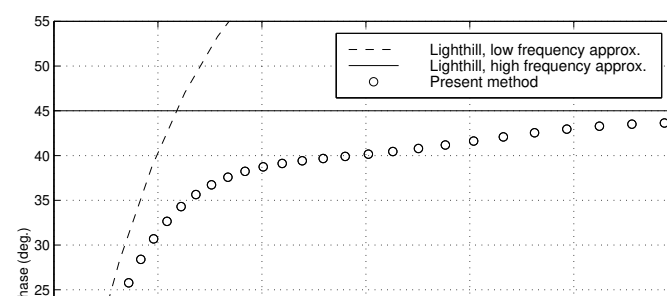


(a) Velocity profile





(a) Amplitude



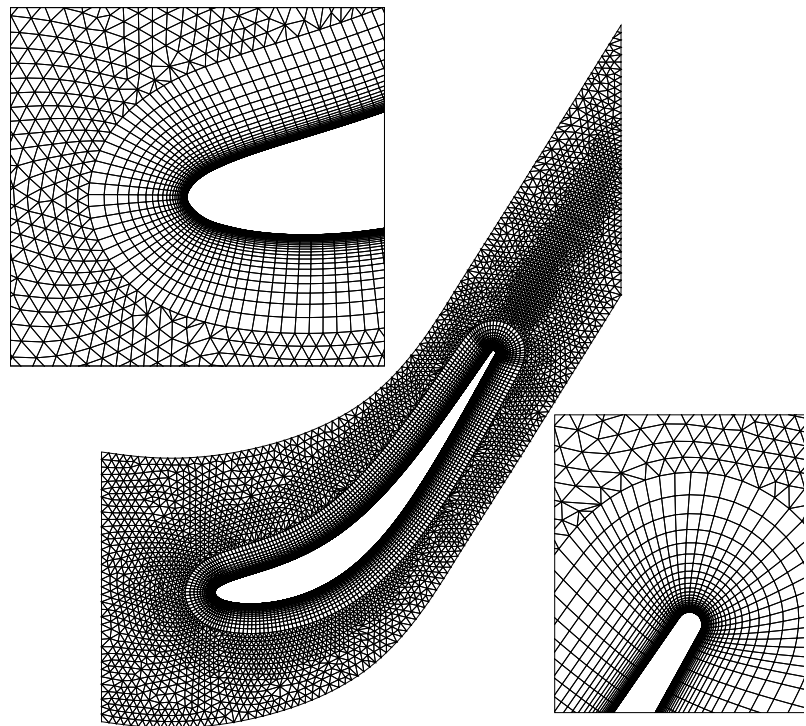


Figure 4.8: 11<sup>th</sup> Standard configuration. Viscous mesh

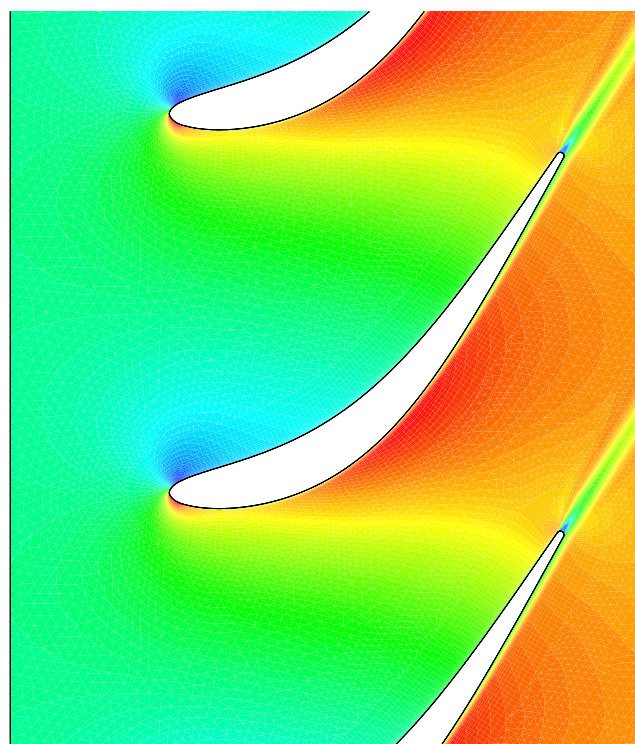


Figure 4.9: 11<sup>th</sup> Standard configuration - subsonic case. Steady-state Mach contours

data is given in Fig. 4.10. For the suction surface, both the viscous and inviscid computations somewhat overpredict the Mach number distribution at around mid-chord. However, a similar solution was obtained by Fransson et al. (1998) and the reasons for the discrepancy are discussed in some detail. Here, we will consider that the steady-state flow has been captured adequately for the purposes of providing a starting point for the linearised unsteady flow.

For the transonic off-design case the inlet flow angle is  $34^\circ$ , the outlet isentropic Mach number is 1 and the inlet Reynolds number, based on the blade's chord, is 860,000. The maximum  $y+$  value is around 5. The predicted Mach number contours are plotted in Fig. 4.11a. A particular feature of the flow, the recirculation bubble on the suction surface, is shown in Fig. 4.11b. Because of the significant viscous features, the Navier-Stokes analysis shows a much better agreement with the measured data, with perhaps the exception of the trailing-edge behaviour (Fig. 4.12). However, as discussed by Fransson et al. (1998), the pre-shock Mach number is very sensitive to the experimental inlet conditions. In any case, as expected, a viscous analysis is required to predict the separation bubble of the suction side which occurs between 10 – 30% blade chord, a feature that can be seen from the flow deceleration in Fig. 4.12. As will be discussed below, such differences in the steady-state flow will lead to major discrepancies for unsteady flow predictions.

**Linearised unsteady flow results** The unsteadiness due to bending motion of the blade in the direction normal to its chord was computed using the linearised flow solver. The reduced frequency is 0.21 for the subsonic case and 0.15 for the transonic case. Three different sets of flow calculations were performed for each case: (i) inviscid linearised using an inviscid base steady-state flow, (ii) viscous linearised with frozen turbulence using viscous fully-turbulent base flow, and (iii) viscous fully-linearised using the same viscous base flow as in (ii). In calculations (ii), neither the laminar nor the turbulent viscosities were linearised and their values were kept fixed at their steady-state values. Calculations (iii) were performed with a fully-linearised Spalart-Allmaras turbulence model.

The amplitude and phase of the predicted unsteady pressure coefficient<sup>2</sup> distribution are compared to measured data in Figs. 4.13 and 4.14 for the subsonic case. The first noticeable feature is the similarity of the amplitude predictions for

---

<sup>2</sup> $\tilde{c}_p = \frac{\tilde{c}_p}{h(p_{01}-p_1)}$ , where  $h$  is the bending amplitude and  $c$  the blade chord.

the three modelling levels, though some deviations can be observed for the phase plots. This result is somewhat expected because of the similarity of the inviscid and viscous steady-state solutions. There is reasonable overall agreement with the measured data, though the undershoot at around 50% chord is not captured in any of the computations. An inspection of the phase plots reveals that the negative to positive (or stable to unstable) phase jump, is predicted much further downstream than the measured position. However, the fully non-linear viscous unsteady calculations of Franson et al. (1998) exhibit the same trend and hence the cause of the discrepancy is not due to linearisation.

The amplitude and phase of the predicted unsteady pressure distribution is compared to measured data in Figs. 4.15 and 4.16 for the transonic case. The discrepancies between different the three modelling levels is now more pronounced. The linearised inviscid approach is seen to overpredict the unsteady pressure coefficient on the suction side of the blade both in the recirculation region (0 – 30% of chord) and around the trailing-edge. In the recirculation region, the full linearisation of the viscous terms yields better results than freezing the turbulence model and the two approaches are seen to be equivalent elsewhere.

## 4.5 Concluding Remarks

- A finite-volume scheme has been presented for the solution of the linearised viscous flows for turbomachinery applications. The method employs an edge-based data structure and uses a nearest neighbour stencil for the discretisation of the Laplacian operator. Both 2D and 3D structured, unstructured or block structured grids with mixed elements can be used without any modification of the numerical scheme.
- The proposed time-linearised Navier-Stokes analysis is applicable to off-design conditions where viscous effects are not limited to the boundary layer.
- The method is computationally very efficient, making it a useful tool for routine aeroelasticity design calculations. For a given frequency and an interblade phase angle, the unsteady flow computation is about the same as the background steady-state flow computation. Although not reported in the main body of the Chapter, the time-linearised viscous analysis results for the 11<sup>th</sup> Standard Configuration are in very good agreement with the

non-linear time-marching viscous predictions of Fransson et al. (1998). It is anticipated that the non-linear computations will take about an order of magnitude longer. However, the issue whether linearised methods are applicable to all flow regimes is not one that is addressed here.

- The transonic flow results show that the linearisation of the turbulence model plays an important role wherever the viscous effects are important, exemplified here by the recirculation bubble. When there are no such effects, the frozen turbulence approach should produce very similar results. In other words, an inspection of the steady-state solution should provide guidance as to which modelling level would be appropriate.
- Although only 2D cases are presented in this Chapter, 3D flows have also been studied<sup>3</sup> albeit with a very significant increase in CPU effort. A fully-linearised turbulence model requires fine meshes near the wall, hence the problem size becomes much larger than those cases where a wall function is used. In such cases the unsteady shear stresses are neglected so that a linearised wall function is not needed.

---

<sup>3</sup>An application to 3D fan flutter prediction is reported in Vahdati et al. (2000).

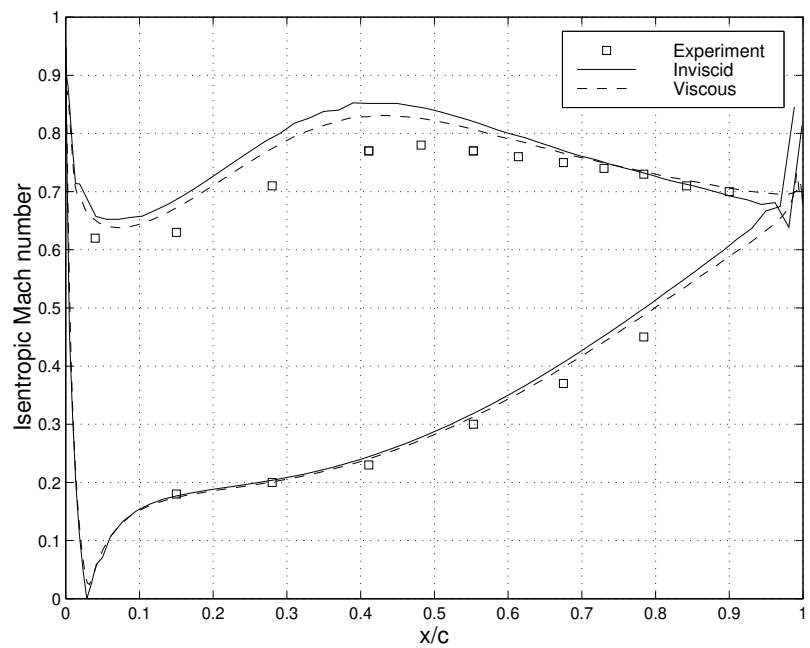
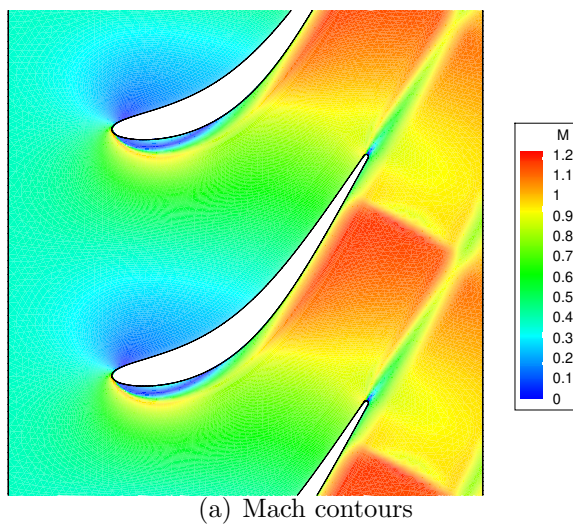
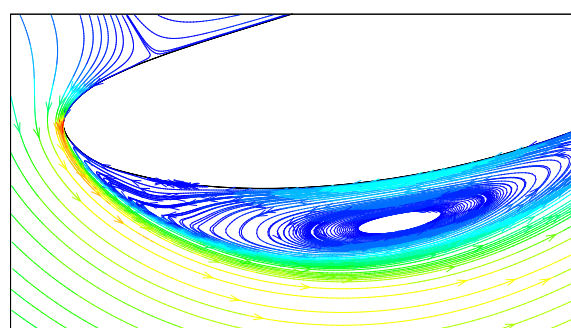


Figure 4.10: 11<sup>th</sup> Standard configuration - subsonic case. Isentropic Mach number distribution on the blade



(a) Mach contours



(b) Particle traces in the separation bubble

Figure 4.11: 11<sup>th</sup> Standard configuration - transonic case. Steady-state Mach contours

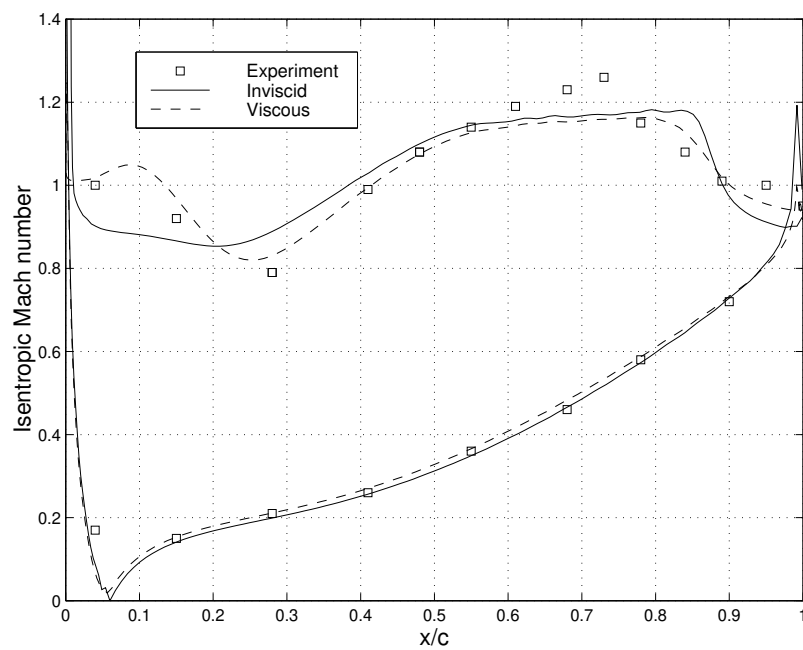


Figure 4.12: 11<sup>th</sup> Standard configuration - transonic case. Isentropic Mach number distribution on the blade

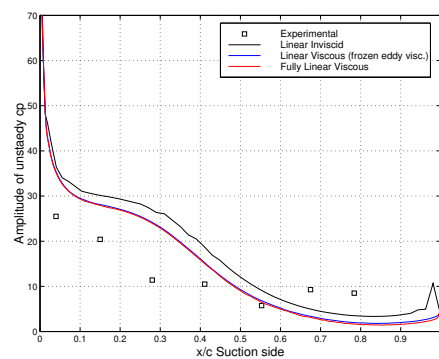
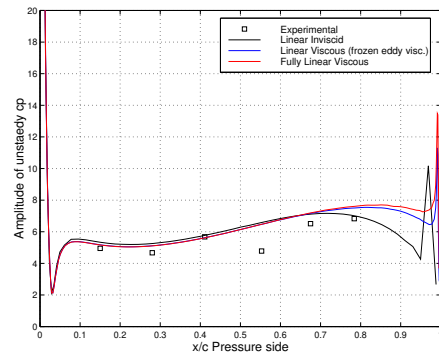


Figure 4.13: 11<sup>th</sup> Standard configuration - subsonic case. Amplitude of  $\tilde{c}_p$  ( $\omega = 0.21$ ,  $\phi = 180^\circ$ )

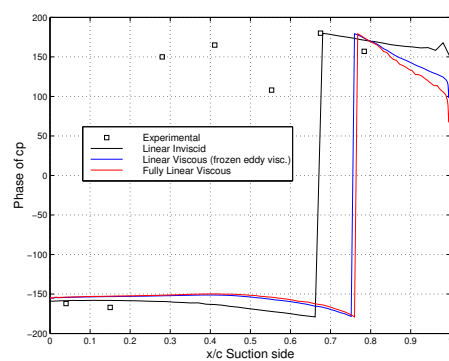
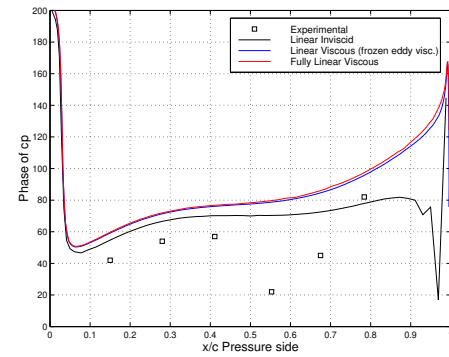


Figure 4.14: 11<sup>th</sup> Standard configuration - subsonic case. Phase of  $\tilde{c}_p$  ( $\omega = 0.21$ ,  $\phi = 180^\circ$ )

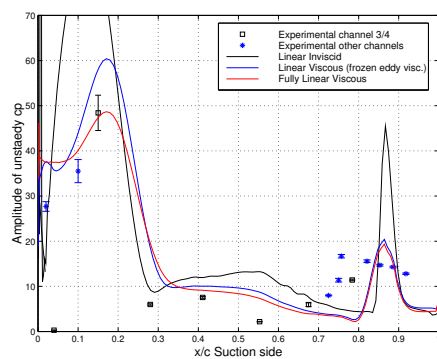
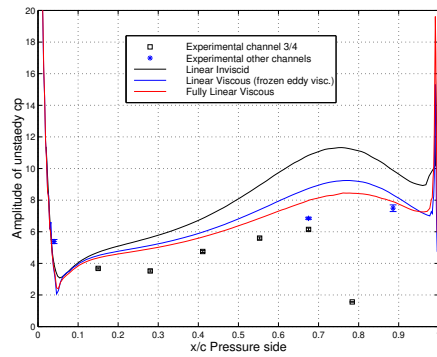


Figure 4.15: 11<sup>th</sup> Standard configuration - transonic case. Amplitude of  $\tilde{c}_p$  ( $\omega = 0.15$ ,  $\phi = 180^\circ$ )

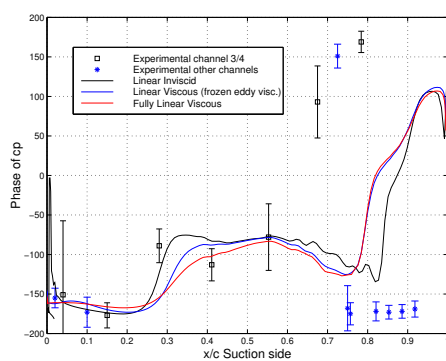
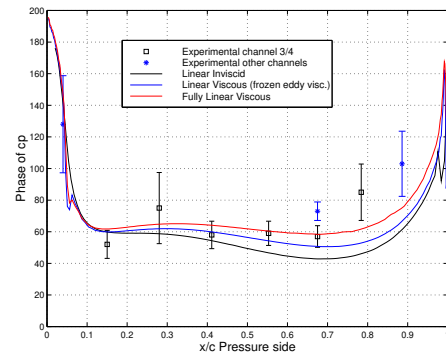


Figure 4.16: 11<sup>th</sup> Standard configuration - transonic case. Phase of  $\tilde{c}_p$  ( $\omega = 0.15$ ,  $\phi = 180^\circ$ )

# Chapter 5

## Stator-Rotor Interaction in a Transonic Turbine Stage

This chapter presents a detailed numerical analysis of a stator-rotor interaction in a typical high pressure (HP) turbine stage of contemporary turbomachines using both linear and non linear unsteady flow representations. The sources of unsteadiness on the rotor passage are evaluated from the steady-state outlet stator solution. These disturbances are Fourier transformed and split into vortical and potential components in order to assess the influence of each on the rotor unsteady aerodynamics. The computed results are compared with the experimental data measured at the Osney Laboratory's rotating turbine facility. Good qualitative, and in most cases quantitative, agreement has been obtained. In the final part of the chapter, the results of the linearised method are compared with those obtained from a non-linear time marching technique. There is a surprising overall agreement, which indicates that the unsteady flow field generated by relative blade motion can be considered a quasi linear phenomenon for the HP turbine studied.

### 5.1 Introduction

Two different numerical techniques for the calculation of steady and unsteady aerodynamics have been presented in the previous two chapter. These two methods will now be used for the investigation of the unsteady pressure fluctuations on a typical rotor blade. The unsteadiness is caused by its relative motion with respect the upstream stationary nozzle guide vane (NGV). The data required for such an in-

vestigation consists only of the two blade geometries, the stationary flow boundary conditions upstream of the NGV blade and downstream of the rotor blade and the rotational speed. The analysis process begins with the calculation of the steady-state flow-field for the given set of flow conditions and rotational speed. The next step is the evaluation of the unsteady rotor pressure fluctuations caused by both wake and potential effects. A description of the unsteady phenomena of interest, unsteady pressure fluctuations on the rotor blade, will be given in some detail. The details of the experimental work carried out at Oxford Osney Laboratory will also be included for the sake of completeness.

### 5.1.1 Description of the problem

The first step towards the unsteady aerodynamics analysis of turbomachinery blades, is the computation of the corresponding steady non-linear flow. A multistage steady-state flow will be presented in section 5.2.3 and its complex features such secondary flows, tip-leakage losses will be discussed in some details.

Once the steady-state flow is known the question is the selection of a “best analysis” for the prediction of unsteady effects. Before offering an answer to this, it is appropriate to discuss, first, what one would hope to get out of such calculations. The focus of this chapter is a numerical tool that can be used by designers as a part of an industrial design system. Major concerns due to flow unsteadiness are the possibility of blade flutter and excessive forced response. Flutter is by definition a linear problem since it is concerned with possible growth of infinitesimal unsteady perturbations. A growing body of evidence suggests that the forced response problem is also largely linear. Comparison between linear and non-linear calculations, for levels of unsteadiness typical of engine conditions, show that the linear calculations predict the forced response to within 5% (Hall 1991, Suddhoo et al. 1991). This level of accuracy is perfectly adequate for all practical engineering design purposes and is probably within the level of other modelling errors.

For these reasons an unsteady linear Navier-Stokes analysis is performed on the rotor blade in order to evaluate the magnitude of unsteady loads caused by its relative motion with respect the upstream nozzle guide vane. Such a route offers great advantages over non-linear time marching methods in terms of speed and storage, while still retaining the key features of the flow.

The sources of unsteadiness are evaluated from the NGV outlet non-uniformities

and imposed as boundary conditions at the inlet of the rotor passage. More specifically the NGV outlet non-uniformities are Fourier decomposed and split into vortical and potential components. Each Fourier mode is associated with its own unsteady frequency and interblade-phase angle as described in appendix C. Two linear calculations are performed for each Fourier mode: the vortical-rotor interaction, also labelled wake-rotor interaction, and the potential flow interaction. Following this route it is possible to estimate the relative influence of the NGV wake and potential flow field on the rotor unsteady aerodynamics. Since the governing equation are linear the two unsteady solutions can be superimposed to give the total unsteady loads for a given Fourier mode. This approach is relatively straightforward as well as being a suitable tool for an industrial design system.

Number of NGV blades	36
Number of rotor blades	60
Rotor tip diameter	554 mm
Rotor tip clearance	0.5 mm
NGV-rotor spacing	0.346 NGV axial chord
Design speed	8434 RPM
NGV inlet total pressure $p_{01}$	804505 Pa
NGV inlet total temperature $T_{01}$	374.4 K
NGV outlet isentropic Mach number $M_{2is}$	0.96

Table 5.1: Stage characteristics of Rig RT27a

The turbine stage used for this investigation is the well-known benchmark Rig RT27a of the Oxford Osney Laboratory. This turbine stage represents a typical HP stage of contemporary turbomachines and its characteristics are summarised in table 5.1. The computed results are compared with measured Rig RT27a data in order to achieve a better understanding of the unsteady effects and to assess the applicability bounds of the linear methods for the analysis of unsteady 3D NGV-rotor interaction.

### 5.1.2 Experimental details

Rig RT27a was designed to provide steady and unsteady flow data for typical turbine blade geometries at representative engine conditions. The turbine stage was mounted in a transient flow turbine test facility based on an isentropic light piston tunnel at the Osney laboratory, Oxford (Moss et al. 1997). The rotor blade is a transonic shroudless design of 0.5 m tip diameter with an NGV-rotor spacing of 0.346 NGV axial chord. Fig. 5.1 shows a meridional view of the stator-rotor configuration. The rotor blade presents an evident tip clearance which has been set to 0.05 cm ( $\approx 1\%$  of rotor span). The rotor instrumentation, described by Moss et

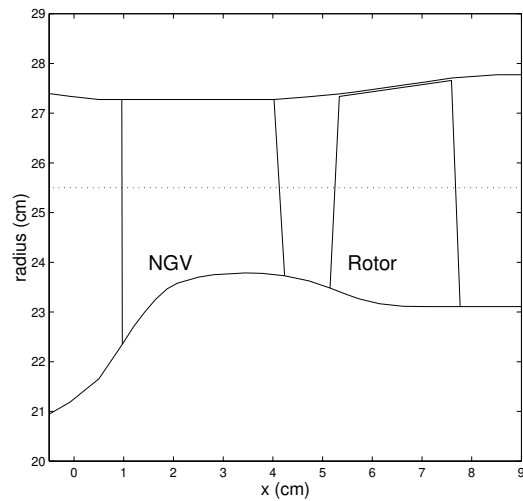


Figure 5.1: Meridional view of the RT27a turbine stage

al. (1997), consists of 78 flush-mounted miniature pressure transducers, “surface

kulites”, and 12 “leading-edge” pitot transducers. The latter are protruded from the leading-edge with a small bell-mouth to reduce sensitivity to incidence changes. The kulite transducers are arranged at span-wise positions of 5, 10, 50, 90 and 95% of annulus height; these sections will be referred to as root, mid-root, mid-height, mid-tip and top.

Prior to a run, the rotor is accelerated to 6000 RPM, in vacuum, by an air motor. Once this rotational speed is reached, a fast-acting annular valve opens and the air (at suitable temperature and pressure generated by a free-sliding piston in the pump tube) passes through the turbine stage for a duration of 200 ms. The rotor accelerates to 9500 RPM and the data are recorded for some 17 ms while the rotor passes through the design condition. Since the blade passing frequency is approximately 5 kHz, the 17 ms acquisition time is sufficient to capture 85 wake passing cycles. The experimental data presented by Moss et al. (1997), have been assembled from over 400 signals captured during 120 tunnel runs. The tolerance on the pressure measurements is  $\pm 1.75\%$  with a 95% confidence limit. This is equivalent to a Mach number accuracy of  $\pm 0.02$  at a Mach number of 0.65.

## 5.2 Steady State Flow Analysis

The analysis of the steady-state flow-field for the coupled NGV-rotor configuration is presented in this section. The flow is assumed to be fully turbulent and the high Reynolds number version of the Spallart-Allmaras (1992) turbulence model is used together with a slip boundary condition on the solid walls. The wall shear stresses are evaluated using a generalized law of the wall as the one reported by White (1991). Apart from predicting midspan pressure more accurately, 3D calculations provide us with hub to tip distribution of the dependent variables and take the tip losses into account. When the air is turned through a row of axial blades, the flow far from the end walls, hub or casing, may often be considered as 2D. However near the end walls, the inlet boundary layer flow contains span-wise velocity gradients, and transverse velocities are produced once it is turned. The 2D flow is termed the *primary* flow and the 3D effects near the end walls are called *secondary* flows. Furthermore a turbomachinery rotor blade must have a small but finite clearance relative to its surrounding casing. The clearance, as in the case of rotor RT27a, is typically 1% of the blade’s span. However, the flow which leaks through this small gap has a surprisingly large effect on the aerodynamics of the machine especially

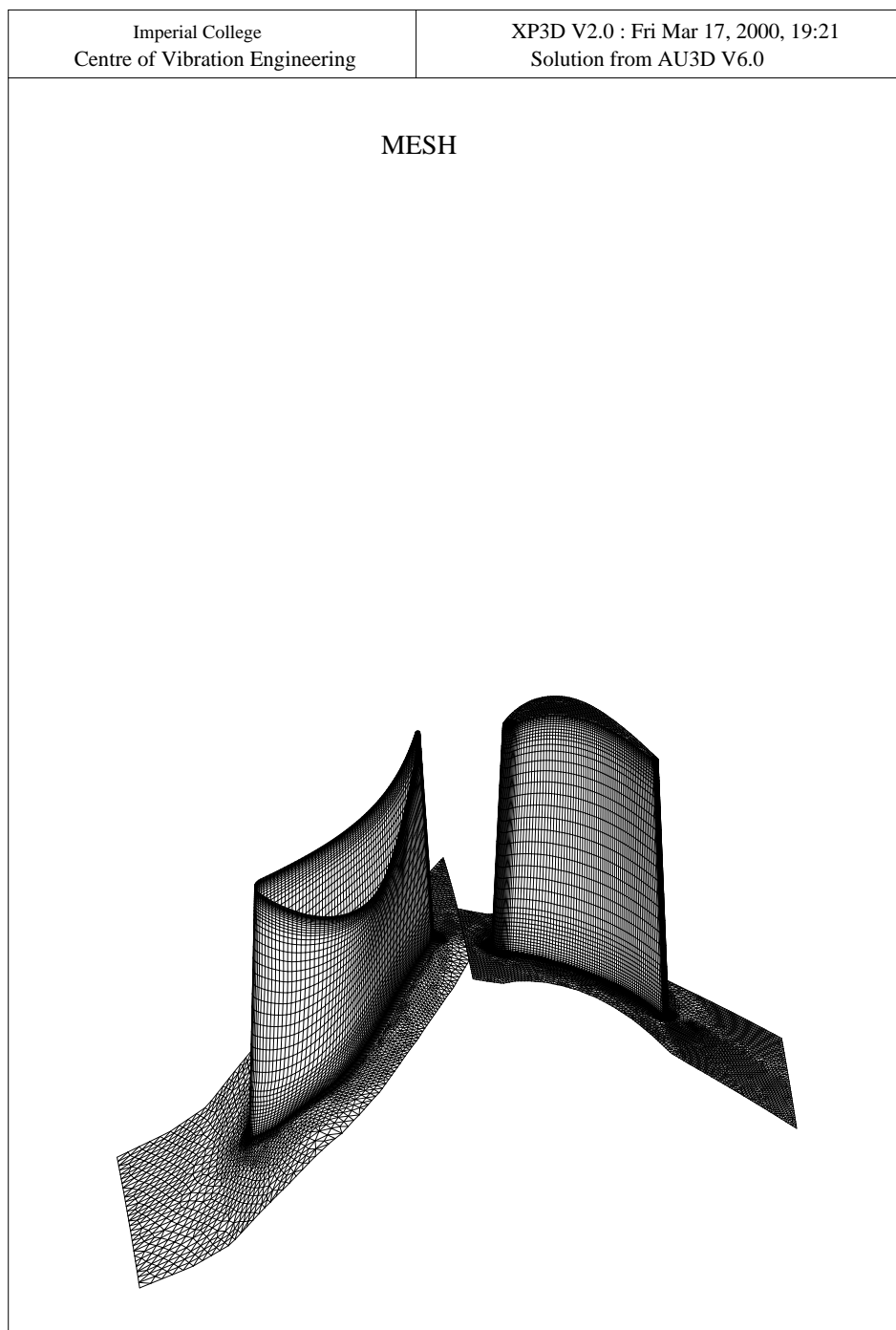
when the blade is relatively short. In order to predict secondary flow effects and to take into account tip-leakages, the hub and tip sections must be treated as solid walls and a tip clearance must be included in the computational mesh.

### 5.2.1 Computational mesh

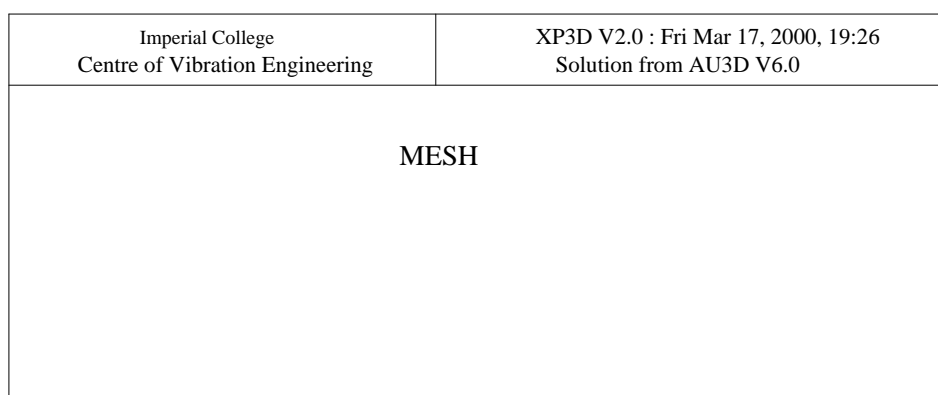
The computational meshes for the NGV and rotor passages were generated independently using the LEVMAP mesh generator described in chapter 2. These two meshes were then assembled together for a coupled NGV-rotor steady-state calculation. The NGV outflow and rotor inflow are treated as two separate boundaries and they are responsible for the interaction between the two domains via a mixing layer process (Dawes 1990, Denton 1990). A 3D view of the grid is shown in Fig. 5.2a while Fig. 5.2b shows a meridional view of the blade surfaces together with one periodic boundary. The points in the radial direction are clustered towards the end walls because of the strong secondary flow expected in these regions. Also, additional grid radial-levels are used in the rotor tip-gap region to capture the tip leakage effects. Both grids have 48 points in the radial direction, the locations at the NGV-outlet and rotor-inlet being identical (Fig. 5.2b). As shown in Fig. 5.3a, 42 of the radial grid levels, define the rotor geometry while the remaining six are positioned in the tip-gap region. Fig. 5.3b shows the triangulation of the rotor tip section.

Both the NGV and the rotor boundary layer regions are discretised by a twelve-layer of O-type mesh formed by hexahedra elements. Such a resolution is sufficient for a viscous computation which uses the law of the wall to evaluate the wall shear stresses.

Fig. 5.4 shows the mid-height radial section of the computational mesh. The NGV grid contains 4,717 points per radial level which yields a total of 226,416 points. The inclusion of the NGV passage in the steady-state computation is mainly justified by the need of (i) predicting a correct steady-state inlet conditions for the rotor passage and (ii) the evaluation of the spatial non-uniformities at the NGV-outlet. For these reason the NGV-grid is refined in the trailing-edge and outflow regions. The rotor grid contains 338,244 points distributed in the following way: each one of the six radial section in the tip-clearance region contains 7,850 points while each one of the remaining 42 sections contains 6,932 points. The number of points positioned in the rotor tip section of Fig. 5.3b is 918. Table 5.2 lists the number



(a) 3D view



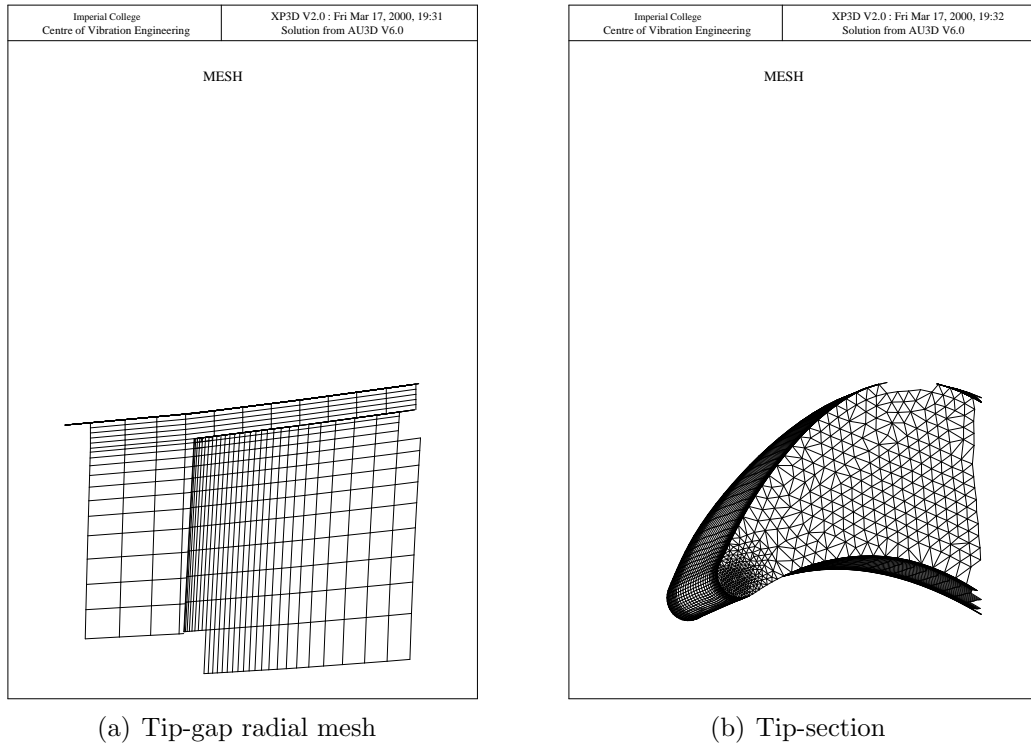


Figure 5.3: Computational mesh at tip end wall of RT27a rotor blade

of points in each boundary of a rotor radial section.

The tip clearance grid is relatively coarse since the main interest is not to predict accurately the structure of the tip-leakage flow, but only to take into account its main effect on the hub-to-tip pressure distribution. Since the main parameters which can affect the pressure distribution towards the tip are the size of the clearance and the pressure jump across the blade, the tip-grid of Fig. 5.3 is considered to be sufficient for the purposes of the current analysis.

Periodic boundary (axial direction)	126
Inflow boundary (tangential direction)	41
Outflow boundary (tangential direction)	43
Blade suction side (axial direction)	110
Blade pressure side (axial direction)	108

Table 5.2: Number of point on domain boundaries of RT27a rotor blade

### 5.2.2 Boundary conditions and computational details

The boundary conditions, together with the rotor rotational speed, specify at which point in the turbine stage characteristic the calculation is performed. The nominal design condition has been chosen for this numerical analysis. The rotor rotational speed is the one reported in table 5.1. The NGV inlet conditions are the following; constant stagnation pressure ( $p_{01}$  in table 5.1), constant stagnation temperature ( $T_{01}$  in table 5.1), flow direction without tangential component ( $\alpha_{x\theta} = 0$ ) and flow angle in the  $x - r$  plane reported in Fig. 5.5a. The final boundary condition is applied at the rotor outlet where the static pressure distribution of Fig 5.5b is specified. A sequence of three agglomerated grid levels were generated for both the NGV and the rotor domains so that a 4-grid W-cycle algorithm was used for the steady state computations. Starting from free-stream conditions the computation took around 300 multigrid cycles to converge. The calculation was performed on a 500 MHz DEC Alpha machine where the 300 multigrid cycles were completed in about 8 hours. The average  $y+$ , which indicates the resolution of the viscous body fitted O-grid, was of around 150 while the maximum was  $\approx 500$ . Both these values are within the logarithmic part of the turbulent boundary layer thus justifying the grid-resolution in this region.

### 5.2.3 Results of steady-state flow calculation

Fig. 5.6 shows the computed steady state static pressure on the rotor blade surface together with particle traces. The pressure distribution on the pressure surface is, in the main, 2D even though the particle traces show a significant radial component, especially towards the tip region where the tip-clearance pressure jump tends to drive the flow from the pressure side towards the suction side of the blade. The 3D effects are much more evident from the suction surface (Fig. 5.6b). The flow behaves in a 2D way only in the middle section, while secondary flow effects are very much evident towards both end walls. In particular, the separation line caused by the suction side leg of the horseshoe vortex is clearly visible at the hub end wall. The migration of the separation line towards mid-section is caused by the rotation of the passage vortex. Such a separation line is also present at the tip end wall but the flow pattern is more complicated. This is caused by the interaction of the passage and tip-leakage vortices which result in counter-rotating flow structures. Section 5.2.4 will present a more detailed discussion of these secondary flow effects.

Fig. 5.7 shows a comparison of predicted and measured isentropic Mach number blade distributions at mid-height section. The two experimental Mach number distributions are calculated from the time-mean unsteady static pressures but using two different values of the rotor-relative total pressures at the leading-edge: the experimental and the computed values. The discrepancy between the two measured curves can be considered to be an indicator of the experimental sensitivity to the rotor relative inlet total pressure. Fig. 5.8 shows the comparison between the measured and computed leading-edge pressure values along the radial direction. In addition to the distribution obtained from the 3D steady-state computation, Fig. 5.7 reports the result of a quasi-3D calculation performed at mid-height section. The true 3D result agrees, with the measurements, better in the forward part of the blade suction surface while it overestimates the exit pressure. Fig. 5.9 shows a comparison of the predicted isentropic Mach number blade distributions at 5, 10, 90 and 95% spans with the time-averaged measured data. The overall agreement is reasonably good although some discrepancies are worth mentioning. As for the mid-height blade distribution of Fig. 5.7, the computed results in the trailing-edge region of the suction surface underestimate the measured isentropic Mach number. The reasons for such discrepancies are not entirely clear. However, it should be noted that experimental data represent averaged unsteady flow which, under certain circumstances may be different from the true steady flow. This is probably the case of regions where shock waves are present, i.e. towards the trailing-edge region of the suction surface.

One feature that is common to Figs. 5.7 and 5.9 is that the pressure-side isentropic Mach number distribution is almost the same for all span-wise positions, a feature that is also evident from Fig. 5.6a. The suction-side results show considerable deviations from the base 2D flow due to secondary and tip-leakage flows effects. Fig. 5.9a shows that forward position of the suction side is unloaded relative to midspan values. At mid-root, the unloading in the forward position is less pronounced and the results are closer to the midspan values. This trend of a increasing load on the forward position continues all the way to the tip.

#### 5.2.4 Secondary and tip-clearance flow

Three main vortices were identified in the rotor blade passage: the *horseshoe* vortex, the *passage* vortex and the *tip-leakage* vortex. The formation of first two vortices is

connected to the presence of velocity gradients near the end wall boundary layers while the tip-leakage vortex is caused by the fast moving flow in the gap region. The horseshoe vortex has two legs, namely the suction and pressure side legs. This vortex is formed around the leading-edge of the blade at the end wall regions, in the same way as around any blunt body with its axis perpendicular to the wall. The high energy fluid, at the edge of the end wall boundary layer, flows away from the leading-edge stagnation point, not only around the blade, but also downwards because of the lower energy of the fluid below. When this high energy fluid reaches the end wall, it flows upstream forming a saddle point where the upstream flow separates from the surface. Fig. 5.10 shows the static pressure contours as well as the particle traces at 1% span. The two separation lines caused by the pressure and the suction leg of the horseshoe vortex can be seen clearly. The suction side leg remains close to the blade and then, as indicated in Fig. 5.6, travels up the suction surface, while the pressure side leg crosses the blade passage to the suction side of the other blade. The detail is very complex, but the same main features were noted by other researchers (Sieverding 1985, Gregory-Smith 1997).

The passage vortex is associated with the turning of the vorticity vector, and its main effect occurs in the middle of the passage. Its rotation is in the same sense as the pressure side leg of the horseshoe vortex and the two evolve and merge together. Fig. 5.11 shows the particle traces at two consecutive axial planes. At an axial plane 15% chord downstream of the leading-edge, a recirculating flow pattern, formed by the passage vortex and pressure side leg of the horseshoe vortex, is centered in the middle of the passage. Within the blade passage the vortex is convected by its own flow field from the pressure surface towards the suction surface as indicated in Fig. 5.11b. The formation of the passage vortex is a natural consequence of the interaction between the shear flow at the end wall and the turning of the blade. The mainstream flow sets up a pressure gradient across the blade passage, from the suction to the pressure surfaces, which can be approximated by the following relationship:

$$\frac{\partial p}{\partial r} = \frac{\rho u_r^2}{r} \quad (5.1)$$

where  $r$  is the local radius of the turning of the flow caused by the blade passage. The slower moving boundary layer fluid is subjected to this same pressure gradients, but since the velocity  $u_r$  in the boundary layer is smaller than the mainstream one,

the radius of curvature  $r$  must be smaller. Thus in a 3D blade row, the flow on the end wall is directed from pressure to suction surface as shown in Fig. 5.10, and to preserve continuity, there is a back flow further away from the end wall, leading to the vortical flow shown in Fig. 5.11.

The flow at the tip is somewhat more complicated. The orifice formed by the tip gap experiences essentially the same pressure difference as that across the blade. Fig. 5.12 shows the static pressure contours as well as the particle traces for a radial section inside the tip-gap. This pressure ratio across the gap accelerates the flow up to supersonic conditions. The clearance flow then emerges from the gap with very high velocity at an oblique angle relative to the passage flow. The resulting strong interaction with the passage flow, including the developing passage vortex of Fig. 5.12, causes the leakage flow to roll up into a vortex known as tip-leakage vortex. Such a vortex results in a structure which has a vorticity in direction to that of the passage vortex. Yamamoto (1988) investigated the interaction mechanism between tip leakage flow and the passage vortex in some detail. At the trailing-edge, the leakage flow pushes the passage vortex away from the suction surface, a feature that is evident from Fig. 5.12. Also Yamamoto (1988) suggests that the interaction between the two vortex structures results in an elongation and distortion of the passage vortex. In particular, the leakage flow pushes the secondary flow towards midspan. This seems to be in an agreement with what is shown in Fig. 5.6. Another important feature of the tip-clearance flow is the formation of a dividing stream surface between the fluid which is swept into the gap and that which is driven across the passage in the usual way. Such a stream surface is evident in Fig. 5.12 where it lies at about one fifth of the blade pitch from the pressure surface. The exact position of the division stream surface is a function of the clearance and probably other parameters such as the blade loading (Sjolander & Amrud 1987). Fig. 5.12 also shows the absence of the stagnation point due to the presence of the clearance. On the other hand, the two separation lines of the horseshoe vortex are still present. For larger clearances, Sjolander & Amrud (1987) show that the tip horseshoe vortex disappears.

## 5.3 Rotor Unsteady Flow Analysis

In this section unsteady results obtained using the linear frequency domain approach are presented. First, the sources of unsteadiness obtained from the NGV outlet steady-state solution are discussed. Potential- and vortical-rotor interactions were evaluated for the first two tangential Fourier modes and the superimposed results compared with the available experimental data. Sections 5.3.3 and 5.3.4 present a physical interpretation of the two type unsteady interactions, i.e. potential and vortical. As reported in Appendix C, there is a third type of unsteady interaction caused by the entropy variation across the NGV wake. This interaction produces unsteady pressure variations which are of one order of magnitude less than those obtained from the potential and vortical NGV non-uniformities. For this reason the entropy mode is included in the vortical mode, also associated with the NGV-wake. This means that the total unsteady flow-filed in the rotor passage is given by the superimposition of the potential and vortical modes.

### 5.3.1 Sources of unsteadiness

The sources of unsteadiness in the rotor passage are represented by the steady-state tangential non-uniformities at the outflow boundaries of the stator blade. Such non-uniformities, which can be assumed to be approximately steady in the stator frame of reference, are unsteady in the rotor frame of reference since the rotor is moving through them. Fig. 5.13 shows the computed steady-state solution at the NGV outlet. The static pressure distribution shows a weak shock wave towards the hub section where the average outlet Mach number is just above unity. The Mach number contours in Fig. 5.13b show the potential field associated with the static pressure contours but the wake profile is not evident apart from the hub section of the blade where the wake seems to have a quite strong radial variation. The total pressure contours, on the other hand, clearly exhibit the wake structure which appears to run almost radially, with the exception of the root region. The rotor blades move through the steady NGV-outlet from left to right of Fig. 5.13 and they see the spatial non-uniformities as unsteady perturbations. Such spatial non-uniformities are periodic in the tangential coordinate and they can be decomposed into Fourier components for each radial section. The unsteady velocities contain two parts: a rotational (vortical) part, associated with the NGV wake, and an

irrotational (potential) part associated with pressure variations. In the same way, the unsteady density contains two parts: an entropic part associated with the NGV wake and an irrotational (potential) part, again associated with the pressure variation. Such a grouping means that each Fourier mode of the steady flow solution at the NGV outlet can be seen as summation of three different modes: vortical, potential and entropic. Appendix C shows how to calculate such modes for each Fourier harmonic using Goldstein's splitting theorem and the linearised acoustic equations.

The vortical component of the spatial non-uniformities is associated with velocity variations with zero divergence and hence with the velocity defect in the NGV wake. Fig. 5.14a shows the first two Fourier components of the absolute velocity variations associated with the vortical component. The first harmonic, usually referred as 'gust' (Manwaring & Wisler 1993), clearly shows the three-dimensionality of the NGV-wake towards the root section. Very large velocity deficit occurs half a cycle or so earlier than the mid-height wake. Such wake inclination was also measured by Moss et al. (1997). Fig. 5.14b shows the pressure perturbation which is associated only with the potential field of the NGV outlet. Neither Fourier component has strong 3D features. The first two harmonics of the density perturbation associated with the entropic mode are shown in Fig. 5.14c. Fig. 5.15 shows the vortical and potential components of the absolute velocity non-uniformities at the NGV outlet. These two plots have been obtained by a summation of the first twenty vortical and potential Fourier components.

### 5.3.2 Comparison with measured data

The computed unsteady flow results, obtained from the superimposition of the potential and vortical calculations, will now be compared with the experimental data of Moss et al. (1997). The comparison is made for three different spanwise positions, namely mid-root, mid-height and tip. The remaining two sections, root and mid-tip, are not considered because of the unavailability of experimental data for the rotor suction surface. Fig. 5.16 shows the amplitude and the phase angle of the first Fourier component of the unsteady pressure for these three radial sections. A striking feature of Fig. 5.16 is that the pressure amplitude on the pressure surface is overpredicted for all three sections. This significant discrepancy is more evident in the mid-root section where shape of the predicted amplitude

shows a maximum at mid-chord whereas the measured data indicate a minimum. On the other hand, at mid-height and tip, the shape of the predicted amplitude is similar to the measured ones even though there is a factor of two discrepancy. As it will be discussed in section 5.4, the reason of such discrepancy cannot be attributed to a possible non-linear behaviour. Unlike the amplitude, the phase angle on the pressure side is in good agreement especially at mid-height and tip sections. The suction side predictions give a good representation, both in term of amplitude and phase angle. At mid-height, the suction side prediction has some discrepancies with the measured data in the region around  $x/c_x \approx 0.75$  where the measured and computed data are out of phase and of different amplitudes.

Fig. 5.17 shows the comparison between the predicted and measured data for the second Fourier component of the unsteady pressure. Unlike the first Fourier component, and perhaps very surprisingly, the overall agreement is very good for the all three sections both in terms of amplitude and phase angle.

### 5.3.3 Vortical-flow interaction effects

As discussed earlier the vortical flow non-uniformities at the NGV outlet are associated with a rotational velocity perturbation with zero divergence. Such a vortical flow component at the NGV outlet is shown in Fig. 5.14a for the first two tangential Fourier modes. Vortical-flow interaction, also labelled wake-rotor interaction, has been studied and interpreted by several authors (Hodson 1985, Giles 1987, Korakianitis 1992a, 1992b, 1993) and it is now fairly well understood. Before analysing the hub-to-tip distribution of the pressure amplitude, a brief description of the wake-rotor interaction at mid-height section is given.

Figs. 5.18 and 5.19 show the dimensionless absolute velocity and pressure fluctuations together with the unsteady particle traces during one blade passing cycle in the rotor passage. The wakes are first bent by the potential flow field of the rotor as shown in Fig. 5.18a. When the leading-edge in the rotor stagnation region interacts with the lower momentum fluid in the wake, unsteady, recirculating flow patterns are established as shown in Fig. 5.18a. These recirculating flow patterns, generated as the wake is being cut, result in a counterclockwise rotating vortex downstream the wake centerline (indicated with a dotted line) and in

a clockwise vortex upstream the centerline (Fig. 5.18a). The upstream unsteady vortex is associated with a local increase of pressure while the downstream counterclockwise flow pattern causes a local decrease in pressure. After the wake is cut, a segment of wake is produced in the rotor passage and the two ends of the segment travel at local steady fluid speed. Since the flow is faster at the suction side, the wake centerline begins a counterclockwise rotation as it moves through the rotor passage. At the same time, the lower momentum fluid moves from the wake end near the pressure side to the wake end near the suction side, causing a thicker wake in the suction side and a thinner one in the pressure side (this is due to the direction of rotation of the two vortices). Broadly speaking, as the wake centerline moves downstream in the rotor passage, its influence in the unsteady pressure fluctuation tends to be more pronounced on the suction side of the blade. This is evident in the blade crown were the unsteady pressure amplitudes reach their maximum. As the recirculating flow patterns moves downstream, the wake is sheared, distorted and enlarged while the amplitude of the unsteady pressure is decreased and its region of influence increased. Near the trailing-edge of the blade, there is an expansion region on the suction side which causes a local increase in pressure amplitude across the the line of the trailing-edges. This is also evident from Fig. 5.16b in the region  $0.5 < x/c_x < 0.75$ .

Fig. 5.20a shows the unsteady pressure amplitude computed by using the first Fourier harmonic of vortical flow component at the NGV outlet. The pressure surface exhibits more 3D features than the suction surface. The amplitude of disturbances on the pressure surface is higher towards the forward part of the root section. This because of the stronger vortical field indicated in Fig. 5.14a. On the other hand the resistance of the wake effect is reduced if compared with mid-height and tip sections (blue region at the root trailing-edge in Fig. 5.20a). The reason for this reduced resistance can be tracked to the lower wake exit angle at root section. Infact Korakianitis (1993) showed that the wakes from lower stator exit angles act for a shorter part of the blade passing cycle. On the suction surface, the perturbations reach their peak on the crown of the blade as shown in Fig. 5.20b. In addition, a region of high pressure amplitude is noticeable in the region were the suction side separation line of the horseshoe vortex is located (see Fig. 5.6b). The propagative aspect of the vortical flow interaction can be easily seen from an ispection of the unsteady pressure animation. The perturbation starts at the

leading-edge and then propagates towards the rotor outlet with the steady-state local fluid velocity.

The unsteady pressure amplitude caused by the second Fourier component of the NGV-outlet vortical flow non-uniformities of Fig. 5.14b is shown in Fig. 5.21. The 3D effects are much stronger than those due to the the first Fourier harmonic, especially in the pressure surface where the pressure amplitude distribution differs significantly from Fig. 5.20a. In contrast, the suction surface disturbances have a qualitatively similar behaviour to Fig. 5.20b.

### 5.3.4 Potential-flow interaction effects

An analysis of the temporal variation of the potential-flow interaction is given in this section. The potential flow at the NGV outlet is shown in Fig. 5.14b for the first two harmonics. Such a potential flow does not show particoular 3D features although its amplitude is higher towards the root section. Fig. 5.22 shows the predicted amplitude of the unsteady pressure distribution on the rotor blade due to the first Fourier component of the potential flow.

In the suction side, the unsteady pressure exhibits 3D effects across the suction side leg of the horseshoe vortex. Fig. 5.22b shows that the unsteadiness is much higher towards the leading-edge and that there is an exponential decay downstream. This is compatible with the potential flow theory illustrated in appendix C. Such a decay rate can also be seen from Fig. 5.16.

The unsteady pressure perturbation on the pressure surface exhibits a 2D behaviour and it results in a ‘stationary’ wave centered at the middle of the blade. Such a feature can be seen from Fig.5.16 where the maximum amplitude is located at  $x/c_x \approx -0.75$  with a phase nearly constant along the axial direction. Thus, on the pressure side, the potential-flow unsteadiness does not decay exponentially but, on the contrary, seems to follow a different behaviour.

With the help of the unsteady pressure animation, it is possible to distinguish two separate regions for the potential flow interaction. As the rotor passage moves, it cut the potential flow field in an upstream region attached to the NGV outlet and in a rotor passage region centered on the pressure surface. The upstream interaction, which decays exponentially downstream, is responsible for the high perturbations at the leading-edge of the blade and it does not interact with the

rotor steady pressure field. In the region inside the rotor passage, the prescribed potential flow interaction from the stator outlet and the potential flow field of the rotor itself influence each other. Korakianitis (1992a, 1992b, 1993) showed that this interaction is strongly influenced by the stator-to-rotor pitch ratio and, consequently, by the inter-blade phase angle as reported in Appendix C. For equal rotor and stator pitches, the inter-blade phase angle becomes  $2\pi$ . In this scenario, the potential flow interaction affects only the leading-edge of the blade while for a larger ratio (and smaller inter-blade phase angle) the interaction affects the whole of the rotor assembly.

Although the pressure variation due to the potential-flow interaction is a pressure disturbance entering the rotor passages, this pressure disturbance does not “propagate” downstream the rotor blade at the sonic or any other velocity. The potential-flow disturbance is a pressure field which is located in the traverse of the rotor assembly; it is affected by the potential-flow interaction of the rotor itself, but it does not propagate. The interaction between the pressure disturbance and the rotor pressure field occurs in the middle of the passage and it is located in the pressure side of the blade.

The unsteady pressure perturbations generated by the second Fourier component of the potential flow field of the NGV outlet is shown in Fig. 5.23. The resulting potential flow interaction shows a large 3D effect when compared with the distribution in Fig. 5.22. The unsteady pressure behaviour, on the other hand, is very similar to that previously discussed. The disturbance on the suction side decays more rapidly than the first harmonic and this is in perfect agreement with the potential flow theory. The interaction between the disturbance and the rotor pressure field is again visible in the pressure surface of the blade where a pressure pulsation is still present. However such pulsation on the pressure surface seems to possess a propagative behaviour in the spanwise direction. From the unsteady pressure animation, it is evident that the interaction starts at the blade root, where the inlet disturbance is higher (Fig. 5.23a), and propagates towards the tip section growing in amplitude.

A possible cause of this propagative 3D effect can be attributed to the presence of centrifugal and Coriolis forces created by the blade rotation. It has been demonstrated by several authors (Kerrebrock 1977, Atassi & Golubev 1997) that, for non-uniform mean flow, such forces deflect the fluid motion and couple together

the potential and vortical modes. Because of such coupling neither convected vortical nor irrotational acoustic disturbances exist. Instead, (i) nearly-convected or vorticity-dominated modal disturbances, that contains pressure, and (ii) acoustic or pressure-dominated modal disturbances, that contain vorticity, occur (Montgomery & Verdon 1997a).

### 5.3.5 Summary of the main findings

The unsteady pressure on a 3D HP turbine rotor blade due to potential-flow and viscous-wake interaction from the upstream NGV was computed using a linear flow representation. The potential-flow and the viscous-wake from the upstream NGV are modelled as inlet distortions at the rotor-inlet boundary. The superimposed solutions for the first (blade passing frequency) and second Fourier modes were compared with available experimental data. The overall agreement was considered to be satisfactory although the pressure side perturbations due to the first Fourier mode were overestimated. The main conclusions of this unsteady analysis can be summarised as follow:

- The wake-rotor interaction is characterised by the cutting of the NGV wake by the rotor blade. Such a process generates a wake segment in the rotor passage which interact with the potential flow-field of the rotor itself. The vortical pattern upstream of the wake centerline generates an increase in local pressure while the vortical pattern downstream of the wake centerline generates a decrease in local pressure.
- At mid-height section, where the flow is quasi 2D, the perturbations due to wake-rotor interaction are higher at the crown of the blade. This is true for both the first and second Fourier component.
- The perturbation caused by vortical-rotor propagates from inlet towards the rotor outlet with the steady-state local fluid velocity.
- Two separate regions for the potential-flow interaction can be distinguished in the rotor domain. The first region is attached to the stator outlet and interacts with the rotor leading-edge. Such interaction is strong but decays exponentially downstream. The second region is located in the rotor passage and it is the consequence of the interaction between the potential-flow at the

rotor inlet and the potential flow field of the rotor itself. Such interaction results in a ‘stationary’ pressure wave centered at the middle of the rotor pressure surface.

- Such a pressure pulsation on the blade passage is ‘stationary’ only for the first Fourier component. The second Fourier components of the potential-flow mode exhibits a propagative radial behaviour although for a given radial section it still results in a ‘stationary’ pulsation. This 3D behaviour can be explained by the presence of centrifugal and Coriolis forces which couple together vortical and acoustic modes.
- The importance of including both potential and vortical disturbances is clearly demonstrated. Strong 3D effects for both interactions are positioned across the suction side leg of the horseshoe vortex.

## 5.4 Linear versus Non-linear Analysis

An evaluation of whether non linearity could be responsible for discrepancies between the linear predicted results and measured data is presented in this section. A non-linear time-marching solution technique was employed to calculate the unsteady flow field in a coupled stator-rotor configuration. The stator to rotor pitch ratio is 3:5 thus three stator blades and five rotor blades have to be included in the computational domain. Because of the large number of point needed for a 3D calculation, the comparison between linearised and non-linear methods was made using a quasi-3D version of the code at mid-height section.

### 5.4.1 Analysis at mid-height section

Fig. 5.24 shows the predicted steady-state Mach number contours, using a quasi-3D representation, together with the Kulite sensor position. The isentropic Mach number blade distribution is compared with the time-averaged experimental data and the 3D calculation in Fig. 5.7. The non-linear time marching simulation for a coupled system of 3 NGV blades and 5 rotor blades run for eight blade frequency cycles before reaching a periodic solution suitable for comparison with the linear prediction. The unsteady pressure time-hystory on the rotor surface has been

Fourier decomposed and the first three modes were considered. Higher Fourier components are strongly affected by the artificial diffusion/dispersion of the numerical algorithm (Sbardella 1997).

Figs. 5.25, 5.26 and 5.27 compare the results obtained using the linear and non-linear methods with the experimental data for the first three Fourier modes. For the first Fourier mode the discrepancies between linear and non-linear results are located in the leading-edge region of the blade. Such mismatch is maximum for  $x \approx 0.35$  where linear perturbation is 50% the non-linear one. In the pressure side and in the second part of the suction side the discrepancies are within a 10% limit. On the other hand, the phase of the unsteady pressure perturbation is nearly the same for the linear and non-linear representations. The comparison between the linear and non-linear second Fourier component of Fig. 5.26 indicates an even better agreement between the two representations. The error in amplitude prediction is well within a 10% limit. The phase is also in good agreement. The third Fourier component of the linear result underestimates by a factor of 50% the non-linear results as shown in Fig. 5.27. The phase still presents an overall good agreement. This discrepancy could be a direct consequence of two non-linear effects: (i) the steady-state NGV outlet solution underestimate the amplitude, for this particular Fourier mode, of the time-averaged non-linear solution. This is evident in the leading-edge part ( $0 < x/c_x < 0.3$ ) of rotor suction side of Fig. 5.27a. Infact, in this region the non-linear amplitude is higher than the linear one by a constant factor of  $\approx 1.75$ . (ii) Another cause of these discrepancies can be recover from the energy transfer between different Fourier modes. Although Fig. 5.27a evidentiates such non-linear features, it should be noted that the amplitude of this perturbances is much lower than those obtained for the first two Fourier modes of Figs. 5.25 and 5.26.

### 5.4.2 Reconstructed wave-forms

In this section the reconstructed wave forms over two blade passing cycles are reported. The waves are obtained by an inverse Fourier transform of the first three modes presented in Figs 5.25, 5.26 and 5.27. The position on the rotor blade surface of the various wave-forms is shown in Fig. 5.24

## 5.5 Concluding Remarks

An extended analysis of the steady and unsteady aerodynamics in a rotor passage typical of high-pressure turbine stage of contemporary turbomachines has been presented. The main highlight of this study are summarised as follow:

- A steady state 3D calculation for a coupled NGV-rotor configuration is essential in order to correctly predict the rotor primary and secondary flow as well as to evaluate the flow non-uniformities at the NGV outlet. A good representations of such non-uniformities is compulsory for the evaluation of the aerodynamic forcing functions which need to be imposed at the rotor inlet in a linear unsteady calculation. For this reson, the use of steady-state non-reflecting boundary conditions at the NGV outlet/rotor inlet boundaries is essential.
- Both vortical and potential interactions are essential for a complete unsteady flow representation. The vortical interaction is strong in the crown of the blade while the potential one in the leading-edge region of the blade.
- The potential-flow interactions reveals 3D effects which can be justified by the coupling of vortical-acoustic modes due to the presence of centrifugal and Coriolis forces in the rotor passage. This coupling is more evident in the second Fourier mode.
- Non linear effect are minimal for the first two Fourier components thus justifying a liner unsteady approach.
- The linear unsteady approach offeres great advantages over its non-liner counterpart: (i) much more efficient in term of CPU speed and storage. (ii) Much faster pre-processing since the linear calculations are performed using a single passage mesh while non-linear methods require the assembling of multiblade-multirow meshes<sup>1</sup>. (iii) Much faster post-processing analysis since the computed data represents the complex amplitude of the unsteady perturbation for a given Fourier mode.

---

<sup>1</sup>This advantage is even more enfatised when multigrid-solver are used

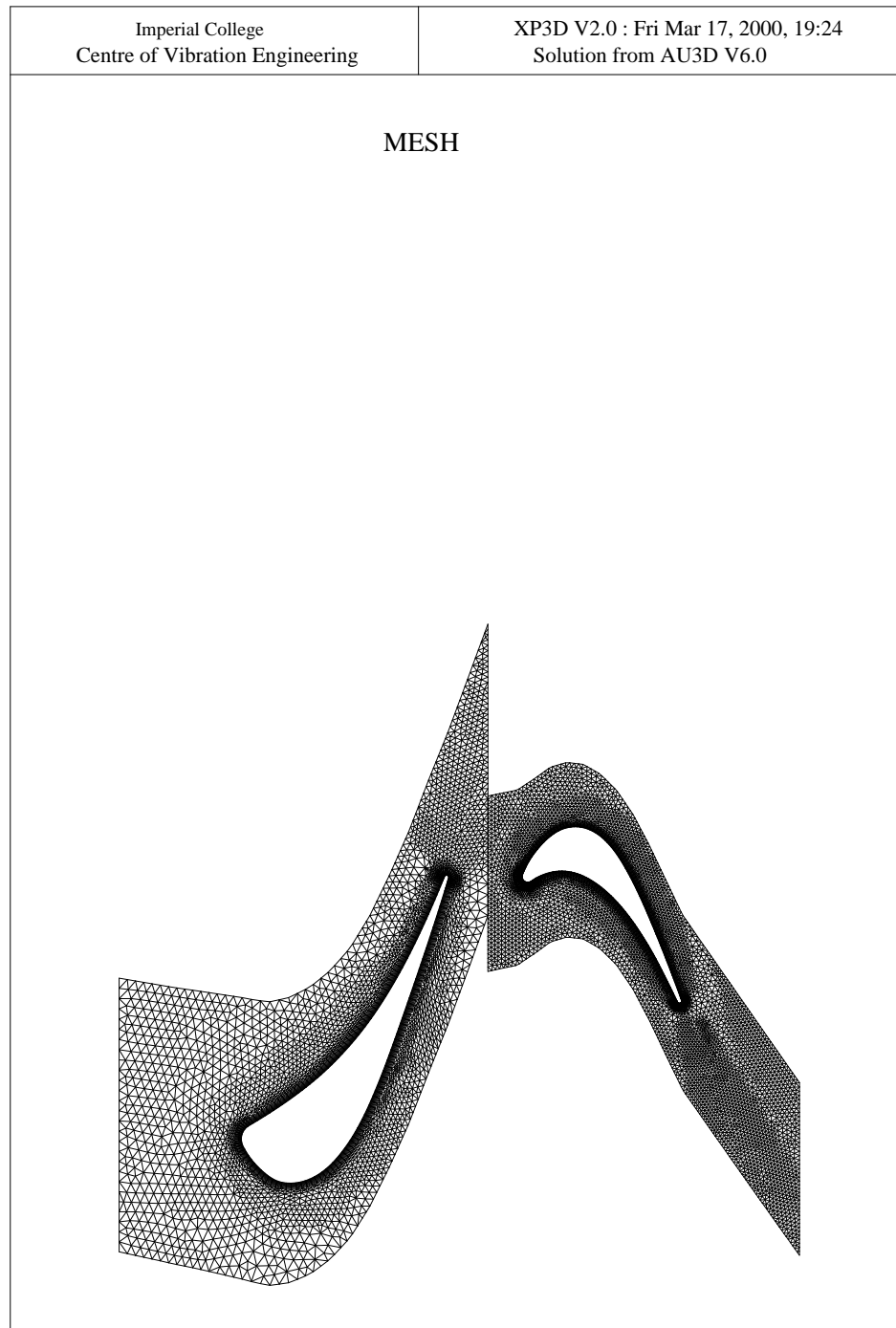
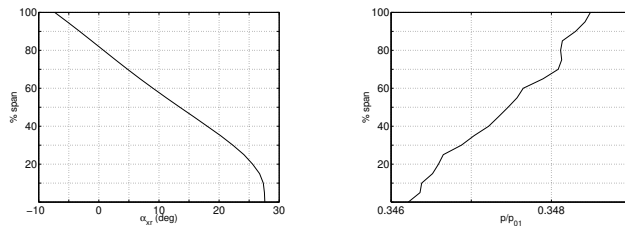


Figure 5.4: Computational mesh at mid-height section of RT27a turbine stage



(a) NGV inlet flow angle in the  $x - r$  plane      (b) Rotor outlet static pressure

Figure 5.5: Boundary conditions of RT27a turbine stage

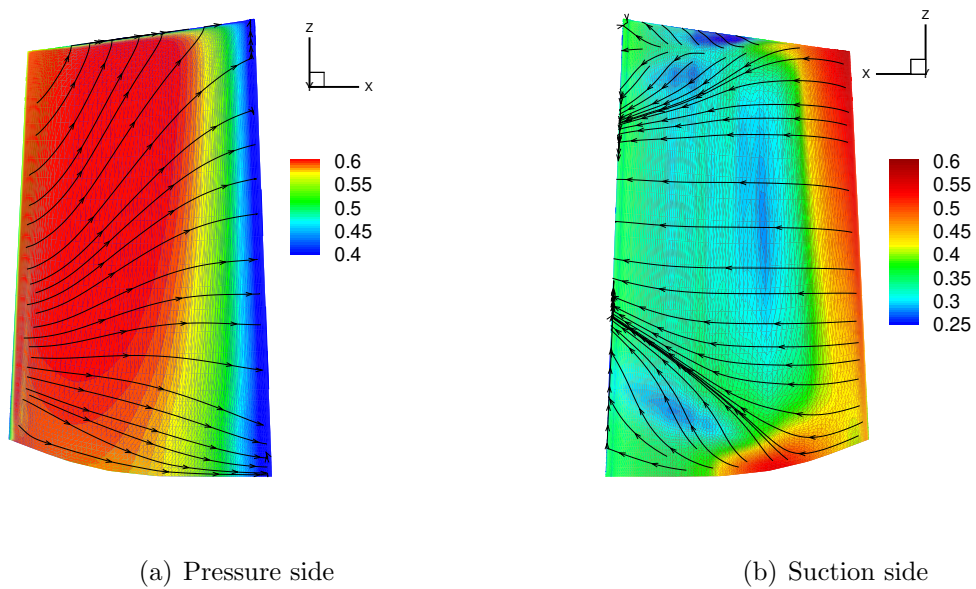


Figure 5.6: Steady state pressure contours  $\frac{p}{p_{01}}$  and particle traces on the RT27a rotor surface

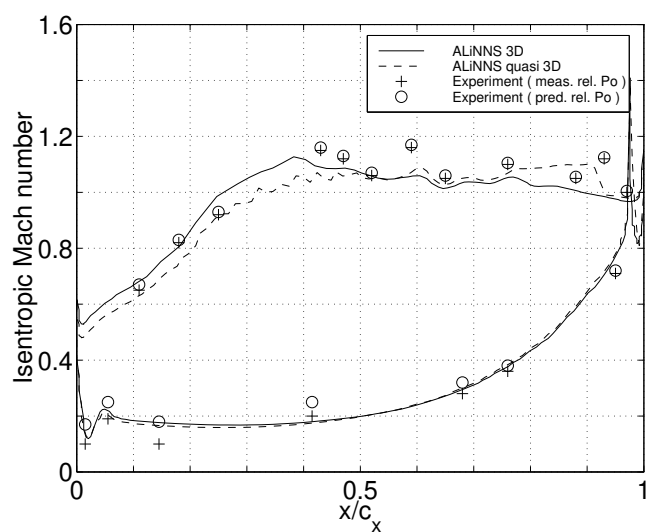


Figure 5.7: Isentropic steady-state Mach number distribution at mid-height section of RT27a rotor blade

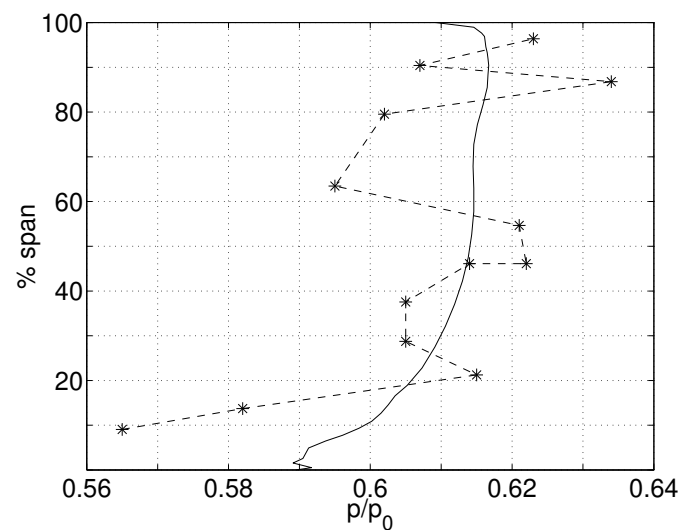


Figure 5.8: RT27a rotor leading-edge pressure levels. (\*) Leading-edge kulite measured data, (-) computed

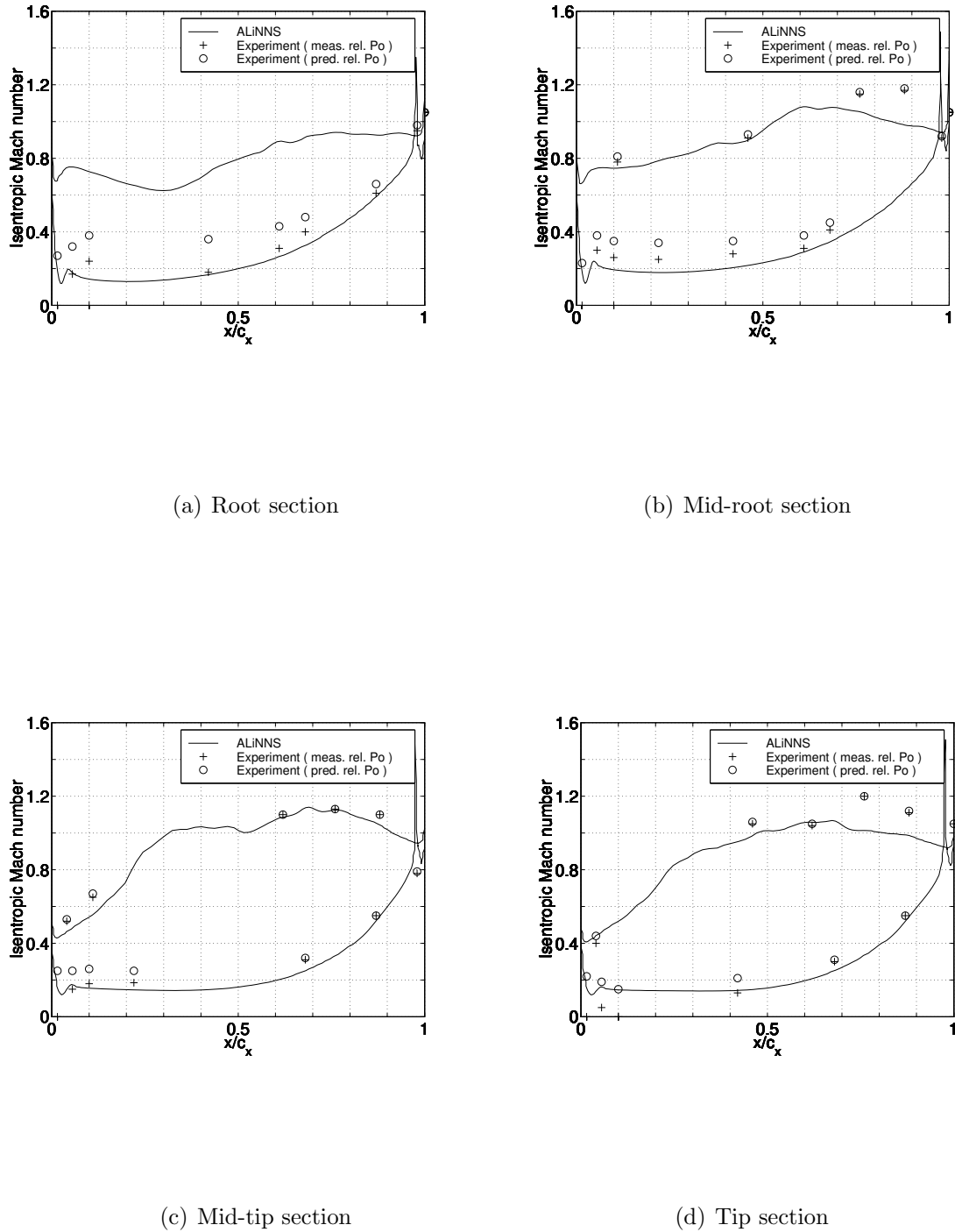


Figure 5.9: RT27a rotor blade: isentropic steady-state Mach number distribution at different span-wise positions

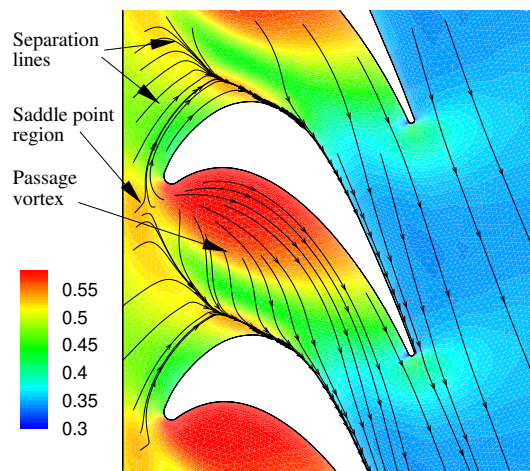


Figure 5.10: Steady state pressure contours  $\frac{p}{p_{01}}$  and particle traces at 1% span of RT27a rotor blade

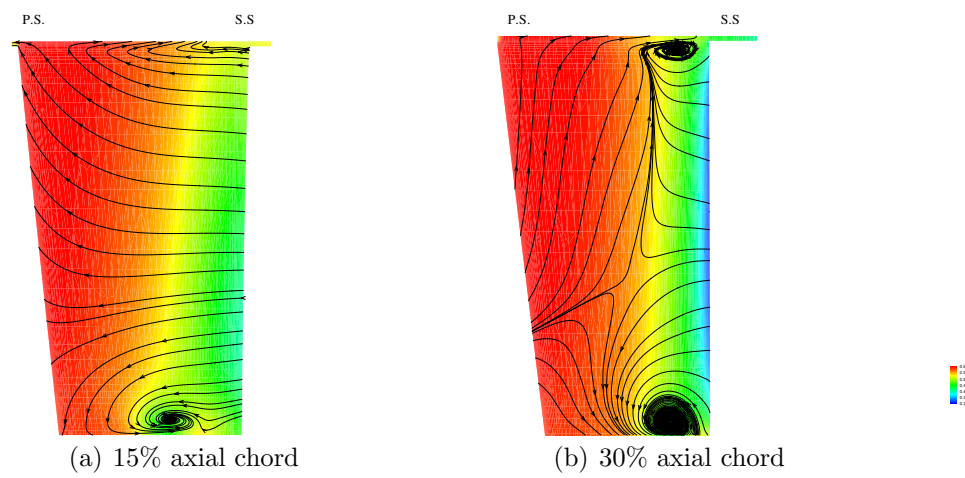


Figure 5.11: Pressure contours  $\frac{p}{p_{01}}$  and particle traces at different  $r\theta - r$  planes in the RT27a rotor passage

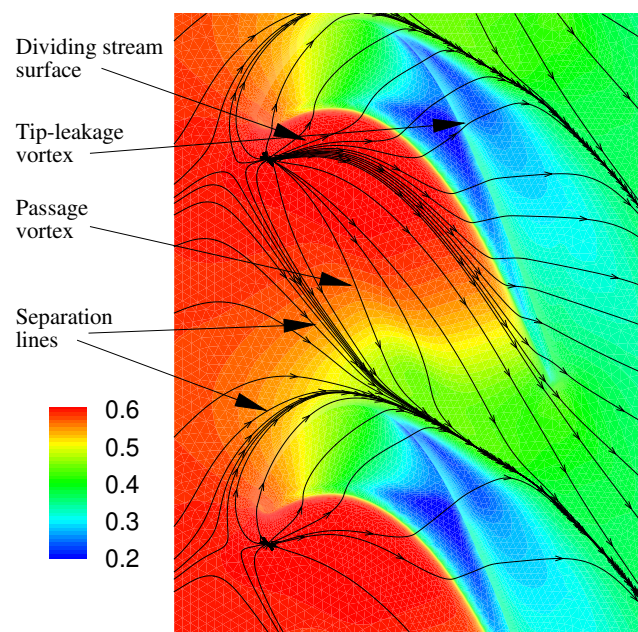
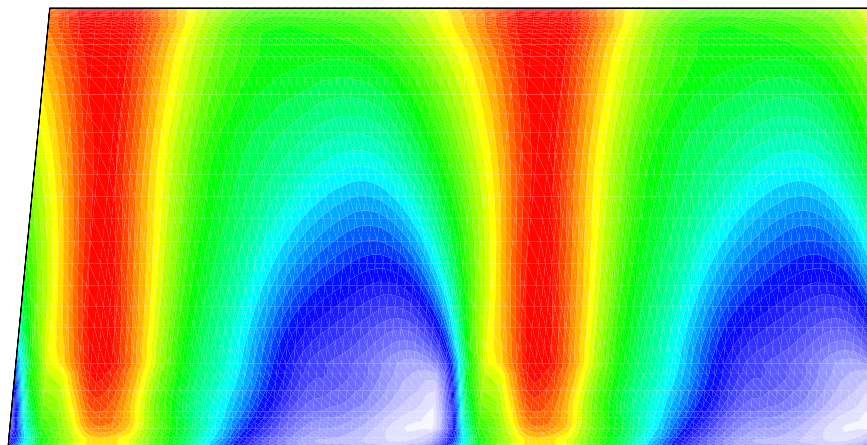
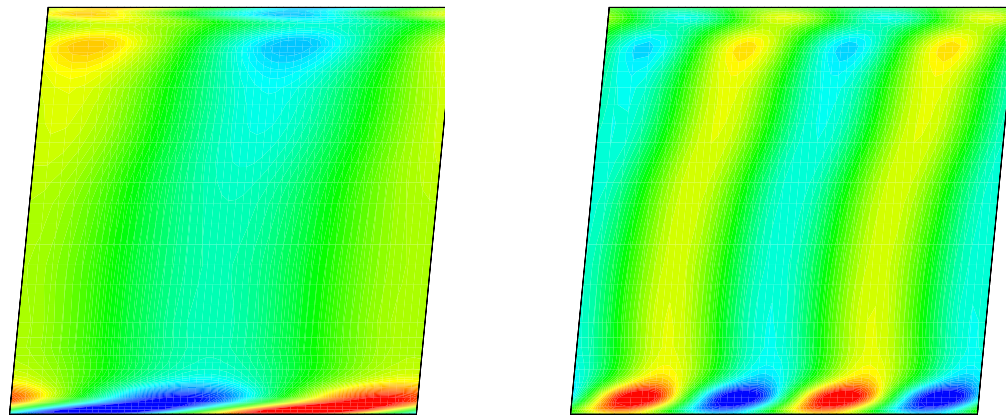


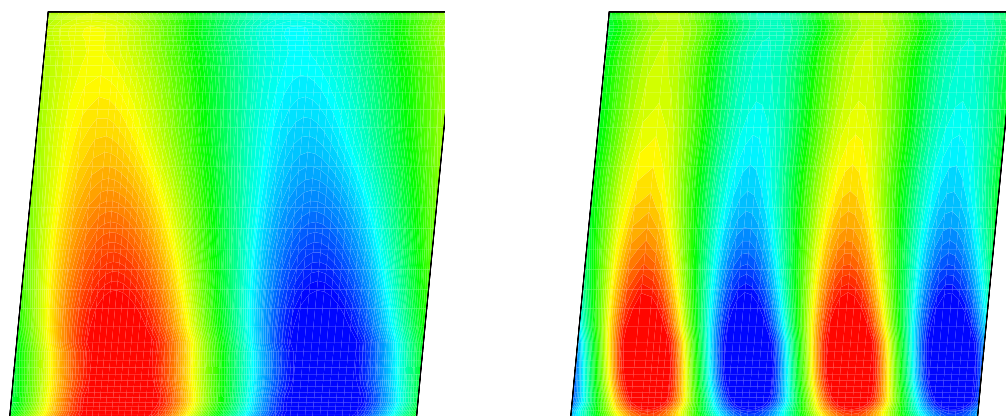
Figure 5.12: Steady state pressure contours  $\frac{p}{p_{01}}$  and particle traces inside the RT27a rotor tip-gap region



(a) Dimensionless static pressure



(a) Vortical component of dimensionless absolute velocity



(b) Dimensionless pressure

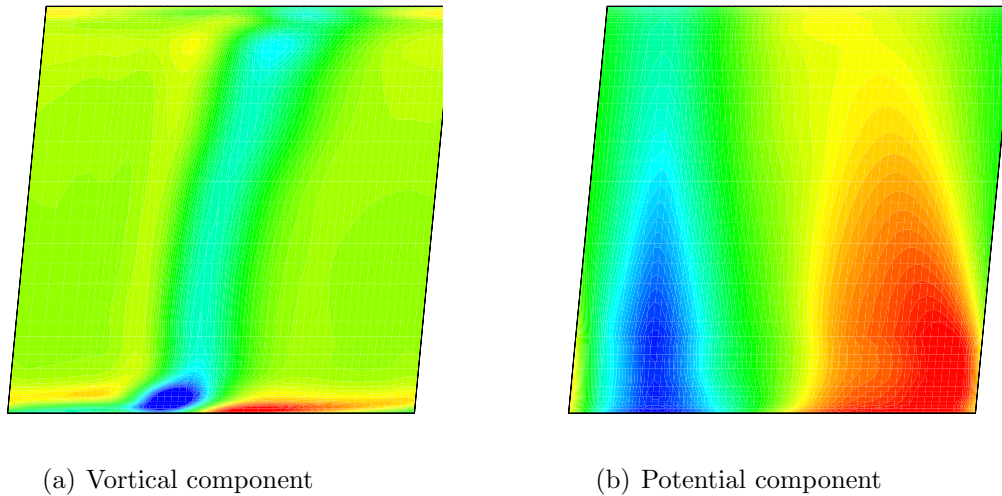
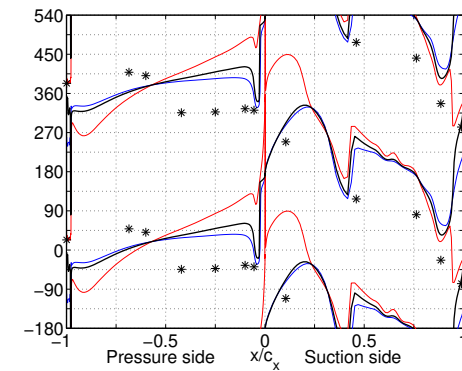
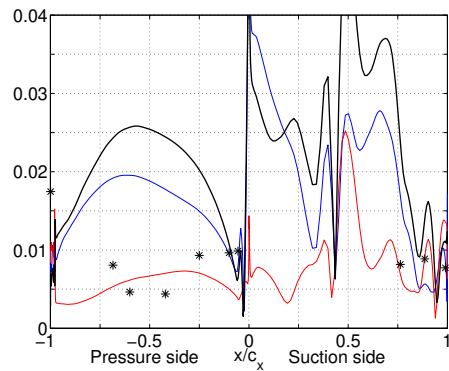
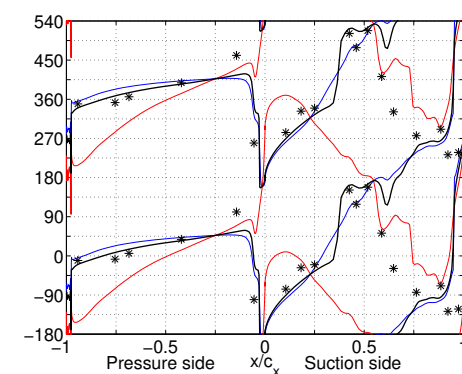
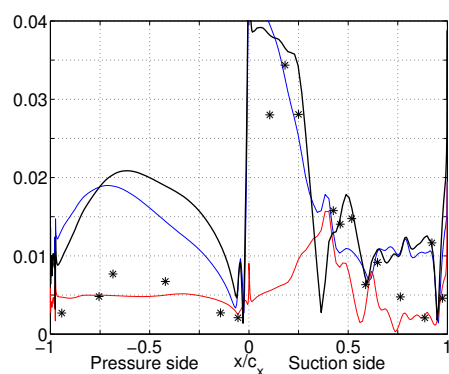


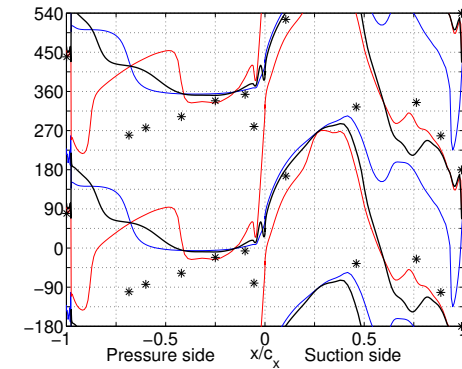
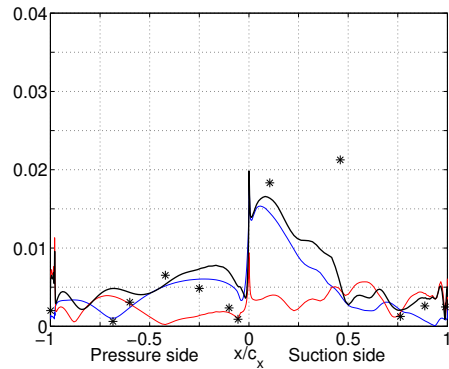
Figure 5.15: Vortical and potential components of dimensionless absolute velocity variation at RT27a NGV outlet (reconstructed using first twenty harmonics)



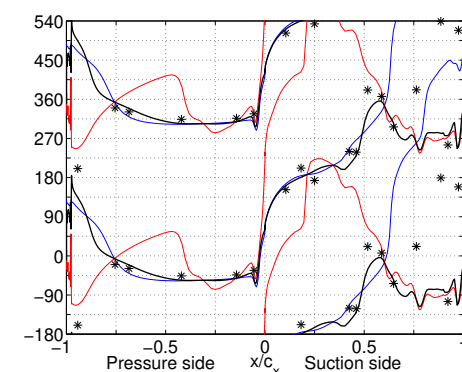
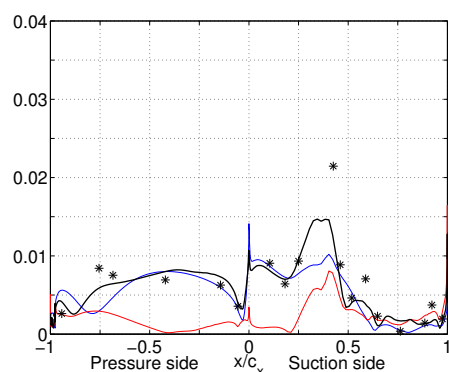
(a) Mid-root section (10% span)



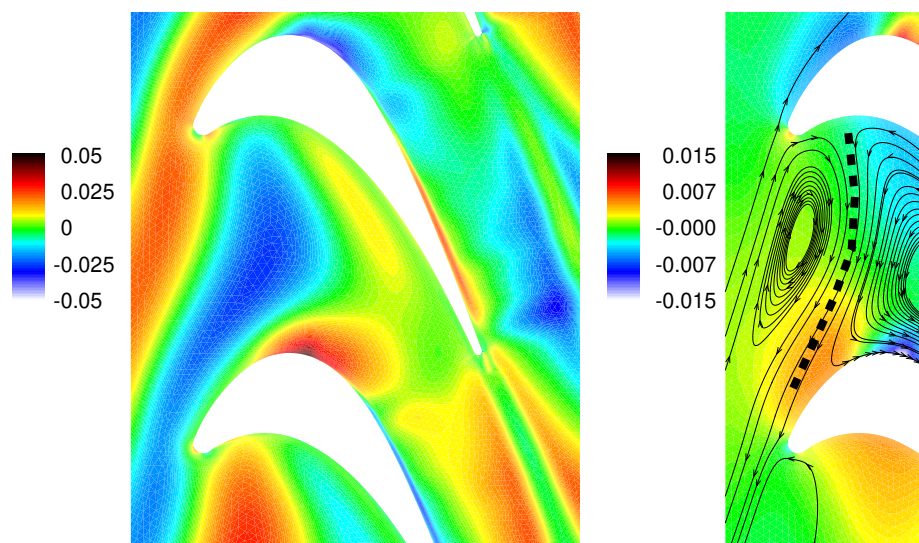
(b) Mid-height section (50% span)

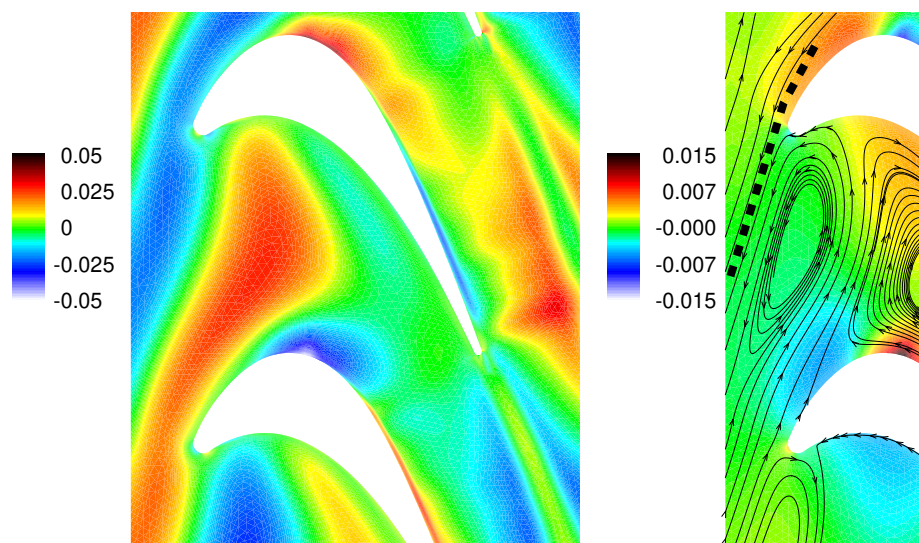


(a) Mid-root section (10% span)



(b) Mid-height section (50% span)

(a)  $t = 0$

(a)  $t = 3/6$

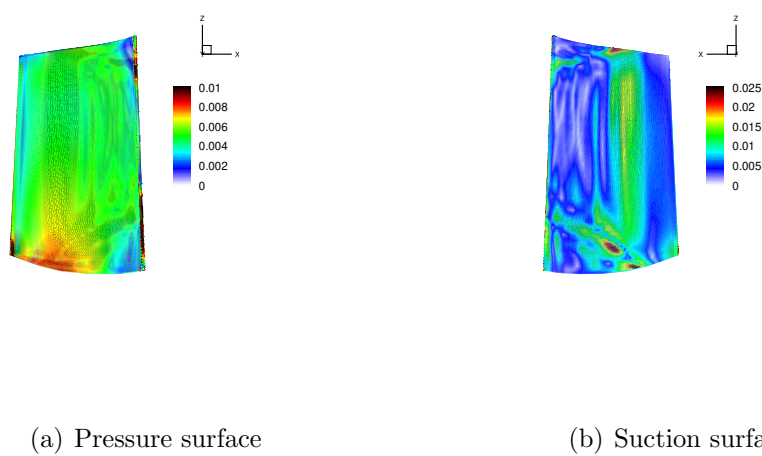


Figure 5.20: Unsteady pressure on RT27a rotor blade due to Wake-rotor interaction  
(first Fourier component)

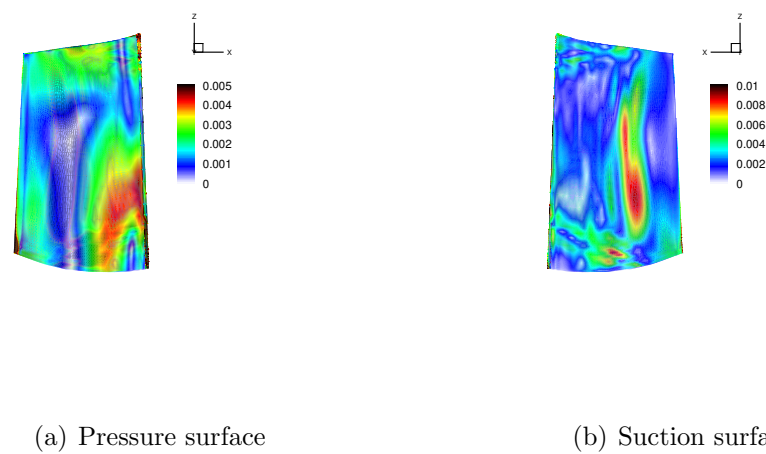


Figure 5.21: Unsteady pressure on RT27a rotor blade due to Wake-rotor interaction  
(second Fourier component)

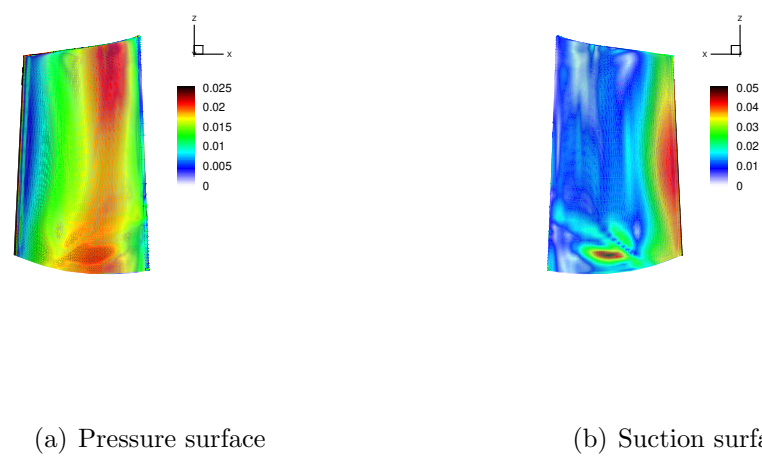


Figure 5.22: Unsteady pressure on RT27a rotor blade due to potential flow interaction (first Fourier component)

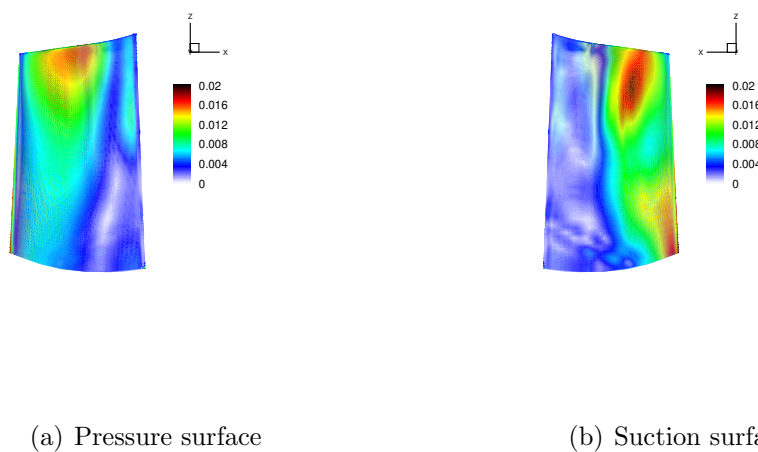


Figure 5.23: Unsteady pressure on RT27a rotor blade due to potential flow interaction (second Fourier component)

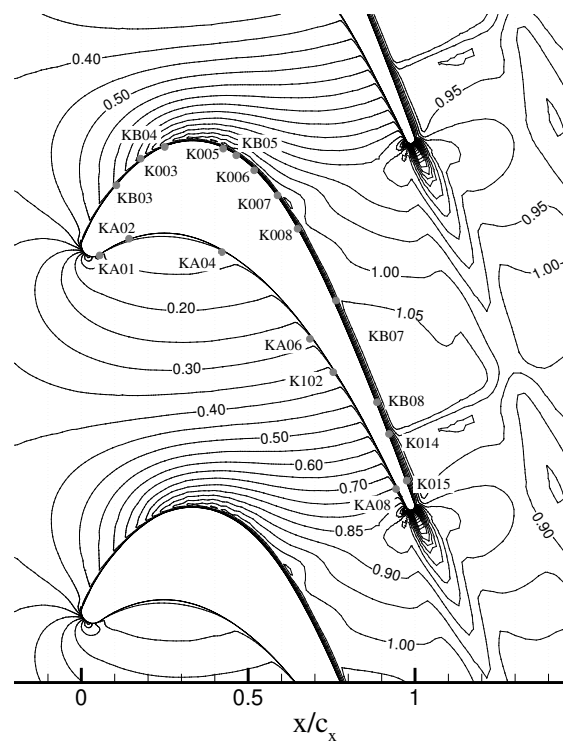


Figure 5.24: Steady-state Mach number contours on RT27a rotor mid-section and Kulite sensor position

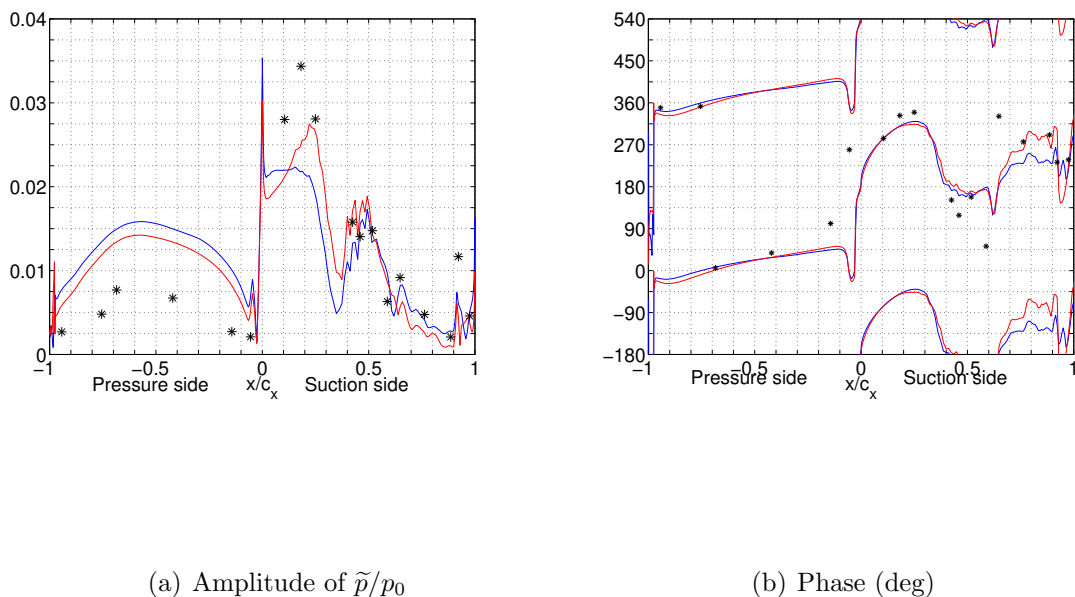


Figure 5.25: RT27a rotor blade mid-section. First Fourier component of dimensionless unsteady pressure. Linear method (blue), non-linear method (red) and measured data (stars).

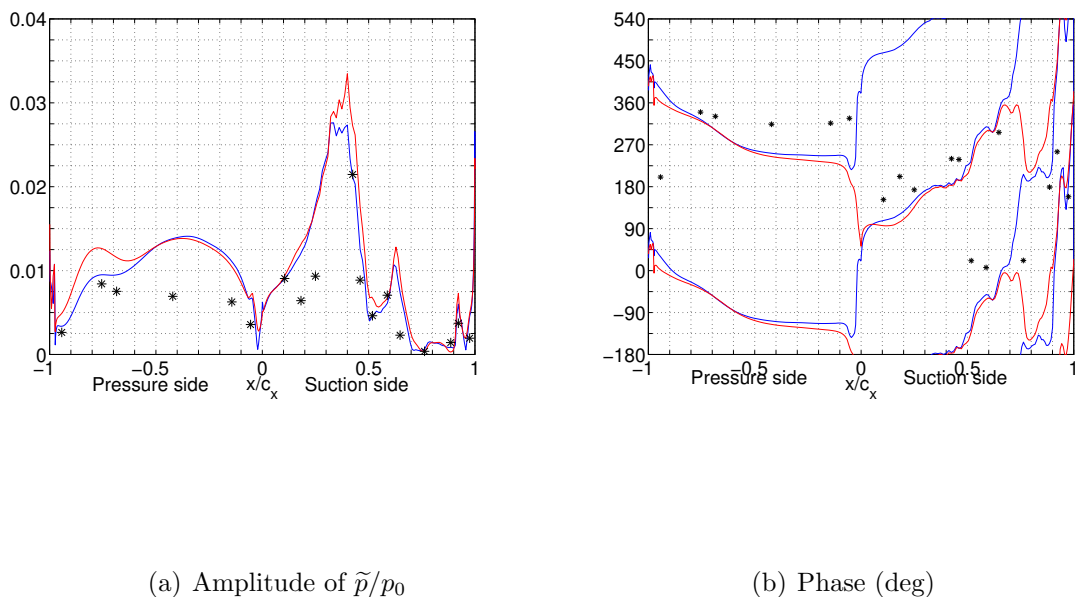


Figure 5.26: RT27a rotor blade mid-section. Second Fourier component of dimensionless unsteady pressure. Linear method (blue), non-linear method (red) and measured data (stars).

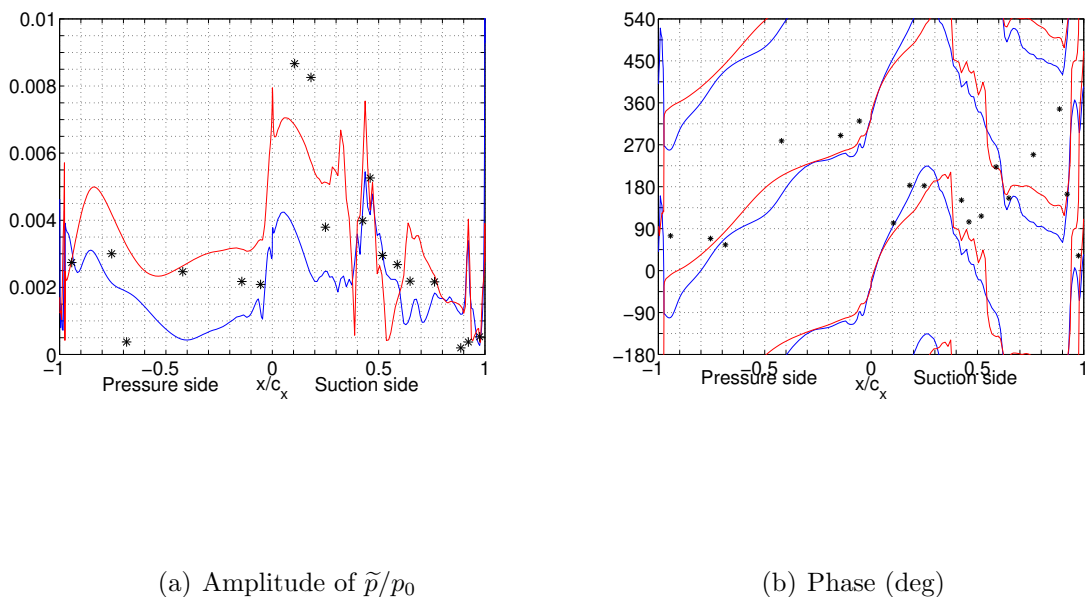
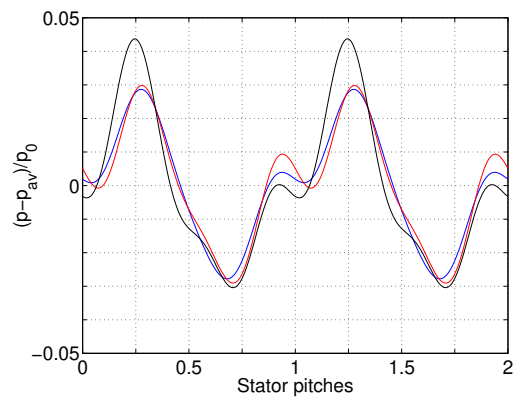
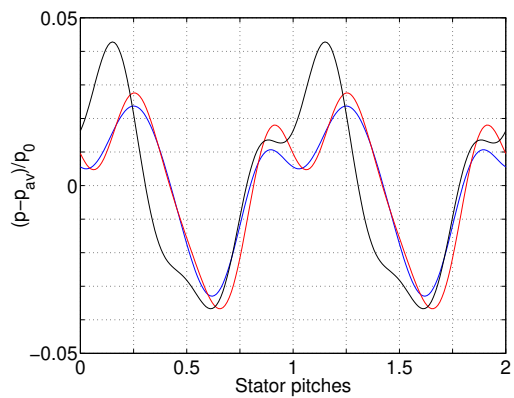
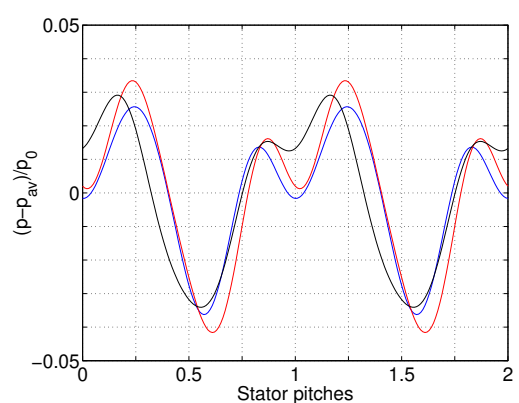
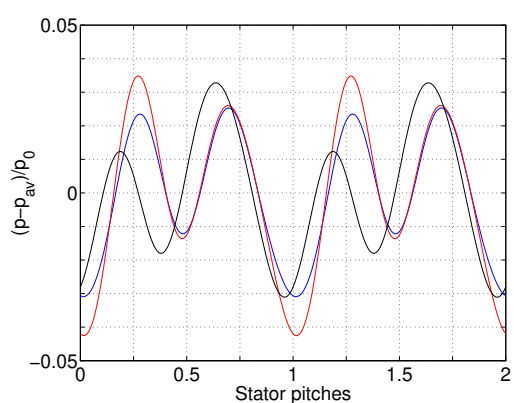
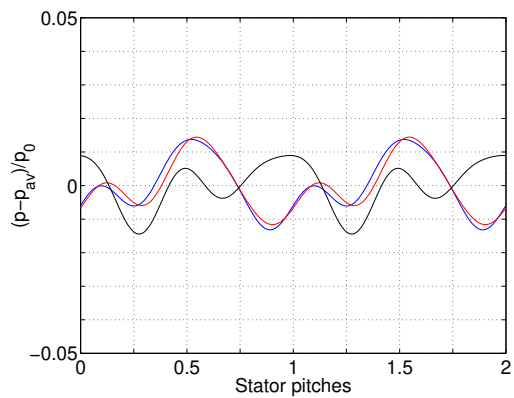
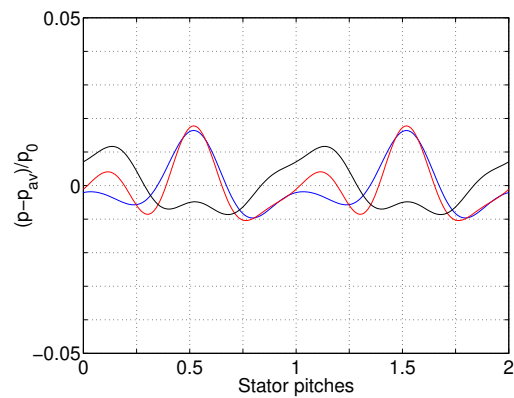
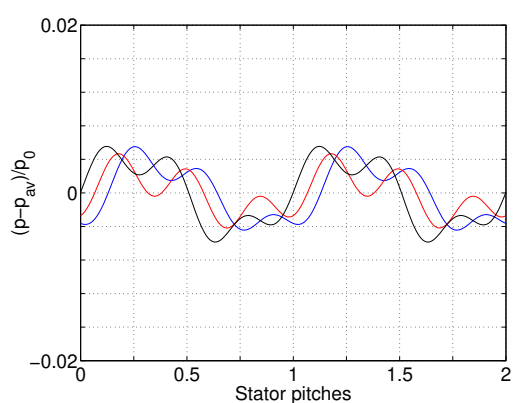
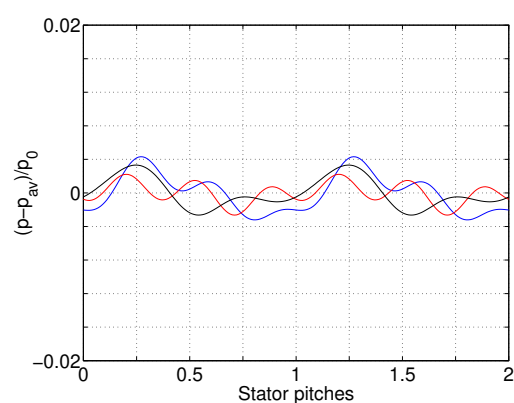
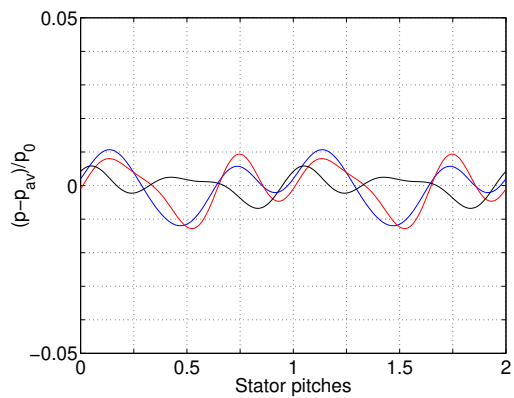
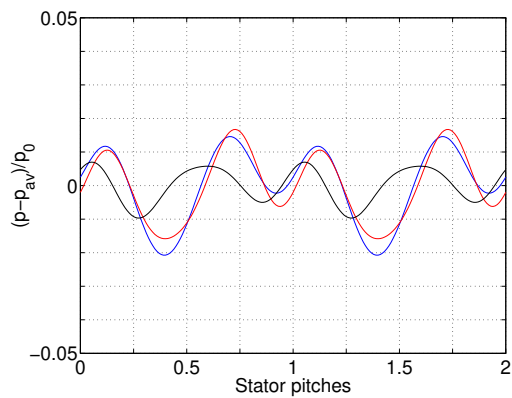
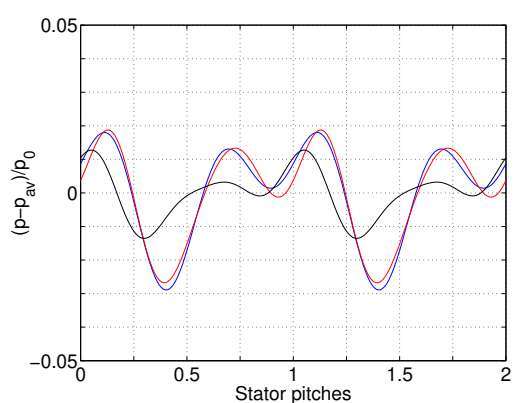
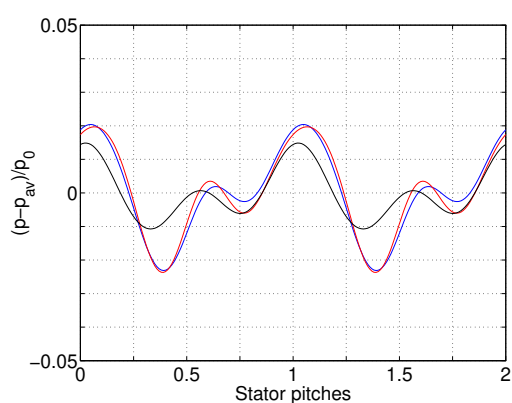


Figure 5.27: RT27a rotor blade mid-section. Third Fourier component of dimensionless unsteady pressure. Linear method (blue), non-linear method (red) and measured data (stars).

(a) KB03:  $x/c = 0.105$  suction side(b) K003:  $x/c = 0.182$  suction side(c) KB04:  $x/c = 0.250$  suction side(d) K005:  $x/c = 0.425$  suction side

(a) K007:  $x/c = 0.588$  suction side(b) K008:  $x/c = 0.648$  suction side(c) KB07:  $x/c = 0.763$  suction side(d) KB08:  $x/c = 0.886$  suction side

(a) KA01:  $x/c = 0.055$  pressure side(b) KA02:  $x/c = 0.143$  pressure side(c) KA04:  $x/c = 0.421$  pressure side(d) KA06:  $x/c = 0.685$  pressure side

# Chapter 6

## Conclusions and Recommendations for Further Work

A unified flow solver for the solution of the steady-state, non-linear time-marching and linearised unsteady Favre averaged Navier-Stokes equations on 2D and 3D turbomachinery passages has been presented, analysed and implemented. The spatial discretisation has been obtained using a finite volume scheme on mixed element meshes, consisting of triangles and quadrilaterals in 2D, and of tetrahedra, pyramids, triangular prisms and hexahedra in 3D. The resulting finite volume method is a node centered edge-based algorithm which is applied in a uniform way to all element types. An important feature of the method is the derivation of an edge-based coefficient for the discretisation of the Laplacian operator, which results in a nearest neighbour stencils. The time relaxation for both the steady state and the linearised unsteady version of the code has been obtained using the same preconditioned Runge Kutta time stepping algorithm. This multistage time-integration technique has been used as the smoother for a full approximation storage agglomeration multigrid method. For non-linear unsteady aerodynamics a dual time stepping technique has been implemented. The scheme is fully implicit and uses the same preconditioned multigrid algorithm developed for steady-state predictions, in order to iteratively invert the equations at each physical time step. The numerical procedure has been tested and compared with available analytical and experimental data in order to assess the validity, the accuracy and the efficiency of the method. The three different numerical flow representations have been used for a detailed computational analysis of a stator-rotor interaction in a typical high pressure turbine stage. Steady state and unsteady results have been compared with the ex-

perimental data obtained at Osney Laboratory. Also comparison between linear and non-linear unsteady results has been reported in order to assess the range of applicability of the linear method.

### Highlights of the numerical procedure

- (i) The semi-structured mesh generator presented in Chapter 2 combines together the advantages of both structured and unstructured grids. Particular feature of the blade passage, such as leading- and trailing-edges, wake region are discretized without generating superfluous points. Moreover complex geometric feature such as tip-gap are handled in a straightforward way.
- (ii) The use of hybrid grids improves standard unstructured schemes in terms of accuracy, speed and storage. Accuracy is improved by using quadrilateral/hexahedral elements in regions where highly stretched cells are necessary to resolve steep directional gradients (i.e. boundary layer regions). In these regions, standard triangular/tetrahedral elements would produce angles which are virtually zero. In such situations a finite-volume discretisation may suffer an accuracy degradation due to the irregular shape of the resulting median-dual control volume. Another advantage of hybrid grids, over standard unstructured grids, is a decreased cost of the discretisation itself. For a given distribution of vertices, a tetrahedral mesh discretisation is roughly twice as expensive to evaluate as a hexahedral mesh discretisation. A decreased number of edges in the mesh is the reason for this difference.
- (iii) A further advantage of the hybrid grid solver presented is its flexibility in handling structured grids, block structured grids, unstructured grids or combination of thereof without any modifications.
- (iv) The viscous fluxes are split into two components: Laplacian terms and mixed derivative terms. The former terms contain Laplacian operators only and they are discretized using a side-data Laplacian weight which results in a nearest neighbour stencils. The mixed derivative terms are evaluated from the gradient informations and thus their discretisation does not result in a compact stencil. The compact stencil of the Laplacian terms is of paramount importance in the boundary layer region, avoiding even-odd decoupling and allowing a stronger diagonal dominance

in the preconditioner matrix employed in the relaxation algorithm.

- (v) The time relaxation algorithm uses an agglomeration multigrid method. The coarse grid levels are constructed automatically from the fine grid by agglomerating fine grid control volumes together. Since the coarse grid control volumes may have arbitrary polygonal shapes, the type of elements constituting the fine grid is irrelevant. In this way the discrete equations on coarse grid levels are assembled automatically without the explicit creation of a coarse grid.
- (vi) The multigrid smoother consists of a preconditioned point- or line-Jacobi Runge Kutta relaxation algorithm, which guarantees efficient damping of high frequency error modes on highly stretched grids. The line-Jacobi preconditioner is used for viscous flow calculation which use a no-slip conditions at solid walls. The point-Jacobi preconditioner is used for calculation which use a flow-tangency condition at solid walls.

### **Importance of linearised unsteady viscous representations**

- (i) A linearised unsteady Navier-Stokes representations offers the possibility of predicting unsteady flows at off-design conditions where viscous effects are not limited to the boundary layer.
- (ii) Steady-state viscous effects are often important even at design conditions. In fact, Navier-Stokes simulations are used in order to predict secondary flow effects, correct mass flow in compressor passages where the adverse pressure gradient cause a thicker boundary layer, tip-leakage flow, losses caused by the trailing-edge base flow in turbine blades, etc. Using a linearised unsteady Navier-Stokes representations means that the same computational mesh can be used for both calculating the steady base flow and the unsteady perturbations. Interpolation of the steady-state unknown from viscous grids into inviscid ones are avoided and no additional numerical smoothing is needed.
- (iii) The linearisation of the turbulence model may play an important role in situation were viscous effect are not confined to the boundary layer region. When there are not such effects, the frozen turbulence approach should produce very similar

results.

(iv) When a steady viscous flow calculation, which uses the law of the wall in order to compute the wall shear stresses, is performed, the issue a linearisation of the wall function arises. Such a linearisation has been attempted during the research project. However, the results obtained using a linearised wall function and the ones obtained neglecting unsteady wall shear stresses were similar. Moreover the linearisation of the wall function required the use of the linearised turbulence mode since wall shear stresses and eddy viscosity are related in the Spalart Allmaras model. For this reason the unsteady wall shear stresses were neglected with no need of a linearised law of the wall.

### Applicability of linear methods for forced response prediction

To establish boundaries, which effectively define when linear methods should produce accurate results, is not a simple task. This is mainly due to the large number of parameters which influence the unsteady flows caused by relative blade motion. Comparisons between linear and non-linear results should be made for all type of flow regimes as well as different size of stator-rotor axial spacing and different stator-to-rotor pitch ratios. Also, 3D effects need to be explored in more details. From the results obtained in Chapter 5, the following conclusion are drawn.

- (ii) The wake-rotor interaction is strong in the crown of the blade. In this region, the computed results show that non-linearities are negligible.
- (i) High unsteady pressure fluctuations, mainly caused by the upstream potential flow field, are located at the leading-edge of the blade. In this region non-linearities may play an important role even though the linearised results follow a correct trend. Furthermore, such discrepancies are more evident for the blade passing frequency then higher mode number. For this reason, the linear method should still produce meaningful results for interactions in where shock waves are moving in the region between the stator and rotor bladerows<sup>1</sup>.

---

<sup>1</sup>The presence of shock waves increase the amplitude of Fourier modes with higher frequencies then the blade passing frequency.

- (iii) Localised non-linearities are located in region where the steady-state flow differs from the time-average flow. This is often the case when non-linear features, such as shock waves, are present.
- (iv) High unsteady pressure fluctuations are placed across the suction side legs of the horseshoe vortex at both hub and tip end walls. These suction side legs, of the horseshoe vortex, travel from the end walls towards mid section because of the rotation of the passage vortecies thus unsteadiness present a pronounce 3D behaviour.

## Further Work

- (i) The preconditioned agglomeration multigrid needs to be improved in order to enhance both performance and robustness. A more accurate prolongation operator need to be developed. This task is non-trivial because of the absence of an underlying grid. The preconditioner may cause some instabilities at stagnation points, where large variations of the flow angle appear at significant velocity values. This loss of robustness can be attributed to a flow-angle sensitivity thus improvement in this direction should be made.
- (ii) Further testing of the linearised unsteady method needs to be undertaken for real 3D geometries. In addition the inclusion of the quadratic source terms (QST) (Giles 1992) in the linearised frequency-domain equations should be implemented. The magnitude of such terms is a quadratic function of the level of unsteadiness. In this way after a first linearised calculation, the unsteadiness are used to evaluate the QST which are then used as source terms for a second linearised analysis. Such method should take into account for the differences between the steady-state flow and the time-average flow.

# Bibliography

- Abarbanel, S., Gottlieb, D. and Hesthaven, J.S. (1999). Well-posed Perfectly Matched Layer for Advective Acoustics. *Journal of Computational Physics* 154, 266–283.
- Adamczyk, J.J., Stevans, W. and Jutras, R. (1982). Supersonic Stall Flutter of High-Speed Fans. *Journal of Engineering for Power* 104(3), 675–682.
- Aftosmis, M., Gaitonde, D. and Tavares, T.S. (1994). On the Accuracy, Stability and Monotonicity of Various Reconstruction Algorithms for Unstructured Meshes. AIAA Paper 91-0610.
- Anderson, J.D.Jr. (1990). *Modern Compressible Flow*. McGraw-Hill Inc.
- Anderson, W.K. and Bonhaus, D.L. (1994). An Implicit Upwind Algorithm for Computing Turbulent Flows on Unstructured Grids. *Computers and Fluids* 23(1), 1–21.
- Arnone, A. (1995). Multigrid Methods for Turbomachinery Navier-Stokes Calculations. In *Solution techniques for large-scale CFD problems*, pp. 293–332. John Wiley & Sons.
- Arnone, A. and Swanson, R.C. (1993). A Navier-Stokes Solver for Turbomachinery Applications. *Journal of Turbomachinery* 115, 305–313.
- Atassi, H.M. and Golubev, V.V. (1997). Unsteady Disturbances in Swirling Turbomachinery Flows. In *8th International Symposium on Unsteady Aerodynamics and Aeroelasticity of Turbomachines (ISUAAT)*, Stockholm, pp. 131–146.
- Baker, T.J. (1990). Unstructured Mesh Generation by a Generalized Delaunay Algorithm. Technical Report 464, AGARD.
- Barth, T.J. (1990). On unstructured grid solvers. Technical Report Lecture series VKI-LS 1990-03, Von Karman Institute of Fluid Dynamics.

- Barth, T.J. (1991). Numerical Aspects of Computing High Reynolds Number Flows on Unstructured Meshes. AIAA Paper 91-0721.
- Barth, T.J. (1993). Recent Developments in High Order k-Exact Reconstruction on Unstructured Meshes. AIAA Paper 93-0668.
- Barth, T.J. and Jespersen, D.C. (1989). The design and Applications of Upwind Schemes on Unstructured Meshes. AIAA Paper 89-0366.
- Beam, R.M. and Warming, R.F. (1976). An Implicit-Difference Algorithm for Hyperbolic System in Conservation Law Form. *Journal of Computational Physics* 22, 87–109.
- Bendiksen, O.O. (1991). A New Approach to Computational Aeroelasticity. AIAA Paper 91-0939.
- Brackbill, J.U., and Saltzman, J.S. (1982). Adaptative Zoning for Singular Problems in two Dimensions. *Journal of Computational Physics* 46, 442–368.
- Brenneis, A. and Eberle, A. (1990). Application of an Implicit Relaxation Method Solving the Euler Equations for Time-Accurate Unsteady Problems. *Journal of Fluids Engineering* 112, 510–520.
- Cebeci, T. (1977). Calculation of Unsteady Two-Dimensional Laminar and Turbulent Boundary Layers with Fluctuations in External Velocity. *Royal Society (London) A* 355, 225–238.
- Choi, Y.H. and Merkle, C.L. (1993). The Application of Preconditioning in Viscous Flows. *Journal of Computational Physics* 105, 207–223.
- Cicarelli, G. and Sieverding, C.H. (1996). The Effects of Vortex Shedding on the Unsteady Pressure Distribution around the Trailing Edge of a Turbine Cascade. ASME Paper 96-GT-356.
- Cizmas, P.G.A. and Hall, K.C. (1995). A Viscous-Inviscid Model of Unsteady Small-Disturbance Flows in Cascades. AIAA Paper 95-2655.
- Clark, W.S. and Hall, K.C. (1999). A Time-Linearized Navier-Stokes Analysis of Stall Flutter. ASME Paper 99-GT-383.
- Collar, A.R. (1946). The Expanding Domain of Aeroelasticity. *Journal of Royal Aeronautical Society* 51, 613–636.
- Cumpsty, N.A. (1989). *Compressor Aerodynamics*. Longman Scientific & Technical.

- Dawes, W.N. (1988). Development of a Three-dimensional Navier-Stokes Solver for Application to all Types of Turbomachinery. ASME paper 88-GT-70.
- Dawes, W.N. (1990). Towards Improved Throughflow Capability: The Use of 3D Viscous Flow Solvers in a Multistage environment. ASME paper 90-GT-18.
- Dawes, W.N. (1992). The Extension of a Solution-Adaptative 3D Navier-Stokes Solver towards Geometries of Arbitrary Complexity. ASME paper 92-GT-363.
- Dawes, W.N. (1993). Simulating Unsteady Turbomachinery Flows on Unstructured Meshes which Adapt both in Time and Space. ASME paper 93-GT-104.
- Denton, J.D. (1983). An Improved Time Marching Method for Turbomachinery Flow Calculation. *Journal of Engineering for Power* 105, 514–524.
- Denton, J.D. (1990). The Calculation of Three Dimensional Viscous Flow through Multistage Turbomachines. ASME paper 90-GT-19.
- Denton, J.D. (1993). Loss Mechanism in Turbomachines. *Journal of Turbomachinery* 115, 621–656.
- Donea, J., Giuliani, S. and Halleux, J.P. (1982). An Arbitrary Lagrangian-Eulerian Finite Element Method for Transient Dynamic Fluid-Structure Interactions. *Computer Methods in Applied Mechanics and Engineering* 33, 689–723.
- Dowell, E.H., Curtiss, H.C.Jr., Scanlan, R.H. and Sisto, F. (1989). *A Modern Course in Aeroelasticity* (Second ed.). Kluwer Academic Publishers.
- Emmons, H.W., Pearson, C.E. and Grant, H.P. (1955). Compressor Surge and Stall Propagation. *ASME Transaction* 27, 455–469.
- Enfeldt, B. (1988). On Godunov-Type Methods for Gas Dynamics. *SIAM Journal of Numerical Analysis* 25, 294–318.
- Enfeldt, B. (1991). On Godunov-Type Methods Near Low Densities. *Journal of Computational Physics* 92, 273–295.
- Engquist, B. and Gustafsson, B. (1987). Steady State Computations for Wave Propagation Problems. *Mathematics of Computation* 49, 39–64.
- Engquist, B. and Majda, A. (1977). Absorbing Boundary Conditions for the Numerical Simulation of Waves. *Mathematics of Computation* 31, 629–651.

- Erdos, J.I., Alzner, E. and McNally, W. (1977). Numerical Solution of Periodic Transonic Flow through a Fan Stage. *AIAA Journal* 15, 1559–1568.
- Essers, J.A., Delanaye, M. and Rogiest, P. (1995). Upwind-Biased Finite-Volume Technique Solving Navier-Stokes Equations on Irregular Meshes. *AIAA Journal* 33(5), 833–842.
- Ewins, D.J. (1974). Vibration Modes of Mistuned Bladed Disks. *Journal of Engineering for Power* 98(3), 349–354.
- Feiereisen, J.M., Montgomery, M.D. and Fleeter, S. (1994). Unsteady Aerodynamic Forcing Functions: A Comparison Between Linear Theory and Experiment. *Journal of Turbomachinery* 116, 676–685.
- Ferm, L. (1995). Non-Reflecting Boundary Conditions for the Steady Euler Equations. *Journal of Computational Physics* 122, 307–316.
- Fleeter, S. (1979). Aeroelasticity Research for Turbomachinery Applications. *Journal of Aircraft* 16(5), 320–326.
- Fransson, T.H., Jöcker, M., Bölcş, A. and Ott, P. (1998). Viscous and Inviscid Linear/Nonlinear Calculations versus quasi 3D Experimental Cascade Data for a new Aeroelastic Turbine Standard Configuration. ASME Paper 98-GT-490.
- Frink, N.T. (1992). Upwind Scheme for Solving the Euler Equations on Unstructured Tetrahedral Meshes. *AIAA Journal* 30, 70–77.
- Frink, N.T. (1996). Assessment of an Unstructured-Grid Method for Predicting 3-D Turbulent Viscous Flows. AIAA Paper 96-0292.
- Gerolymos, G.A. (1992). Coupled 3D Aeroelasticity Analysis of Bladed Disks. ASME Paper 92-GT-171.
- Giles, M.B. (1987). Calculation of Unsteady Wake/Rotor Interaction. AIAA Paper 87-0006.
- Giles, M.B. (1988). Non-Reflecting Boundary Conditions for the Euler Equations. Technical Report TR-88-1, MIT, Computational fluid Dynamics Lab.
- Giles, M.B. (1990a). Non-Reflecting Boundary Conditions for the Euler Equations Calculations. *AIAA Journal* 28(12), 2050–2058.
- Giles, M.B. (1990b). Stator/Rotor Interaction in a Transonic Turbine. *AIAA Journal of Propulsion and Power* 6(5), 621–627.

- Giles, M.B. (1991). UNSFLO: A numerical method for the calculation of unsteady flow in Turbomachinery. Technical Report 205, MIT, Gas Turbine Laboratory.
- Giles, M.B. (1992). An Approach for Multi-Stage Calculations Incorporating Unsteadiness. ASME Paper 92-GT-282.
- Givoli, D. (1991). Non-reflecting Boundary Conditions. *Journal of Computational Physics* 94, 1–29.
- Godunov, S.K. (1959). A Difference Method for the Numerical Calculation of Discontinuous Solutions of the Hydrodynamic Equations. *Matematicheskii Sbornik* 47, 271–290.
- Goldstein, M.E. (1978). Unsteady Vortical and Entropic Distortions of Potential Flows Round Arbitrary Obstacles. *Journal of Fluid Mechanics* 89, 433–468.
- Golub, G.H. and Van Loan, C.F. (1991). *Matrix Computations*. The Johns Hopkins University Press.
- Gregory-Smith, D.G. (1997). Physics of Secondary Flows. In *Secondary and Tip-clearance Flows in Axial Turbines*, Lecture Series VKI LS 1997-01.
- Greitzer, E.M. (1976a). Surge and Rotating Stall in Axial Flow Compressor, Part I: Theoretical Compression System Model. *Journal of Engineering for Power* 98, 190–198.
- Greitzer, E.M. (1976b). Surge and Rotating Stall in Axial Flow Compressor, Part II: Experimental Results and Comparison with Theory. *Journal of Engineering for Power* 98, 199–217.
- Grosclaude, T., Bréard, C. and Sayma, A.I. (1999). Extension of the LEVMAP Mesh Generator to Radial-Flow Blades. Technical Report VUTC/AP/99005, Imperial College, London.
- Gustafsson, B. (1988). Far-Field Boundary Conditions For Time-Dependent Hyperbolic Systems. *SIAM Journal on Scientific and Statistical Computing* 9(5), 812–828.
- Hall, K.C. and Clark, W.S. (1991). Prediction of Unsteady Aerodynamic Loads in Cascades Using the Linearized Euler Equations on Deforming Grids. AIAA Paper 91-3378.

- Hall, K.C. and Clark, W.S. (1993). Linearized Euler Predictions of Unsteady Aerodynamic Loads in Cascades. *AIAA Journal* 31(3), 540–550.
- Hall, K.C. and Crawley, E.F. (1989). Calculation of Unsteady Flows in Turbomachinery Using the Linearized Euler Equations. *AIAA Journal* 27, 777–787.
- Hall, K.C. and Lorence, C.B. (1993). Calculation of Three-Dimensional Unsteady Flows in Turbomachinery Using the Linearized Harmonic Euler Equations. *Journal of Turbomachinery* 115, 800–809.
- Hall, K.C., Clark, W.S. and Lorence C.B. (1994). A Linearized Euler Analysis of Unsteady Transonic Flows in Turbomachinery. *Journal of Turbomachinery* 116, 477–488.
- Hall, K.C., Lorence, C.B. and Clark, W.S. (1993). Nonreflecting Boundary Conditions for Linearized Unsteady Aerodynamic Calculations. AIAA Paper 93-0882.
- Harten, A. (1983a). High Resolution Schemes for Hyperbolic conservation Laws. *Journal of Computational Physics* 49, 357–393.
- Harten, A. (1983b). On Upstream Differencing and Godunov-Type Schemes for Hyperbolic Conservation Laws. *SIAM Review* 25, 35–61.
- He, L. (1990). An Euler solution for unsteady flows around oscillating blades. *Journal of Turbomachinery* 112, 714–722.
- He, L. and Denton, J.D. (1991a). Inviscid-Viscous Coupled Solution for Unsteady Flows through Vibrating Blades: Parts 1. ASME Paper 91-GT-125.
- He, L. and Denton, J.D. (1991b). Inviscid-Viscous Coupled Solution for Unsteady Flows through Vibrating Blades: Parts 2. ASME Paper 91-GT-126.
- Hedstrom, G.W. (1979). Nonreflecting Boundary Conditions for Nonlinear Hyperbolic Systems. *Journal of Computational Physics* 30, 222–237.
- Hesthaven, J.S. (1998). On the Analysis and Construction of Perfectly Matched Layers for the Linearized Euler Equations. *Journal of Computational Physics* 142, 129–147.
- Higdon, R.L. (1986a). Absorbing Boundary Conditions for Difference Approximations to the Multi-Dimensional Wave Equations. *Mathematics of Computation* 47(176), 437–459.

- Higdon, R.L. (1986b). Initial-Boundary Value Problems for Linear Hyperbolic Systems. *SIAM Review* 28(2), 177–217.
- Higdon, R.L. (1987). Numerical Absorbing Boundary Conditions for the Wave Equations. *Mathematics of Computation* 49(179), 65–90.
- Hirsch, C. (1990). *Numerical Computation of Internal and External Flows*, Volume 1-2. John Wiley & Sons.
- Hixon, R., Shih, S.H. and Mankbadi, R.R. (1995). Evaluation of Boundary Conditions for Computational Aeroacoustics. *AIAA Journal* 33(11), 201–219.
- Hodson, H.P. (1985). An Inviscid Blade-to-Blade Prediction of a Wake-Generated Unsteady Flow. *Journal of Engineering for Gas Turbine and Power* 107, 337–343.
- Holmes, D.G., Mitchell, B.E. and Lorence C.B. (1997). Three Dimensional Linearized Navier-Stokes Calculations for Flutter and Forced Response. In *8th International Symposium on Unsteady Aerodynamics and Aeroelasticity of Turbomachines (ISUAAT)*, Stockholm, pp. 211–224.
- Hu, F.Q. (1996). On Absorbing Boundary Conditions for Linearized Euler Equations by a Perfectly Matched Layer. *Journal of Computational Physics* 129, 201–219.
- Jameson, A. (1985). Multigrid Algorithms for Compressible Flow Calculations. Technical Report MAE 1743.
- Jameson, A., (1991). Time Dependent Calculations Using Multigrid, with Applications to Unsteady Flows Past Airfoils and Wings. AIAA Paper 91-1596.
- Jameson, A. (1993). Artificial Diffusion, Upwind Biasing, Limiters and their Effect on Accuracy and Multigrid Convergence in Transonic and Hypersonic Flows. AIAA Paper 93-3359.
- Jameson, A. (1995). Positive Schemes and Shock Modelling for Compressible Flows. *International Journal for Numerical Methods in Fluids* 20, 743–776.
- Jameson, A., Schmidt, W. and Turkel, E. (1981). Numerical Simulation of the Euler Equations by Finite Volume Methods using Runge-Kutta Time Stepping Schemes. AIAA Paper 81-1259.
- Jay, R.L. and Fleeter, S. (1987). Unsteady Aerodynamics Measurements in Forced Vibration Research. In *AGARD Manual on Aeroelasticity in Axial-*

- Flow Turbomachines, Unsteady Turbomachinery Aerodynamics*, Volume 1, pp. 9.1 – 1.38. AGARD-AG-297.
- Jorgenson, P.C. and Turkel, E. (1993). Central Difference TVD Schemes for Time Dependent and Steady State Problems. *Journal of Computational Physics* 107, 297–308.
- Jorgenson, P.C.E. and Chima, R.V. (1989). Explicit Runge-Kutta Method for Unsteady Rotor/Stator Interaction. *AIAA Journal* 27, 743–749.
- Kallinderis, Y. and Ward, S. (1992). Prismatic Grid Generation with an Efficient Algebraic Method for Aircraft Configurations. AIAA Paper 92-2721.
- Kerrebrock, J.L. (1977). Small Disturbances in Turbomachine Annuli with Swirl. *AIAA Journal* 15, 794–803.
- Kiock, R., Lehthaus, F., Baines, N.C. and Sieverding, C.H. (1986). The Transonic Flow through a Plane Turbine Cascade as Measured in Four European Wind Tunnels. *Journal of Engineering for Gas Turbines and Power* 108, 277–285.
- Korakianitis, T. (1992a). On the Prediction of Unsteady Forces on Gas Turbine Blades: Part 1 - Description of the Approach. *Journal of Turbomachinery* 114, 114–122.
- Korakianitis, T. (1992b). On the Prediction of Unsteady Forces on Gas Turbine Blades: Part 2 - Analysis of the Results. *Journal of Turbomachinery* 114, 123–131.
- Korakianitis, T. (1993). On the Propagation of Viscous Wakes and Potential Flow in Axial-Turbine Cascades. *Journal of Turbomachinery* 115, 118–127.
- Lane, F. (1956). System Mode Shapes in the Flutter of Compressor Blade Rows. *Journal of the Aeronautical Science* 23(1), 54–66.
- Lax, P. (1973). *Hyperbolic Systems of Conservation Laws and the Mathematical Theory of Shock Waves*, Volume 11. SIAM Regional Series and Applied Mathematics.
- Leveque, R. (1985). A Large Time Step Generalization of Godunov's Method for Systems of Conservation Laws. *SIAM Journal of Numerical Analysis* 22, 1051–1073.

- Lighthill, M.J. (1954). The Response of Laminar Skin Friction and Heat Transfer to Fluctuations in the Stream Velocity. *Royal Society (London) A 224*, 1–23.
- Lindquist, D.R. and Giles, M.B. (1991). On the Validity of Linearized Unsteady Euler Equations with Shock Capturing. AIAA Paper 91-1598-CP.
- Liou, M. (1996). A Sequel to AUSM: AUSM+. *Journal of Computational Physics 129*, 364–382.
- Liou, M. and Steffen, C. (1993). A New Flux Splitting Scheme. *Journal of Computational Physics 107*, 23–39.
- Magagnato, F. (1999). Unsteady Flow Past a Turbine Blade Using Non-Linear Two-Equation turbulence models. In *IMECHE Conference Transactions. Turbomachinery: Fluid Dynamics and Thermodynamics*, Volume Volume A, pp. 221–230.
- Manwaring, S.R. and Kirkeng, K.L. (1997). Forced Response Vibrations of a Low Pressure Turbine due to Circumferential Temperature Distortions. In *8th International Symposium on Unsteady Aerodynamics and Aeroelasticity of Turbomachines (ISUAAT)*, Stockholm, pp. 379–392.
- Manwaring, S.R. and Wisler, D.C. (1993). Unsteady Aerodynamic and Gust Response in Compressor and Turbines. *Journal of Turbomachinery 115*, 724–740.
- Marshall, J.G. and Giles, M.B. (1997). Some Applications of a Time-Linearized Euler Method to Flutter and Forced Response in Turbomachinery. In *8th International Symposium on Unsteady Aerodynamics and Aeroelasticity of Turbomachines (ISUAAT)*, Stockholm, pp. 225–240.
- Marshall, J.G. and Imregun, M. (1996). A Review of Aeroelasticity Methods with Emphasis on Turbomachinery Applications. *Journal of Fluids and Structures 10*, 237–267.
- Mattioli, E. (1989). *Aerodinamica*. Levrotto & Bella, Torino.
- Mavriplis, D.J. (1995a). Three-Dimensional Multigrid Reynolds-Averaged Navier-Stokes Solver for Unstructured Meshes. *AIAA Journal 3*, 445–453.
- Mavriplis, D.J. (1995b). Unstructured Mesh Generation and Adaptivity. Technical Report 95-26, ICASE.

- Mavriplis, D.J. (1998a). Directional Agglomeration Multigrid Techniques for High-Reynolds Number Viscous Flows. Technical Report 98-7, ICASE.
- Mavriplis, D.J. (1998b). Multigrid Strategies for Viscous Flow Solvers on Anisotropic Meshes. Technical Report 98-6, ICASE.
- Mavriplis, D.J. (1998c). On Convergence Acceleration Techniques for Unstructured Meshes. Technical Report 98-44, ICASE.
- Mavriplis, D.J., and Martinelli, L. (1994). Multigrid Solution of Compressible Turbulent Flow on Unstructured Meshes Using a Two-Equation Model. *International Journal for Numerical Method in Fluids* 18, 887–914.
- Mavriplis, D.J. and Venkatakrishnan, V. (1995a). A Unified Multigrid Solver for the Navier-Stokes Equation on Mixed Element Meshes. Technical Report 95-53, ICASE.
- Mavriplis, D.J. and Venkatakrishnan, V. (1995b). Agglomeration Multigrid for the Three-Dimensional Euler Equations. *AIAA Journal* 33(4), 633–640.
- McDevitt, J.B., Lionel, L.L.Jr. and Deiwert, G.S. (1976). Transonic Flow about Thick Circular-Arc Airfoil. *AIAA Journal* 13(5), 606–613.
- Melson, N.D., Sanetrik, M.D. and Atkins, H.L. (1993). Time-Accurate Navier-Stokes Calculations with Multigrid Acceleration. In *Proceedings of the Sixth Copper Mountain Conference on Multigrid Methods*, Copper Mountain, CO.
- Moinier, P., Müller J. and Giles, M.B. (1999). Edge-based Multigrid and Preconditioning for Hybrid Grids. AIAA Paper 99-3339.
- Montgomery, M.D. and Verdon, J.M. (1997a). A 3D Linearized Euler Analysis for Blade Rows. Part 1: Aerodynamic and Numerical Formulations. In *8th International Symposium on Unsteady Aerodynamics and Aeroelasticity of Turbomachines (ISUAAT)*, Stockholm, pp. 427–444.
- Montgomery, M.D. and Verdon, J.M. (1997b). A 3D Linearized Euler Analysis for Blade Rows. Part 2: Unsteady Aerodynamic Response. In *8th International Symposium on Unsteady Aerodynamics and Aeroelasticity of Turbomachines (ISUAAT)*, Stockholm, pp. 445–464.
- Morgan, K., Peraire, J. and Peiró, J. (1992). Unstructured Grid Methods for Compressible Flows. Technical Report 787, AGARD.

- Moss, R.W., Ainsworth, R.W., Sheldrake, C.D. and Miller, R. (1997). The Unsteady Pressure Field over a Turbine Blade Surface: Visualization and Interpretation of Experimental Data. ASME Paper 97-GT-474.
- Mulder, W.A. (1989). A new Multigrid Approach to Convection Problems. *Journal of Computational Physics* 83, 303–323.
- Mulder, W.A. (1992). A High Resolution Euler Solver Based on Multigrid Semi-coarsening and defect Correction. *Journal of Computational Physics* 100, 91–104.
- Ni, R.H. and Sisto F. (1975). Numerical Computation of Non-stationary Aerodynamics of Flat Plate Cascades in Compressible Flows. ASME Paper 75-GT-5.
- Osher, S. (1984). Riemann Solvers, the Entropy Conditions, and Difference Approximation. *SIAM Journal of Numerical Analysis* 21, 217–235.
- Osher, S. and Chakravarthy, S. (1984). High Resolution schemes and the Entropy Conditions. *SIAM Journal of Numerical Analysis* 21, 955–984.
- Pandolfi, M. (1984). A Contribution to the Numerical Prediction of Unsteady Flows. *AIAA Journal* 22, 602–610.
- Parthasarathy, V., Kallinderis, Y. and Nakajima, K. (1995). Hybrid Adaptation Method and Directional Viscous Multigrid with Prismatic-Tetrahedral Meshes. AIAA Paper 95-0670.
- Peraire, J., Morgan, K., Vahdati, M. and Peiró, J. (1992). The Construction and Behaviour of Some Unstructured Grid Algorithms for Compressible Flows. In *ICFD Conference on Numerical Methods for Fluid Dynamics*. Oxford University Press.
- Peraire, J., Peiró, J. and Morgan, K. (1992). A 3D Finite-Element Multigrid Solver for the Euler Equations. AIAA Paper 92-0449.
- Pierce, N.A. and Giles, M.B. (1997). Preconditioning Multigrid Methods for Compressible Flow Calculations on Stretched Meshes. *Journal of Computational Physics* 136, 425–445.
- Pierce, N.A., Giles, M.B., Jameson, A. and Martinelli, L. (1997). Accelerating Three-Dimensional Navier-Stokes Calculations. AIAA Paper 97-1850.
- Platzer, M.F. (1982). Transonic Blade Flutter: A Survey of New Developments. *Shock and Vibration Digest* 14(7), 3–8.

- Prendergast, K.H. and Xu, K. (1994). Numerical Navier-Stokes Solutions from Gas Kinetic Theory. *Journal of Computational Physics* 114, 9–17.
- Rai, M.M. (1987). Navier-Stokes Simulations of Rotor/Stator Interaction Using Patched and Overlaid Grids. *AIAA Journal of propulsion and power* 3(5), 387–396.
- Rai, M.M. and Madavan, N.K. (1990). Multi-Airfoil Navier-Stokes Simulations of Turbine Rotor-Stator Interaction. *Journal of Turbomachinery* 112, 377–384.
- Roe, P. (1981). Approximate Riemann solvers, parameter vectors and difference schemes. *Journal of Computational Physics* 43, 357–372.
- Roe, P. (1986). Characteristic-Based Schemes for the Euler Equations. *Annual Review of Fluid Mechanics* 18, 337–365.
- Saad, Y. and Schultz, M.H. (1986). GMRES: A Generalized Minimal Residual Algorithm for Solving Nonsymmetric Linear Systems. *SIAM Journal on Scientific and Statistical Computing* 7, 856–869.
- Saxer, A.P. and Felici, H.M. (1996). Numerical Analysis of Three-Dimensional Unsteady Hot Streak Migration and Shock Interaction in a Turbine Stage. *Journal of Turbomachinery* 118, 268–277.
- Saxer, A.P. and Giles, M.B. (1993). Quasi-Three-Dimensional Nonreflecting Boundary Conditions for Euler Equations Calculations. *AIAA Journal of Propulsion and Power* 9(2), 263–271.
- Sayma, A.I. (1998). Low Engine Order Excitation Mechanism in Turbine Blades - A Preliminary Study. Technical Report VUTC/C/97023, Imperial College, London.
- Sayma, A.I., Mehdi, V. and Imregun, M. (2000). Turbine Forced Response Prediction Using an Integrated Non-linear Analysis. *Proc Instn Mech Engrs* 214 (Part K), 45–60.
- Sayma, A.I., Vahdati, M. and Imregun, M. (1999). Fan Forced response Predictions Due to Inlet Distortions and Excitation from Inlet Guide Vanes at High Deflection. In *4th National Turbine Engine High Cycle Fatigue (HCF) Conference*.
- Sayma, A.I., Vahdati, M., Green J.S. and Imregun, M. (1997). Whole-Assembly Flutter Analysis of a Low Pressure Turbine Blade. In *8th International*

- Symposium on Unsteady Aerodynamics and Aeroelasticity of Turbomachines (ISUAAT)*, Stockholm, pp. 347–359.
- Sayma, A.I., Vahdati, M., Sbardella, L. and Imregun, M. (2000). Modelling of Three-dimensional Viscous Compressible Turbomachinery Flows using Unstructured Hybrid Grids. *AIAA Journal* 38(3), 569–584.
- Sbardella, L. (1997). CFD Analysis of Noise Propagation. Technical Report VUTC/C/97004, Imperial College, London.
- Sbardella, L. (1998). LEVMAP 2.0, a Mesh Generator for the CFD Modelling of Turbomachinery Blades: User Guide. Technical Report VUTC/C/97022, Imperial College, London.
- Sbardella, L. and Imregun, M. (1999). Turbulent Viscous Flow Simulations using Hybrid Grids. AIAA Paper 99-0781.
- Sbardella, L. and Imregun, M. (2000). An Efficient Discretisation of Viscous Fluxes on Unstructured Mixed-Element Grids. *Communications in Numerical Methods in Engineering*, To appear.
- Sbardella, L. and Peiró, J. (1997). Numerical Simulation of Stator-Rotor Interaction in a Transonic Turbine Stage. In *International Forum on Aeroelasticity and Structural Dynamics*, Rome.
- Sbardella, L., Sayma, A.I. and Imregun, M. (1997). Semi-Unstructured Mesh Generator for Flow Calculations in Axial Turbomachinery Blading. In *8th International Symposium on Unsteady Aerodynamics and Aeroelasticity of Turbomachines (ISUAAT)*, Stockholm, pp. 541–554.
- Sbardella, L., Sayma, A.I. and Imregun, M. (2000). Semi-structured Meshes for Axial Turbomachinery Blades. *International Journal for Numerical Methods in Fluids* 32, 569–584.
- Schlichting, H. (1979). *Boundary-Layer Theory*. McGraw-Hill, Inc.
- Selman, V. and Formaggia, L. (1996). Unified Construction of Finite Element and Finite Volume Discretisation for Compressible Flows. *International Journal for Numerical Method in Engineering* 39, 1–32.
- Sharma, O.P., Pickett, G.F. and Ni, R.H. (1992). Assessment of Unsteady Flows in Turbines. *Journal of Turbomachinery* 114, 79–90.

- Sieverding, C.H. (1985). Recent Progress in the Understanding of Basics Aspects of Secondary Flows in Turbine Blade Passages. *Journal of Engineering for Gas Turbines and Power* 107, 248–257.
- Sisto, F. (1953). Stall Flutter in Cascades. *Journal of the Aeronautical Science* 20(9), 598–604.
- Sisto, F. (1987a). Introduction and Overview. In *AGARD Manual on Aeroelasticity in Axial-Flow Turbomachines, Unsteady Turbomachinery Aerodynamics*, Volume 1, pp. 1.1 – 1.13. AGARD-AG-297.
- Sisto, F. (1987b). Stall Flutter. In *AGARD Manual on Aeroelasticity in Axial-Flow Turbomachines, Unsteady Turbomachinery Aerodynamics*, Volume 1, pp. 7.1 – 7.11. AGARD-AG-297.
- Sjolander, S.A. and Amrud, K.K. (1987). Effects of Tip Clearance on Blading Loading in a Planar Cascade of Turbine Blades. *Journal of Turbomachinery* 109, 237–244.
- Slack, D.C., Whitaker, D.L. and Walters, R.W. (1994). Time Integration Algorithms for the Two-Dimensional Euler Equations on Unstructured Meshes. *AIAA Journal* 32(6), 1158–1166.
- Smith, S.N. (1972). Discrete frequency sound generation in axial flow Turbomachines. Technical Report 3709, University Engineering Department, Cambridge.
- Spalart, P.R. and Allmaras, S.R. (1992). A One-Equation Turbulence Model for Aerodynamic Flows. AIAA Paper 92-0439.
- Stager, J.L. and Warming, R.F. (1981). Flux Vector Splitting of the Inviscid Gas-Dynamic Equations with Applications to Finite Difference Methods. *Journal of Computational Physics* 40, 263–293.
- Steger, J.L. and Chaussee, D.S. (1980). Generation of Body-Fitted Coordinates Using Hyperbolic Partial Differential Equations. *SIAM Journal on Scientific and Statistical Computing* 4, 431–437.
- Steger, J.L. and Sorenson, R.L. (1979). Automatic Mesh-Point Clustering Near a Boundary in Grid Generation with Elliptic Partial Differential Equations. *Journal of Computational Physics* 33, 405–410.

- Suddhoo, A., Giles, M.B. and Stow, P. (1991). Simulation of Inviscid Blade Row Interaction Using a linear and a non-linear method. ISABE Conference.
- Swanson, R.C. and Turkel, E. (1992). On Central-Difference and Upwind Schemes. *Journal of Computational Physics* 101, 292–306.
- Swanson, R.C., Radespiel, R. and Turkel, E. (1997). Comparison of Several Dissipation Algorithm for Central-Difference Schemes. Technical Report 97-40, ICASE.
- Sweby, P.K. (1984). High Resolution Schemes using Flux Limiters for Hyperbolic Conservation Laws. *SIAM Journal of Numerical Analysis* 21(5), 995–1010.
- Tam, C.K. and Webb, J.C. (1993). Dispersion-Relation-Preserving Finite Difference Schemes for Computational Acoustics. *Journal of Computational Physics* 107, 262–281.
- Thompson, J.F., Thames, F.C. and Mastin, C.W. (1974). Automatic Numerical Generation of Body-Fitted Curvilinear Coordinates System for Field Containing any Number of Arbitrary Two-Dimensional Bodies. *Journal of Computational Physics* 15, 299–319.
- Thompson, K.W. (1987). Time Dependent Boundary Conditions for Hyperbolic Systems. *Journal of Computational Physics* 68, 1–24.
- Thompson, K.W. (1990). Time Dependent Boundary Conditions for Hyperbolic Systems, II. *Journal of Computational Physics* 89, 439–461.
- Tidriri, M.D. (1995). Krylov Methods for Compressible Flows. Technical Report 95-48, ICASE.
- Turkel, E. (1987). Preconditioned Methods for Solving the Incompressible and Low Speed Compressible Equations. *Journal of Computational Physics* 72, 277–298.
- Turkel, E. (1993). Review of Preconditioning Methods for Fluid Dynamics. *Applied Numerical Mathematics* 12, 257–284.
- Turkel, E., Vatsa, V.N. and Radespiel, R. (1996). Preconditioning Methods for Low-Speed Flows. Technical Report 96-57, ICASE.
- Vahdati, M. and Imregun, M. (1995). Non-linear Aeroelasticity Analyses Using Unstructured Dynamic Meshes. In *7th International Symposium on Unsteady*

- Aerodynamics and Aeroelasticity of Turbomachines (ISUAAT)*, Fukuoka, pp. 177–190.
- Vahdati, M., Sayma, A.I., Sbardella, L., Marshall, J.G. and Imregun, M. (2000). Ranking of Numerical Methods for Fan Flutter Prediction. In *9th International Symposium on Unsteady Aerodynamics and Aeroelasticity of Turbomachines (ISUAAT)*, Lyon.
- Van Leer, B. (1974). Towards the Ultimate Conservative Difference Scheme. II. Monotonicity and Conservation Combined in a Second-Order Scheme. *Journal of Computational Physics* 14, 361–370.
- Van Leer, B. (1977a). Towards the Ultimate Conservative Difference Scheme. III. Upstream-Centered Finite-Difference Schemes for Ideal Compressible Flows. *Journal of Computational Physics* 23, 263–275.
- Van Leer, B. (1977b). Towards the Ultimate Conservative Difference Scheme. IV. A new Approach to Numerical Convection. *Journal of Computational Physics* 23, 276–299.
- Van Leer, B. (1979). Towards the Ultimate Conservative Difference Scheme. V. A Second Order Sequel to Godunov’s Method. *Journal of Computational Physics* 32, 101–136.
- Van Leer, B. (1982). Flux Vector Splitting for the Euler Equations. In *8<sup>th</sup> International Conference on Numerical Methods in Fluid Dynamics*, Berlin. Springer Verlag.
- Van Leer, B., Lee, W.Z. and Roe, P. (1991). Characteristic Time-Stepping of Local Preconditioning of the Euler Equations. AIAA Paper 91-1552 CP.
- Van Leer, B., Tai, C.H. and Powell, K.G. (1989). Design of Optimally-Smoothing Multi-Stage Schemes for the Euler Equations. AIAA Paper 89-1933.
- Venkatakrishnan, V. (1995a). A Prospective on Unstructured Grid Flow Solvers. Technical Report 95-3, ICASE.
- Venkatakrishnan, V. (1995b). Implicit Schemes and Parallel Computing in Unstructured Grid CFD. Technical Report 95-28, ICASE.
- Venkatakrishnan, V. and Barth, T.J. (1989). Application of Direct Solvers to Unstructured Meshes for the Euler and Navier-Stokes Equations Using Upwind Schemes. AIAA Paper 89-0364.

- Verdon, J.M. (1987). Linearized Unsteady Aerodynamic Theory. In *AGARD Manual on Aeroelasticity in Axial-Flow Turbomachines, Unsteady Turbomachinery Aerodynamics*, Volume 1, pp. 2.1 – 2.31. AGARD-AG-297.
- Verdon, J.M. (1993). Review of Unsteady Aerodynamics Methods For Turbomachinery Aeroelastic and Aeroacoustic Applications. *AIAA Journal* 31, 235–250.
- Verdon, J.M. and Caspar, J.R. (1984). A Linearized Unsteady Aerodynamic Analysis for Transonic Cascades. *Journal of fluid mechanics* 149, 403–429.
- Wesseling, P. (1992). *An Introduction to Multigrid Methods*. John Wiley & Sons.
- White, F.M. (1991). *Viscous Fluid Flow*. McGraw-Hill, Inc.
- Whitehead, D.S. (1987). Classical Two-dimensional Methods. In *AGARD Manual on Aeroelasticity in Axial-Flow Turbomachines, Unsteady Turbomachinery Aerodynamics*, Volume 1, pp. 3.1 – 3.30. AGARD-AG-297.
- Wilcox, D.C. (1993). *Turbulence Modeling for CFD*. DCW Industries, Inc.
- Wilson, D.G. (1989). *The Design of High-Efficiency Turbomachinery and Gas Turbines*. The MIT Press.
- Woodward, P. and Colella, P. (1984). The numerical Simulation of Two-dimensional Fluid Flow with Strong Shocks. *Journal of Computational Physics* 54, 115–173.
- Yamamoto, A. (1988). Interaction Mechanism Between Tip Leakage Flow and the Passage Vortex in a Linear Turbine Rotor Cascade. *Journal of Turbomachinery* 110, 329–338.
- Zienkiewicz, O.C. and Morgan, K. (1983). *Finite Elements and Approximation*. John Wiley & Sons.

# Appendix A

## Non-Dimensional Variables

All the physical quantities reported in the thesis are considered in their dimensionless form. This Appendix illustrates how these dimensionless quantity are evaluated. The process start defining three reference values for the pressure, temperature and length scale:

$$\begin{aligned} p_{ref} & \quad [\text{Pa}] \\ T_{ref} & \quad [\text{K}] \\ l_{ref} & \quad [\text{m}] \end{aligned} \tag{A.1}$$

The dimensionless pressure and temperature are calculated from their dimensionalised and reference counterparts as:

$$p = \frac{p_{dim}}{p_{ref}} \tag{A.2}$$

$$T = \frac{T_{dim}}{T_{ref}} \tag{A.3}$$

Density, velocity and time are non-dimensionalised using the following reference quantities:

$$\rho_{ref} = \frac{p_{ref}}{RT_{ref}} \quad [\text{Kg/m}^3] \tag{A.4}$$

$$v_{ref} = \sqrt{RT_{ref}} \quad [\text{m/s}] \tag{A.5}$$

$$t_{ref} = \frac{l_{ref}}{\sqrt{RT_{ref}}} \quad [\text{s}]$$

In (A.5)  $R$  indicates the gas constant ( $R = 287 \text{ [m}^2/\text{s}^2\text{K]}$ ). The dimensionless perfect gas relations become:

$$p = \rho T \quad (\text{A.6})$$

$$c = \sqrt{\gamma T} = \sqrt{\gamma \frac{p}{\rho}} \quad (\text{A.7})$$

The reduced frequency  $\omega$  is obtained from the dimensional frequency  $f$  [Hz] via the following relation:

$$\omega = 2\pi f t_{ref} \quad (\text{A.8})$$

The reference Reynolds number is given by

$$Re = \frac{l_{ref} \rho_{ref} v_{ref}}{\mu_{ref}} \quad (\text{A.9})$$

where  $\mu_{ref}$  is evaluated from  $T_{ref}$  using the Sutherland's formula

$$\mu_{ref} = \frac{1.45 T_{ref}^{3/2}}{T_{ref} + 110} 10^{-6} \quad (\text{A.10})$$

The dimensionless dynamic viscosity is evaluated by:

$$\mu = \frac{T_{ref} + 110}{T_{ref} T + 110} T^{3/2} \quad (\text{A.11})$$

## Appendix B

# Spalart Allmaras Turbulence Model

Turbulence modeling, together with grid generation and algorithm development, is one of the three key elements in CFD. However, while for grid generation and algorithm development very precise mathematical theories have evolved, mathematical models that approximate the physical behaviour of turbulent flows achieved far less precision. The reason for that is because turbulence modelling try to approximate an extremely complicated phenomena. The turbulence model used throughout the research project belong to class of models in where the the turbulence length scale is related to some typical flow dimension.

### B.1 One Equation Spalart-Allmaras Model

Using the same convection as for the mean flow equations, the Spalart-Allmaras (1992) one equation turbulence model can be written in a ALE integral conservative form as

$$\frac{\partial}{\partial t} \int_{\mathcal{V}(t)} \rho v_t d\mathcal{V} + \oint_{\mathcal{S}(t)} \left[ \vec{F}_t - \frac{1}{Re} \vec{G}_t \right] \cdot \vec{n} d\mathcal{S} = \int_{\mathcal{V}(t)} S_t d\mathcal{V} \quad (\text{B.1})$$

where the flux vector  $\vec{F}_t$  and  $\vec{G}_t$  and the source term  $S_t$  are given by

$$\vec{F}_t = \rho v_t \vec{u} \quad (\text{B.2})$$

$$\vec{G}_t = \frac{1}{\sigma} (\mu_l + \rho v_t) \vec{\nabla} v_t \quad (\text{B.3})$$

$$S_t = c_{b1} P \rho v_t + \frac{\rho}{Re} \left[ \frac{c_{b2}}{\sigma} (\vec{\nabla} v_t)^2 - c_{w1} f_w \left( \frac{v_t}{d} \right)^2 \right] \quad (B.4)$$

The turbulent eddy viscosity  $\mu_t$  is related to the turbulent unknown  $\rho v_t$  through the relation

$$\mu_t = \rho v_t f_{v1} \quad (B.5)$$

in equations (B.1-B.5) the following functions are used

$$f_{v1} = \frac{\chi^3}{\chi_3 + c_{v1}^3} \quad (B.6)$$

$$\chi = \frac{\rho v_t}{\mu_l} \quad (B.7)$$

$$P = |\vec{\nabla} \times \vec{u}| + \xi f_{v2} \quad (B.8)$$

$$\xi = \frac{1}{Re} \frac{v_t}{\kappa^2 d^2} \quad (B.9)$$

$$f_{v2} = 1 - \frac{\chi}{1 + \chi f_{v1}} \quad (B.10)$$

$$f_w = g \left( \frac{1 + c_{w3}^6}{g^6 + c_{w3}^6} \right)^{1/6} \quad (B.11)$$

$$g = r + c_{w2} (r^6 - r) \quad (B.12)$$

$$r = \frac{\xi}{P} \quad (B.13)$$

For all calculations the following constants are used

$$\begin{aligned} \kappa &= 0.41, & \sigma &= \frac{2}{3}, & c_{b1} &= 0.1355, \\ c_{b2} &= 0.622, & c_{w1} &= \frac{c_{b1}}{\kappa^2} + \frac{1+c_{b2}}{\sigma}, & c_{w2} &= 0.3, \\ c_{w3} &= 2.0, & c_{v1} &= 7.1 \end{aligned} \quad (B.14)$$

## B.2 Linearised Turbulence Model

Following the same procedure as for the mean flow equations, the Spalart-Allmaras turbulence model can be written in a frequency domain linearised form as

$$\begin{aligned} \frac{\partial}{\partial \tau} \int_{\bar{V}} \widehat{\rho v}_t d\bar{V} + \oint_{\bar{S}} \left( \widehat{\vec{F}}_t - \frac{1}{Re} \widehat{\vec{G}}_t \right) \cdot \vec{n} d\bar{S} - \int_{\bar{V}} (i\omega \widehat{\rho v}_t + \widehat{S}_t) d\bar{V} = \\ \widehat{H}_t (\overline{\rho v}_t, \bar{\mathbf{U}}, \widehat{\vec{x}}) \end{aligned} \quad (B.15)$$

The linearised inviscid and viscous fluxes are given by the two relations

$$\hat{\vec{F}}_t = \hat{\rho}\hat{v}_t (\vec{v} - \vec{\Omega} \times \vec{x}) + \bar{\rho}\bar{v}_t \hat{\vec{v}} \quad (\text{B.16})$$

$$\hat{\vec{G}}_t = (\bar{\mu}_l + \bar{\rho}\bar{v}_t) \vec{\nabla}\hat{v}_t + (\hat{\mu}_l + \hat{\rho}\hat{v}_t) \vec{\nabla}\bar{v}_t \quad (\text{B.17})$$

The linearised eddy viscosity is given by

$$\hat{\mu}_t = \hat{\rho}\hat{v}_t f_{v1} \quad (\text{B.18})$$

The terms  $\hat{H}$  and the right-hand side of equation (B.15) indicates the summation of inhomogeneous terms arising from the grid motion.

$$\begin{aligned} \hat{H}_t &= \int_{\mathcal{V}} (i\omega\bar{\rho}\bar{v}_t + \bar{S}_t) d\hat{V} - \oint_{\bar{\mathcal{S}}} \left( \vec{F}_t - \frac{1}{Re} \vec{G}_t \right) \cdot \vec{n} d\bar{S} \\ &\quad + \oint_{\bar{\mathcal{S}}} \bar{\rho}\bar{v}_t (\vec{\Omega} \times \vec{x} - i\omega\hat{x}) \cdot \vec{n} d\bar{S} \end{aligned} \quad (\text{B.19})$$

The linearised source term  $\hat{S}_t$  is given by the relation

$$\hat{S}_t = c_{b1} (\bar{P}\hat{\rho}\hat{v}_t + \hat{P}\bar{\rho}\bar{v}_t) + \frac{2\bar{\rho}}{Re} \left[ \frac{c_{b2}}{\sigma} (\vec{\nabla}\bar{v}_t) (\vec{\nabla}\hat{v}_t) - c_{w1} f_w \frac{\bar{v}_t \hat{v}_t}{d^2} \right] \quad (\text{B.20})$$

with

$$\hat{P} = |\vec{\nabla} \times \hat{\vec{u}}| + \frac{f_{v2}}{Re \kappa^2 d^2} \hat{v}_t \quad (\text{B.21})$$

The functions  $f_{v1}$ ,  $f_{v2}$  and  $f_w$  in (B.18), (B.20) and (B.21) are evaluated using the steady-state unknowns.

# Appendix C

## Aerodynamic Forcing Functions

A method for calculating potential, vortical and entropic components of unsteady flow-field is presented in this appendix. The method, based upon the Goldstein's splitting theorem and the linearised acoustic equations, evaluates the aerodynamic forcing functions from a steady-state solution to impose as on coming unsteadiness to a single bladerow. Such boundary conditions can be used for both linear and non-linear unsteady computations with the difference that, for the linear simulation, only one harmonic at a time can be used. The procedure starts from some steady-state data of the adjacent bladerow boundary, either the outflow of the upstream blade or the inflow of the downstream blade. The steady-state flow data could be either computed or measured.

### C.1 Spatial Non-uniformities

The first step for calculating the aerodynamic forcing functions, originating from an adjacent bladerow, is to analyse the Fourier components of the data at a given far-field boundary. In the reference frame fixed with a given blade row '1', the flow field is steady but possesses spatial flow non-uniformities. In this way, at a given far-field boundary the steady-state primitive variables, in axisymmetric coordinates, can be expressed as the sum of an axisymmetric steady-state part plus a steady-state non-uniform part:

$$\mathbf{V}(x, \theta_1, r) = \bar{\mathbf{V}}(x, r) + \widetilde{\mathbf{V}}(x, \theta_1, r) \quad (\text{C.1})$$

The steady-state non-uniform part can be Fourier decomposed because of periodicity in the tangential direction.

$$\widetilde{\mathbf{V}}(x, \theta_1, r) = \sum \widetilde{\mathbf{V}}_m(x, r) \exp(i\kappa_\theta \theta_1) \quad (\text{C.2})$$

The tangential wave number  $\kappa_\theta$  is given by

$$\kappa_\theta = \frac{2\pi m}{\Delta\theta_1} \quad (\text{C.3})$$

where  $\Delta\theta_1$  is the blade-to-blade spacing and  $m$  is the mode number.

If one considers a bladerow ‘2’, adjacent to bladerow ‘1’, then the tangential positions  $\theta_1$  and  $\theta_2$  are related to the rotational velocities  $\Omega_1$  and  $\Omega_2$  and time  $t$  by:

$$\theta_1 + \Omega_1 t = \theta_2 + \Omega_2 t \quad (\text{C.4})$$

Substituting (C.4) into (C.3) one can obtain:

$$\frac{2\pi m}{\Delta\theta_1} \theta_1 = \frac{2\pi m}{\Delta\theta_1} \theta_2 - \frac{2\pi m (\Omega_1 - \Omega_2)}{\Delta\theta_1} t \quad (\text{C.5})$$

and in a different notation;

$$\frac{2\pi m}{\Delta\theta_1} \theta_1 = -\frac{\phi_2}{\Delta\theta_2} \theta_2 - \omega_2 t \quad (\text{C.6})$$

So the stationary  $m^{th}$  mode in bladerow ‘1’ is equivalent to an unsteady mode in blade row ‘2’ with reduced frequency

$$\omega_2 = \frac{2\pi m (\Omega_1 - \Omega_2)}{\Delta\theta_1} \quad (\text{C.7})$$

and interblade phase angle:

$$\phi_2 = -\frac{2\pi m \Delta\theta_2}{\Delta\theta_1} \quad (\text{C.8})$$

In order to maintain all frequencies  $\omega_2$  positive, the summation in (C.2) has to be for  $m > 0$  in the case of  $(\Omega_1 - \Omega_2) > 0$  and for  $m < 0$  in the case of  $(\Omega_1 - \Omega_2) < 0$ . The harmonic boundary terms that go with this mode are:

$$\widehat{\mathbf{V}}(x, \theta_2, r) = \widetilde{\mathbf{V}}_m(x, r) \exp\left(-\frac{i\phi_2}{\Delta\theta_2} \theta_2\right) \quad (\text{C.9})$$

## C.2 Vortical, Potential and Entropy Splitting

In the development of the linear theory, the flow non-uniformities  $\tilde{\mathbf{V}}(x, \theta, r)$  are assumed to be small relative to the uniform steady flow properties  $\bar{\mathbf{V}}(x, r)$ . Under such approximation it is possible to recover the linearised acoustic equations (Anderson 1990).

$$\frac{1}{c^2} \frac{D\tilde{p}}{Dt} + \bar{\rho} \vec{\nabla} \cdot \tilde{\vec{v}} = 0 \quad (\text{C.10})$$

$$\bar{\rho} \frac{D\tilde{\vec{v}}}{Dt} + \vec{\nabla} \tilde{p} = 0 \quad (\text{C.11})$$

$$\frac{D\tilde{s}}{Dt} = 0 \quad (\text{C.12})$$

According to Goldstein's splitting theorem (Goldstein 1978), the perturbation velocity  $\tilde{\vec{v}}$  can be decomposed into the sum of (i) a rotational component  $\tilde{\vec{v}}_v$  that is purely convected, has zero divergence and is completely decoupled from the fluctuations in pressure or in any other thermodynamic property and (ii) an irrotational disturbance  $\tilde{\vec{v}}_p$  that produces no entropy fluctuations but is directly related to the pressure fluctuations.

$$\tilde{\vec{v}} = \tilde{\vec{v}}_v + \tilde{\vec{v}}_p \quad (\text{C.13})$$

The rotational velocity field is also known as the vortical perturbation, and the irrotational perturbation is also referred to as the potential (or acoustic) perturbation. Finally the fluctuations in entropy are decoupled from the velocity and pressure fluctuations, but do produce density fluctuations which are convected with the flow. Summarizing, three different modes of motion can be solution of the linearised acoustic equations (C.10-C.12): vortical, potential and entropy mode. In the following three paragraphs these modes will be analysed in detail in axisymmetric coordinate, neglecting the radial components of  $\vec{v}$ .

### Vortical mode

The Goldstein's splitting assumes that any vortical perturbation satisfies the following constraints:

$$\vec{\nabla} \cdot \tilde{\vec{v}}_v = 0 \quad (\text{C.14})$$

$$\frac{D\tilde{\vec{v}}_v}{Dt} = 0 \quad (\text{C.15})$$

$$\tilde{p}_v = 0 \quad (\text{C.16})$$

$$\tilde{\rho}_v = 0 \quad (\text{C.17})$$

The steady-state form of (C.15) shows that the vortical propagation wave vector  $\vec{\kappa}$  must be perpendicular to the blade mean flow exit velocity vector. Hence the scalar product must be zero:

$$\vec{\kappa} \cdot \vec{v} = 0 \quad (\text{C.18})$$

The tangential wave number is given in (C.3) while the axial wave number of the vortical mode, derived from (C.18) becomes:

$$\kappa_{x_m} = -\frac{\bar{v}_\theta}{\bar{v}_x} \kappa_{\theta_m} \quad (\text{C.19})$$

From (C.14) and (C.18), it is straightforward to show that the vortical mode magnitude vector must be parallel to the mean flow exit velocity vector. Denoting the complex constant of proportionality  $D_m$  the vortical perturbation can be written as:

$$\tilde{\vec{v}}_v = \bar{\vec{v}} \sum D_m \exp(i\vec{\kappa}_m \cdot \vec{x}) = \bar{\vec{v}} \sum D_m \exp\left[i\kappa_{\theta_m} \left(\theta - \frac{\bar{v}_\theta}{\bar{v}_x} x\right)\right] \quad (\text{C.20})$$

Equation (C.20) shows that the vortical perturbation propagates unattenuated both in the tangential and axial directions ( $\vec{\kappa}$  contains only real part). Section C.3 will show how to calculate the complex constant of proportionality  $D_m$ .

### Potential mode

The potential velocity field can be derived from a potential function

$$\tilde{\vec{v}}_p = \vec{\nabla} \psi_p \quad (\text{C.21})$$

and the perturbation potential is related to the perturbation pressure through the unsteady Bernoulli equation

$$\tilde{p}_p = -\bar{\rho} \frac{D\psi_p}{Dt} \quad (\text{C.22})$$

The isentropic relation gives the perturbation density as a function of the perturbation pressure

$$\tilde{\rho}_p = \frac{1}{c^2} \tilde{p}_p \quad (\text{C.23})$$

Combining equations (C.21) and (C.22) with (C.10) it is possible to obtain the following linear velocity potential equation.

$$\begin{aligned} \frac{1}{c^2} \psi_{p_{tt}} + \frac{2}{c} \left( \bar{M}_x \psi_{p_{xt}} + \bar{M}_\theta \psi_{p_{\theta t}} \right) = \\ (1 - \bar{M}_x^2) \psi_{p_{xx}} - 2\bar{M}_x \bar{M}_\theta \psi_{p_{x\theta}} + (1 - \bar{M}_\theta^2) \psi_{p_{\theta\theta}} \end{aligned} \quad (\text{C.24})$$

The steady-state version of (C.24) has solutions of the form:

$$\psi_p = \sum A_m \exp(i\kappa_{\theta_m}\theta + \chi_m x) \quad (\text{C.25})$$

where the axial decay  $\chi_m$  is

$$\chi_m = \frac{i\bar{M}_x \bar{M}_\theta \pm \text{sign}(\kappa_{\theta_m}) \sqrt{1 - \bar{M}^2}}{1 - \bar{M}_x^2} \kappa_{\theta_m} \quad (\text{C.26})$$

Clearly the qualitative behaviour of this perturbation depends on whether the flow is subsonic or supersonic.

Subsonic mean flow ( $\bar{M} < 1$ ):  $\chi_m$  has both real and imaginary components. If one is interested in perturbation at the inlet boundary, then it is not physical to have perturbation growing exponentially downstream, and so the negative root of (C.26) must be chosen. On the other hand, the positive root must be chosen for perturbation at outlet boundary. It is interesting to note that the rate of decay of the perturbation depends linearly on the tangential wave number component  $\kappa_{\theta_m}$ . As a consequence the most important mode is the fundamental mode  $\kappa_{\theta_1} = \frac{2\pi}{\Delta\theta}$ .

Supersonic mean flow ( $\overline{M} > 1$ ): if the flow is still axially subsonic ( $\overline{M}_x < 1$ ),  $\chi_m$  has only an imaginary component. To determine which root should be chosen in (C.26), the supersonic characteristic theory has to be used (Giles 1991). For an inlet boundary, the positive root should be chosen if the flow angle is positive and negative root if the flow angle is negative, vice-versa for an outlet boundary.

### Entropy mode

This mode is associated only with density fluctuations and like the vortical perturbation is convected with the mean flow, without any axial decay:

$$\tilde{\rho}_e = \bar{\rho} \sum B_m \exp \left[ i\kappa_{\theta_m} \left( \theta - \frac{\bar{v}_\theta}{\bar{v}_x} x \right) \right] \quad (\text{C.27})$$

$$\tilde{\vec{v}}_e = 0 \quad (\text{C.28})$$

$$\tilde{p}_e = 0 \quad (\text{C.29})$$

## C.3 Matching Linear Theory and Available Data

The complex constants  $A_m$ ,  $B_m$  and  $D_m$  can be determined by matching the linear theory with the measured or computed perturbation quantities  $\widetilde{\mathbf{V}}$  (Manwaring 1993).

Using equations (C.20),(C.21), (C.22) and (C.25) the relationship between the linear theory and the perturbation quantities  $\widetilde{\mathbf{V}}$  can be expressed as:

$$\begin{bmatrix} \chi_m & \bar{v}_x \\ i\kappa_m & \bar{v}_\theta \\ -\bar{\rho}(\bar{v}_x \chi_m + i\bar{v}_\theta \kappa_m) & 0 \end{bmatrix} \begin{Bmatrix} A_m \\ D_m \end{Bmatrix} = \begin{bmatrix} \tilde{v}_{x_m} \\ \tilde{v}_{\theta_m} \\ \tilde{p}_m \end{bmatrix} \quad (\text{C.30})$$

and combining (C.27) and (C.25)

$$B_m = \frac{1}{\bar{\rho}} \left( \tilde{\rho}_m - \frac{1}{c^2} \tilde{p}_m \right) \quad (\text{C.31})$$

System (C.30) can also written in a compact notation

$$[\mathbf{T}] \mathbf{a} = \mathbf{b} \quad (\text{C.32})$$

Matrix  $[\mathbf{T}]$  depends on the tangential wave number, thus  $A_m$  and  $D_m$  take different values for each harmonic analysed. Relation (C.32) represents an overdetermined system of equations which can be solved using a least-squares (LS) method which minimizes the L2 norm of the difference between  $[\mathbf{T}]\mathbf{a}$  and  $\mathbf{b}$ . The most widely used method for solving a full column rank<sup>1</sup> LS problem is the method of normal equations (Golub et al. 1991).

Introducing a diagonal weighting matrix  $[\mathbf{W}]$  specifying the relative weighting of the three quantities on the right-hand side of (C.30), a LS solution of (C.32), using the method of normal equations, is given by:

$$[\mathbf{T}]^T [\mathbf{W}] [\mathbf{T}] \mathbf{a} = [\mathbf{T}]^T [\mathbf{W}] \mathbf{b} \quad (\text{C.33})$$

Following the procedure of Feiereisen et al. (1994), only two weighting factors are used in  $\mathbf{W}$ :  $W_v$  for the two velocity components  $\tilde{v}_{x_m}$ ,  $\tilde{v}_{\theta_m}$  and  $W_p$  for the static pressure  $\tilde{p}_m$ :

$$[\mathbf{W}] = \begin{bmatrix} W_v & 0 & 0 \\ 0 & W_v & 0 \\ 0 & 0 & W_p \end{bmatrix} \quad (\text{C.34})$$

The LS method will break down in two distinct cases: (i)  $W_v = 0$  and (ii) incompressible flow with  $W_v = W_p$  (Feiereisen et al. 1994).

## C.4 Example

In order to illustrate the proposed method, let us consider the outflow boundary of a stator blade. The computed data is first Fourier decomposed along the tangential direction and then system (C.33) is solved for each Fourier component, to obtain the vortical, potential and entropy waves amplitudes  $D_m$ ,  $A_m$  and  $B_m$ , using  $W_v = W_p = 0.5$ . These quantities are then used to reconstruct the flow quantities at the boundary using an inverse Fourier transform. The results are shown in Fig. C.1 where the reconstructed variables are obtained using the first Fourier components.

---

<sup>1</sup>A Least squares problem  $[\mathbf{T}]\mathbf{a} = \mathbf{b}$  with  $[\mathbf{T}] \in \mathbb{R}^{m \times n}$ ,  $\mathbf{a} \in \mathbb{R}^n$  and  $\mathbf{b} \in \mathbb{R}^m$  is said to be full column rank when  $\text{rank}[\mathbf{T}] = n$ , i.e. the columns of  $[\mathbf{T}]$  are linear independent.

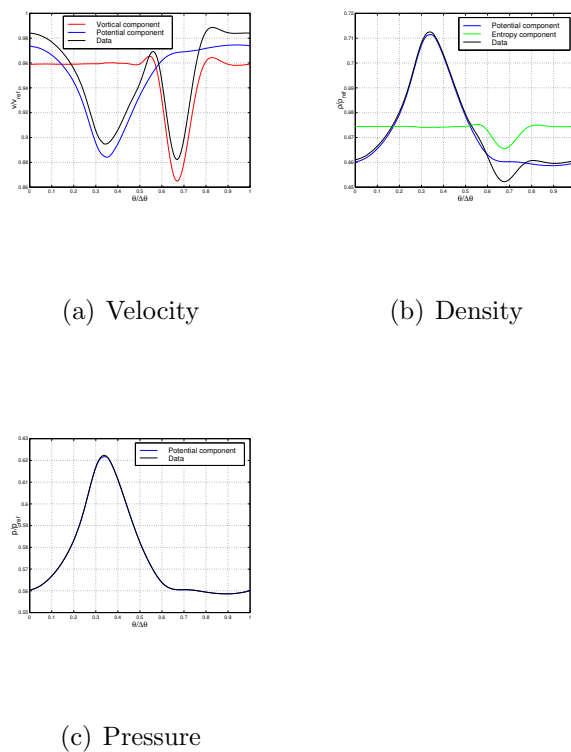


Figure C.1: Comparison between the computed steady data and the reconstructed vortical, potential and entropy components using first 10 harmonics.

# Appendix D

## Preconditioned Agglomeration Multigrid for Hybrid Grids

A preconditioned directional-implicit agglomeration multigrid method has been developed for the solution of the linear and non-linear Navier-Stokes equations on highly anisotropic unstructured hybrid grids in 2D and 3D. The coarse grid levels are constructed automatically from the fine grid by agglomerating fine grid control volumes together. Since the coarse grid control volumes may have arbitrary polygonal shapes, the type of elements constituting the fine grid is irrelevant. In this way the discrete equations on coarse grid levels are assembled automatically without the explicit creation of a coarse grid. The multigrid smoother consists of a preconditioned point- or line-Jacobi Runge-Kutta relaxation algorithm, which guarantees efficient damping of high frequency error modes on highly stretched grids.

### D.1 Introduction

The basic idea of a multigrid strategy is to obtain a faster rate of development of the solution on a fine grid by approximating the fine-grid problem on successively coarser grids. With suitable coarse-grid approximations of the fine-grid problem, the low-frequency error components on the fine grid appear as high-frequency error components on the coarser grids. The low-frequency components on the fine grid, where the discrete solution is desired, are precisely the error components that dramatically slow down the convergence of single-grid schemes. There are two

additional advantages derived from displacing part of the effort in solving a set of discrete equations to coarse grids. First, a larger mesh spacing permits larger time steps thus allowing a faster propagation of the informations in the domain of interest. This point is of particular importance for convection dominated problems such as the ones described by the Euler and Navier-Stokes equations. Such equations exhibit both elliptic and hyperbolic properties in their discrete formulations meaning that the coarse meshes in the multigrid cycle serve the dual role of enhancing both damping and propagation of error modes. Another advantage of the coarse grids is that they require less computational effort because of the reduced degrees of freedom involved compared with the fine grid. For example, in 2D the computational effort needed is decreased roughly by a factor of four on successively coarser meshes.

Multigrid methods have proven to be very effective techniques for accelerating convergence to steady state of both elliptic and hyperbolic problems. For simple elliptic problems, such as a Poisson equation, convergence rates of 0.1 are achievable, meaning that for each multigrid cycle, the numerical error can be reduced by one order of magnitude (Mavriplis 1998b). For hyperbolic problems, such as the Euler equations, the best rate that theoretically can be achieved for a second order discretisation is 0.75, according to the analysis discussed by Mulder (1992).

On the other hand, the development of efficient numerical methods for the solution of the high-Reynolds number viscous flow remains one of the ongoing challenge in the field of computational fluid dynamics. Multigrid Navier-Stokes solvers generally result in convergence rates which are an order of magnitude or more slower than those obtained for inviscid flows (Mavriplis 1998a, Pierce & Giles 1997). The main reason for this breakdown in efficiency of the multigrid algorithm stems from the need to use a computational mesh that is highly resolved in the direction normal to the wall in order to accurately represent the steep gradients in the boundary layer. Indeed, the higher the Reynolds number, the more grid stretching is required, and the worse the convergence rate becomes. The design of an appropriate numerical approach must therefore be based on a careful assessment of the interaction between the discrete method, the computational mesh and the physics of the viscous flow. Over the last few years, different methods have been proposed to overcame the increased stiffness of the discrete system of equations due to high aspect ratio cells. Mulder (1989) proposed a semi-coarsening multigrid strategy in which the mesh is coarsened only in the direction normal to the grid stretching, rather then in

all coordinate simultaneously. One major drawback of semi-coarsening techniques is that they results in coarse grids of higher complexity. While full coarsening approach reduces grid complexity between successively coarser levels by a factor of 4 in 2D, and 8 in 3D, semi-coarsening techniques only achieve a grid complexity reduction of 2, in both 2D and 3D. This increase the costs of a multigrid cycle especially in 3D. More recently Pierce & Giles (1997) and Pierce et al. (1997) have proposed preconditioning methods, coupled with explicit multistage scheme, as a less expensive approach to overcoming multigrid breakdown in the presence of boundary layer anisotropy.

Following the analysis by Pierce et al. (1997), two different form of preconditioner were implemented in the numerical method presented in this research project. These preconditioners are either the point- or line-Jacobian matrix obtained through a linearisation of the first order discretisation of the Navier-Stokes equations. In 3D the point-Jacobian preconditioner is a block-matrix  $5 \times 5$  which can be directly inverted at a reasonable costs. Mavriplis (1998b, 1998a) reviews these multigrid strategies for viscous flow solvers on anisotropic hybrids grids in the context of agglomeration multigrid.

## D.2 Algorithm Description

The main difficulty with multigrid techniques on hybrid unstructured grids is the generation of coarse grids. On structured grids, a sequence of grids can be constructed trivially by omitting alternate grid points in each direction. In the case of unstructured grid four main approaches can be adopted. The first strategy is to produce a sequence of fine grids from a coarse grid by refinement. The advantage is that the inter-grid operators become simple because of the nesting of the grid. The major drawback of such method is the predetermination of the coarsest level in the multigrid. This may be too fine if the geometry is to be captured on the coarse grid. Another method, labelled non-nested multigrid, uses a sequence of grids which are generated independently by a grid generator. Piecewise-linear interpolation operators for the transference of flow variables, residuals and correction are derived during a pre-processing stage by using efficient search procedures. Non-nested multigrid method has been shown to be quite successful on unstructured grid computations (Peraire et al. 1992). However, the generation of the sequence of grid is not automatic and requires a robust mesh generator. In addition, the

development of efficient Piecewise-linear interpolation operators on hybrid grid is not a straightforward task. A third approach is the edge collapse multigrid which uses an automatic point removal algorithm to generate a sequence of coarse grids from an initial fine grid. This is completely automatic and has been successfully adopted for hybrid unstructured meshes (Moinier et al. 1999).

A completely different approach is the generation of coarse grids through agglomeration as developed by Mavriplis & Venkatakrishnan (1995a, 1995b). The central idea of agglomeration multigrid is to form coarse grid levels by fusing fine grid control volumes together as shown in Fig. D.1. Since the coarse grid levels may have arbitrary polygonal shapes (polyhedral in 3D), the type of elements constituting the fine grid is irrelevant.

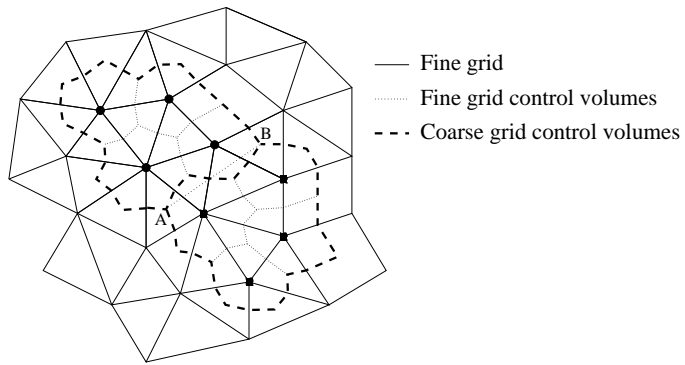


Figure D.1: Example of two agglomerated coarse grid volumes

An edge-based solver performs all the operations utilizing the volumes and edge coefficients only, thus it can handle an arbitrary polyhedral coarse grid in a straightforward way. The fluxes in the coarse grid levels are evaluated using a the first-order Roe'upwind solver for polyhedral grids developed by Barth & Jespersen (1989). The agglomeration procedure can be interpreted as a Galerkin coarse grid approximation (Wesseling 1992). Agglomeration can thus viewed as identifying all of the fine grid cells with the coarse cell to which they belong, and then summing the equations corresponding to these cells. Interpreted in this manner, agglomeration multigrid is similar to algebraic multigrid procedure. In a purely algebraic multigrid, which is strictly valid for linear system, no underlying grid is defined, and only the matrix  $\mathbf{A}$  of a linear system  $\mathbf{A}s = b$  is known. The coarse grid operator is then obtained by a direct summation of the non-zero entries in the fine level matrix. Agglomeration multigrid represents an extension of these ideas to nonlinear systems. In this approach, only the solution independent terms are summed in going from fine to coarse levels. For example in Fig. D.1, edge AB represents the summation of the edge vector in the fine grid which are common between the two coarse agglomerated cells. The solution dependent terms are obtained from coarse level variables interpolated up from the fine level solution, following a Full Approximation Storage scheme (FAS).

### D.2.1 FAS scheme

In this section a description of the full approximation storage (FAS) multigrid scheme is given. Suppose that successively coarser agglomerated grids are introduced, with the grids numbered from 1 to  $K$ , where grid 1 is the original mesh. For  $k > 1$ , the evolution on grid  $k$  is driven by a weighted average of the residuals calculated on grid  $k - 1$ , so that each mesh simulates the evolution that would have occurred on the next finer mesh (Jameson 1985, Wesseling 1992). When the coarsest grid has been reached, changes in the solution calculated on each mesh are consecutively interpolated back to the next finer grid.

The fine grid system of equations is written for both steady-state and unsteady nonlinear flow as well as linearised unsteady flow, as:

$$[\mathbf{P}]^{-1} L_\tau \delta \mathbf{U} = \mathbf{R}(\mathbf{U}) \quad (\text{D.1})$$

with  $L_\tau$  indicating the pseudo time-marching Runge-Kutta operator. The discrete system of equations for a general grid  $k$  can be written as

$$[\mathbf{P}]^{-1} L_\tau \delta \mathbf{U}^k = \mathbf{R}^k - \mathbf{F}^k \quad (\text{D.2})$$

where  $\mathbf{F}^k$  represents the multigrid forcing function which is needed in order to simulates the evolution process in the finer grid. This forcing function is zero for the finer grid ( $k = 1$ ) while for  $k > 1$  it assumes the following form:

$$\mathbf{F}^k = \mathbf{R}(\mathbf{U}_{old}^k) - \Theta_{\text{Res}}^{R^{k-1 \rightarrow k}} (\mathbf{R}(\mathbf{U}_{old}^{k-1}) - \mathbf{F}^{k-1}) \quad (\text{D.3})$$

$$\mathbf{U}_{old}^k = \Theta_{\text{Unk}}^{R^{k-1 \rightarrow k}} \mathbf{U}_{old}^{k-1} \quad (\text{D.4})$$

The symbol  $\Theta$  represent inter-grid transfer operators which will be defined shortly. The coarse grid equations are solver for  $\mathbf{U}^k$  with starting solution  $\mathbf{U}_{old}^k$ . The correction are then interpolated back to the fine grid as

$$\mathbf{U}_{new}^{k-1} = \mathbf{U}_{old}^{k-1} + \Theta^{P^{k \rightarrow k-1}} (\mathbf{U}_{new}^k - \mathbf{U}_{old}^k) \quad (\text{D.5})$$

One of the principal advantages of this FAS algorithm is that it enables an efficient solution strategy which requires little more memory than that of the single grid solver (Wesseling 1992).

A recursive algorithm, which allows the use of an arbitrary number of meshes in either a V or W type cycles, has been implemented following the approach by Peraire et al. (1992).

## D.2.2 Transfer Operators

Three inter-grid transfer operators need to be defined in order to have a complete description of the algorithm.

**Restriction:** transfers the solution and residual vector from fine to coarse grids. Here a simple injection has been employed.

$$\Theta_{\text{Unk}}^{R^{k-1 \rightarrow k}} \mathbf{U}^{k-1} = \frac{1}{\mathcal{V}^k} \sum_{c=1}^{n_c} (\mathcal{V}\mathbf{U})_{I_c}^{k-1} \quad (\text{D.6})$$

$$\Theta_{\text{Res}}^{R^{k-1 \rightarrow k}} \mathbf{R}^{k-1} = \sum_{c=1}^{n_c} \mathbf{R}_{I_c}^{k-1} \quad (\text{D.7})$$

where  $n_c$  represents the number of control volumes in the fine grid  $k-1$  contained in the agglomerated coarse grid control volume. In Fig. D.1 shows two agglomerated coarse control volumes which contains four fine control volumes each.

**Prolongation:** transfers the change of the solution from coarse to fine grid. Since a set of fine control volumes are included in one coarse agglomerated cell only, a simple copy of the coarse grid correction has been used.

$$\Theta^{P^{k \rightarrow k-1}} (\Delta \mathbf{U}^k) = \Delta \mathbf{U}^k \quad (\text{D.8})$$

Multigrid theory (Wesseling 1992) suggests that

$$m_R + m_P > m_E \quad (\text{D.9})$$

where  $m_R$  and  $m_P$  are the order of polynomial that the restriction and the prolongation can transfer exactly, and  $m_E$  is the order of the differential equation, which is 2 for the Navier-Stokes equations. Both transfer operators described in (D.6) and (D.8) can transfer correctly only first order polynomial, thus violating (D.9) in the case of Navier-Stokes equations. Unfortunately, devising higher order transfer operators in the case of agglomerated grids is non-trivial because of the absence of an underlying grid. However, the use of an efficient smoother can alleviate such a drawback by being effective in removing high-frequency errors resulting from the corrections from the fine-grid approximation.

## D.3 Smoother

Having established the multigrid strategy and the transfer operators to be used, it remains to define the smoother  $L_\tau$  in (D.1). Efficient multigrid performance relays heavily on the ability of the smoother to damp on the current mesh all the modes that cannot be resolved without aliasing on the next coarser mesh in the cycle (Pierce & Giles 1997). Moreover for hyperbolic problems, the smoother must enhance the propagation of error modes outside the computational domain. Broadly speaking, relaxation methods are traditionally classified into explicit and implicit scheme. Explicit scheme offers a low operation count, low storage requirements but they suffer from limited stability imposed by the CFL conditions. Implicit schemes

theoretically offer unconditional stability and presumably insensitiveness to the degree of anisotropy in the problem to be solved. In practice direct implicit method are infeasible for large 3D problems due to high operation counts and memory requirements so that the inversion of the Jacobian matrix must be performed using iterative or approximate factorization techniques. Such techniques are only moderately implicit and are not efficient when very large time-steps are employed so that it is not possible to benefit the unconditional stability. Moreover such schemes, often designed for isotropic problems, degrade with increasing anisotropy. Here an efficient solution strategy for highly anisotropic problems based on preconditioned point-Jacobi or line-Jacobi multistage Runge-Kutta scheme has been employed.

### D.3.1 Time-stepping

From (3.32), (3.35) and (4.38), the semi-discrete finite volume discretisation of the Navier-Stokes system of equations appears as

$$[\mathbf{P}]^{-1} L_\tau \mathbf{U}_I = \mathbf{R}_I (\mathbf{U}) \quad (\text{D.10})$$

where  $[\mathbf{P}]^{-1}$  is the preconditioner. A Q-stage scheme for the grid level  $k$  can be written as:

$$\begin{aligned} \mathbf{U}_0^k &= \mathbf{U}_{old}^k \\ &\vdots \\ \mathbf{U}_{q+1}^k &= \mathbf{U}_0^k + \alpha_q [\mathbf{P}] (\mathbf{R}_q^k - \mathbf{F}^k) \\ &\vdots \\ \mathbf{U}_{new}^k &= \mathbf{U}_Q^k \end{aligned} \quad (\text{D.11})$$

where  $\alpha_q$  are the Runge-Kutta parameters. Throughout this work the five-stage Runge-Kutta scheme of Jameson (1993) with alternate evaluation of the physical and artificial dissipation has been used. If one indicates with  $\mathbf{Q}_q^k$  the convective part and with  $\mathbf{D}_q^k$  the dissipation part of the residual  $\mathbf{R}_q^k$  in (D.11) then from Jameson (1993)

$$\begin{aligned} \mathbf{Q}_q^k &= \mathbf{Q} (\mathbf{U}_q^k) \\ \mathbf{D}_q^k &= \beta_q \mathbf{D} (\mathbf{U}_q^k) + (1 - \beta_q) \mathbf{D}_{q-1}^k \\ \mathbf{R}_q^k &= \mathbf{Q}_q^k + \mathbf{D}_q^k \end{aligned} \quad (\text{D.12})$$

If one reduces the linear model corresponding to (D.11) to an ordinary differential equation and indicates with  $\widehat{\mathbf{U}}_{new} = \psi(Z)\widehat{\mathbf{U}}_{old}$  the Fourier amplitude evolution, where  $|\psi(Z)|$  is the amplification factor of the integration, the resulting Fourier symbol has an imaginary part which is proportional to the wave speed and a negative real part proportional to the diffusion. The coefficients  $\alpha_q$  in (D.11) are chosen to maximize the stability interval along the imaginary axis and  $\beta_q$  are chosen to increase the stability interval along the negative real axis. The five-stage scheme which has been found to be particularly effective (Jameson 1993) has coefficients

$$\begin{aligned}\alpha_1 &= 1/4 & \beta_1 &= 1 \\ \alpha_2 &= 1/6 & \beta_2 &= 0 \\ \alpha_2 &= 3/8 & \beta_3 &= 0.56 \\ \alpha_2 &= 1/2 & \beta_4 &= 0 \\ \alpha_2 &= 1 & \beta_5 &= 0.44\end{aligned}\tag{D.13}$$

The stability region of this five-stage Runge-Kutta time-stepping is shown in Fig. D.2.

A first order spatial discretisation on the coarse levels is employed while retaining the second order accurate discretisation on the fine grid. This corresponds to the use of a defect-correction scheme on the coarser levels of the multigrid algorithm (Mavriplis 1998c).

### D.3.2 Preconditioners

Following the approach of Pierce et al (1997), Mavriplis (1998b, 1998a), a point-implicit or a line-implicit Jacobi preconditioner has been used in order to give some degree of implicitness to the multistage scheme. The Jacobi preconditioner can be viewed as a characteristic time-step in contrast with a local time-step also called scalar preconditioner.

**Point-implicit Jacobi Preconditioner** The point-implicit Jacobi preconditioner is based on the form of the discrete residual operator and is obtained by extracting the terms corresponding to the central node in the stencil. Referring to (3.16) and (3.31) the point-Jacobi preconditioner  $[\mathbf{P}]_{PJ}^{-1}$  for a point  $I$  is given by

$$[\mathbf{P}]_{PJ}^{-1} = -\frac{1}{\sigma} \frac{\partial \mathbf{R}_I}{\partial \mathbf{U}_I} = \frac{1}{\sigma} \sum_{s=1}^{m_I} \left( |\vec{\eta}_{IJ_s}| |\mathbf{A}_{IJ_s}| + \tau_{IJ_s} \left. \frac{\partial \mathcal{G}_{IJ_s}}{\partial \mathbf{U}_I} \right|_\mu \right)\tag{D.14}$$

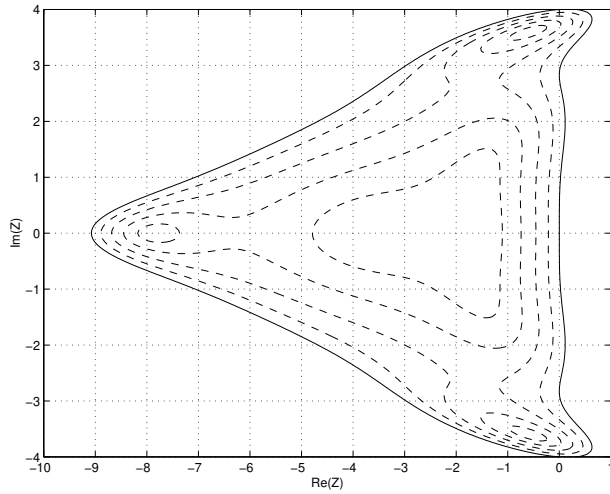


Figure D.2: Stability region and contours defined by  $|\psi(Z)| = 0.2, 0.4, \dots, 1$  for a 5-stage Runge-Kutta time stepping scheme.

where  $\sigma$  is the CFL number. In the derivation of (D.14) the contribution of the source terms has been neglected. For the linearised Navier-Stokes equation the preconditioner assumes the same form and it is evaluated using the steady-state unknown, i.e.

$$\left[ \bar{\mathbf{P}} \right]_{PJ}^{-1} = \frac{1}{\sigma} \sum_{s=1}^{m_I} \left( |\vec{\eta}_{IJs}| |\bar{\mathbf{A}}_{IJs}| + \tau_{IJs} \left. \frac{\partial \bar{\mathcal{G}}_{IJs}}{\partial \bar{\mathbf{U}}_I} \right|_{\bar{\mu}} \right) \quad (\text{D.15})$$

$[\mathbf{P}]_{PJ}^{-1}$  is a  $5 \times 5$  matrix which can be directly inverted using a standard algorithm. The preconditioner  $[\mathbf{P}]_{PJ}^{-1}$  has been obtained considering only the first order dis-

cretisation even when a second order scheme is used. This procedure is analogous to the practice of using a first order discretisation for the Jacobian in implicit methods (defect correction procedure).

Note that for a scalar dissipation scheme, as the one by Jameson et al. (1981), the contribution of the artificial viscosity to  $[\mathbf{P}]_{PJ}^{-1}$  becomes diagonal and the scalar time-step estimate is recovered. Thus for a scalar dissipation scheme the smoother becomes a standard explicit multistage algorithm.

In conjunction with preconditioner (D.14), no other techniques such as residual smoothing (Jameson 1981, Arnnone 1995) are employed.

**Line-implicit Jacobi Preconditioner** In computing high Reynolds number flows, with no-slip boundary condition at solid walls, the problem of grid anisotropy has been tackled by using a directional agglomeration multigrid strategy coupled with a line-implicit smoother. The combination of these two strategies into a single algorithm has been found to result in a more robust and efficient solution method than the use of either strategy alone (Mavriplis 1998b, 1998a).

Directional coarsening techniques were developed in order to overcome the problem related to the directional decoupling in highly stretched grids. Coarsening the grid in the stretching direction allows the smoother to efficiently damp the high error mode along the coarsening direction (Mulder 1989, Pierce et al. 1997). However standard directional coarsening techniques results in sequence of coarse grid levels for which the complexity between successive levels decreases by a factor of 2. The higher complexity of the directionally coarsened levels greatly increases memory overheads and make the use of multigrid W-cycles impractical (Mavriplis 1998b). An alternative approach is obtained with a directional coarsening technique with a fine-to-coarse grid ratio of 4:1. In such case a more efficient smoother in the coarsening direction must be employed. This is obtained by using a lime-implicit preconditioner which achieves superior smoothing of error components along the direction of the implicit lines, as compared with the point-implicit method (Mavriplis 1998b, 1998a). An example of line construction in the boundary layer region of a turbine blade is given in Fig. D.3.

The line-implicit Jacobi preconditioner is obtained by including the complete inviscid and Laplacian operators in the normal direction but only the component corresponding to the central node for the other directions. The resulting matrix represent a tridiagonal  $5 \times 5$  block system which has been solved using a Jacobi

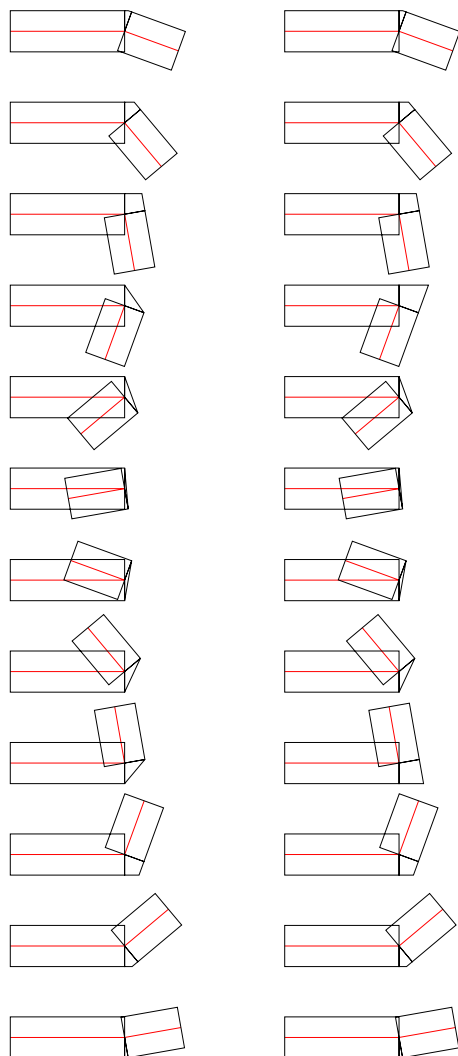
iterative procedure.

## D.4 Example

The steady-state flow over a 2D turbine blade were used in order to assess the efficiency of the line-implicit preconditioner coupled with a full directional coarsening in the boundary layer. The directional line in this region are shown in Fig. D.3 while the control volumes of the fine mesh and three successively agglomerated grid are shown in Fig. D.4 The test case correspond to the 11<sup>th</sup> International Standard Configuration at transonic off-design conditions studied in Chapter 4. Fig. D.5 show the convergence history of the density residual using two and four grids in a W-type cycle. The convergence history of the implicit (single grid) method of Sayma et al. (2000) is also plotted.

## D.5 Concluding Remarks

(i) Efficient steady-state and linearised unsteady calculations can be performed using the multigrid relaxation scheme presented in the Appendix. The line-Jacobi preconditioner is used for turbulent viscous flow solved up to the wall while the point-Jacobi version is used for the other flow representations. (ii) The preconditioned agglomeration multigrid needs to be improved in order to enhance both performance and robustness, especially in 3D. A more accurate prolongation operator need to be developed. This task is non-trivial because of the absence of an underlying grid. The preconditioner may cause some instabilities at stagnation points, where large variations of the flow angle appear at significant velocity values. This loss of robustness can be attributed to a flow-angle sensitivity thus improvement in this direction should be made.

Figure D.3: 11<sup>th</sup> Standard Configuration. Directional lines

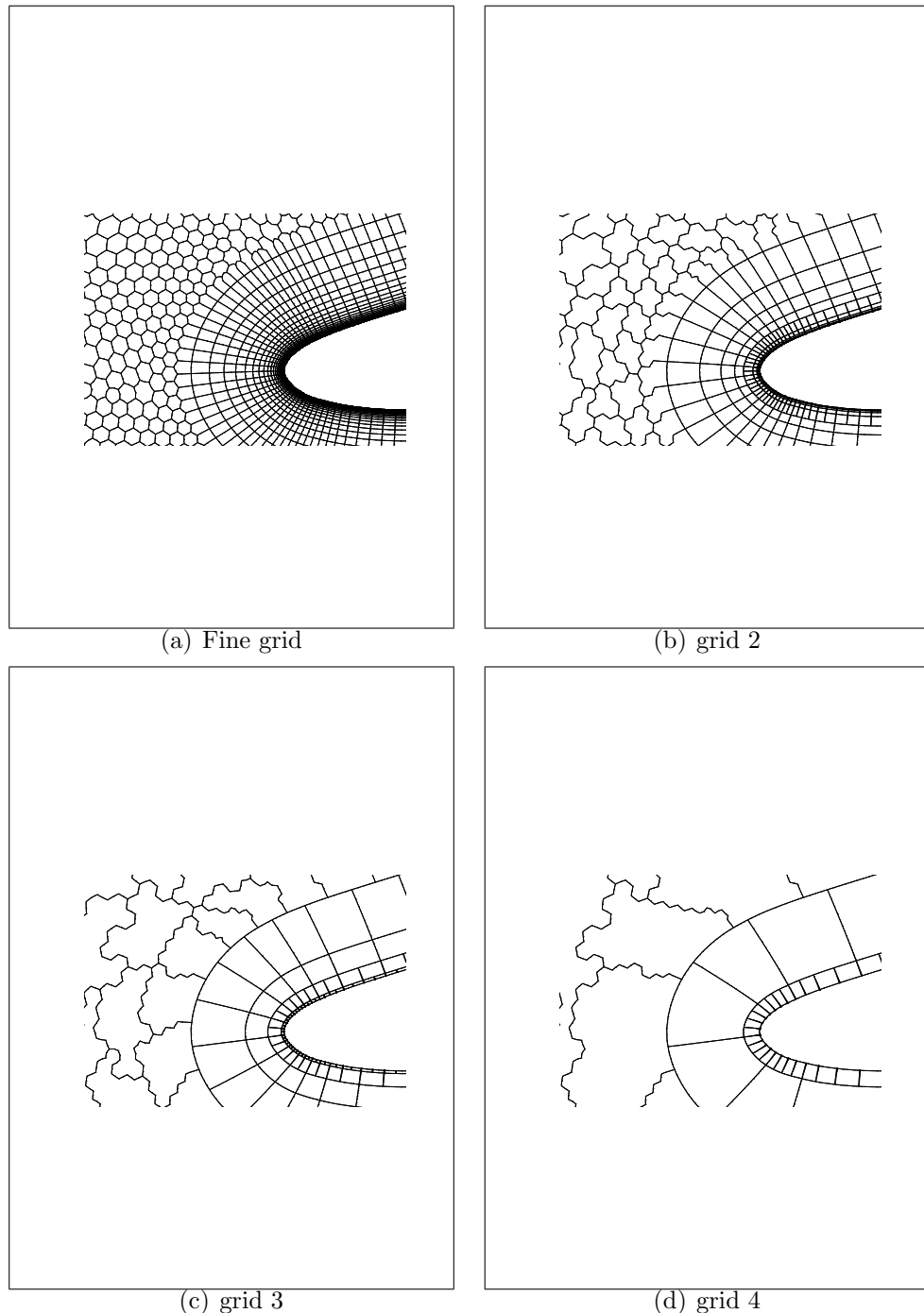


Figure D.4: 11<sup>th</sup> Standard Configuration (turbulent flow calculation up to the wall). Agglomerated control volumes

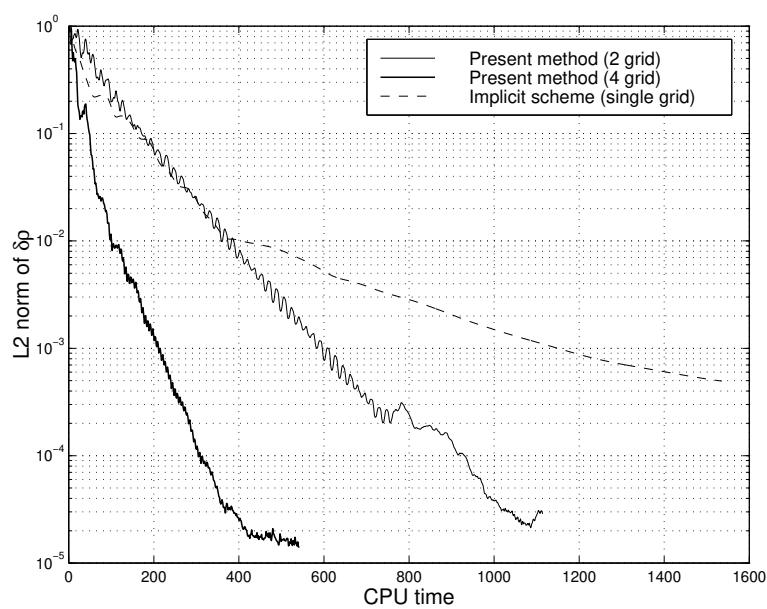


Figure D.5: 11<sup>th</sup> Standard Configuration (turbulent flow calculation up to the wall): convergence histories